# University of Alberta

Intrafractional Tumour-Tracked Irradiation using a Linac-MR

by

Jihyun Yun

A thesis submitted to the Faculty of Graduate Studies and Research
in partial fulfillment of the requirements for the degree of

Doctor of Philosophy

in

Medical Physics

Department of Physics



Fall 2013

Edmonton, Alberta

To my wife, *Woohyun*.

## Abstract

Intrafractional tumour tracking is of considerable interest as a means to minimize the PTV in treating mobile tumours. By utilizing the intrafractional MR imaging feature of linac-MR, this thesis seeks to develop a direct, non-surrogate based intrafractional tumour tracking system, and physically demonstrate its feasibility by delivering highly conformal dose to a moving target undergoing simulated lung tumour motions.

An autocontouring algorithm was developed to determine the shape and position of a lung tumour from each intrafractional MR image. Because our linac-MR systems are equipped with low field MRI (0.2/0.5 T), the algorithm was initially evaluated using a lung motion phantom simulating low field MR images by using a single 3 T scanner. Also, an initial *in-vivo* study was performed to verify the feasibility of lung tumour autocontouring using real patient data.

Motion prediction software was developed to compensate for the tumour motions during system delay (time interval between detection of current tumour position and beam delivery) in MRI-based tracking. Prediction accuracy was evaluated using 1D superior–inferior lung tumour motions of 29 lung cancer patients for system delays of 120 – 520 ms.

In our prototype linac-MR, MLC motors are operated in the close proximity of the MRI. Due to this, we investigated (1) appropriate RF shielding around the motors to mitigate the negative effects of RF motor noise in MR images, and (2) the effect of strong external magnetic field on the functionality of MLC motors.

Intrafractional tumour-tracked irradiation to a moving target was physically demonstrated using the prototype linac-MR. Two different motion patterns (sine and modified cosine) were used to simulate lung tumour motions. Comparing the film measurement results from moving target irradiation with our tracking system to static target irradiation, 50 % beam width revealed minimal differences of < 0.5 mm, while the increase in 80 % - 20 % penumbra width was limited to 0.4 and 1.7 mm in the sine and modified cosine patterns, respectively.

The performance of our tracking system shown in this research illustrates potential dosimetric advantages of intrafractional MR tumour tracking in treating mobile tumours as shown for the phantom study.

## Acknowledgements

I have always felt grateful that I can be a part of the Linac-MR team at the CCI, the world's most innovative research group in our field. During my Ph.D, there have been many numbers of mentors, colleagues, and friends whom I cannot thank enough. Here, I intend to acknowledge and show them my sincere appreciation.

I certainly owe the most to my supervisor Dr. B. Gino Fallone. Despite many challenges during my research, he always stayed positive and provided critical feedback as well as financial support. I must acknowledge my co-supervisor Dr. Marc MacKenzie, who initiated and essentially built a roadmap of my project. Special thanks to Dr. Don Robinson and Dr. Satyapal Rathee, who never said no to my uncountable number of visits to their offices for many different scientific issues. I appreciate Dr. Keith Wachowicz, who has been deeply involved with my project and my number one source of MRI knowledge. Thanks to Drs. Ron S. Sloboda, Sharon Morsink, and Steve Jiang who kindly spent their time and effort to review and improve my thesis.

It has been a lot of fun talking, debating, and laughing together with my colleagues during my study. Thank-you to: Sandra, Lesley, Amr, Yingli, Artur, Katie, Eugene, and Danielle. I will always remember the moments with you.

The Medical Physics department at the CCI is full of warm-hearted experts, and with their help I was able to accomplish my goal. I appreciate you all. It has been a great journey.

## Table of Contents

## List of Tables

## List of Figures

## List of Abbreviations

| | |
|---|---|
| 2D | Two dimensional |
| 3D | Three dimensional |
| 4D | Four dimensional |
| ABC | Active-breathing control |
| ANN | Artificial neural networks |
| AP | Anterior-Posterior |
| bSSFP | Balanced steady state free precession |
| BW | Bandwidth |
| CBCT | Cone beam CT |
| CCI | The Cross Cancer Institute |
| CNR | Contrast-to-noise ratio |
| CRT | Conformal radiation therapy |
| CT | Computed tomography |
| CTV | Clinical target volume |
| EPID | Electronic portal imaging devices |
| FE | Frequency encoding |
| FID | Free induction decay |
| FSB | Forced shallow breathing with abdominal compression |
| FT | Fourier transform |
| GE | Gradient echo |
| GTV | Gross tumour volume |
| ICRU | International commission of radiation units and measurements |
| IGRT | Image-guided radiation therapy |
| IM | Internal margin |
| IMRT | Intensity modulated radiation therapy |
| ITV | Internal target volume |
| IW | Initial weights |
| kV | Kilovoltage |
| Linac | Linear accelerator |
| LR | Left-Right |

| | |
|---|---|
| MLC | Multi-leaf collimators |
| MR/MRI | Magnetic resonance imaging |
| MV | Megavoltage |
| NMR | Nuclear magnetic resonance |
| NSCLC | Non-small cell lung cancer |
| OR | Organs at risk |
| PD | Proton density |
| PE | Phase encoding |
| PET | Positron emission tomography |
| PRV | Planning organ at risk volume |
| PSO | Particle swarm optimization |
| PTV | Planning target volume |
| RF | Radio frequency |
| RG | Respiratory gating |
| RPM | Real-time position management |
| RTRT | Real-time tumor tracking |
| SAR | Specific absorption rate |
| SE | Spin echo |
| SI | Superior-Inferior |
| SM | Set-up margin |
| SNR | Signal-to-noise ratio |
| SSFP | Steady state free precession |
| TFT | Thin film transistors |
| US | Ultrasound |
| XBRT | External beam radiation therapy |

## List of Symbols

| | |
|---|---|
| ~ | Approximately |
| $\alpha$ | Tipping angle |
| $B_0$ | Main static magnetic field |
| $B_1$ | Circularly polarized magnetic field |
| $E_Z$ | Zeeman splitting energy |
| $FT/FT^{-1}$ | Fourier transform/Inverse Fourier transform |
| $G$ | Linear magnetic field gradient |
| $^1H$ | Hydrogen nuclei |
| $k$ | Boltzmann constant |
| $M$ | Net magnetization |
| $M_0$ | Net magnetization at equilibrium |
| $M_{XY}$ | Transverse magnetization |
| $M_Z$ | Net magnetization in Z direction |
| $P(\vec{r})$ | Spin density and signal effects due to relaxation at location $\vec{r}$ |
| $S$ | Spin angular momentum |
| $S(t)$ | MR signal at time $t$ |
| $T_1$ | Longitudinal relaxation time constant |
| $T_2$ | Transverse relaxation time constant |
| $TE$ | Echo time |
| $TR$ | Repetition time |
| $\gamma$ | Gyromagnetic ratio |
| $\mu$ | Nuclear magnetic moment |
| $\omega_0$ | Larmor frequency |

# Chapter 1: Introduction

## *1.1. OVERVIEW OF THE THESIS*

As a proven method for treating and curing cancer, radiation therapy has been evolved for more than 100 years. Medical physicists today have many options to play their role in clinic to deliver the prescribed dose of radiation accurately, effectively and safely. Nevertheless, radiotherapy treatment of mobile tumours (e.g. lung tumour) that show extensive intrafractional motion with radiation is still a difficult task. Although various tumour tracking techniques have been developed to overcome this issue, all currently available tracking systems share their shortcomings in tracking accuracy due to the indirect nature of their tracking mechanisms based on internal and/or external tumour surrogates. In this thesis, we seek to develop a direct, non-surrogate based intrafractional tumour tracking system using a linac-MR, and physically demonstrate its feasibility by delivering highly conformal dose to a moving target undergoing simulated lung tumour motions.

The structure of this thesis is as follows: Chapter 1 introduces modern external beam radiation therapy techniques, discusses their shortcomings in treating mobile tumours, and provides justification for this research. Chapter 2 presents theories that are relevant to this research including magnetic resonance imaging (MRI), artificial neural networks (ANN), and particle swarm optimization (PSO). Chapter 3 introduces lung tumour autocontouring software that is compatible with MR images. A modified version of this chapter has been

published in *Medical Physics*.[1] Chapter 4 presents an initial *in-vivo* study evaluating the lung tumour autocontouring software using real patient data. A modified version of this chapter was presented at the 54th annual meeting of the American Association of Physicists in Medicine (AAPM).[2] Chapter 5 introduces tumour motion prediction software designed specifically for MRI-based tracking environment. A modified version of this chapter has been published in *Medical Physics*.[3] Chapter 6 discusses the effect of strong external magnetic field on the functionality of MLC motors. A modified version of this chapter has been published in *Medical Physics*.[4] Chapter 7 presents appropriate RF shielding around the MLC motors to mitigate the negative effects of RF motor noise in MR images. A modified version of this chapter has been published in *Physics in Medicine and Biology*.[5] Chapter 8 describes physical demonstration of intrafractional tumour tracking using a prototype linac-MR. A modified version of this chapter has been published in *Medical Physics*.[6] Chapter 9 is a concluding chapter to the thesis.

## 1.2. EXTERNAL BEAM RADIATION THERAPY

In current cancer treatment, approximately half of all patients receive some form of radiation treatment.[7] External beam radiation therapy (XBRT) is the most widely used treatment method, which refers to the delivery of ionizing radiation beam to a tumour volume where the source of radiation is located outside of the patient's body. Therapeutic radiation dose can be delivered using x-rays (high energy photons) or charged particles (electrons, protons, heavy ions,

etc). In clinic, the most common source of radiation is a medical linear accelerator, i.e. linac, that produces high energy photon and electron beams.

### 1.2.1. Target volume definition

The ultimate goal of radiation therapy is to deliver the prescribed therapeutic dose of radiation to the tumour volume while minimizing the unnecessary dose to its surrounding normal tissues and critical structures. In practice, however, some amount of unwanted dose is inevitably delivered to surrounding tissues. This is due to the uncertainty in defining tumour region, inter or intrafractional tumour motion and deformation, patient positioning errors, and/or the geometric uncertainty of machine parameters. To account for these uncertainties in radiation therapy, the International Commission of Radiation Units and Measurements (ICRU) suggested several target volume definitions as shown in Fig. 1.1.

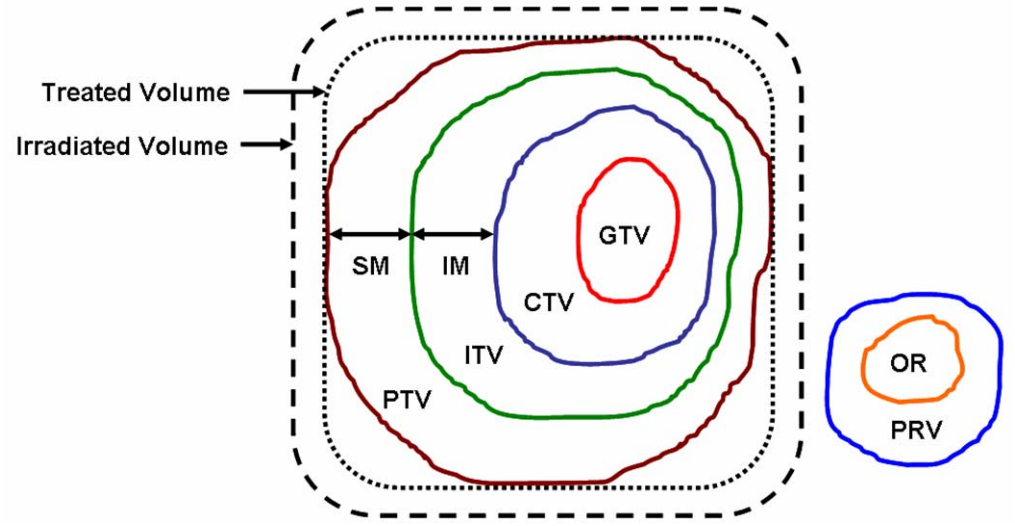


**Figure 1.1 Target volume definitions in radiation therapy (ICRU 50 and ICRU 62 reports).**

Target volumes are defined in ICRU 50 and ICRU 62 reports as the following:[8, 9]

(1) Gross tumour volume (GTV): GTV is defined as the palpable or visible extent of the malignant tumour, evaluated by physical exams and various imaging techniques.

(2) Clinical target volume (CTV): CTV is composed of the GTV and a margin around the GTV to include direct, local subclinical spread of tumour.

(3) Internal Margin (IM): A margin added to the CTV compensating for expected movements and variation in size, shape and position of the CTV.

(4) Internal target volume (ITV): ITV represents the volume encompassing the CTV and the IM.

(5) Set-up margin (SM): A margin added to the ITV to account specifically for uncertainties in patient positioning and alignment of the therapeutic beams.

(6) Planning target volume (PTV): PTV is a geometrical concept used for treatment planning, which is composed of the CTV, IM and SM. The PTV is defined to ensure the delivery of prescribed dose to the CTV.

(7) Organs at risk (OR): OR are normal tissues whose radiation sensitivity may significantly influence treatment planning and/or prescribed dose.

(8) Planning organ at risk volume (PRV): PRV is an expansion of the OR to compensate for any movement of the OR and the set-up errors during treatment.

(9) Treated volume: Volume enclosed by prescribed isodose surface.

(10) Irradiated volume: Volume that receives a significant dose compared to normal tissue tolerance.

### 1.2.2. 3D conformal radiation therapy

3D conformal radiation therapy (CRT) is a modern radiation therapy technique that can deliver conformal dose to the tumour, i.e. radiation beam can be shaped to match the target volume.[10] 3D CRT treatments are planned based on patient specific, 3D anatomical information obtained from computed tomography (CT) and/or MRI. Based on the 3D anatomy, treatment plans are developed to achieve dose distributions where higher dose regions are concentrated within the tumour volume while minimizing the amount of unnecessary dose to surrounding healthy tissues.

### 1.2.3. Intensity modulated radiation therapy

Intensity modulated radiation therapy (IMRT) is an advanced radiation therapy technique that is capable of (1) beam conformation as in 3D CRT, as well as (2) beam intensity modulation.[10] In IMRT, several radiation beam orientations, each with its own fluence distribution, are designed. In general, multi-leaf collimators (MLC) and/or compensators are used to modulate beam intensity within each beam.

IMRT can be used for any XBRT, delivering beams of non-uniform fluences to a patient from different directions. The directions and intensities of beams are optimized to deliver tightly bounded dose distributions to the target volume with steep dose gradients outside of its boundaries.

### 1.2.4. Treatment errors

3D CRT or IMRT can deliver conformal dose to the target volume. However, this is beneficial only if (1) the target volume is accurately defined, and (2) the therapeutic dose is delivered to the target volume exactly as it is planned. Only in this case, the steep dose gradients achieved in both techniques will spare normal tissues located nearby the target volume.

In practice, however, certain amounts of treatment errors are inevitable due to the following reasons:

(1) Uncertainty in target volume definition

Accurate definition of the CTV is a major concern in conformal beam delivery. Advanced imaging modalities such as CT, MRI, or positron emission tomography (PET) can visualize structural or physiological abnormalities, which might be the indication of the extent of the GTV. However, currently no imaging modality can directly visualize the microscopic spread of malignant tumour cells. Thus, defining the CTV involves certain patient population based assumptions or estimations to best approximate the tumour extent.

If the CTV over or underestimates the microscopic spread of the disease, both 3D CRT and IMRT lose their significance of being conformal. Further, conformal beam delivery to the underestimated CTV may cause worse treatment outcomes compared to the ones using non-conformal radiation beam, due to seriously under dosed tumour cells.[10]

(2) Organ motion

Inter or intrafractional organ motion is another important reason why the actual received dose distribution deviates from the planned dose distribution.[11] Interfractional organ motion causes the CTV changes on a daily basis, and this is mainly associated with the organs closely located or a part of the digestive system. In case of prostate, several studies have shown that the interfractional motion can occur up to 20 mm.[11] The patient's weight gain or loss can also affect the CTV location.

Intrafractional organ motion, i.e. the organ motion occurring while the patient is being irradiated, is mainly due to respiratory and cardiac motions. Respiratory induced organ motion mainly impacts the thoracic and abdominal tumours. In case of liver, the peak-to-trough motion during deep breathings can be up to 80 mm in the superior-inferior (SI) direction.[11]

(3) Patient set-up errors

Patient set-up errors can be inter and/or intrafractional, causing the difference between the intended position of the target volume and the actual one with respect to the treatment beam.

The interfractional set-up error is mainly due to the patient misalignment, coming from several sources including mechanical (e.g. laser misalignment), patient related (e.g. movement of skin marks, fixation failure due to patient motion), and/or the variations in patient positioning among radiation therapists.[12] The intrafractional set-up error is caused by the patient's periodic motions (e.g. breathing or heartbeat cycles) or random motions (e.g. passing gas) while being irradiated.

The magnitude of set-up errors varies depending on treatment sites.

Previous studies have reported the interfractional set-up errors, i.e. deviations between different fractions during a treatment series, ranging from 1.1 - 2.5 mm for head and neck to 1.7 – 5.8 mm for breast.[12] Systematic set-up errors, i.e. the deviations between the planned patient position and the average patient position over an entire course of treatment, range from 1.6 – 4.6 mm for head and neck to 1.0 – 4.1 mm for breast.[12] These data were obtained using various kinds of immobilization for both sites. In breast treatment, systematic set-up errors increased up to 14.4 mm without immobilization.

## *1.3. IMAGE-GUIDED RADIATION THERAPY*

Image-guided radiation therapy (IGRT) utilizes frequent pre- or post-treatment session imaging in the treatment room to guide the radiation therapy. The main goal of IGRT is the optimal reduction of the IM and the SM shown in Fig. 1.1.[13] These margins are added to the CTV to compensate for the organ movement and the patient set-up errors during the course of radiation treatment.

Before IGRT was implemented in clinic, patient set-up was done by aligning the patient's skin marks to the treatment beam. Since the skin marks are generated during the treatment simulation, any organ movement occurred between the simulation day and the actual treatment day is unknown. Also, it is unsafe to assume that the patient positioning between the two days would be identical, even if immobilization devices are used.[14] Due to these reasons, large IM and SM must be added to the CTV.

Using IGRT, however, the patient can be imaged during set-up procedure prior to the actual beam delivery in each fraction. From this, interfractional

variations due to daily patient positioning errors or changes in anatomy can be constantly monitored and minimized,[15] which leads to the reduction of the SM required to ensure the delivery of sufficient dose to the target volume. The following sections provide a brief summary of imaging modalities implemented in current IGRT.

### 1.3.1. Portal imaging

In current radiation therapy, the target volume is typically irradiated from several directions with appropriate radiation fields, i.e. radiation ports. Using portal imaging, 2D beam's eye view images of the treated volume and its surroundings can be acquired at any beam direction while the patient is in treatment position.

Portal imaging was initially performed with diagnostic quality kilovoltage (kV) imaging in 1958.[16] In this system, a retractable x-ray source was placed within the head of the linac, and an image intensifier was used to acquire the image. Another design using kV imaging was suggested by Biggs *et al*. in 1985.[17] Here, the x-ray tube was mounted on the side of the linac head, and radiographic film was used for image acquisition. Compared to megavoltage (MV) imaging, kV imaging can provide better contrast using less patient dose. Despite these advantages, kV imaging based portal imaging was not developed further in the future linac designs. This might be due to the workflow issues in clinic,[18] difficulty in film registration,[19] and mechanical constraints, e.g. the collimator rotation was blocked in Biggs's system.[17]

Electronic portal imaging devices (EPID) are the most widely used IGRT technology,[13] which utilize the therapy x-ray beam (MV beam) itself to create 2D portal images of the patient. The patient is located between the beam source (head of the linac) and a detector attached on the opposite side. Although radiographic films were used for image acquisition in the past, typical modern EPID are equipped with an electronic flat panel imager using thin film transistors (TFT) fabricated from hydrogenated amorphous silicon (a-Si:H).[20] Using EPID, 2D MV radiographic images of the patient can be acquired on the treatment day, while the patient is positioned in the treatment position.

EPID can be used for (1) localization and/or (2) verification imaging.[20] In localization imaging, portal images are created prior to the delivery of treatment dose and used for patient set-up adjustments. Whereas in verification imaging, portal images are acquired during the actual beam delivery generating a record of how the treatment was performed. In this case, portal images are used to verify the correct dose delivery.

Although very useful, additional radiation dose to the patient must be considered when using EPID, because they utilize the therapy x-ray beam for imaging.[21] Also, MV imaging provides poor soft tissue contrast compared to kV imaging.[21, 22] Despite the source of radiation, the image quality in projection imaging using flat panel detectors is further degraded due to the 2D nature of imaging, which overlays 3D structures onto a 2D plane.

### 1.3.2. Cone beam CT

The shortcoming of the projection imaging can be largely compensated by cone beam CT (CBCT), which can provide volumetric imaging using a 2D imager while the patient is in the treatment position. During CBCT, hundreds of projections are acquired while the linac gantry rotates around the patient with a rotation time ranging from 30 – 120 seconds.[23] CBCT might be performed using MV or kV x-ray beams.[24-26] However, kV CBCT was shown to be superior in terms of soft tissue contrast and signal-to-noise ratio (SNR).[22]

More common, clinical CBCT systems are composed of a retractable kV x-ray source and an electronic flat panel detector that are mounted on the linac gantry orthogonal to the treatment beam direction. This system can produce patient images with sub-millimetre spatial resolution and high SNR,[27] and has been used for patient set-up verifications.[28] Compared to projection imaging, relatively larger radiation dose to the patient during imaging is one drawback of CBCT, which depends on the imaging parameters and anatomic sites.[28, 29] Also, utilizing CBCT for set-up verifications is only possible prior to treatment, because the slow volumetric imaging data acquisition requires mechanical rotation that cannot be performed during beam delivery.[13]

### 1.3.3. Ultrasound

Additional radiation dose to the patient is always a concern in both portal imaging and CBCT, because they require ionizing radiation for imaging. Ultrasound (US) is an example of IGRT technique that is free of ionizing radiation. In US, a transducer transmits brief pulses of US waves, and the

reflections of the waves from different tissue interfaces are used to produce an image.[30] US visualizes soft tissues, and has been used for daily target localizations mainly in prostate and upper abdominal regions.[31-33] Studies have reported that the performance of US in target localization is functionally equivalent to CT in prostate.[34] Also, US can be used as a useful adjunct to CT in planning partial breast radiotherapy.[35] However, US is not suitable to image gaseous regions such as lung, and there exists significant inter-operator variability in the image quality and the patient alignment processes.[33]

## *1.4. MANAGING INTRAFRACTIONAL TUMOUR MOTIONS*

IGRT has improved target localization and delivery of highly conformal radiation dose to the target volume.[15, 23] Using IGRT, interfractional variations due to daily patient positioning errors or changes in anatomy can be monitored and minimized. However, a problem still emerges when treating tumours with extensive intrafractional motions, e.g. lung tumour. At present, a method of directly imaging and tracking tumours during actual beam delivery does not exist, and this presents potential limitations to accurate radiotherapy treatments. Currently available techniques to deal with the intrafractional tumour or organ motions are the following.

### 1.4.1. Extra margin

Extra margins can be added to the CTV to ensure sufficient target coverage despite the intrafractional tumour motions. According to the ICRU

target volume definition shown in Fig. 1.1, the IM should be added to the CTV to compensate for expected movement of the CTV. Several studies reported the appropriate margins for different treatment sites.[36-38] This approach, however, may result in radiation-induced complications due to excessive normal tissue irradiation adjacent to the tumour.[39]

### 1.4.2. Respiratory gating

Respiratory motion is the major source of intrafractional tumour motions, especially for abdominal and thoracic tumours including lung, pancreas, kidneys, liver, etc.[40, 41] Several techniques have been used to reduce the range of respiratory motion in radiotherapy, including active-breathing control (ABC) or forced shallow breathing with abdominal compression (FSB).[42] In ABC, the patient must follow the breathing instructions, thus many infirm patients may have difficulties to comply. FSB may cause problems for the patients with particularly poor pulmonary function, and those with percutaneous gastrostomy tube. Similarly, the patients with large abdominal aortic aneurysms may not be suitable for FSB.[43]

The respiratory gating (RG) techniques were developed to treat the above-mentioned abdominal and thoracic tumour sites while patients are under free-breathing, as opposed to controlled breathing as in ABC or FSB. RG requires some form of internal or external markers to monitor the patient's breathing cycle during treatment. Among various commercial RG devices, the Varian real-time position management (RPM) system (Varian Medical Systems, Palo Alto, CA) uses an external marker block placed on the patient's abdominal region,[40] whereas

the real-time tumor tracking (RTRT) system (Hokkaido university, Sapporo, Japan) requires a gold seed implanted near the tumour.[44] In RG, therapeutic radiation is delivered only during a particular time interval of the patient's breathing cycle referred to as a gating window.[41] The gating window is typically open when the patient's breath is in the exhaled state where the tumour moves the least.[40] Several clinical studies have shown the feasibility of margin reduction and tumour dose escalation using RG techniques in lung, liver, and breast cancer treatments.[45-47]

Disadvantages of RG are the following: (1) treatment efficiency is low, typically 30 – 50 %, because the beam is on for only a portion of breathing cycle.[41] This increases the overall treatment time of each fraction in practice. (2) Patients with irregular breathing cycles cannot be treated using RG.[41] (3) RG relies on the location of surrogates to determine the beam on/off timings during treatment. This may cause critical errors in target localization if the correlations between internal tumour motion and surrogates displacement are not sufficiently known or change during treatment.[48]

### 1.4.3. Intrafractional tumour tracking

Both "Intrafractional tumour tracking" and "real-time tumour tracking" refer to the method to continuously track the tumour with radiation beam during beam delivery. This will be referred to as intrafractional tumour tracking hereinafter in this thesis. Two different approaches, invasive or non-invasive, have been proposed for target localization in intrafractional tumour tracking.

Non-invasive approach:

RPM system[49] is the only non-invasive target localization approach suggested for intrafractional tumour tracking. During treatment, the location of an external marker block placed on a patient's chest is monitored by an infrared camera at 30 Hz. This data is used to estimate the internal tumour position based on the correlation between the location of marker block and the tumour centroid, where the correlation is established prior to the treatment using planning CT images.

Invasive approach:

(1) CyberKnife (Accuray Incorporated, Sunnyvale, CA)[50] uses both external and internal tumour surrogates to estimate tumour positions during beam delivery. The patient wears a customized vest that contains several external markers. These markers are monitored by a camera to update the external patient motion. Also, metallic surrogates need to be surgically inserted near the tumour, and these are periodically imaged by two orthogonal kV x-ray systems. The frequency of x-ray imaging is defined by the user. During treatment, the position of tumour is estimated by the assumed correlation between the external patient motion and the location of internal surrogates. This correlation is established prior to the treatment and periodically updated using the x-ray images.

(2) Both RTRT system[51] and VERO system (BrainLAB, Feldkirchen, Germany, and Mitsubishi Heavy Industries, Tokyo, Japan)[52, 53] use metallic seeds as internal tumour surrogates. The locations of these surrogates are continuously monitored during beam delivery by two orthogonal diagnostic x-ray systems

running in fluoroscopic mode. Using these images, internal tumour positions are estimated. Fluoroscopic imaging adds additional dose to the patient. In RTRT system, the maximum skin dose was 1.37 ± 0.06 mGy/min (imaging at 30 Hz)[54] during tracking. In VERO system, the additional dose was 0.117 mGy per pair of stereo x-ray shots.[53]

(3) 4D Localization System (Calypso Medical, Seattle, WA)[55, 56] using radio frequency (RF) tracking is the only invasive target localization method that is free of radiation. A cylindrical RF transponder (8 mm in length × 2 mm in diameter) called "Beacon" is implanted to the patient near or within the tumour prior to the treatment. During treatment, 3D location of the beacon is continuously monitored at 10 Hz by a non-contact detector array positioned above the patient. Using this data, internal tumour positions are estimated.

Although various methods have been developed for intrafractional target localization, the use of MLC for intrafractional beam conformation is common. Previous studies have shown the feasibility of intrafractional MLC control to track 3D translational tumour motions,[57] as well as 2D rotational tumour motions with shape deformation.[58, 59] One exception is Cyberknife, which uses a beam collimator called "Iris" that can generate variable sizes of approximately circular beam.[60]

### 1.4.4. Current limitations of intrafractional tumour tracking

Intrafractional tumour tracking is one of the most promising techniques in managing tumour or organ motions. If this technique is accurately executed, the

IM illustrated in Fig. 1.1 may be significantly reduced or eliminated. At present, however, accurate target localization remains the biggest challenge in intrafractional tumour tracking. Whether invasive or non-invasive, all current target localization methods are based on indirect tracking through the use of internal and/or external tumour surrogates. Reliance on surrogates, however, has been shown to be problematic for accurate tumour tracking for the following reasons:

(1) Implanted seeds, for liver and prostate tumours,[61] have been shown to migrate by up to 5.1 mm and 4.5 mm from their initial positions, respectively. In some cases, the seeds might be completely dislodged during the course of the radiation treatment. Imura *et al.*, in a study of 57 patients, reported that 25 % of total surrogates was lost during the course of lung tumour treatments.[62]

(2) Tracking using external surrogates assumes good correlations between internal tumour motion and external surrogate displacement, whereas mismatches between tumour and surrogates up to 9 mm have been shown.[63, 64]

(3) Any deformation of tumour shape is completely unknown during tracking. Moreover, since the implanted seeds are usually placed only within the tumour, the motion of the nearby soft tissue and healthy organs, and their relationship to the tumour, are not known during tracking.

Due to the indirect nature of surrogates based tracking mechanisms, the shape and position of the tumour must be inferred from the location of the surrogates during tracking. Therefore, to account for the uncertainty in correlation between tumour position and surrogates, extended regions surrounding the lesion must be irradiated in order to ensure sufficient target coverage.[36]

## 1.5. HYBRID RADIOTHERAPY-MRI SYSTEMS

Current challenges in intrafractional tumour tracking come from the indirect, surrogates based tracking mechanisms. Thus, a logical solution is to develop a tracking system that can directly track the tumour during beam delivery without the need of surrogates. To achieve this, such system must be able to acquire intrafractional images of the tumour with (1) high enough temporal resolution to monitor intrafractional tumour motions, and (2) sufficient spatial resolution and soft tissue contrast to visualize the tumour and detect its location without having to rely on surrogates. MRI satisfies these imaging requirements. Previous studies have reported that MRI provides excellent soft tissue contrast and sufficient temporal and spatial resolutions to observe organ motions at various anatomical sites including lung, breast, prostate, etc.[65-68]

As explained before, the linac is the most common source of therapeutic radiation in clinic, and MRI is a radiation free imaging modality suitable for intrafractional imaging. Thus, hybrid radiotherapy-MRI systems should be considered as a promising platform to realize direct, non-surrogates based intrafractional tumour tracking in addition to reducing patient set-up errors via improved tumour localization.

Several groups have proposed hybrid radiotherapy-MRI systems.[69-72] A common feature of these systems is the intrafractional MR imaging capability, i.e. MR imaging during beam delivery. A group at the University Medical Center Utrecht (Utrecht, Netherlands) has proposed the integration of a 1.5 T MRI (solenoid superconducting magnet) with a 6 MV linac.[70] In this design, the

therapeutic x-ray beam path is perpendicular to the main magnetic field direction, where the beam must pass through the outer cover of the MRI including the cryostat.

ViewRay (Cleveland, OH) has developed another hybrid radiotherapy-MRI system.[71, 72] Their system consists of a 0.35 T MRI (double doughnut superconducting magnet, Helmholtz type) coupled with a rotating gantry that houses three radiotherapy heads (located 120° apart) each containing its own Co-60 source. The rotating gantry is placed in between the double donut magnet, and the path of therapeutic radiation beam is perpendicular to the main magnetic field direction.

Our group at the Cross Cancer Institute (CCI) in Edmonton, AB, Canada has proposed the coupling of a 6 MV linac with a low field MRI, referred to as "linac-MR". Our linac-MR design has two configurations. The first configuration called a perpendicular configuration is shown in Fig. 1.2. In this design, the linac is mounted on the side of the biplanar magnet, such that the treatment beam is oriented perpendicular to the main magnetic field. As shown in Fig. 1.2.b, the linac and MRI rotate in unison to deliver radiation from different angles.

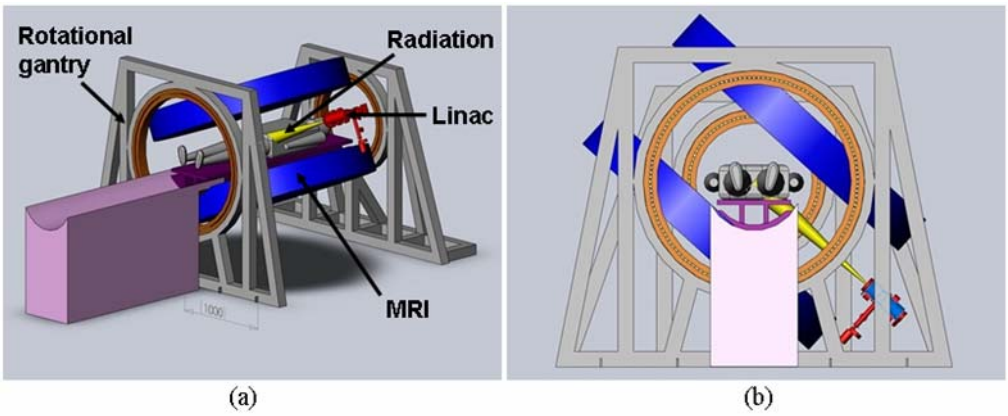


**Figure 1.2 Perpendicular configuration of linac-MR.**

A prototype linac-MR of the perpendicular configuration was installed in 2009 at the CCI, which is composed of a 6 MV linac coupled to a 0.2 T MRI (biplanar permanent magnet). Using this, the CCI group demonstrated the world's first MR imaging during irradiation.[69]

The second configuration called a parallel configuration is shown in Fig. 1.3. Here, the linac is mounted exterior to the biplanar magnet on the magnet's symmetry axis, such that the treatment beam is oriented parallel to the main magnetic field. As shown in Fig. 1.3.b, the linac and MRI rotate in unison to deliver radiation from different angles.

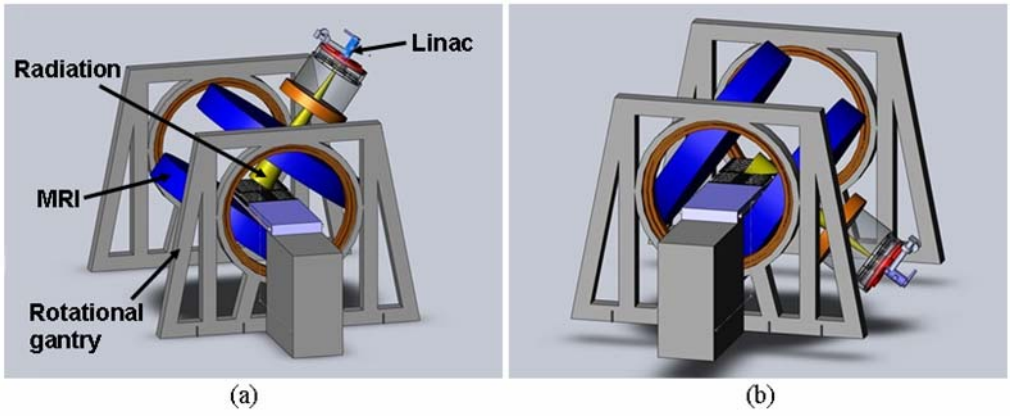


**Figure 1.3 Parallel configuration of linac-MR.**

There exist dosimetric advantages in the parallel configuration compared to the perpendicular configuration. The advantages include (1) decrease in beam penumbra, (2) dose increase to the PTV, (3) no lateral shift in dose distribution, and (4) reduction of the hot and cold spots at tissue-air interfaces.[73] The CCI group is currently installing the parallel configuration linac-MR that is composed of a 6 MV linac and a 0.5 T MRI.

## 1.6. RESEARCH MOTIVATION

All currently available intrafractional tumour tracking systems share the same fundamental limitation, the lack of intrafractional imaging capability. This is the main reason why the indirect, surrogates based tracking techniques have long been used in clinic, despite their disadvantages mentioned in Sec. 1.4.3.

Our linac-MR system has the potential to overcome this fundamental limitation by its intrafractional MR imaging feature. If this feature can be successfully integrated into tumour tracking processes, it will be possible to develop a direct, non-surrogate based intrafractional tumour tracking system that is free of ionizing radiation and invasive implantation of surrogates. In this research, our objective is to investigate the requirements to realize intrafractional tumour tracking using the linac-MR, and prove its feasibility through experimental demonstrations. Emphasis is given to lung tumours, because they are of special interest for tracking due to the potential for complicated, large ranges of intrafractional motions.

## 1.7. REFERENCES


[1] J. Yun, E. Yip, K. Wachowicz, S. Rathee, M. Mackenzie, D. Robinson, and B. G. Fallone, "Evaluation of a lung tumor autocontouring algorithm for intrafractional tumor tracking using low-field MRI: A phantom study," Med. Phys. **39**(3), 1481-1494 (2012).

[2] E. Yip, J. Yun, Z. Gabos, K. Wachowicz, S. Rathee, and B. G. Fallone, "Evaluation of a Real Time Tumour Autocontouring Algorithm Using In-Vivo Lung MR Images with Various Contrast to Noise Ratios," presented at the 54th Annual Meeting of the AAPM, Charlotte, NC, July 29 - August 2, 2012.

[3] J. Yun, M. Mackenzie, S. Rathee, D. Robinson, and B. G. Fallone, "An artificial neural network (ANN)-based lung-tumor motion predictor for intrafractional MR tumor tracking," Med. Phys. **39**(7), 4423-4433 (2012).

[4] J. Yun, J. St. Aubin, S. Rathee, and B. G. Fallone, "Brushed permanent magnet DC MLC motor operation in an external magnetic field," Med. Phys. **37**(5), 2131-2134 (2010).

[5] M. Lamey, J. Yun, S. Rathee, and B. G. Fallone, "Radio frequency noise from an MLC: a feasibility study of the use of an MLC for linac-MR systems," Phys. Med. Biol. **55**(4), 981-994 (2010).

[6] J. Yun, K. Wachowicz, M. Mackenzie, S. Rathee, D. Robinson, and B. G. Fallone, "First demonstration of intrafractional tumor-tracked irradiation using 2D phantom MR images on a prototype linac-MR," Med. Phys. **40**(5), 051718 (12pp.) (2013).

[7] National Cancer Institute fact sheet 7.1: radiation therapy for cancer. http://www.cancer.gov/cancertopics/factsheet/Therapy/radiation (2010).

[8] ICRU, *Prescribing, Recording and Reporting Photon Beam Therapy, Report 62*, (ICRU, Bethesda, 1999).

[9] ICRU, *Prescribing, Recording and Reporting Photon Beam Therapy, Report 50*, (ICRU, Bethesda, 1993).

[10] F. M. Khan, *The physics of radiation therapy*, 3rd ed. (Lippincott Williams & Wilkins, Philadelphia, 2010).

[11] K. M. Langen and D. T. L. Jones, "Organ motion and its management," Int. J. Radiat. Oncol. Biol. Phys. **50**(1), 265-278 (2001).

[12] C. W. Hurkmans, P. Remeijer, J. V. Lebesque, and B. J. Mijnheer, "Set-up verification using portal imaging; review of current clinical practice," Radiother. Oncol. **58**(2), 105-120 (2001).

[13] D. Verellen, M. D. Ridder, and G. Storme, "A (short) history of image-guided radiotherapy," Radiother. Oncol. **86**(1), 4-13 (2008).

[14] P. Y. Song, M. Washington, F. Vaida, R. Hamilton, D. Spelbring, B. Wyman, J. Harrison, G. T. Y. Chen, and S. Vijayakumar, "A comparison of four patient immobilization devices in the treatment of prostate cancer patients with three dimensional conformal radiotherapy," Int. J. Radiat. Oncol. Biol. Phys. **34**(1), 213-219 (1996).

[15] F. Sterzing, R. Engenhart-Cabillic, M. Flentje, and J. Debus, "Image-Guided Radiotherapy A New Dimension in Radiation Oncology," Deutsches Arzteblatt International **108**(16), 274-280 (2011).

[16] M. Weissbluth, C. J. Karzmark, R. E. Steele, and A. H. Selby, "The stanford medical linear accelerator. 2. installation and physical measurements," Radiology **72**(2), 242-253 (1959).

[17] P. J. Biggs, M. Goitein, and M. D. Russell, "A diagnostic x-ray field verification device for a 10 MV linear-accelerator," Int. J. Radiat. Oncol. Biol. Phys. **11**(3), 635-643 (1985).

[18] R. W. Byhardt, J. D. Cox, A. Hornburg, and G. Liermann, "Weekly localization films and detection of field placement errors," Int. J. Radiat. Oncol. Biol. Phys. **4**(9-10), 881-887 (1978).

[19] I. Rabinowitz, J. Broomberg, M. Goitein, K. McCarthy, and J. Leong, "Accuracy of radiation-field alignment in clinical-practice," Int. J. Radiat. Oncol. Biol. Phys. **11**(10), 1857-1867 (1985).

[20] L. E. Antonuk, "Electronic portal imaging devices: a review and historical perspective of contemporary technologies and research," Phys. Med. Biol. **47**(6), R31-R65 (2002).

[21] C. Walter, J. Boda-Heggemann, H. Wertz, I. Loeb, A. Rahn, F. Lohr, and F. Wenz, "Phantom and in-vivo measurements of dose exposure by image-guided radiotherapy (IGRT): MV portal images vs. kV portal images vs. cone-beam CT," Radiother. Oncol. **85**(3), 418-423 (2007).

[22] B. A. Groh, J. H. Siewerdsen, D. G. Drake, J. W. Wong, and D. A. Jaffray, "A performance comparison of flat-panel imager-based MV and kV cone-beam CT," Med. Phys. **29**(6), 967-975 (2002).

[23] L. A. Dawson and M. B. Sharpe, "Image-guided radiotherapy: rationale, benefits, and limitations," Lancet Oncology **7**(10), 848-858 (2006).

[24] W. Swindell, R. G. Simpson, J. R. Oleson, C.-T. Chen, and E. A. Grubbs, "Computed tomography with a linear accelerator with radiotherapy applications," Med. Phys. **10**(4), 416-420 (1983).

[25] S. Midgley, R. M. Millar, and J. Dudson, "A feasibility study for megavoltage cone beam CT using a commercial EPID," Phys. Med. Biol. **43**(1), 155-169 (1998).

[26] D. A. Jaffray and J. H. Siewerdsen, "Cone-beam computed tomography with a flat-panel imager: Initial performance characterization," Med. Phys. **27**(6), 1311-1323 (2000).

[27] D. A. Jaffray, J. H. Siewerdsen, J. W. Wong, and A. A. Martinez, "Flat-panel cone-beam computed tomography for image-guided radiation therapy," Int. J. Radiat. Oncol. Biol. Phys. **53**(5), 1337-1349 (2002).

[28] C. A. McBain, A. M. Henry, J. Sykes, A. Amer, T. Marchant, C. M. Moore, J. Davies, J. Stratford, C. McCarthy, B. Porritt, P. Williams, V. S. Khoo, and P. Price, "X-ray volumetric imaging in image-guided radiotherapy: The new standard in on-treatment imaging," Int. J. Radiat. Oncol. Biol. Phys. **64**(2), 625-634 (2006).

[29] M. K. Islam, T. G. Purdie, B. D. Norrlinger, H. Alasti, D. J. Moseley, M. B. Sharpe, J. H. Siewerdsen, and D. A. Jaffray, "Patient dose from kilovoltage cone beam computed tomography imaging in radiation therapy," Med. Phys. **33**(6), 1573-1582 (2006).

[30] D. A. Kuban, L. Dong, R. Cheung, E. Strom, and R. De Crevoisier, "Ultrasound-based localization," Sem. Rad. Onc. **15**(3), 180-191 (2005).

[31] M. Fuss, B. J. Salter, S. X. Cavanaugh, C. Fuss, A. Sadeghi, C. D. Fuller, A. Ameduri, J. M. Hevezi, T. S. Herman, and C. R. Thomas, "Daily ultrasound-based image-guided targeting for radiotherapy of upper abdominal malignancies," Int. J. Radiat. Oncol. Biol. Phys. **59**(4), 1245-1256 (2004).

[32] A. Chandra, L. Dong, E. Huang, D. A. Kuban, L. O'Neill, I. Rosen, and A. Pollack, "Experience of ultrasound-based daily prostate localization," Int. J. Radiat. Oncol. Biol. Phys. **56**(2), 436-447 (2003).

[33] S. Kim and T.-S. Suh, "Imaging in radiation therapy," Nuclear engineering and technology **38**(4), 327-342 (2006).

[34] J. Lattanzi, S. McNeeley, W. Pinover, E. Horwitz, I. Das, T. E. Schultheiss, and G. E. Hanks, "A comparison of daily CT localization to a daily ultrasound-based system in prostate cancer," Int. J. Radiat. Oncol. Biol. Phys. **43**(4), 719-725 (1999).

[35] T. S. Berrang, P. T. Truong, C. Popescu, L. Drever, H. A. Kader, M. L. Hilts, T. Mitchell, S. Y. Soh, L. Sands, S. Silver, and I. A. Olivotto, "3D ultrasound can contribute to planning CT to define the target for partial breast radiotherapy," Int. J. Radiat. Oncol. Biol. Phys. **73**(2), 375-383 (2009).

[36] L. Ekberg, O. Holmberg, L. Wittgren, G. Bjelkengren, and T. Landberg, "What margins should be added to the clinical target volume in radiotherapy treatment planning for lung cancer?," Radiother. Oncol. **48**(1), 71-77 (1998).

[37] C. Beltran, M. G. Herman, and B. J. Davis, "Planning target margin calculations for prostate radiotherapy based on intrafraction and interfraction motion using four localization methods," Int. J. Radiat. Oncol. Biol. Phys. **70**(1), 289-295 (2008).

[38] M. Suzuki, Y. Nishimura, K. Nakamatsu, M. Okumura, H. Hashiba, R. Koike, S. Kanamori, and T. Shibata, "Analysis of interfractional set-up

errors and intrafractional organ motions during IMRT for head and neck tumors to define an appropriate planning target volume (PTV)- and planning organs at risk volume (PRV)-margins," Radiother. Oncol. **78**(3), 283-290 (2006).

[39] J. H. Hendry, B. Jeremic, and E. H. Zubizarreta, "Normal tissue complications after radiation therapy," Rev. Panam. Salud. Publica. **20**(2-3), 151-160 (2006).

[40] C. Saw, E. Brandner, R. Selvaraj, H. Chen, M. Saiful Huq, and D. Heron, "A review on the clinical implementation of respiratory-gated radiation therapy," Biomed Imaging Interv J **3**(1), e40 (2007).

[41] S. B. Jiang, "Technical aspects of image-guided respiration-gated radiation therapy," Medical Dosimetry **31**(2), 141-151 (2006).

[42] P. J. Keall, G. S. Mageras, J. M. Balter, R. S. Emery, K. M. Forster, S. B. Jiang, J. M. Kapatoes, D. A. Low, M. J. Murphy, B. R. Murray, C. R. Ramsey, M. B. Van Herk, S. S. Vedam, J. W. Wong, and E. Yorke, "The management of respiratory motion in radiation oncology report of AAPM Task Group 76," Med. Phys. **33**(10), 3874-3900 (2006).

[43] S. S. Lo, B. S. Teh, J. J. Lu, and T. E. Schefter, *Stereotactic Body Radiation Therapy*, (Springer-Verlag Berlin and Heidelberg GmbH & Co. K, Berlin, 2012).

[44] H. Shirato, S. Shimizu, T. Kunieda, K. Kitamura, M. van Herk, K. Kagei, T. Nishioka, S. Hashimoto, K. Fujita, H. Aoyama, K. Tsuchiya, K. Kudo, and K. Miyasaka, "Physical aspects of a real-time tumor-tracking system for gated radiotherapy," Int. J. Radiat. Oncol. Biol. Phys. **48**(4), 1187-1195 (2000).

[45] R. Wagman, E. Yorke, E. Ford, P. Giraud, G. Mageras, B. Minsky, and K. Rosenzweig, "Respiratory gating for liver tumors: Use in dose escalation," Int. J. Radiat. Oncol. Biol. Phys. **55**(3), 659-668 (2003).

[46] S. S. Korreman, A. N. Pedersen, T. J. Nottrup, L. Specht, and H. Nystrom, "Breathing adapted radiotherapy for breast cancer: Comparison of free

breathing gating with the breath-hold technique," Radiother. Oncol. **76**(3), 311-318 (2005).

47 P. Giraud, E. Morvan, L. Claude, F. Mornex, C. Le Pechoux, J. M. Bachaud, P. Boisselier, V. Beckendorf, M. Morelle, and M. O. Carrere, "Respiratory Gating Techniques for Optimization of Lung Cancer Radiotherapy," J Thorac Oncol. **6**(12), 2058-2068 (2011).

48 C. Ozhasoglu and M. J. Murphy, "Issues in respiratory motion compensation during external-beam radiotherapy," Int. J. Radiat. Oncol. Biol. Phys. **52**(5), 1389-1399 (2002).

49 A. Sawant, R. Venkat, V. Srivastava, D. Carlson, S. Povzner, H. Cattell, and P. Keall, "Management of three-dimensional intrafraction motion through real-time DMLC tracking," Med. Phys. **35**(5), 2050-2061 (2008).

50 Y. Suh, S. Dieterich, B. Cho, and P. J. Keall, "An analysis of thoracic and abdominal tumour motion for stereotactic body radiotherapy patients," Phys. Med. Biol. **53**(13), 3623-3640 (2008).

51 T. Harada, H. Shirato, S. Ogura, S. Oizumi, K. Yamazaki, S. Shimizu, R. Onimaru, K. Miyasaka, M. Nishimura, and H. Dosaka-Akita, "Real-time tumor-tracking radiation therapy for lung carcinoma by the aid of insertion of a gold marker using bronchofiberscopy," Cancer **95**(8), 1720-1727 (2002).

52 T. Depuydt, D. Verellen, O. Haas, T. Gevaert, N. Linthout, M. Duchateau, K. Tournel, T. Reynders, K. Leysen, M. Hoogeman, G. Storme, and M. D. Ridder, "Geometric accuracy of a novel gimbals based radiation therapy tumor tracking system," Radiother. Oncol. **98**(3), 365-372 (2011).

53 Y. Kamino, K. Takayama, M. Kokubo, Y. Narita, E. Hirai, N. Kawawda, T. Mizowaki, Y. Nagata, T. Nishidai, and M. Hiraoka, "Development of a four-dimensional image-guided radiotherapy system with a gimbaled X-ray head," Int. J. Radiat. Oncol. Biol. Phys. **66**(1), 271-278 (2006).

54 H. Shirato, S. Shimizu, K. Kitamura, T. Nishioka, K. Kagei, S. Hashimoto, H. Aoyama, T. Kunieda, N. Shinohara, H. Dosaka-Akita, and K. Miyasaka, "Four-dimensional treatment planning and fluoroscopic real-time tumor

tracking radiotherapy for moving tumor," Int. J. Radiat. Oncol. Biol. Phys. **48**(2), 435-442 (2000).

[55] R. L. Smith, K. Lechleiter, K. Malinowski, D. M. Shepard, D. J. Housley, M. Afghan, J. Newell, J. Petersen, B. Sargent, and P. Parikh, "Evaluation of Linear Accelerator Gating with Real-Time Electromagnetic Tracking," Int. J. Radiat. Oncol. Biol. Phys. **74**(3), 920-927 (2009).

[56] T. R. Willoughby, P. A. Kupelian, J. Pouliot, K. Shinohara, M. Aubin, M. Roach, L. L. Skrumeda, J. M. Balter, D. W. Litzenberg, S. W. Hadley, J. T. Wei, and H. M. Sandler, "Target localization and real-time tracking using the calypso 4D localization system in patients with localized prostate cancer," Int. J. Radiat. Oncol. Biol. Phys. **65**(2), 528-534 (2006).

[57] B. Cho, P. R. Poulsen, A. Sloutsky, A. Sawant, and P. J. Keall, "First Demonstration of Combined Kv/Mv Image-Guided Real-Time Dynamic Multileaf-Collimator Target Tracking," Int. J. Radiat. Oncol. Biol. Phys. **74**(3), 859-867 (2009).

[58] S. Han-Oh, B. Y. Yi, F. Lerma, B. L. Berman, M. Gui, and C. Yu, "Verification of MLC based real-time tumor tracking using an electronic portal imaging device," Med. Phys. **37**(6), 2435-2440 (2010).

[59] J. Q. Wu, D. Ruan, B. Cho, A. Sawant, J. Petersen, L. J. Newell, H. Cattell, and P. J. Keall, "Electromagnetic Detection and Real-Time DMLC Adaptation to Target Rotation During Radiotherapy," Int. J. Radiat. Oncol. Biol. Phys. **82**(3), E545-E553 (2012).

[60] G. G. Echner, W. Kilby, M. Lee, E. Earnst, S. Sayeh, A. Schlaefer, B. Rhein, J. R. Dooley, C. Lang, O. Blanck, E. Lessard, C. R. Maurer Jr, and W. Schlegel, "The design, physical properties and clinical utility of an iris collimator for robotic radiosurgery," Phys. Med. Biol. **54**(18), 5359-5380 (2009).

[61] K. Kitamura, H. Shirato, S. Shimizu, N. Shinohara, T. Harabayashi, T. Shimizu, Y. Kodama, H. Endo, R. Onimaru, S. Nishioka, H. Aoyama, K. Tsuchiya, and K. Miyasaka, "Registration accuracy and possible migration of internal fiducial gold marker implanted in prostate and liver treated with

real-time tumor-tracking radiation therapy (RTRT)," Radiother. Oncol. **62**(3), 275-281 (2002).

62 M. Imura, K. Yamazaki, H. Shirato, R. Onimaru, M. Fujino, S. Shimizu, T. Harada, S. Ogura, H. Dosaka-Akita, K. Miyasaka, and M. Nishimura, "Insertion and fixation of fiducial markers for setup and tracking of lung tumors in radiotherapy," Int. J. Radiat. Oncol. Biol. Phys. **63**(5), 1442-1447 (2005).

63 D. Ionascu, S. B. Jiang, S. Nishioka, H. Shirato, and R. I. Berbeco, "Internal-external correlation investigations of respiratory induced motion of lung tumors," Med. Phys. **34**(10), 3893-3903 (2007).

64 D. P. Gierga, J. Brewer, G. C. Sharp, M. Betke, C. G. Willett, and G. T. Y. Chen, "The correlation between internal and external markers for abdominal tumors: Implications for respiratory gating," Int. J. Radiat. Oncol. Biol. Phys. **61**(5), 1551-1558 (2005).

65 C. Plathow, S. Ley, C. Fink, M. Puderbach, W. Hosch, A. Schmahl, J. Debus, and H. U. Kauczor, "Analysis of intrathoracic tumor mobility during whole breathing cycle by dynamic MRI," Int. J. Radiat. Oncol. Biol. Phys. **59**(4), 952-959 (2004).

66 M. J. Ghilezan, D. A. Jaffray, J. H. Siewerdsen, M. van Herk, A. Shetty, M. B. Sharpe, S. Z. Jafri, F. A. Vicini, R. C. Matter, D. S. Brabbins, and A. A. Martinez, "Prostate gland motion assessed with cine-magnetic resonance imaging (cine-MRI)," Int. J. Radiat. Oncol. Biol. Phys. **62**(2), 406-417 (2005).

67 N. He, C. M. Xie, W. D. Wei, C. C. Pan, W. Y. Wang, N. Lv, and P. H. Wu, "A new, preoperative, MRI-based scoring system for diagnosing malignant axillary lymph nodes in women evaluated for breast cancer," Eur J Radiol. **81**(10), 2602-2612 (2012).

68 J. Dinkel, C. Hintze, R. Tetzlaff, P. E. Huber, K. Herfarth, J. Debus, H. U. Kauczor, and C. Thieke, "4D-MRI analysis of lung tumor motion in patients with hemidiaphragmatic paralysis," Radiother. Oncol. **91**(3), 449-454 (2009).

[69] B. G. Fallone, B. Murray, S. Rathee, T. Stanescu, S. Steciw, S. Vidakovic, E. Blosser, and D. Tymofichuk, "First MR images obtained during megavoltage photon irradiation from a prototype integrated linac-MR system," Med. Phys. **36**(6), 2084-2088 (2009).

[70] B. W. Raaymakers, J. J. Wlagendijk, J. Overweg, J. G. M. Kok, A. J. E. Raaijmakers, E. M. Kerkhof, R. W. van der Put, I. Meijsing, S. P. M. Crijns, F. Benedosso, M. van Vulpen, C. H. W. de Graaff, J. Allen, and K. J. Brown, "Integrating a 1.5 T MRI scanner with a 6 MV accelerator: proof of concept," Phys. Med. Biol. **54**(12), N229-N237 (2009).

[71] J. F. Dempsey, D. Benoit, J. R. Fitzsimmons, A. Haghighat, J. G. Li, D. A. Low, S. Mutic, J. R. Palta, H. E. Romeijn, and G. E. Sjoden, "A device for realtime 3D image-guided IMRT," Int. J. Radiat. Oncol. Biol. Phys. **63**(2), 1095 (2005).

[72] S. Mutic, "First Commercial Hybrid MRI-IMRT System," presented at the 54th Annual Meeting of the AAPM, Charlotte, NC, July 29 - August 2, 2012.

[73] C. Kirkby, B. Murray, S. Rathee, and B. G. Fallone, "Lung dosimetry in a linac-MRI radiotherapy unit with a longitudinal magnetic field," Med. Phys. **37**(9), 4722-4732 (2010).

# Chapter 2: Theory

## *2.1. MAGNETIC RESONANCE IMAGING*

MRI is a powerful non-invasive imaging technique that is based on the principle of nuclear magnetic resonance (NMR). MRI can provide 2D, 3D, or 4D (3D + temporal) anatomical imaging with superb soft tissue contrast compared to other imaging modalities used for radiotherapy including x-ray, CT, or PET. Because MRI plays an important role in this thesis, a brief introduction of MRI concepts is provided in this chapter.

### 2.1.1. Basic NMR physics

An atomic nucleus is primarily made of protons and neutrons. Any atomic nucleus with an odd number of protons and/or an odd number of neutrons possesses non-zero spin angular momentum, *S*. These nuclei also possess a nuclear magnetic moment, $\mu$, according to the following relationship:[1]

$$\vec{\mu} = \gamma \vec{S} \qquad \textbf{(Eq. 2.1)}$$

The proportionality constant $\gamma$ is the gyromagnetic ratio, which is quite varied among nuclei. Among the nuclei that have non-zero *S*, if the sum of the number of protons and neutrons is odd (i.e. odd mass number), the nucleus possesses a half-integer spin such as 1/2, 3/2, etc. For example, hydrogen nuclei ($^1$H) have 1/2 spin with $\gamma$ value of 42.6 MHz/T. Due to its relatively large $\gamma$ compared to other nuclei and abundance in human body (~ 70 % of human body is made of water, where each water molecule contains two $^1$H), $^1$H is predominantly used in MRI.

In the absence of external magnetic field ($B_0 = 0$), the direction of $\mu$ or "spins" is randomly distributed as shown in Fig. 2.1.a. Thus, the net magnetization (i.e. vector sum of all $\mu$) within the given volume, $M_0$, is zero.

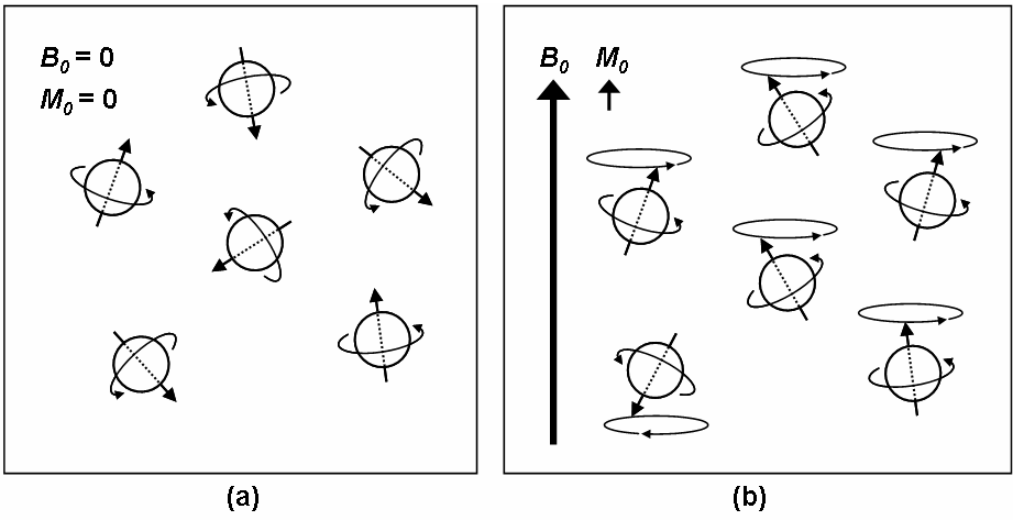


**Figure 2.1 Spin distribution in a given volume: (a) randomly distributed spins when $B_0 = 0$. In this case, net magnetization in the volume is zero. (b) In the presence of $B_0$, the spins start to precess around $B_0$. In this case, net magnetization in the volume is produced in $B_0$ direction.**

However, when a static external magnetic field $B_0$ is applied as shown in Fig. 2.1.b, the spins placed near or within $B_0$ start experiencing torque that attempts to align the direction of $\mu$ with the direction of $B_0$. Due to the torque, spins start to precess around $B_0$, and the rate of this precession is referred to as the Larmor frequency, $\omega_0$, defined by[1]

$$\omega_0 = \gamma \cdot B_0 \qquad \textbf{(Eq. 2.2)}$$

While the spins are aligning themselves with $B_0$, two different energy states are created: (1) a lower energy state where the spins align parallel to $B_0$, and (2) an upper energy state where the spins align anti-parallel to $B_0$. This is because $^1$H is a 1/2 spin nucleus, which was found to have two possible energy states. The

energy difference between the two states is referred to as Zeeman splitting energy, $E_Z$, and we can induce transitions between the two states by applying an electromagnetic RF pulse of equal energy as $E_Z$.

At a given temperature $T$, the ratio of spin populations in the upper and lower energy states is governed by thermal equilibrium condition given as

$$\frac{N_+}{N_-} = e^{-E_z/kT} \qquad \textbf{(Eq. 2.3)}$$

where $N_+$ and $N_-$ represent the spin population in the upper and lower energy states respectively, and $k$ refers to the Boltzman constant ($1.38 \times 10^{-23}$ J/K).

Assuming the spins are in thermal equilibrium at room temperature (300 K), the net magnetization in a given volume is in alignment with $B_0$ due to very slight excess of spins in lower energy state. For example, if 1.5 T $B_0$ is applied, there are only 9 more spins aligned with $B_0$ for every 2 million spins. Despite this fact, due to the abundance of water molecule in human body, there can be 6 million billion excessive spins within $2 \times 2 \times 5$ mm$^3$ volume. From this, a net magnetization aligned with $B_0$, $M_0$, as shown in Fig. 2.1.b, is formed which is utilized to generate MR images.

## 2.1.2. Excitation of the spins and signal generation

In this thesis, the direction of $B_0$ is defined parallel to Z axis as shown in Fig. 2.2.a. In general, the magnitude of $B_0$ is several orders of magnitude greater than the magnitude of $M_0$. Thus, any useful signal originated from $M_0$ is overwhelmed by $B_0$ in practice. Instead of direct investigation, $M_0$ can be tipped away from its original location. As explained earlier, if an electromagnetic RF

pulse of energy equal to $E_Z$ is applied to $^1$H, transitions between the two energy states can occur. It was found that the frequency of this RF pulse must be equal to $\omega_0$ to possess the equal energy as $E_Z$.[2]

At the quantum level, if the RF pulse with $\omega_0$ is applied, $^1$H will absorb the RF energy and jump up to the higher energy level. At the macro level, as shown in Fig. 2.2.a, this can be observed as the net magnetization $M$ spirals down towards the XY plane if the observer is in the external laboratory frame of reference. Or, if the observer is in rotating frame of reference that rotates at $\omega_0$ around Z axis, $M$ would seem to be smoothly tipped down towards X'Y' plane as shown in Fig. 2.2.b. Here, the electromagnetic RF pulse, $B_1(t)$, is applied perpendicular to $B_0$, and its amplitude is considerably smaller than $B_0$.

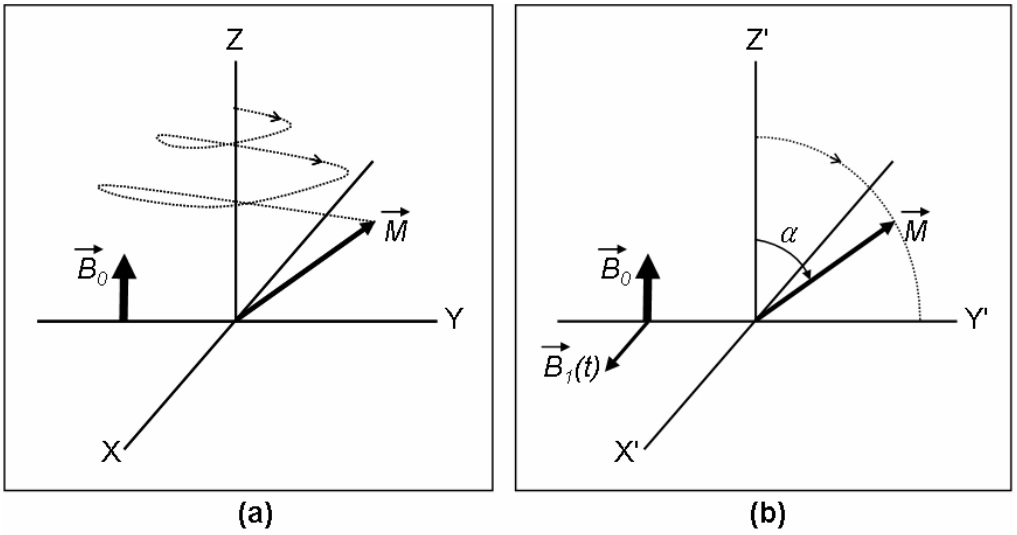


**Figure 2.2 Motion of net magnetization vector *M* observed from (a) external lab frame XY, and (b) rotating frame X'Y'**

The motion of $M$ in rotating frame is described by the Bloch equation[3]

$$d\vec{M}/dt = \gamma \vec{M} \times \vec{B}_1 \qquad \textbf{(Eq. 2.4)}$$

where the tipping angle $\alpha$, i.e. the angle between $M$ before and immediately after the RF pulse, is determined by the duration of RF pulse shown as

$$\alpha(t) = \gamma \int B_1(t)\, dt \qquad \textbf{(Eq. 2.5)}$$

If the RF pulse is turned off after $M$ is tipped down to the XY plane, $M$ will continue to precess around $B_0$ at $\omega_0$. This rotating magnetic field in XY plane is referred to as transverse magnetization, $M_{XY}$, and it produces electromagnetic radiation. Thus, the absorbed RF energy is now being retransmitted and generating the NMR signal as shown in Fig. 2.3.a. The greater the magnitude of $M_{XY}$, the greater the NMR signal. A receiving coil is used to detect the NMR signal. Since $M_{XY}$ rotates at $\omega_0$, it will produce a sinusoidal RF signal with frequency $\omega_0$. However, the amplitude of this RF pulse will decay with an exponential time constant, because the magnitude of $M_{XY}$ decreases as the spins relax back to the equilibrium position. This is referred to as free induction decay (FID) shown in Fig. 2.3.b.

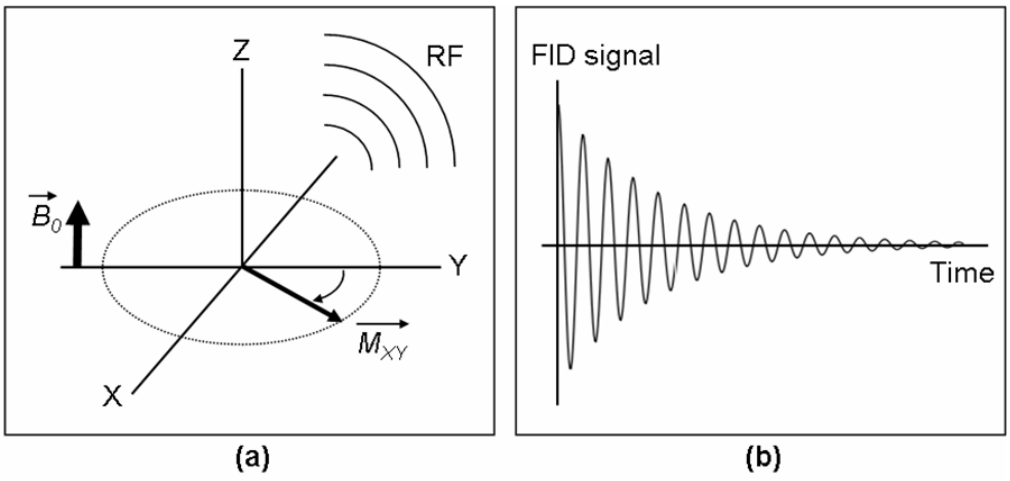


**Figure 2.3 $M_{XY}$ after RF excitation: (a) rotating $M_{XY}$ retransmits RF pulse via FID (observed in lab frame). (b) time domain signal of FID.**

## 2.1.3. Contrast mechanisms in MRI

MRI has three main contrast mechanisms that distinguish different tissue types: (1) proton density (PD), (2) spin-lattice relaxation time ($T_1$), and (3) spin-spin relaxation time ($T_2$). In general, all of these mechanisms simultaneously contribute to generate an MR image. In practice, however, images are usually acquired with one contrast mechanism that is weighted more than the others (e.g. $T_1$ weighted images, $T_2$ weighted images, etc).

### 2.1.3.1. Proton density

PD represents the number of mobile $^1$H per unit volume of tissue. The higher the number of $^1$H in a given tissue volume, the greater the magnitude of $M_{XY}$, thus the brighter the signal on the PD weighted images. This mechanism can be used to distinguish different tissues, because the amount of available protons ($^1$H in water) depends on tissue types.

### 2.1.3.2. $T_1$ relaxation

$T_1$ relaxation is also called longitudinal relaxation or spin-lattice relaxation, because it is related to the recovery of longitudinal magnetization ($M_Z$), and this process occurs by exchanging the energy of the spins with its surroundings (i.e. lattice). The magnitude of $M_Z$ becomes zero immediately after 90° RF pulse (i.e. $\alpha$ = 90). Then, the spins start to relax back to its equilibrium state where $M_Z = M_0$. This recovery of $M_Z$ is shown by[3]

$$dM_Z(t)/dt = -(1/T_1)\cdot(M_0 - M_Z(t)) \qquad \textbf{(Eq. 2.6)}$$

where $T_1$ is the longitudinal or spin-lattice time constant. After 90° RF pulse, the solution becomes

$$M_Z(t) = M_0(1 - e^{-t/T_1}) \qquad \textbf{(Eq. 2.7)}$$

Because $T_1$ is unique in each tissue type, different tissues relax back to the equilibrium at different rates as illustrated in Fig. 2.4.

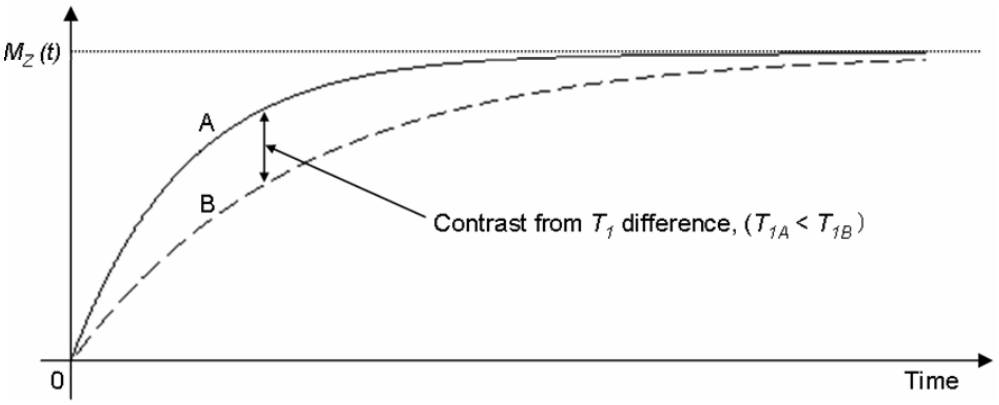


**Figure 2.4 $T_1$ relaxation and $M_Z$ recovery after 90° RF pulse in two different tissue types A and B. Tissue B has longer $T_1$ value, thus requires more time for the recovery of $M_Z$.**

Thus, if a second 90° RF pulse is applied during relaxation, the tissue with shorter $T_1$ will have $M_{XY}$ with greater magnitude, which will generate brighter signal on the $T_1$ weighted images.

### 2.1.3.3. $T_2$ relaxation

$T_2$ relaxation is also called transverse relaxation or spin-spin relaxation, because it is related to the decay of transverse magnetization ($M_{XY}$), and this process occurs due to the temporary and random interactions between neighboring excited spins. The magnitude of $M_{XY}$ starts to decay immediately after 90° RF pulse due to dephasing of the spins, which is described by[3]

$$dM_{XY}(t)/dt = -M_{XY}/T_2 \qquad \textbf{(Eq. 2.8)}$$

where $T_2$ is the transverse or spin-spin time constant. After 90° RF pulse, the solution becomes

$$M_{XY}(t) = M_0 \cdot e^{-t/T_2} \qquad \textbf{(Eq. 2.9)}$$

Because $T_2$ is unique in each tissue type, signals from different tissues will decay at different rates as illustrated in Fig. 2.5.

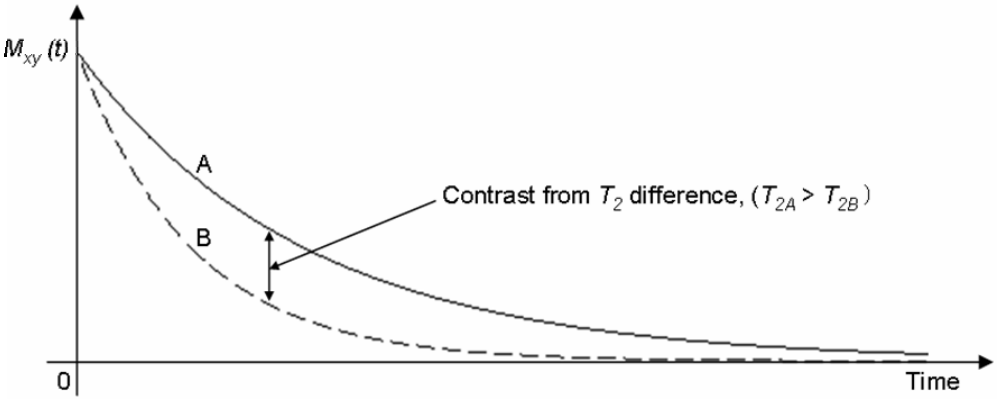


**Figure 2.5 $T_2$ relaxation and $M_{XY}$ decay after 90° RF pulse in two different tissue types A and B. Tissue A has longer $T_2$ value, thus requires more time for the decay of $M_{XY}$.**

As explained above, higher magnitude of $M_{XY}$ generates greater amount of signal. Thus, the signal from tissues with higher $T_2$ value, meaning that its $M_{XY}$ will decay slower, will appear to be brighter on the $T_2$ weighted images.

In an ideal situation where $B_0$ is perfectly uniform everywhere in a given volume, $T_2$ relaxation should be the only source causing the dephasing of the spins, i.e. the decay of $M_{XY}$, governed by Eq. 2.9. In practice, however, $B_0$ includes certain degree of inhomogeneity ($\Delta B$) due to various reasons: magnetic materials inside or outside of the patient, technical problems, scanning at the edge of the magnetic field, etc. This $B_0$ inhomogeneity causes additional dephasing of the spins, and this is accounted for by $T_2$* given as

$$1/T_2^* = 1/T_2 + \gamma \cdot \Delta B \qquad \textbf{(Eq. 2.10)}$$

where $T_2$* is the transverse relaxation time constant including $B_0$ inhomogeneity effects.

### 2.1.4. MR image formation

The spins ($^1$H) in a given volume can be excited by applying the RF pulse at $\omega_0$, and the excited spins retransmit NMR signals also at $\omega_0$. Thus, if all the spins in the volume precess at $\omega_0$, the retransmitted signal will also have only one frequency, $\omega_0$. To form an MR image, however, we need to be able to differentiate the signals from the spins in different 3D locations within the scanning volume. To achieve this, we create a known change in $B_0$ by applying a linear magnetic field gradient, $G$, across the volume that we want to image. $G$ is typically zero at the center of the magnet and linearly increases or decreases with distance. As shown in Eq. 2.2, any changes in $B_0$ will cause the changes in $\omega_0$. Hence, by applying $G$ across the scanning volume, the spins in different 3D locations will retransmit NMR signals at different $\omega_0$ after excitation. These signals are used to form an MR image.

MR image formation typically involves the following process: slice selection, phase encoding, frequency encoding, signal acquisition, k-space filling and inverse Fourier transform. Brief discussions of these processes follow using a coordinate convention shown in Fig. 2.6, where slice selection occurs in Z direction (superior-inferior), phase encoding occurs in Y direction (anterior-posterior), and frequency encoding occurs in X direction (left-right). These are chosen for explanation purposes in this thesis. In practice, these encoding directions are inter-changeable and can occur along oblique vectors.

### 2.1.4.1. Slice selection

When $G$ is applied across the scanning volume, the resonance frequency of the spins starts to vary from $\omega_0$ depending on their locations within the $G$ field. This is illustrated in Fig. 2.6 with $G_Z$ (linear gradient in Z direction) applied.

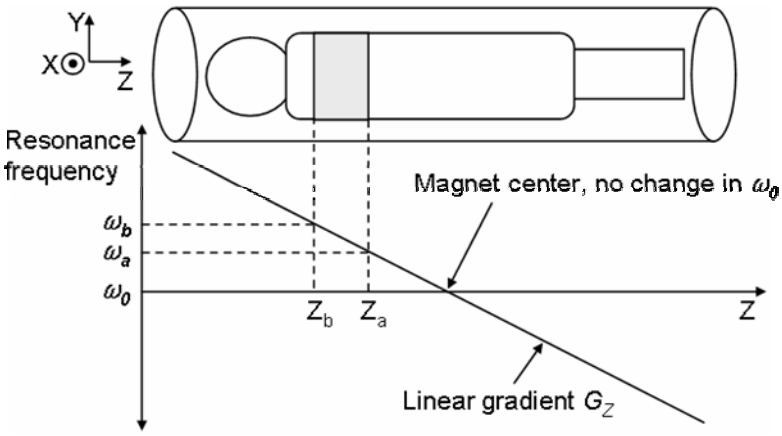


**Figure 2.6 Slice selection in the presence of linear gradient $G_z$**

In this figure, $B_a$, the external magnetic field at $Z_a$ is given as

$$B_a = B_0 + \Delta B_z, \text{where } \Delta B_z = G_z \cdot Z_a \qquad \textbf{(Eq. 2.11)}$$

Then, $\omega_a$, the resonance frequency of the spins located at $Z_a$ is given as

$$\omega_a = \gamma \cdot (B_0 + G_z \cdot Z_a) \qquad \textbf{(Eq. 2.12)}$$

Thus, a transverse slice defined by $Z_a$ and $Z_b$ can be selectively excited by applying an RF pulse that has bandwidth (BW) between $\omega_a$ and $\omega_b$ in the presence of $G_Z$. BW refers to the range of frequencies included in the RF pulse. Likewise, a coronal or a sagittal slice can be selected using $G_Y$ or $G_X$, respectively. Any oblique plane of the volume can also be selected by using appropriate combination of $G_X$, $G_Y$, and $G_Z$. In general, $M_0$ is tipped away from its original direction in the presence of slice selection gradient.

### 2.1.4.2. Phase encoding

After slice selection, signals from the spins outside of the selected slice are disregarded. Assuming the thickness of selected slice is very small with respect to morphological structures, the issue of spatial localization of the spins in 3D volume now becomes a 2D problem. All slice selection gradients are turned off at the completion of slice selection. At this moment, all of the excited spins within the selected slice are in-phase and precessing at $\omega_0$, where the slab has a finite thickness $\Delta Z$ ($\Delta Z = Z_b - Z_a$ from Fig. 2.6). This is described in Fig. 2.7.a following the same coordinate convention as in Fig. 2.6.

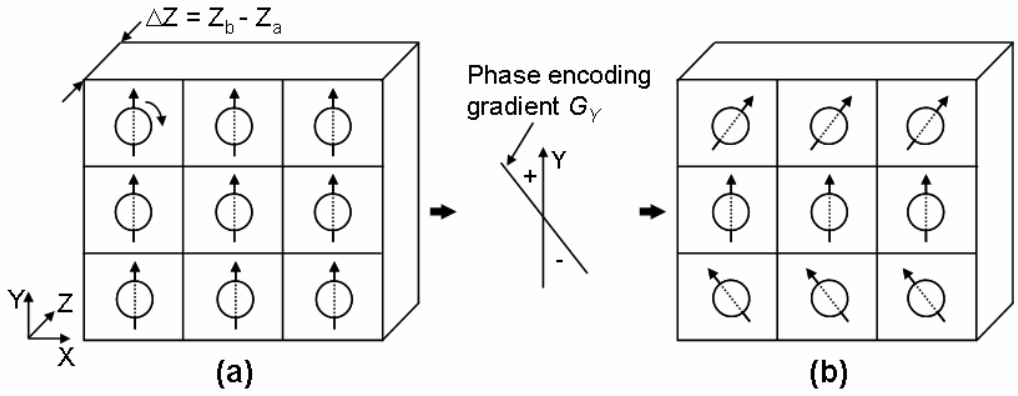


**Figure 2.7 Phase encoding process: (a) immediately after slice selection. All spins in XY plane are in-phase (i.e. pointing the same direction) and precessing at $\omega_0$ assuming clockwise direction. (b) Phase encoding result.**

Phase encoding (PE) further differentiates the signals from the spins within the slice in Y direction using a PE gradient $G_Y$. Here, Y direction is arbitrary chosen for explanation. If $G_Y$ is applied across the slice shown in Fig. 2.7.a ($G_Y$ is zero at the middle row), the spins will be exposed to, from top to bottom rows, positive, zero, and negative $G_Y$. Accordingly, the spins will precess at faster, the same, and slower speed than $\omega_0$, as illustrated in Fig. 2.7.b. Once the

spin phases in the different rows are sufficiently differentiated, $G_Y$ is turned off. This leaves all spins precessing at $\omega_0$ but with different phases in the different rows. Although the direction of $G$ is different, the same relationship holds between the resonance frequency of the spins and gradient strength as given in Eqs. 2.11 - 2.12.

### 2.1.4.3. Frequency encoding

After PE, the spins within the slice can be differentiated in Y direction using their phase differences as illustrated in Fig. 2.8.a.

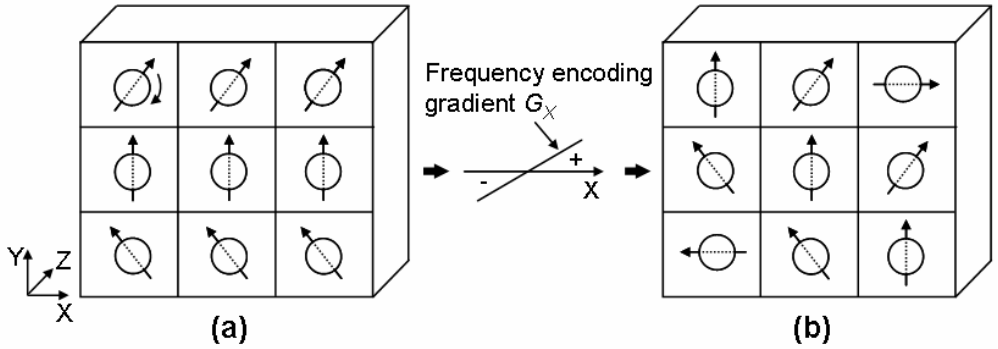


**Figure 2.8 Frequency encoding process: (a) immediately after phase encoding. All spins in each row are in-phase. (b) Frequency encoding result.**

Frequency encoding (FE) further differentiates the spins in X direction using a FE gradient $G_X$. If $G_X$ is applied across the slice shown in Fig. 2.8.a ($G_X$ is zero at the middle column), the spins will be exposed to, from left to right columns, negative, zero, and positive $G_X$. Accordingly, the spins precess at slower, the same, and faster speed as illustrated in Fig. 2.8.b.

### 2.1.4.4. Signal acquisition

The precessing spins shown in Fig. 2.8.b retransmit RF signal, and this signal is acquired while the FE gradient $G_X$ is being applied. Due to $G_X$, the spins in each column precess at different frequencies. Hence, three different resonance frequencies will be detected from the retransmitted signal, and this will provide the positional information of the spins in X direction with further analysis.

Because the PE gradient $G_Y$ must be turned off during signal acquisition, only a single $G_Y$ can be applied in Y direction before each signal acquisition. Due to $G_Y$, a fixed, known amount of phase change is applied to the spins at specific Y location at each PE. In practice, PE is repeated as many times as needed before each signal acquisition with different gradient strength that is linearly incremented each time. Thus, the rate of phase change for a spin at a specific Y location is also linearly incremented at each PE. Because a rate of phase change is also a frequency, a similar concept as used in FE is used to obtain the spin locations in Y direction through PE. This will provide the positional information of the spins in Y direction with further analysis.

### 2.1.4.5. The Fourier transform

The Fourier transform (FT) is used to determine the magnitude of the signal at each frequency. The relationship between the two domains, frequency domain and time domain, is given as

$$f(\delta) = FT(F(\varepsilon)) = \int F(\varepsilon) \cdot e^{-i2\pi\delta\varepsilon} d\varepsilon \qquad \textbf{(Eq. 2.13)}$$

$$F(\varepsilon) = FT^{-1}(f(\delta)) = \int f(\delta) \cdot e^{i2\pi\delta\varepsilon} d\delta \qquad \textbf{(Eq. 2.14)}$$

where $F(\varepsilon)$ represents the received signal in time domain ($\varepsilon$ represents time), and $f(\delta)$ represents the Fourier transform of $F(\varepsilon)$ referred to as $FT(F(\varepsilon))$. Here, the Fourier space is in temporal frequency (cycles/time) represented by $\delta$. The time signal $F(\varepsilon)$ can be recovered by taking the inverse Fourier transform of $f(\delta)$ referred to as $FT^{-1}(f(\delta))$. Due to their reciprocal relationship, $f(\delta)$ and $F(\varepsilon)$ are referred to as a Fourier transform pair. FT plays a major role in MR image construction, because it can provide the frequency and corresponding magnitude of the received time domain signal that are directly related to the spatial location and density of the spins, respectively.

### 2.1.4.6. K-space and MR image formation

K-space stores the acquired MR signal prior to image formation. Assuming that the entire slice is excited and the signals are detected uniformly without $T_2$* relaxation, the resulting MR signal, $S(t)$, is given as[4]

$$S(t) = \int P(\vec{r}) \cdot e^{i\omega_0 t} d\vec{r} \qquad \textbf{(Eq. 2.15)}$$

where $P(\vec{r})$ represents the spin density as well as signal effects due to relaxation at location $\vec{r}$ within the slice. Recovering $P(\vec{r})$ from the measured MR signal is the goal of image formation.

Once the gradient field $G_X$ or $G_Y$ is applied, $B_0$ changes accordingly, which causes $\omega_0$ to change as the following (the FE gradient $G_X$ is used as an example):

$$\omega_X = \omega_0 + \gamma \cdot G_X \cdot X \qquad \textbf{(Eq. 2.16)}$$

where $\omega_X$ is the resonance frequency of the spins located at $X$ in the presence of $G_X$. Then, Eq. 2.15 becomes

$$S(t) = \int P(X) \cdot e^{i\omega_x t} dX = e^{i\omega_0 t} \int P(X) \cdot e^{i(\gamma \cdot G_x \cdot X)t} dX \quad \textbf{(Eq. 2.17)}$$

where $P(X)$ represents the spin density and signal effects due to relaxation at location $X$ within the slice. The exponential term, $e^{i\omega_0 t}$, can be disregarded in further derivation considering the equation in the rotating frame of reference as explained earlier. Also, in practice, the signal at $\omega_0$ is demodulated to avoid high frequency components.

If we make a substitution by introducing a parameter $k_X$ given as[4]

$$k_X = -\frac{\gamma \cdot G_X \cdot t}{2\pi} \quad \textbf{(Eq. 2.18)}$$

where $t$ is encoding time during which $G_X$ is applied. Then, Eq. 2.17 can be rewritten as

$$S(t) = \rho(k_X) = \int P(X) \cdot e^{-i \cdot (2\pi \cdot X) \cdot k_X} dX \quad \textbf{(Eq. 2.19)}$$

Here, $\rho(k_X)$ and $P(X)$ is a Fourier transform pair as shown in Eq. 2.13. This reciprocal Fourier space is referred to as k-space, which is in the spatial frequency domain (cycles/distance).

Each row of k-space ($k_X$) is filled with *S(t)* at each signal acquisition in the presence of $G_X$. Eq. 2.19 is rewritten as

$$S(t) = \rho(k_X) = FT(P(X)) \quad \textbf{(Eq. 2.20)}$$

Therefore, $P(X)$ can be recovered from the measured signal *S(t)* as the following

$$P(X) = FT^{-1}(\rho(k_X)) = FT^{-1}(S(t)) \quad \textbf{(Eq. 2.21)}$$

Equations 2.15 - 2.21 can also be applied if the PE gradient $G_Y$ is applied. K-space is filled one row at a time during signal acquisitions, where incremental variation of $G_Y$ determines $k_Y$. Once k-space is fully filled, a 2D inverse FT is applied to the entire k-space data to form a 2D MR image.

## 2.1.5. Imaging sequence

An imaging sequence is a predefined set of RF pulses and gradient fields applied repeatedly during an MR study, in order to excite the spins within the volume of interest.

### 2.1.5.1. Spin echo imaging

Spin echo (SE) imaging uses two consecutive RF excitation pulses to refocus the spins in XY plane. Immediately after the initial slice selection RF pulse that tips the magnetization by an angle $\alpha$ and creates a component in the XY plane, the excited spins start to dephase according to $T_2$* relaxation. SE imaging applies a second 180° RF pulse, at time $TE/2$ after the first RF pulse, to reverse the positions of the spins in XY Plane. This effectively refocuses the spins, and they form a "spin echo" at the echo time, $TE$. This process acquires one line in k-space, and thus the sequence is repeated at $TR$ (repetition time) intervals with different values for PE gradient to fill the 2D k-space. A typical SE pulse diagram is shown in Fig. 2.9.

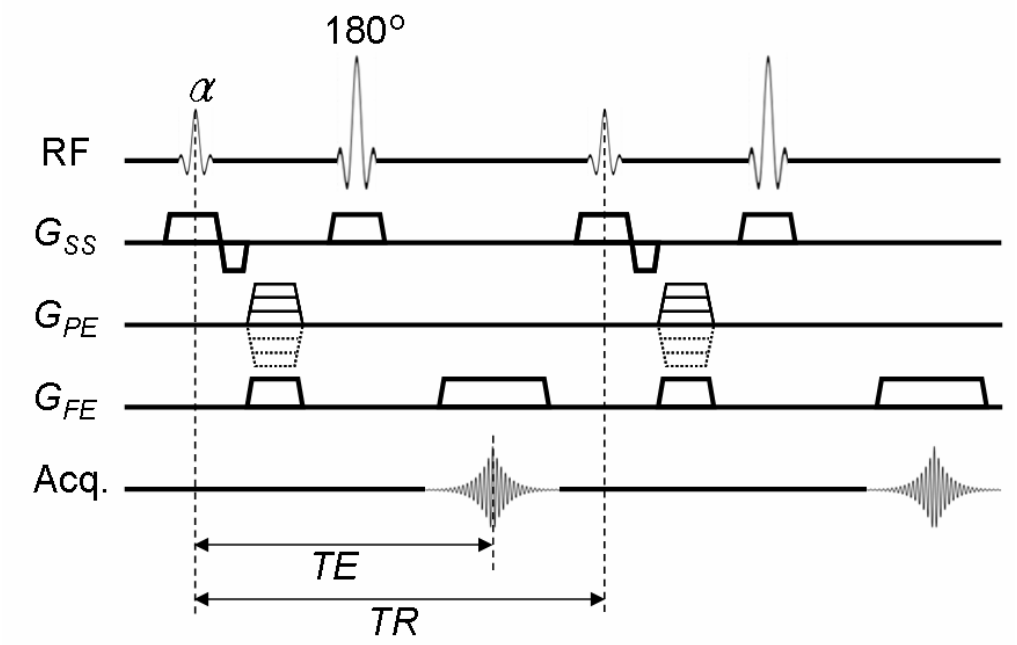


**Figure 2.9 Spin echo imaging sequence, where $\alpha$: tipping angle, $G_{SS}$: slice selection gradient, $G_{PE}$: phase encoding gradient, $G_{FE}$: frequency encoding gradient, $TE$: echo time, $TR$: repetition time.**

As explained earlier, $T_2$* accounts for the spin dephasing effect due to $B_0$ inhomogeneity. This can be eliminated in SE imaging due to the refocusing of the excited spins. However, more acquisition time is required for SE imaging because of the second RF pulse.

### 2.1.5.2. Gradient echo imaging

After the slice selection RF pulse is applied, gradient echo (GE) imaging uses a magnetic field gradient to intentionally dephase and rephase/refocus the spins in XY plane to form a "gradient echo." A typical GE pulse diagram is shown in Fig. 2.10.

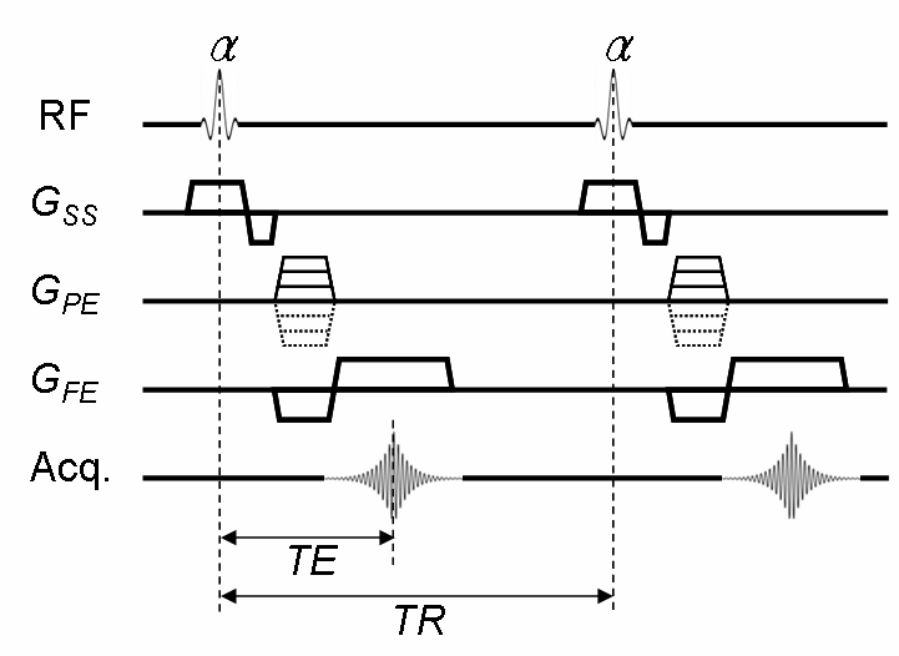


**Figure 2.10 Gradient echo imaging sequence.**

The spins are dephased while the negative gradient is applied and rephased with the positive gradient. Signal acquisition occurs while the spins are being rephased. Compared to SE imaging, GE imaging is typically faster, because it does not require the second RF pulse. However, GE imaging is sensitive to $B_0$ inhomogeneity effect and the amplitude of signal decays faster following $T_2$* relaxation. In both SE and GE sequences, *TE* and *TR* can be varied to obtain image contrast weighted with PD, $T_1$, or $T_2$.

### 2.1.5.3. Steady state free precession imaging

Steady state free precession (SSFP) imaging is a modification of GE imaging using a smaller flip angle (< 90°) and a *TR* shorter than $T_1$ and $T_2$ of the object. In SSFP imaging, a series of RF excitation pulses is repeatedly applied

every *TR*. If the *TR* is small enough, the MR signal remains constant from *TR* to *TR*. An example of an SSFP sequence is shown in Fig. 2.11.

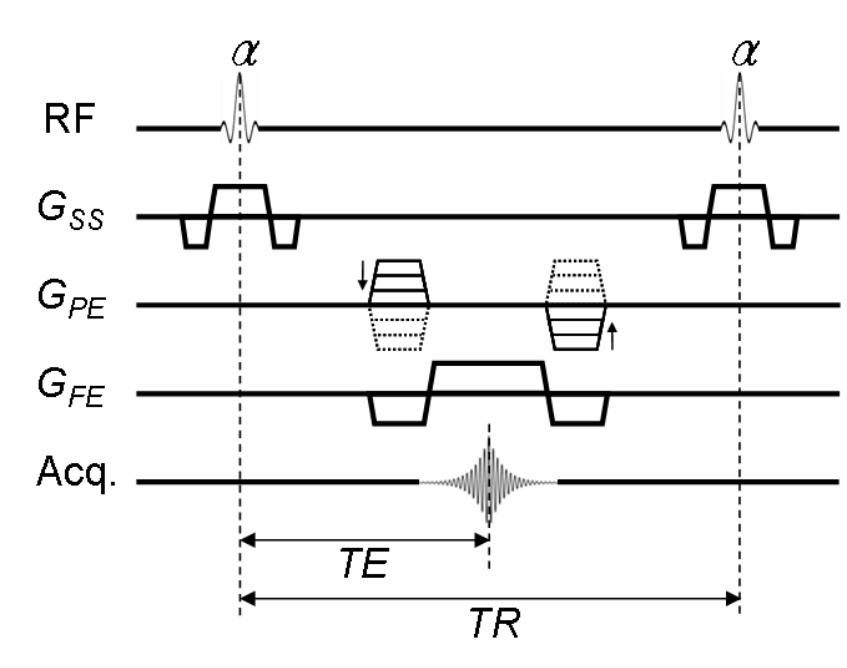


**Figure 2.11 Steady state free precession imaging sequence.**

The SSFP signal is given as[5]

$$\mathrm{SSFP}_{\mathrm{signal}} = M_0 \sin\theta \frac{1-e^{-TR/T_1}}{1-(e^{-TR/T_1}-e^{-TR/T_2})\cos\theta - e^{-TR/T_1}\cdot e^{-TR/T_2}} e^{-TE/T_2} \qquad \textbf{(Eq. 2.22)}$$

If *TR* is very short, i.e. $TR << T_2 < T_1$, Eq. 2.22 can be simplified as

$$\mathrm{SSFP}_{\mathrm{signal}} \approx \frac{M_0 \sin\theta}{(T_1/T_2)\cdot(1-\cos\theta)+(1+\cos\theta)} e^{-TE/T_2}, \text{ where } TR << T_2 \qquad \textbf{(Eq. 2.23)}$$

Because of $T_1/T_2$ term in the denominator of Eq. 2.23, SSFP imaging is said to have "$T_2/T_1$" contrast weighting.

Due to its short *TR* value, SSFP imaging requires relatively short imaging time while providing the highest possible SNR per unit time among all known imaging sequences.[6] The high temporal resolution and SNR make SSFP imaging

well suited for tumour tracking applications. However, banding (a spatial region where signal loss occurs) is a problem in SSFP imaging occurring from $B_0$ inhomogeneities, and/or susceptibility effects.[5]

## 2.2. ARTIFICIAL NEURAL NETWORK

An artificial neural network (ANN) is a mathematical model inspired by biological neural networks structure. Among many types of ANNs, we used a multilayer feedforward ANN to develop tumour motion prediction software, which is an essential component of this thesis. A brief introduction of the ANN and learning mechanism are provided in the following chapter.

### 2.2.1. Individual neuron model

A neuron is a fundamental information-processing unit of a neural network. The structure of a biological neuron is illustrated in Fig. 2.12.a. The neuron receives chemical messages from other neurons through dendrites. The messages are processed within cell body, and its decision is transmitted to other neurons via axon and synaptic terminals.

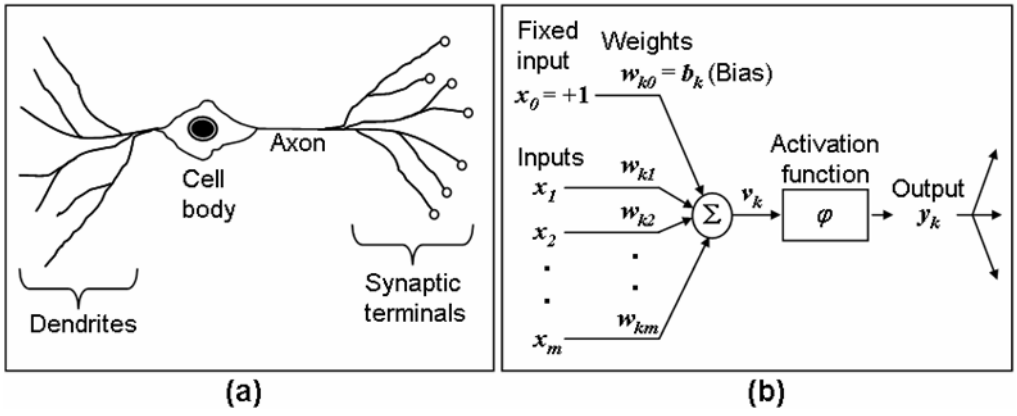


**Figure 2.12 Individual neuron structure: (a) biological neuron, (b) artificial neuron model.**

An artificial neuron model is shown in Fig. 2.12.b. Here, each input signal is weighted differently through a corresponding weight parameter, and their sum becomes the input of an activation function as the following

$$v_k = \sum_{j=0}^{m} w_{kj} \cdot x_j \qquad \textbf{(Eq. 2.24)}$$

where $x_0, \ldots, x_m$ are the inputs associated with corresponding weights $w_0, \ldots, w_m$, respectively. The neuron model includes a fixed input, $x_0 = +1$, associated with $w_{k0}$. $w_{k0}$ is also referred to as bias, $b_k$, which has the effect of shifting the $v_k$ value. Since $v_k$ is the input of the activation function, a single output issue (i.e. only one output value is possible when all inputs are zeros) can be avoided using $b_k$.

The activation function $\varphi$ is shown in Fig. 2.13, which is a sigmoid function with output values between 0 and 1.

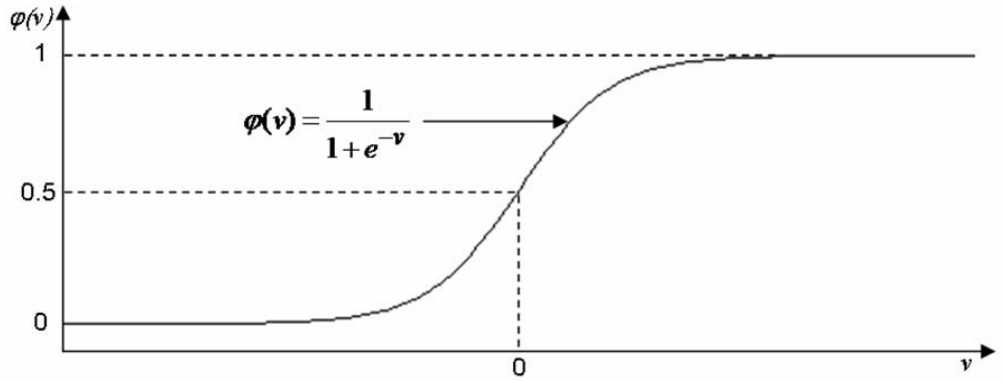


**Figure 2.13 Activation function** $\varphi(v) = 1/(1+e^{-v})$

Hence, the output of the neuron model is given as,

$$y_k = \varphi(v_k) \qquad \textbf{(Eq. 2.25)}$$

where $y_k$ and $v_k$ are the output and input of the activation function $\varphi$, respectively. $y_k$ is transmitted to other neighboring neurons.

## 2.2.2. Multilayer feedforward ANN

A multilayer feedforward ANN typically consists of an input layer, one or more hidden layers, and an output layer. The input signal (i.e. input values) propagates through the ANN in a forward direction, from input layer to output layer, on a layer-by-layer basis. An error value is calculated from the ANN output, and the error signal is projected back in a backward direction on a layer-by-layer basis to adjust each weight within the ANN. This is illustrated in Fig. 2.14, where *N* represents each neuron model.

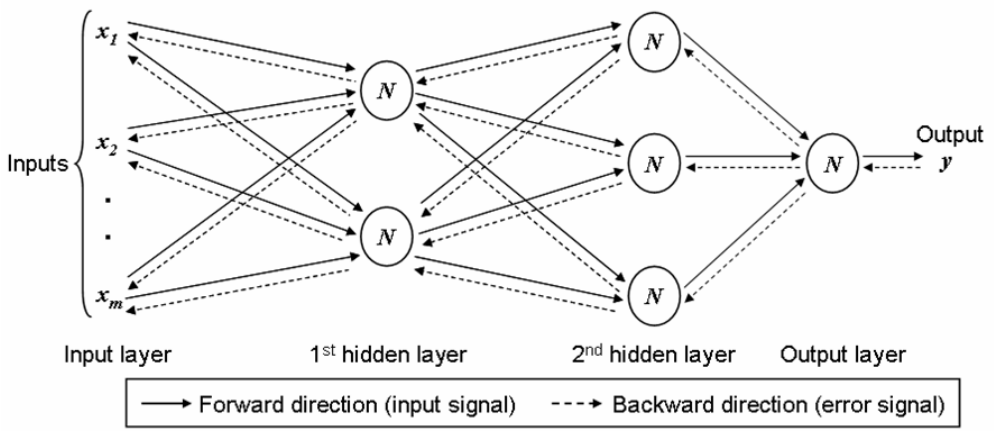


**Figure 2.14 Illustration of forward & backward directions in a multilayer feedforward ANN.**

## 2.2.3. Back-propagation algorithm

A back-propagation (BP) algorithm is one type of ANN training method. The BP algorithm uses a supervised learning method, meaning that it requires a training data set consist of many numbers of known input/output pairs. Using the pairs, a given ANN learns the relationship between inputs and desired outputs

through many numbers of iterations. During iterative training, one epoch refers to one complete presentation of the entire training data set through the ANN.

Figure 2.15 provides detailed signal flow from a hidden neuron $j$, $\mathbf{N}_j$, to an output neuron $k$, $\mathbf{N}_k$. Depending on ANN structure, multiple neurons may exist in the hidden layer as well as in the output layer.

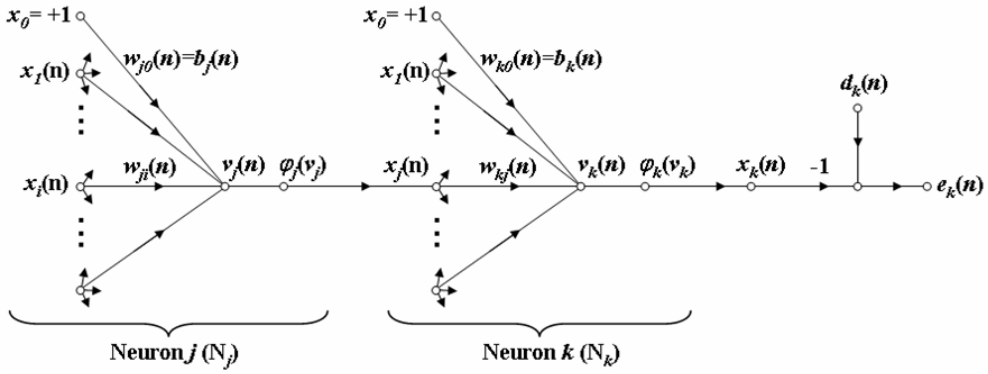


**Figure 2.15 Detailed signal flow from a hidden neuron $\mathbf{N}_j$ to an output neuron $\mathbf{N}_k$**

An error of the ANN at the $n^{\text{th}}$ iteration during training (i.e. presentation of the $n^{\text{th}}$ input/output pair to the ANN) is referred to as $e_k(n)$, which is defined as

$$e_k(n) = d_k(n) - x_k(n) \qquad \textbf{(Eq. 2.26)}$$

where $d_k(n)$ and $x_k(n)$ are the desired and actual outputs for $\mathbf{N}_k$, respectively. Using this, a cost function for the $n^{\text{th}}$ input/output pair, $\Psi(n)$, is defined as

$$\Psi(n) = \frac{1}{2}\sum_{k=1}^{C} {e_k}^2(n) \qquad \textbf{(Eq. 2.27)}$$

where $C$ is the number of neurons in the output layer. Also, a cost function for the entire training data set is given as

$$\Psi_{\text{avg}} = \frac{1}{N}\sum_{n=1}^{N} \Psi(n) \qquad \textbf{(Eq. 2.28)}$$

where $N$ refers to the total number of input/output pairs in the training data set.

The objective of ANN training is to find a set of weights within a given network that minimizes $\Psi_{avg}$. In the BP algorithm, the weights are updated each time when the input/output pair is introduced to the ANN until one epoch is completed. The updated weights are given as

$$w_{\text{updated}} = w_{\text{previous}} + \Delta w \qquad \textbf{(Eq. 2.29)}$$

where $\Delta w$ is proportional to the partial derivative of $\Psi(n)$ with respect to each weight within the network. Detailed explanation of $\Delta w$ follows.

### 2.2.3.1. Weight updating for output layer neurons

$\mathbf{N_k}$ illustrated in Fig. 2.15 is one of the output layer neurons. For $\mathbf{N_k}$, the partial derivative of $\Psi(n)$ is given as the following using the chain rule of calculus[7]

$$\frac{\partial \Psi(n)}{\partial w_{kj}(n)} = \frac{\partial \Psi(n)}{\partial e_k(n)} \cdot \frac{\partial e_k(n)}{\partial x_k(n)} \cdot \frac{\partial x_k(n)}{\partial v_k(n)} \cdot \frac{\partial v_k(n)}{\partial w_{kj}(n)} \qquad \textbf{(Eq. 2.30)}$$

Here, $v_k(n)$ is calculated as

$$v_k(n) = \sum_{j=0}^{m} w_{kj}(n) \cdot x_j(n) \qquad \textbf{(Eq. 2.31)}$$

where $m$ refers to the total number of inputs, $x_j(n)$, applied to $\mathbf{N_k}$ except the bias. Also,

$$x_k(n) = \varphi_k(v_k(n)) \qquad \textbf{(Eq. 2.32)}$$

By finding the partial derivative of Eqs. 2.27, 2.26, 2.32, and 2.31, the four terms in Eq. 2.30 yield, in order, the following

$$\frac{\partial \Psi(n)}{\partial w_{kj}(n)} = e_k(n) \cdot (-1) \cdot \varphi_k'(v_k(n)) \cdot x_j(n) \qquad \textbf{(Eq. 2.33)}$$

where $\varphi_k'(v_k(n)) = \frac{\partial\{\varphi_k(v_k(n))\}}{\partial v_k(n)}$.

Also, because $\Delta w$ is proportional to $\frac{\partial \Psi(n)}{\partial w_{kj}(n)}$, $\Delta w_{kj}(n)$ is given as

$$\Delta w_{kj}(n) = -\eta \cdot \frac{\partial \Psi(n)}{\partial w_{kj}(n)} \qquad \textbf{(Eq. 2.34)}$$

where $\eta$ is a learning rate that determines the convergence rate of the BP algorithm. Thus, from Eqs. 2.33 and 2.34,

$$\Delta w_{kj}(n) = -\eta \cdot \frac{\partial \Psi(n)}{\partial w_{kj}(n)} = -\eta \cdot e_k(n) \cdot (-1) \cdot \varphi_k'(v_k(n)) \cdot x_j(n) \qquad \textbf{(Eq. 2.35)}$$

A local gradient $\delta_k(n)$ is defined as the following, which points to the required changes in weights,[7]

$$\delta_k(n) = -\frac{\partial \Psi(n)}{\partial v_k(n)} = -\frac{\partial \Psi(n)}{\partial e_k(n)} \cdot \frac{\partial e_k(n)}{\partial x_k(n)} \cdot \frac{\partial x_k(n)}{\partial v_k(n)}$$

$$= e_k(n) \cdot \varphi_k'(v_k(n)) \qquad \textbf{(Eq. 2.36)}$$

Then, Eq. 2.35 can be rewritten as

$$\Delta w_{kj}(n) = \eta \cdot \delta_k(n) \cdot x_j(n) \qquad \textbf{(Eq. 2.37)}$$

Using this, each weight associated with $\mathbf{N_k}$ is updated by

$$w_{kj}(n+1) = w_{kj}(n) + \Delta w_{kj}(n) \qquad \textbf{(Eq. 2.38)}$$

### 2.2.3.2. Weight updating for hidden layer neurons

The weights associated with hidden layer neurons are updated in a similar way as for output layer neurons. In hidden layer neurons, however, the local gradient is calculated differently from the output layer neurons.

The definition of local gradient is the same for both hidden and output layer neurons. For a hidden layer neuron $\mathbf{N}_j$ shown in Fig. 2.15, the local gradient $\delta_j(n)$ is defined as

$$\delta_j(n) = -\frac{\partial \Psi(n)}{\partial v_j(n)} \qquad \textbf{(Eq. 2.39)}$$

Where $\Psi(n)$ is defined in Eq. 2.27. Compared to Eq. 2.36, the only difference in Eq. 2.39 is the index change from $k$ to $j$. By using the chain rule, Eq. 2.39 is rewritten as

$$\delta_j(n) = -\frac{\partial \Psi(n)}{\partial v_j(n)} = -\frac{\partial \Psi(n)}{\partial x_j(n)} \cdot \frac{\partial x_j(n)}{\partial v_j(n)} \qquad \textbf{(Eq. 2.40)}$$

Here, the first partial derivative term of Eq. 2.40 is given as

$$\frac{\partial \Psi(n)}{\partial x_j(n)} = \sum_{k=1}^{C} e_k(n) \cdot \frac{\partial e_k(n)}{\partial x_j(n)} = \sum_{k=1}^{C} e_k(n) \cdot \frac{\partial e_k(n)}{\partial v_k(n)} \cdot \frac{\partial v_k(n)}{\partial x_j(n)} \qquad \textbf{(Eq. 2.41)}$$

In Fig. 2.15, $e_k(n) = d_k(n) - x_k(n) = d_k(n) - \varphi_k(v_k(n))$. Thus,

$$\frac{\partial e_k(n)}{\partial v_k(n)} = -\varphi_k'(v_k(n)) \qquad \textbf{(Eq. 2.42)}$$

Also, $v_k(n)$ is given in Eq. 2.31 and its partial derivative is

$$\frac{\partial v_k(n)}{\partial x_j(n)} = w_{kj}(n) \qquad \textbf{(Eq. 2.43)}$$

By using Eqs. 2.42 and 2.43, Eq. 2.41 is given as

$$\frac{\partial \Psi(n)}{\partial x_j(n)} = -\sum_{k=1}^{C} e_k(n) \cdot \varphi_k'(v_k(n)) \cdot w_{kj}(n) \qquad \textbf{(Eq. 2.44)}$$

Here, the first two terms are equivalent to the local gradient of the output layer neuron $\mathbf{N}_k$ that is previously shown in Eq. 2.36, $\delta_k(n) = e_k(n) \cdot \varphi_k'(v_k(n))$. Thus,

$$\frac{\partial \Psi(n)}{\partial x_j(n)} = -\sum_{k=1}^{C} \delta_k(n) \cdot w_{kj}(n) \qquad \textbf{(Eq. 2.45)}$$

The second partial derivative term of Eq. 2.40 is given as

$$\frac{\partial x_j(n)}{\partial v_j(n)} = \frac{\partial \varphi_j(v_j(n))}{\partial v_j(n)} = \varphi_j'(v_j(n)) \qquad \textbf{(Eq. 2.46)}$$

Therefore, $\delta_j(n)$ is given as

$$\delta_j(n) = \varphi_j'(v_j(n)) \cdot \sum_{k=1}^{C} \delta_k(n) \cdot w_{kj}(n) \qquad \textbf{(Eq. 2.47)}$$

Using this result, the weights associated with $\mathbf{N}_j$ are updated as the following.

$$\Delta w_{ji}(n) = \eta \cdot \delta_j(n) \cdot x_i(n) \qquad \textbf{(Eq. 2.48)}$$

$$w_{ji}(n+1) = w_{ji}(n) + \Delta w_{ji}(n) \qquad \textbf{(Eq. 2.49)}$$

### 2.2.3.3. Summary of the BP algorithm

The BP algorithm is used for ANN training according to the following steps.[7]

(1) Randomly choose the initial weights for a given ANN from a uniform distribution, where its mean is zero and its variance is determined to make the standard deviation of the input for a corresponding activation function stay within the transition between the linear and saturated parts of the activation function.

(2) Present an epoch of examples, i.e. known input/output pairs within one complete training data set, to the ANN and update its weights for each input/output pair through forward and backward computations. Forward computation refers to the proceeding of input values through the ANN from the input layer to hidden and output layers as described in solid lines in Fig. 2.14. Backward computation includes (1) local gradients computations in a given layer of the ANN via Eqs. 2.36 and 2.47, and (2) updating each weight via Eqs. 2.37 - 2.38, and Eqs. 2.48 - 2.49.

(4) Iterate forward and backward computations and keep updating the weights by presenting another epoch of training data to the ANN until a user defined stopping criterion is satisfied.

## 2.3. PARTICLE SWARM OPTIMIZATION

The performance of ANN in a given task is strongly dependent on its structure (i.e. number of hidden layers, number of neurons in a given layer, number of inputs, etc) and initial weights (IW).[8, 9] However, there exists no analytical solution to determine the optimal ANN structure and IW, and these are typically determined by a human expert through trial and error processes. To automate this process, the particle swarm optimization (PSO)[10] was used in this research. A brief introduction to PSO is provided in this section.

PSO is one type of population-based, stochastic optimization method, which is inspired by the social behavior of bird flocking or fish schooling when they search for a target; for example, food. The goal of PSO is to search and converge to the global optimum solution in a given multi-dimensional solution

space.

PSO begins by generating a swarm of particles that are randomly distributed over an *n*-dimensional solution space with different positions and velocities. Each of these particles represents a potential solution to a given optimization problem. For example, a particle A's position in the solution space indicates a current solution of the optimization problem represented by A. Also, A's velocity determines its position update at next iteration, meaning that the current solution represented by A will be updated toward a new, more optimized solution at next iteration.

The particles will "fly" through the solution space, in order to find a specific location where the solution at that location will produce the optimum result with regard to a user defined fitness function. During PSO process, each particle keeps track of (1) its position in the solution space and (2) its best solution so far achieved. Each particle's best solution is referred to as *pbest*, the personal best solution. Also, the entire swarm's best solution is tracked and referred to as *gbest*, the global best solution.

As explained earlier, each particle's position in the solution space is updated in each iteration. Firstly, the particle's updated velocity is calculated as the following,[11] assuming the iterations occur in discrete time steps.

$$V_{updated} = V_{prev} + c_1 \cdot rand_1 \cdot (pbest - P_{prev}) + c_2 \cdot rand_2 \cdot (gbest - P_{prev})$$

**(Eq. 2.50)**

where, $V_{updated}$: updated velocity a particle, $c_1$, $c_2$: a user defined unitless weight, $rand_1$, $rand_2$: a rational random number between 0 and 1, $V_{prev}$, $P_{prev}$: previous

velocity and position of a particle. In PSO, $V_{updated}$ is determined by both individual (*pbest* and $V_{prev}$) and social (*gbest*) components, and their contributions are weighted by the user defined $c_1$, $c_2$ values.

After each particle's velocity update, the particle's updated position is determined as the following:[11]

$$P_{updated} = P_{prev} + V_{updated} \cdot T \qquad \textbf{(Eq. 2.51)}$$

where, $P_{updated}$: updated position of a particle. In PSO, velocity ($V_{updated}$) is regarded as displacement per iteration rather than displacement per time. Thus, the value of $T$ is fixed at 1.

## 2.4. REFERENCES


1 R. Eisberg and R. Resnick, *Quantum Physics of Atoms, Molecules, Solids, Nuclei, and Particles*, 2nd edition. (John Wiley & Sons, Inc., USA, 1985).

2 J. Beutel, H. L. Kundel, and R. L. Van Metter, *Handbook of Medical Imaging, Volume 1. Physics and Psychophysics*, (SPIE, Bellingham, WA, 2000).

3 F. Bloch, "Nuclear Induction," Physical Review **70**(7-8), 460-474 (1946).

4 T. R. Brown, B. M. Kincaid, and K. Ugurbil, "NMR Chemical Shift Imaging in Three Dimensions," Proceedings of the National Academy of Sciences of the United States of America **79**(11), 3523-3526 (1982).

5 M. A. Bernstein, K. F. King, and X. J. Zhou, *Handbook of MRI pulse sequences*, (Academic Press, Burlington, MA, 2004).

6 G. B. Chavhan, P. S. Babyn, B. G. Jankharia, H.-L. M. Cheng, and M. M. Shroff, "Steady-State MR Imaging Sequences: Physics, Classification, and Clinical Applications," Radiographics **28**(4), 1147-1160 (2008).

7 S. S. Haykin, *Neural networks : a comprehensive foundation*, 2nd ed. (Prentice Hall, Upper Saddle River, NJ, 1999).

[8] H. R. Maier and G. C. Dandy, "The effect of internal parameters and geometry on the performance of back-propagation neural networks: an empirical study," Environmental Modelling & Software **13**(2), 193-209 (1998).

[9] L. F. A. Wessels and E. Barnard, "Avoiding false local minima by proper initialization of connections," IEEE Transactions on Neural Networks **3**(6), 899-905 (1992).

[10] J. Kennedy and R. Eberhart, "Particle swarm optimization," in Proceedings of the 1995 IEEE International Conference on Neural Networks, Perth, Australia, Nov. 27-Dec. 1, 1995.

[11] Y. H. Shi and R. Eberhart, "A modified particle swarm optimizer," in Proceedings of the 1998 IEEE International Conference on Evolutionary Computation, Anchorage, Alaska, May 4-9, 1998.

# Chapter 3: Evaluation of a lung tumour autocontouring algorithm for intrafractional tumour tracking using low-field MRI

*A version of this chapter has been published: J. Yun, E. Yip, K. Wachowicz, S. Rathee, M. Mackenzie, D. Robinson, and B. G. Fallone, "Evaluation of a lung tumor autocontouring algorithm for intrafractional tumor tracking using low-field MRI: A phantom study," Med. Phys.* ***39****(3), 1481-1494 (2012).*

## *3.1. INTRODUCTION*

Image-guided radiotherapy (IGRT) promises improved targeting and delivery of highly conformal radiation dose to tumours. Using IGRT, interfractional variations due to daily patient positioning errors or changes in anatomy can be monitored and minimized.[1] A problem still emerges, however, when treating mobile tumours such as those occurring in lung.

Lung tumours are often difficult to treat due to their potential for complicated, large ranges of intrafractional motion and deformation over time. Various studies have shown that lung tumour may move up to 40 mm in superior–inferior (SI), 15 mm in anterior–posterior (AP), and 10 mm in left–right (LR) directions during normal breathing.[2-4] Volume changes up to 20 % and rotations up to 50 degrees with respect to each axis have also been reported.[5] Unfortunately, a method of directly imaging and tracking lung tumours during actual radiation

delivery does not currently exist, and this presents potential limitations to accurate radiotherapy treatments.

Currently available commercial systems deal with this problem by indirect tracking methods using several types of tumour surrogates. For example, the Varian Real-time Position Management (RPM) system (Varian Inc., Palo Alto, CA)[6] uses a single external surrogate, whereas Cyberknife (Accuray Inc., Sunnyvale, CA)[7] requires both internal and external surrogates. The 4D Localization system (Calypso Medical, Seattle, WA)[8] uses electromagnetic transponders called "beacons" as internal surrogates, and the Real-time Tumor-tracking Radiation Therapy (RTRT) system (Hokkaido University, Sapporo, Japan)[9] requires internal seeds and orthogonal kV imaging to perform tumour tracking. In addition to these commercial systems, several groups are actively researching real-time (i.e. intrafractional) tumour tracking systems.[10-13]

Despite the wide variety of techniques currently in use, all current tracking methods remain based on indirect tracking through the use of internal or external tumour surrogates. Reliance on surrogates, however, has been shown to be problematic for accurate tumour tracking for the following reasons: (1) Utilizing internal surrogates requires invasive procedures, and these implanted surrogates have been known to migrate from their initial positions during the course of the radiation treatment,[14] and (2) Tracking with external surrogates must rely on ambiguous correlations between internal tumour motion and external surrogate displacement.[15] More importantly, any deformation of tumour shape is completely unknown during treatment.

Due to the indirect nature of these tracking mechanisms, the shape and

position of the tumour must be inferred from the location of the surrogates used. Therefore, extended regions surrounding the lesion must be irradiated in order to ensure sufficient target coverage,[16] which includes the uncertainty caused by poor correlation between tumour position and surrogates. This approach, however, may result in medical complications due to excessive normal tissue irradiation adjacent to the tumour.[17]

On-line radiotherapy-MR systems, which have been proposed by several groups,[18-21] may overcome these difficulties by providing direct, intrafractional MR images of tumours without the need for surrogates. Our laboratory reported the first integrated radiotherapy-MR system known as a linac-MR.[19] This system can provide 2D intrafractional MR images including a beam's eye view depicting the plane of largest tumour motion.

Time consuming, manual contouring of tumour shape would effectively negate the potential advantages of fast tumour imaging. Thus a rapid and reliable tumour autocontouring algorithm is required in order to perform useful intrafractional tumour tracking. This algorithm must detect tumour shape and position in each intrafractional MR image during treatment, thus allowing for appropriate intrafractional radiation beam adjustment.

In this chapter, we investigate the feasibility of real-time autocontouring of tumour in MR images by means of a phantom and simulation study. This investigation is focused primarily on the requirements for lung tumour autocontouring in low field MR images, at 0.2 T and 0.5 T. The development of an MR compatible, lung tumour motion phantom is also presented.

## 3.2. MATERIALS AND METHODS

An overview of intrafractional tumour tracking scheme is explained in Sec. 3.2.1. Section 3.2.2 describes our autocontouring algorithm. Section 3.2.3 describes the fabrication of an MR compatible motion phantom incorporating a lung tumour like target imbedded in lung analogue materials, which is used to simulate lung tumour MR images at low fields. These images are used to evaluate the tracking performance of our algorithm, which is detailed in Sec. 3.2.4.

### 3.2.1. Overview of intrafractional tumour tracking

Figure 3.1 shows an overview of intrafractional tumour tracking scheme proposed in this thesis.

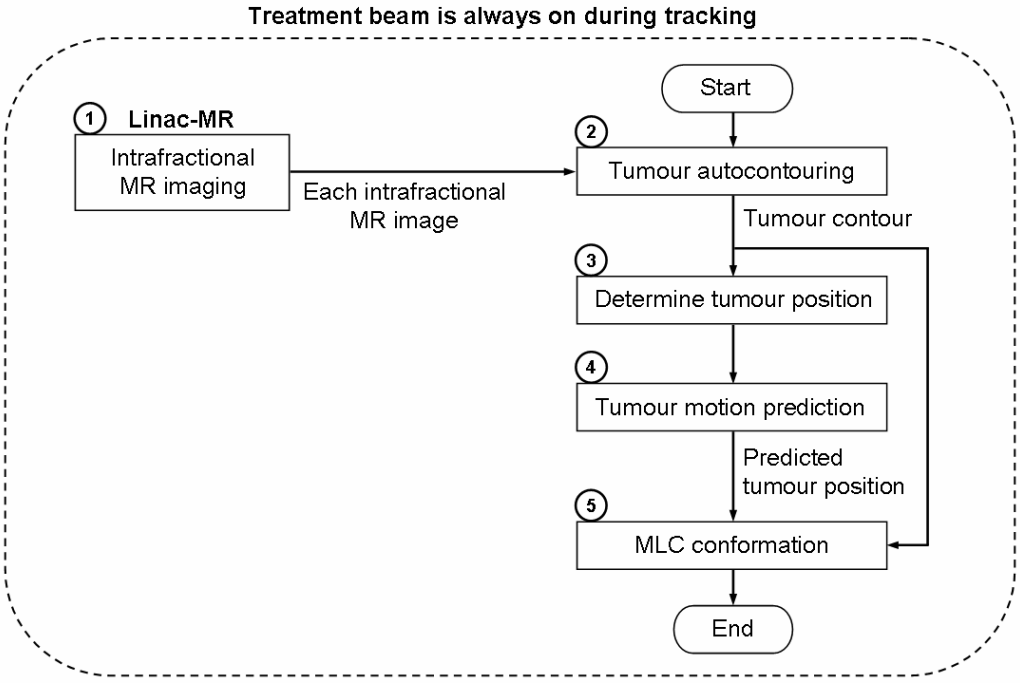


**Figure 3.1 Intrafractional tumour tracking scheme using a linac-MR**

Our tracking scheme is designed such that the treatment beam is always on during tumour tracking. In Step 1 of Fig. 3.1, an intrafractional MR image of a tumour/target volume and surrounding anatomy is acquired using a linac-MR. In Step 2, the tumour shape is automatically contoured using our in-house built tumour autocontouring software (presented in this chapter). In Step 3, the tumour position (i.e. centroid position) is calculated based on the autocontoured tumour shape, referred to as a current tumour position. In Step 4, a future tumour position is predicted based on the current and previous tumour positions using our in-house built tumour motion prediction software (presented in Chapter 5 of this thesis). This step is necessary to compensate for the intrafractional tumour motion during the time required for MLC conformation. In Step 5, the MLC is driven in real-time to conform the treatment beam to the current tumour shape (from Step 2) at the predicted tumour position (from Step 4). Steps 2 – 5 are repeated each time a new intrafractional image is acquired during tracking.

### 3.2.2. Lung tumour autocontouring algorithm

An autocontouring algorithm was developed to determine both the position and shape of a lung tumour from each intrafractional MR image. The algorithm was developed in accordance with the following scenario: (1) A pre-treatment, dynamic MR scan is performed with the treatment unit (i.e. linac-MR), using the same MR sequence and patient set-up intended for treatment. (2) During treatment, the linac-MR will provide 2D intrafractional, dynamic MR imaging of a lung tumour. The plane of MR imaging will be selected to visualize the maximum tumour dimensions for the beam's eye view. (3) MR images will be

acquired at an imaging rate of 3 - 4 fps. This rate is the minimum requirement for lung tumour tracking based on AAPM Task Group 76 report,[22] which recommended less than 500 ms time delay (including 100 - 200 ms beam repositioning time) between acquisition of tumour position and beam repositioning in order to take clear advantage of real-time tracking over other tracking methods. To satisfy this, the tumour position must be updated approximately every 300 ms, which is the imaging rate assumed in this study.

Figure 3.2 illustrates the step-by-step autocontouring processes. In Fig. 3.2, Steps 1 - 3 describe the pre-treatment processes that must occur in preparation for the autocontouring session during treatment (Sec. 3.2.2.1). Steps 4 - 14 describe the main algorithm (Sec. 3.2.2.2). Each step of the algorithm is examined using an example lung tumour MR image obtained from a previous study.[23] This image was acquired at 1.5 T with a half-Fourier single-shot turbo-spin-echo sequence, and reprinted in Fig. 3.3 with permission from Eur. J. Radiol. 29, 152–159 (1999). 

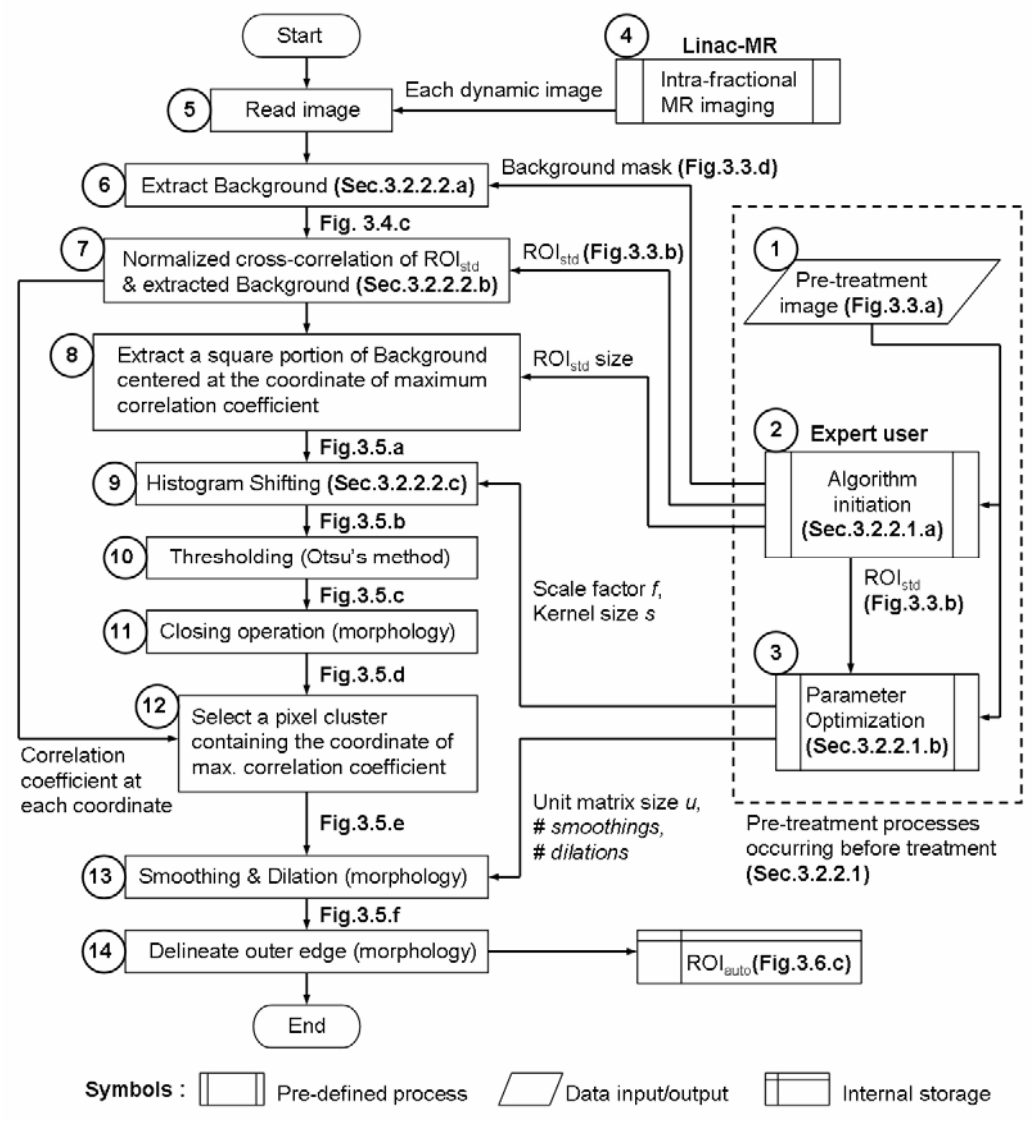


**Figure 3.2 Flow chart for overall autocontouring processes**

## 3.2.2.1. Pre-treatment processes

Pre-treatment processes consist of Steps 1 – 3 in Fig. 3.2. In Step 1, the pre-treatment processes commence with the acquisition of pre-treatment images. A single image is chosen from these images as an input for Steps 2 and 3. This image should be the one image of the series that is least impacted by motion artifacts, often an image at the end of an exhale period.

### 3.2.2.1.a. Algorithm initiation (Step 2)

In Step 2, an expert user draws two contours on the pre-treatment image: (1) the lung tumour on the image, which we call a standard region of interest ($ROI_{std}$) as shown in Fig. 3.3.b, and (2) the region covering the maximum anticipated range of tumour motion, which is herein after referred to as the "Background" as shown in Fig. 3.3.c. This may be determined by observing the maximum extension tumour movement from the pre-treatment MR images over several breathing cycles. During autocontouring, the algorithm expects that the tumour will reside within the Background region of each MR image. Therefore, the pre-treatment image must be taken by the treatment unit (e.g. linac-MR) to have the most similar patient anatomy, image size, resolution as the one that will be acquired during the autocontouring session. A binary mask (an array of ones and zeros) called "Background mask" is generated as shown in Fig. 3.3.d, where the delineated region has a pixel value of one.

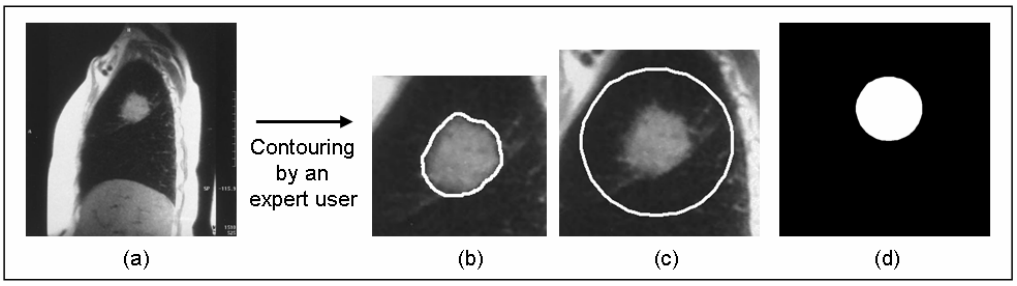


**Figure 3.3 Algorithm initiation (Step 2 in Fig. 3.2). (a) Pre-treatment image (b) $ROI_{std}$ contour (c) Background contour (d) Background mask**

### 3.2.2.1.b. Parameter optimization (Step 3)

Prior to the autocontouring session for each patient, the following five parameters must be chosen: (1) the scaling factor ***f*** in the histogram shifting (HS)

algorithm,[24] (2) kernel size ***s*** in the HS algorithm,[24] (3) unit matrix size ***u*** of smoothing filter, (4) **number of smoothing** operations, and (5) **number of dilation** operations. The HS algorithm[24] is used for edge detection or edge enhancement within an image, which performs the following transformation with the choice of two parameters ***f*** and ***s***:

$$X'_{k,l} = X_{k,l} - [f \times \min(X_{kernel(i,j)})] \qquad \textbf{(Eq. 3.1)}$$

where,

$X'_{k,l}$ : new gray level of the center pixel of a kernel at $(k,l)$, a kernel size ***s*** is determined by Step 3

$X_{k,l}$ : original gray level of the center of the kernel located at $(k,l)$

***f*** : scaling factor between 0 and 1, determined by Step 3

$\min(X_{kernel(i,j)})$ : minimum pixel value within the kernel $X_{i,j}$ (centered at $k,l$) covering all $(i,j)$ within the size ***s***

These five parameters are optimized in Step 3. This is to determine a set of parameters that if the autocontouring is performed with these parameters, the autocontoured tumour shape will be the closest to the tumour shape contoured by an expert user. The parameters vary depending on the MR image characteristics such as signal intensity, contrast, resolution, etc. Therefore, the pre-treatment image used in parameter optimization must be taken by the treatment unit (e.g. linac-MR) to have the most similar image characteristics as the one that will be acquired during the autocontouring session.

In Step 3, an ROI delineated by an expert user ($ROI_{std}$) is compared to an autocontoured tumour shape ($ROI_{auto}$) obtained from the same MR image. Dice's coefficient ($D$) is used as a measure of similarity, which is defined as:

$$D = 2 \times Area(ROI_{std} \cap ROI_{auto}) / \{Area(ROI_{std}) + Area(ROI_{auto})\} \quad \textbf{(Eq. 3.2)}$$

The goal of optimization is to maximize $D$ as the following:

(1) Autocontouring occurs with different possible combinations of the 5 parameters from: $\boldsymbol{f}$ = 1, 0.95,…,0.5, $\boldsymbol{s}$ = 10, 15,…,30 % of $ROI_{std}$ size, $\boldsymbol{u}$ = 3 × 3 or 5 × 5, **number of smoothings** = 0, 1,…, 20, **number of dilations** = 0, 1,…, 20.

(2) From the autocontouring process performed with each combination, an $ROI_{auto}$ is determined. A $D$ value is calculated between the $ROI_{auto}$ and $ROI_{std}$.

(3) The combination of parameters that produces the maximum $D$ ($D_{max}$) is chosen as the optimum combination. Typical $D_{max}$ values of 0.93 – 0.95 are achieved at the end of parameter optimization.

### 3.2.2.2. Main algorithm

After the pre-treatment processes are completed, the main algorithm (Steps 4 – 14 in Fig. 3.2) is applied to each intrafractional MR image to contour the tumour. This is an automated process requiring no further input from the user.

#### 3.2.2.2.a. Background extraction (Steps 4 – 6)

Step 4 describes the acquisition and reconstruction of intrafractional MR images by the linac-MR system. Each image will be fed into the algorithm on-line in Step 5. In Step 6, the algorithm extracts the Background region from the image input as shown in Fig. 3.4. Subsequent processing from Step 7 through 14 assumes that the tumour will reside within the Background (Fig. 3.4.c) during autocontouring.

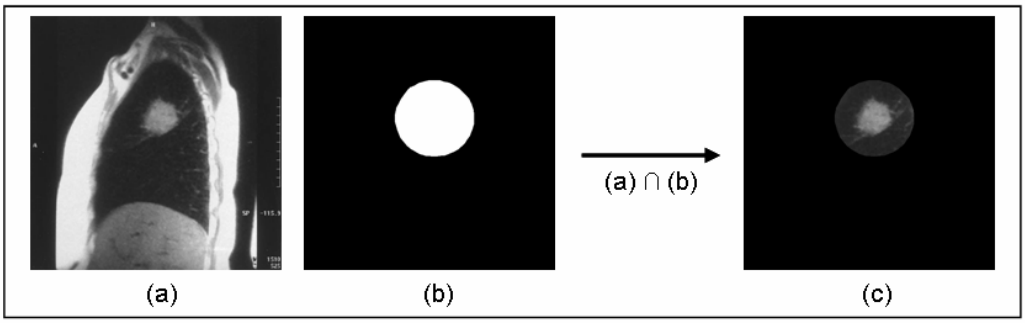


**Figure 3.4 Background extraction (Step 6 in Fig. 3.2). (a) Each MR image (b) Background mask from Step 2 (c) Background (extracted by multiplying each MR image and the Background mask)**

### 3.2.2.2.b. Determination of approximate tumour position (Steps 7 - 8)

The Background contains a tumour as well as large amount of undesirable anatomy surrounding the tumour (e.g. blood vessels, normal lung parenchyma, etc). Steps 7 and 8 are implemented to minimize the undesirable anatomy presented to the subsequent steps (Steps 9 - 14), so that the interference from the surrounding anatomy can be minimized in determination of the tumour shape. Also, because the subsequent steps are applied only to the result of Step 8 that could be considerably smaller than the entire Background, less computing time is required.

In Step 7, a Fast Normalized Cross-Correlation (FNCC)[25] is applied between the $ROI_{std}$, i.e. a portion of Fig. 3.3.b enclosed by $ROI_{std}$ contour, and the Background shown in Fig. 3.4.c. In Step 8, a square portion of the Background (Fig. 3.4.c) is extracted, where the center of the square is located at the coordinate of the maximum correlation coefficient. The size of this square is user adjustable, but calculated to match 120 % of the $ROI_{std}$ size as a default. This is a conservative assumption based on a study by Plathow *et al*.[5] that provides an

adequate coverage for tumour volume changes during autocontouring. The coordinate of the maximum correlation coefficient indicates an approximate tumour position within the Background. However, this may not be the exact center of the tumour, because the tumour shape in each MR image is expected to change during treatment, whereas the $ROI_{std}$ stays the same. Hence, the coordinate of the maximum correlation coefficient may not always coincide with the center of the tumour.

### 3.2.2.2.c. Determination of tumour shape (Steps 9 – 14)

The output of Step 8 is shown in Fig. 3.5.a, which is a square portion (240 % of the $ROI_{std}$ size) extracted from the Background. This is referred to as the "most probable tumour region." In this report, 240 % is chosen for better visualization of the surrounding anatomy of the tumour and the results of subsequent steps (Fig. 3.5.b - Fig. 3.5.f). The following steps are applied to the output of Step 8 to determine the tumour shape:

(1) In Step 9, the HS algorithm[24] is applied to the most probable tumour region for edge enhancement. The result is shown in Fig. 3.5.b.

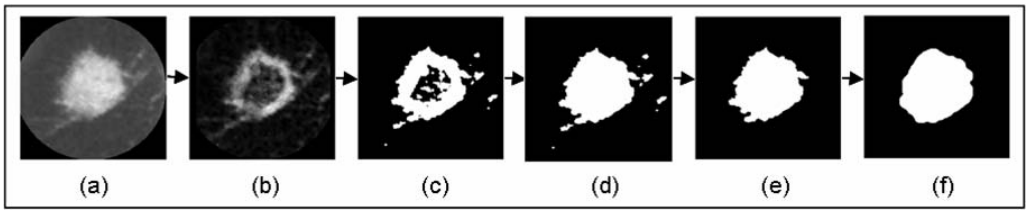


**Figure 3.5 (a) most probable tumour region (b) HS result with $f$ = 1, $s$ = 19 × 19 (c) threshold result (d) holes filled (e) selected tumour shape (f) final tumour contour after smoothing ($u$ = 5 × 5, 12 smoothings, 2 dilations)**

(2) In Step 10, a pixel threshold method is used to transform Fig. 3.5.b into

a binary mask as shown in Fig. 3.5.c. A pixel threshold value is calculated by Otsu's method,[26] which finds an optimal threshold from a gray-level histogram that will maximize the separation between the two classes such as background and objects. There is no other parameter involved in this step. The result of thresholding undergoes a morphological closing[27] operation in Step 11.

(3) The result of Step 11 is shown in Fig. 3.5.d, which contains many isolated pixel clusters in addition to the tumour. In Step 12, the algorithm determines only the tumour shape and rejects other pixel clusters. This occurs by selecting the pixel cluster containing the coordinate of maximum correlation coefficient obtained from Step 7, which represents the most likely position of the tumour. The result is shown in Fig. 3.5.e.

(4) In Step 13, a final tumour shape is determined by applying morphological smoothing and dilation operations.[27] A unit matrix size $u$ for the smoothing filter, the number of smoothing, and the number of dilation operations were pre-determined from Step 3.

(5) In Step 14, the outer edge of the tumour shape is delineated by applying a morphological gradient operation.[27] A typical result is shown in Fig. 3.6.c for the sample image used in this report.

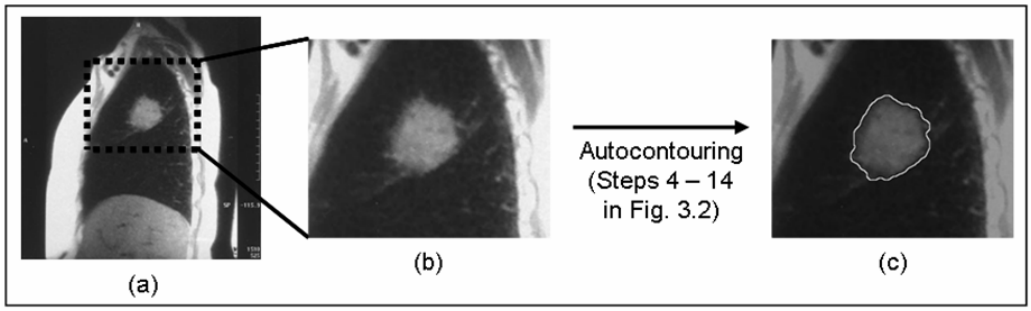


**Figure 3.6 (a), (b) original tumour image (c) autocontoured tumour shape with $f$ = 1, $s$ = 19 × 19, $u$ = 5 × 5, 12 smoothings, 2 dilations.**

## 3.2.3. Simulating low field contrast-to-noise ratio of lung tumour in a clinical 3 T system

To evaluate the performance of our autocontouring algorithm, phantom images were acquired which would best reflect the image quality characteristic of lung tumour MR images at low fields with special attention to contrast-to-noise ratio (CNR). Further, as our laboratory's linac-MR designs are based on low field MR systems (0.5 T and 0.2 T), the performance of our autocontouring algorithm must be evaluated in these situations. Hence, a series of experiments were devised to image a special lung contrast phantom in a high-field clinical scanner (Achieva 3 T, Philips Medical Systems, Andover, MA), which could then be used to simulate the relative signal levels and relaxation behaviors of a lung tumour and normal lung parenchyma at arbitrarily chosen lower fields.

### 3.2.3.1. MR contrast parameters and CNR

The ability to distinguish two different types of tissues in an image is largely dependent on CNR. In the case of a lung tumour, even if the contrast between lung tumour and normal lung parenchyma is substantial, excessive noise

can hamper clear distinction of the tumour. Also, even if the noise is low, it will be difficult to make a clear distinction of the tumour with insufficient contrast.

In MRI, the relationship between CNR and $B_0$ (polarizing magnetic field strength) is generally complex. CNR is also closely related to signal–to-noise ratio (SNR) as:

$$CNR = \frac{S_T - S_N}{\sigma} = \left(SNR_T - SNR_N\right) \qquad \textbf{(Eq. 3.3)}$$

where $S_T$ and $S_N$ refer to the MR signal of lung tumour and normal lung parenchyma respectively, and $\sigma$ is the noise measured as the standard deviation of a region with uniform background signal. $SNR_T$ and $SNR_N$ are the signal to noise ratios for the tumour and normal parenchyma, respectively. The difference between $S_T$ and $S_N$ arises from several factors intrinsic to tissue type, including NMR relaxation parameters that vary in a non-linear fashion with respect to $B_0$.

One of the contributions to signal difference (i.e. contrast) in Eq. 3.3 is relative proton density (PD). PD for lung parenchyma is reported to be roughly 0.2 - 0.35 relative to muscle,[28] whereas PD of lung tumour is very similar to muscle at 1.04.[29] From these values, one can infer that the lung parenchyma will have a relative PD to tumour of 0.19 - 0.34. This large difference contributes to the high inherent contrast in the imaging of solid lung tumours. Other intrinsic factors such as the spin-spin relaxation times ($T_2$), spin-lattice relaxation times ($T_1$), and $T_2$* relaxation times also affect contrast to a certain extent depending on sequence type, chosen parameters (TE/TR), and the strength of $B_0$.

Investigations into NMR relaxation times of lung tumour and normal lung parenchyma, and their dependencies on $B_0$ have been published in the literature[30]

as the following:

(1) At lower magnetic field strengths, $T_1$ for normal lung parenchyma and lung tumour are expected to be 455 ± 86 ms and 372 ± 185 ms at 0.2 T ($\Delta T_1$ of 83 ms) respectively, compared to 599 ± 114 ms and 532 ± 271 ms at 0.5 T ($\Delta T_1$ of 68 ms), and 829 ± 157 ms and 826 ± 421 ms at 1.5 T($\Delta T_1$ of 3 ms).[30] Therefore, from the point of view of $T_1$ alone, the shorter $T_1$ at lower fields offer a relative signal enhancement due to the more rapid recovery of longitudinal magnetization. Also, the greater difference in $T_1$ between the two tissues ($\Delta T_1$) at low fields may lead to more favorable tumour contrast.

(2) $T_2$ for normal lung parenchyma and lung tumour are quite similar, 79 ± 29 ms and 68 ± 45 ms respectively, and have only minor dependencies on $B_0$.[30]

(3) $T_2$* for normal lung parenchyma is known to be significantly longer at lower fields[31] and may lead to increased signal for some sequences. As solid lung tumours are less sensitive to susceptibility effects that arise from air-tissue interfaces, they will have a considerably higher $T_2$* compared to lung parenchyma,[32] and are likely to be less sensitive to change in $B_0$. Nevertheless, our dynamic MR sequence of choice, balanced steady state free precession (bSSFP), is largely independent of $T_2$*, so its impact will be limited.[33]

$B_0$ affects SNR, and, by extension, the CNR in MR images (Eq. 3.3). MR signal is proportional to $B_0^2$ due to two complementary factors:[34] (1) the difference in population of the two spin states increases linearly with $B_0$; and (2) the increase of Larmor frequency ($\propto B_0$) generates greater flux in MR coils by Faraday induction. However, MR noise is also known to be dependent on $B_0$.[34]

MR noise arises from resistance in the coils and electronics ($\propto B_0^{1/4}$), and resistance from the body ($\propto B_0$).[34] For our range of $B_0$ (scaling down from 3 T to 0.5 T/0.2 T), body noise ($\propto B_0$) is likely to be the dominant source of noise.[35] Thus, if the effects of different relaxation times can be accounted for in each tissue type (i.e. built into a phantom), a general assumption may be made that $SNR_T$ and $SNR_N$ (and therefore CNR) will vary linearly with $B_0$.

Our approach was to build a lung phantom that replicates the low field (0.2 T and 0.5 T) $T_1$ and $T_2$ values of lung tumour and normal lung parenchyma in the 3 T environment. This phantom would also have a correct relative PD between tumour and normal parenchyma. As the appropriate contrast parameters were built into the phantom, images acquired using a 3 T MRI with this phantom will yield the correct low field contrast even if the MR sequence parameters (such as flip angle, TR/TE) are changed. Because these images have correct low field contrast, CNR may be scaled down to the appropriate levels at 0.2 T and 0.5 T by the addition of Gaussian noise.

### 3.2.3.2. Phantom construction

Our phantom and its experimental set-up are shown in Fig. 3.7. The phantom contains a moving lung compartment within a thorax region. A lung tumour model is located approximately at the center of the lung compartment, and this model is surrounded by simulated normal lung parenchyma. The lung compartment is driven by a programmable motor using a rigid aluminum rod (grounded to the waveguide), creating 1D motion along the axis of the cylindrical

lung compartment similar to the dominant superior-inferior motion of lung tumours.

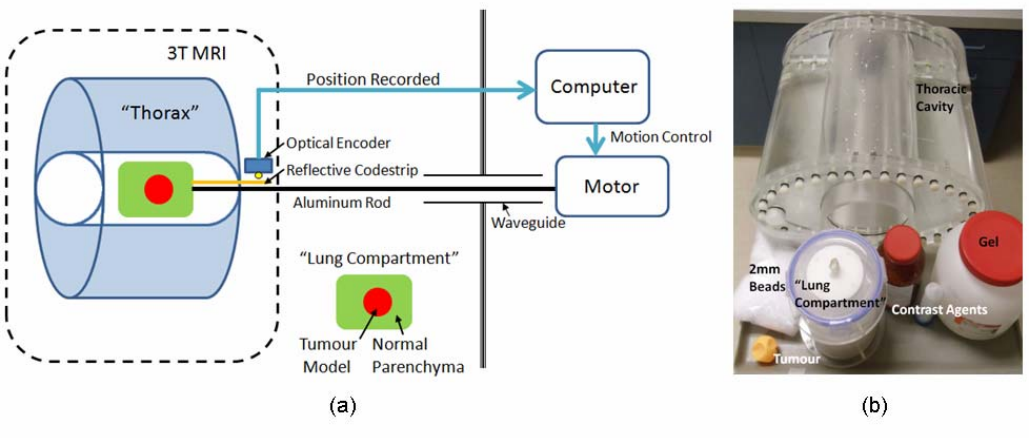


**Figure 3.7 (a) Schematic diagram of the experiment set-up (b) Lung tumour motion phantom.**

The lung compartment of the phantom contains two different tissue equivalents, a solid lung tumour and normal lung parenchyma. The idea of creating a specific tissue-equivalent MR phantom is not new. Methods have been devised for creating MR phantoms that can simulate relaxation and dielectric properties of various tissues in the body at 1.5 T.[36] However, building a lung parenchyma equivalent phantom is particularly challenging because of its low PD. In general, this cannot be achieved by using standard phantom materials such as solutions, gels and aqueous media. Our lung parenchyma equivalent requires a low relative PD (approximately 0.3) compared to the tumour. To achieve this, plastic beads (ColorFill vase fillers, ~ 2 mm diameter) that contribute no MR signal are mixed with porcine skin gelatin in a 70 : 30 ratio by volume. The resulting mixture has the relative PD similar to lung parenchyma. This is verified by performing a PD-weighted (short TE, long TR) scan on the phantom and

comparing the signal of the tumour region and parenchyma regions. $T_1$ and $T_2$ relaxation parameters are modified by doping the gelatin with MR contrast agents.

The lung tumour model is a shaped plastic container (~ 40 mm diameter, ~ 0.3 mm wall thickness) filled with a $MnCl_2$ and $CuSO_4{:}5H_2O$ solution. Two different shapes are fabricated; an ideal, spherical tumour shape, and a more realistic, non-spherical tumour shape. An aqueous solution (approximately 100 % water) is used in this study as the solid tumour equivalent, even though a real tumour, similar to tissue,[29] contains only ~ 75 % water.[37] This will result in overestimation of $SNR_T$ by 33 %. Also, as previously explained, our simulated normal lung parenchyma has correct *relative* PD to the tumour. Therefore, both $SNR_T$ and $SNR_N$ is overestimated by 33 %, and this will be compensated by adding additional Gaussian noise in the post processing steps explained later in this report.

Specific concentrations of $MnCl_2$ and $CuSO_4{:}5H_2O$ are required to achieve the $T_1$ and $T_2$ relaxation times for 0.5 T and 0.2 T as reported by Bottomley *et al*.[30] These are: (1) for lung tumour model, 0.020 g/L and 0.016 g/L of $MnCl_2$ in de-ionized water to generate the equivalent 0.5 T and 0.2 T relaxation times respectively; and (2) for normal lung parenchyma, 0.0125 g/L $MnCl_2$ gel/plastic bead mixture generating 0.5 T relaxation times, and 0.016 g/L $MnCl_2$ + 0.06 g $CuSO_4{:}5H_2O$ gel/plastic mixture producing 0.2 T relaxation times. In addition, 3.6 g/L NaCl is added to all solutions to simulate the electric conductivity of tissues.[38] To simulate the "body noise," the thoracic cage is filled with substantial amounts of materials that have similar electric conductivity to the body. Approximately 12 liters of generic MR tissue phantom solution (1.25 g/L

$CuSO_4$:$5H_2O$ + 3.6 g/L of NaCl) is used to simulate coil loading in realistic situations.[38]

Relaxation times are determined from experiments in 3 T MRI as the following: (1) $T_1$ times are measured with a $T_1$ mapping algorithm using inverse recovery sequence (TE = 11 ms, TR = 1400 ms) with 6 different delay times (t = 100, 200, 300, 400, 500, 600 ms), and (2) $T_2$ relaxation times are measured with a 32 echo multi-spin-echo sequence (TE = 6.2, 12.4, 18.6 ms…, TR = 1048 ms). In Table 3.1 and Table 3.2, the measured relative PD and relaxation times of our phantom are compared to reported values in the literature.[30]

**Table 3.1 MR contrast parameters for 0.2 T contrast phantom, measured at 3 T**

| | Lung Tumour | | Normal Lung Parenchyma | |
|---|---|---|---|---|
| | Literature | Measured | Literature | Measured |
| T1 | 372 ± 185[30] | 352 ± 4 | 455 ± 86[30] | 470 ± 9 |
| T2 | 69 ± 45[30] | 67 ± 2 | 79 ± 29[30] | 83 ± 5 |
| Relative PD to tumour | N/A | N/A | 0.19 - 0.34[28, 29] | 0.27 |

**Table 3.2 MR contrast parameters for 0.5 T contrast phantom, measured at 3 T**

| | Lung Tumour | | Normal Lung Parenchyma | |
|---|---|---|---|---|
| | Literature | Measured | Literature | Measured |
| T1 | 532 ± 271[30] | 519 ± 2 | 599 ± 114[30] | 604 ± 5 |
| T2 | 69 ± 45[30] | 61 ± 2 | 79 ± 29[30] | 97 ± 6 |
| Relative PD to tumour | N/A | N/A | 0.19 - 0.34[28, 29] | 0.30 |

### 3.2.4. Dynamic MR study: Evaluation of autocontouring and tracking performance

A series of dynamic studies were performed with the phantom to evaluate the autocontouring algorithm in low field images. In this study, dynamic MR imaging was performed with 3 T MRI replacing the role of linac-MR in Step 4 in

Fig. 3.2. Also, autocontouring was performed off-line after a session of dynamic MR imaging was completed.

For the 0.2 T contrast parameters, we created two separate lung compartments differing in tumour shape: a spherical tumour model, and another with an elongated, irregularly shaped tumour model. The same procedure is repeated with the 0.5 T contrast phantom. Hence, the study was performed with four different lung compartments in total. In each case, the lung compartment was moving inside of the thoracic cage during the scan.

The lung compartment was driven in accordance with four different pre-determined motion patterns during the dynamic study. The motion patterns used in our dynamic studies are shown in Fig. 3.8. The first pattern is a sine wave of 40 mm peak-to-peak amplitude and a period of 4 seconds. This pattern was created to simulate very large amount of regular, predictable lung tumour motion. The other three patterns were obtained from three different patient datasets. Suh *et al*.[39] analyzed thoracic and abdominal tumour motions from 42 patients using Cyberknife Synchrony (Accuray Incorporated, Sunnyvale, CA). This group provided us with clinical data containing 3D lung tumour positions that were estimated and recorded with a temporal frequency of 25 Hz during actual treatments. Because lung tumours show the largest motions in the superior-inferior (SI) direction, we selected three lung tumour motion patterns that incorporated relatively large SI motions, approximately 15 mm amplitude on average, and with varying periods. Each study took approximately 3 minutes, and the patterns represent 1D motion of lung tumour in the SI direction.

To provide an independent, reference measurement of tumour position, an optical encoder (model #: AEDR-8300-1Q2, Avago technologies, San Jose, CA) was attached to the thoracic cage as shown in Fig. 3.7. Paired with the encoder, a reflective code strip (resolution: 180 lines per inch) is attached to the moving compartment that contains the tumour model. Because all other parts of the phantom are stationary, and the tumour model is fixed in the lung compartment, any change in the tumour position in the SI direction is measured by the encoder as a change in counts (1 count ≈ 0.035 mm).

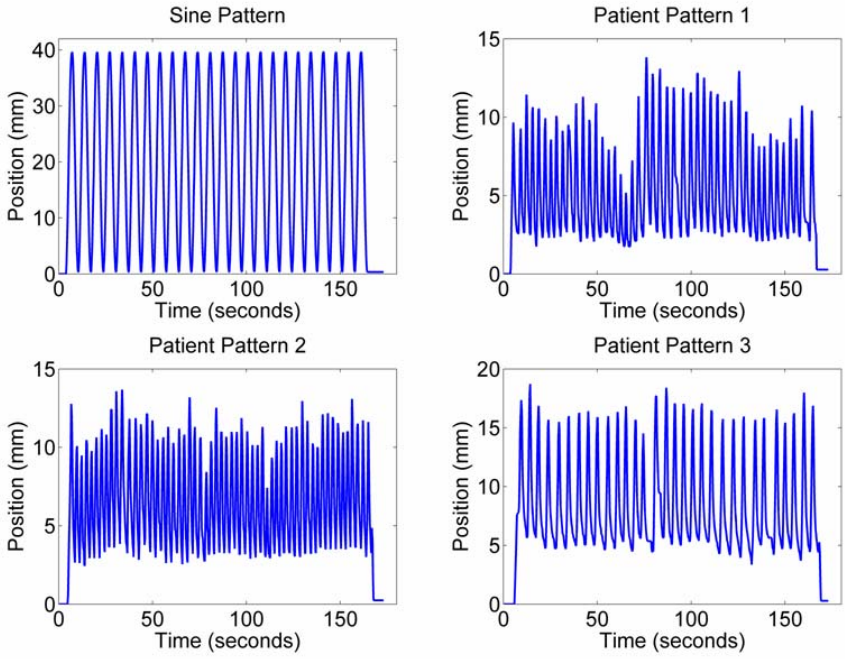


**Figure 3.8 Motion Patterns used to drive lung compartment. A sine pattern (upper left) and three lung tumour motion patterns from patient data**

### 3.2.4.1. MR imaging sequence

For each motion pattern, we performed the following two MR scans in order: (1) a high resolution turbo-spin-echo (TSE) scan acquired when the tumour

is stationary in its starting position, followed by (2) a dynamic bSSFP scan while the tumour is undergoing motion.

A TSE scan (FOV = 40 cm × 40 cm, voxel size = 0.4 mm × 0.4 mm × 4 mm, 5 slices, TE = 87 ms, TR = 1798 ms) was chosen as a reference scan due to its high SNR, very high resolution, and minimal susceptibility to artifacts. The high resolution of this scan allows for visualization of the thin walls (~ 0.3 mm) of the tumour model, allowing the true shape of the tumour to be easily contoured. The middle slice that covers the largest extent of the tumour is contoured manually and considered as a standard shape in this study.

For dynamic imaging, we used a 2D bSSFP sequence acquired at ~ 4 fps (identical FOV to TSE scan = 40 cm × 40 cm, 3.1 mm × 3.1 mm × 20 mm, TE = 1.1 ms, TR = 2.2 ms, Dynamic Scan Time = 275 ms) in the coronal plane. Imaging parameters are selected to balance between CNR and spatial resolution while maintaining the imaging speed requirements of ~ 4 fps. The imaging plane is chosen so that the tumour is near isocenter where distortion is minimized. Prior to each dynamic acquisition, an external synchronization pulse is sent to the optical encoder. Using this pulse, the optical encoder records the position of the tumour at the mid-point of each dynamic scan when the signal acquisition is occurring at the center of k-space. The first images of the dynamic scans are acquired prior to the commencement of motion, with the phantom in the same position as the reference TSE scan. These images are visually inspected to ensure alignment with the high-resolution TSE image.

MR images were acquired with a 6 channel Philips torso coil. As parallel imaging is not used in this experiment, noise is approximately uniform in the

image. Noise is measured as the standard deviation of each individual image in a 10 × 10 pixel region in the corner of the image containing no signal. To ensure there is no positive noise bias, noise is measured in the real and imaginary images and averaged, rather than measured in the magnitude images only.

### 3.2.4.2. Image post processing (CNR modification)

Gaussian noise is added to the images acquired on the 3 T scanner in order to reflect the lower CNR at 0.5 T and 0.2 T. Downscaling of CNR from 3 T images could be achieved by amplifying the measured background noise by a factor of 6 and 15 for 0.5 T and 0.2 T images respectively. As mentioned previously, noise is increased by another 33 % to account for the difference in absolute PD between real solid tumours and the aqueous tumour model used in our phantom. Combining these two corrections, noise amplification factors of 8 and 20 were applied to simulate the 0.5 T and 0.2 T images, respectively. Assuming statistical independence, the standard deviation of the added noise can be derived from the standard deviation of measured noise,

$$(N \cdot \sigma_{meas})^2 = \sigma_{meas}^2 + \sigma_{added}^2 \qquad \textbf{(Eq. 3.4)}$$

$$\sigma_{added} = \sqrt{N^2 - 1} \cdot \sigma_{meas} \qquad \textbf{(Eq. 3.5)}$$

where $N$ is the noise amplification factor and $\sigma_{meas}$ and $\sigma_{added}$ are the standard deviation of the measured and added noise, respectively. Noise is independently measured and amplified in the real and imaginary images and combined to generate the magnitude image. After noise addition, the image is interpolated to a 256 × 256 matrix prior to autocontouring.

### 3.2.4.3. CNR measurements

At the end of each dynamic scan (~ 3 minutes), an extra set of 100 dynamic images is acquired. This was performed when the phantom is stationary, located at the last position of the motion pattern. As a result, 16 different sets of images (2 tumour models × 2 field strengths × 4 motion patterns = 16 sets) were obtained, each set containing 100 images. Using these, CNR is measured for each set. The mean pixel values in the regions of interest within the tumour and the surrounding tissue were taken, as the value of $S_T$ and $S_N$ in Eq. 3.3 respectively. Noise is measured as the standard deviation of pixels in a 10 × 10 region in the corner of the real and imaginary images. This noise measurement is performed after noise has been added for CNR modification, but prior to the 256 × 256 interpolation.

### 3.2.4.4. Data analysis

For each dynamic study (~ 600 images), the post-processed images are fed into the autocontouring algorithm offline. These images are autocontoured with the following parameters: (1) 0.2 T images ($f$ = 0.6, $s$ = 11 × 11, $u$ = 5 × 5, 9 smoothings, 0 dilations), (2) 0.5 T images ($f$ = 0.7, $s$ = 11 × 11, $u$ = 5 × 5, 9 smoothings, 0 dilations). There are no considerable changes in these values for both field strengths. The algorithm returns an autocontoured tumour shape and its centroid from each image, and these results were used to evaluate the autocontouring and tracking performance of our algorithm. The following two steps (Sec. 3.2.4.4.a - Sec. 3.2.4.4.b) were applied to each dynamic study.

#### 3.2.4.4.a. Contour shape fidelity

To evaluate the quality of the contours generated from the autocontouring algorithm, we first manually contoured the tumour in a reference TSE scan (Fig. 3.9). From this manual contour, a binary mask was generated, and considered as a standard tumour shape. The optical encoder readings were used to linearly translate this mask, generating a standard set of masks that corresponds to the standard tumour shape in each dynamic image. Similarly, a set of autocontoured masks is produced from the autocontouring algorithm.

The autocontoured mask has lower resolution (256 × 256) than the manually contoured mask (1024 × 1024). For comparison, the low resolution mask is re-sampled to 1024 × 1024 resolution using the nearest neighbor method, which maintains the pixelated appearance of the low resolution image. We performed one-to-one comparison of the tumour shape between the two sets of masks, and their similarities are evaluated by calculating Dice's coefficient as previously described in Sec. 3.2.2.1.b (Eq. 3.2).

#### 3.2.4.4.b. Centroid position accuracy

We also evaluated the algorithm's ability to accurately determine and track the centroid position of a moving tumour. First, we determined an initial centroid position of the tumour from a high resolution image. This image was acquired when the tumour was located on its initial position of the motion pattern, and the tumour shape was manually contoured. The initial centroid position served as the reference point (i.e. zero count) for optical encoder reading. Second, the tumour position change during each dynamic acquisition was continuously recorded by

the encoder. As previously explained, the encoder reads the tumour position when the signal acquisition is occurring at the center of k-space. Third, the centroid position of the tumour in each dynamic image was determined by the autocontouring algorithm. Last, a one-to-one comparison of the centroid position of the tumour in each image was made between the encoder reading and the result from our algorithm.

Mean and standard deviation of the difference between the two (either positive or negative) are calculated from all the images within the motion pattern. Root mean square error (RMSE) is also calculated to give an indication of overall error as:

$$\varepsilon_{RMS} = \sqrt{\frac{\sum_{i=1}^{n} (y_{i,centroid} - y_{i,encoder})^2}{n}} \qquad \textbf{(Eq. 3.6)}$$

Where $y_{i,centroid}$ is the centroid position of the autocontoured tumour and $y_{i,encoder}$ is the position of the tumour measured by the optical encoding device.

## *3.3. RESULTS AND DISCUSSION*

### 3.3.1. Simulated lung tumour images with low field CNR

A close up view of the tumour and its surrounding tissue acquired using TSE and post-processed bSSFP are shown in Fig. 3.9. As predicted, the thin wall of tumour container is visualized by the high resolution TSE scan to aid in manual contouring, but it is not detected in the bSSFP image to affect the autocontouring algorithm.

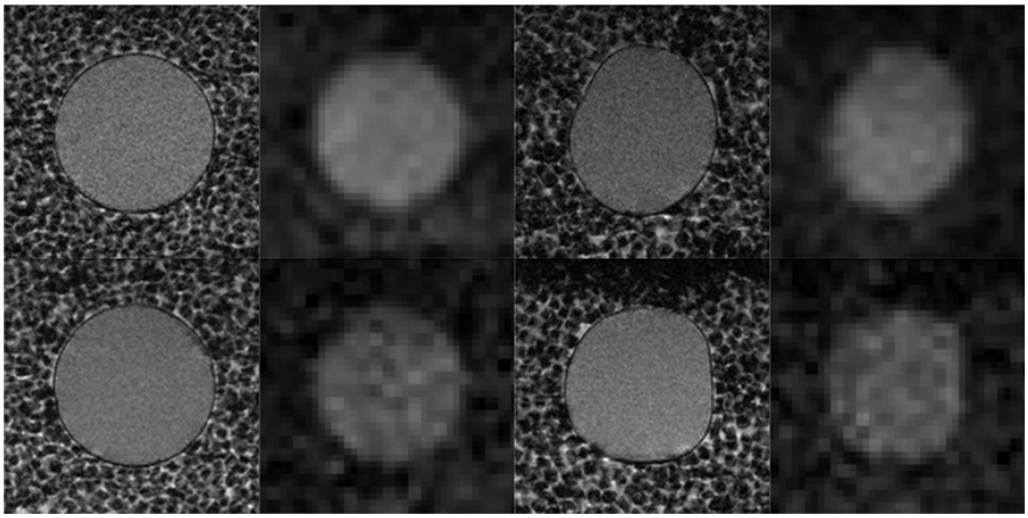

**Figure 3.9 First row, from left to right: 1) High Resolution, static TSE scan (spherical tumour, middle slice) for reference. 2) Lower resolution, dynamic bSSFP scan (noise added, 0.5 T equivalent). 3) High Resolution, static TSE scan (non-spherical tumour, middle slice). 4) Lower resolution, dynamic bSSFP scan (noise added, 0.5 T equivalent). Second row: equivalent images for 0.2 T experiments.**

## 3.3.2. CNR of acquired images

After the images are acquired at 3 T, noise is added to generate 0.2 T and 0.5 T equivalent images (Fig. 3.10). The CNR of these images are shown in Table 3.3. In summary, the measured CNR ranges from 10.3 - 12.3 for 0.5 T images and from 4.2 - 4.5 for 0.2 T images.

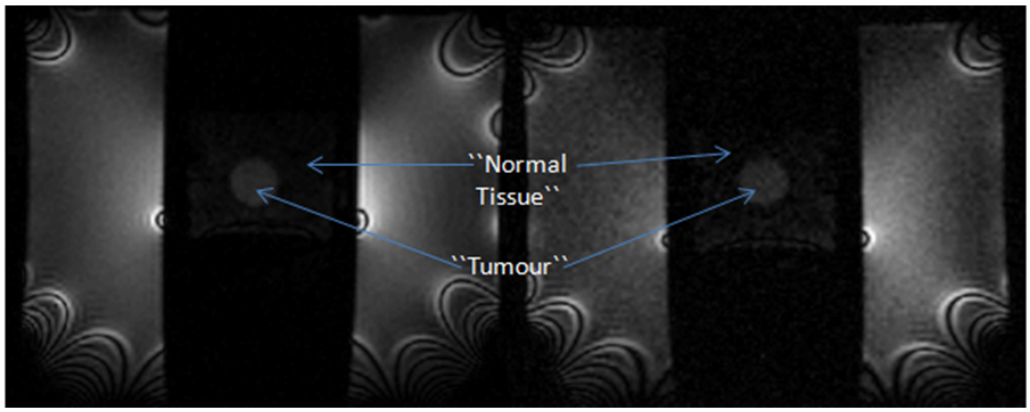


**Figure 3.10 Sample dynamic bSSFP images from the experiment, after noise addition. Image on the left reflects 0.5 T CNR whereas image on the right reflects 0.2 T CNR.**

**Table 3.3 CNR for spherical and non-spherical tumour models in 0.5 T and 0.2 T equivalent images. The standard deviation of the CNR is given in brackets.**

| | 0.5 T CNR | | 0.2 T CNR | |
|---|---|---|---|---|
| | Spherical Tumour | Non-Spherical Tumour | Spherical Tumour | Non Spherical Tumour |
| No Motion | 12.3 (0.9) | 10.3 (0.8) | 4.3 (0.4) | 4.5 (0.4) |
| Sine Pattern | 12.3 (1.0) | 10.5 (0.9) | 4.4 (0.3) | 4.4 (0.4) |
| Patient Pattern 1 | 12.1 (1.0) | 10.7 (0.8) | 4.4 (0.4) | 4.3 (0.3) |
| Patient Pattern 2 | 12.1 (1.0) | 11.2 (0.8) | 4.4 (0.4) | 4.3 (0.3) |
| Patient Pattern 3 | 11.9 (0.9) | 11.2 (0.9) | 4.2 (0.4) | 4.2 (0.4) |

### 3.3.3. Contour shape fidelity

Dice's coefficients for the phantom experiment are shown in Table 3.4. Dice's coefficient of > 0.96 is achieved in the 0.5 T equivalent images, and Dice's coefficient of > 0.93 is achieved in the 0.2 T equivalent images. Approximately 5 ms was required for our algorithm to autocontour the tumour in each dynamic image. The algorithm was coded in LabVIEW 2011 (National Instruments, Austin, TX) and tested on 32 bit computer system (Windows7, Intel i7-2600k, 4 GB RAM).

### 3.3.4. Centroid position accuracy

Differences between the centroid positions determined by autocontouring and those from the encoder reading are summarized in Table 3.4. Mean and standard deviation represents the systematic and random errors in tumour tracking, while root mean square error (RMSE) is a representation of overall error. RMSE

of < 0.55 mm is achieved for 0.5 T equivalent images, whereas RMSE of < 0.92 mm is achieved for 0.2 T equivalent images.

**Table 3.4 Dice's Coefficients, centroid error and RMSE in autocontouring and tracking**

| | Dice's Coefficient Mean(Std) | Centroid Error (mm) Mean(Std) | Centroid RMSE (mm) |
|---|---|---|---|
| **0.5 T CNR (spherical)** | | | |
| No Motion | 0.965 (0.009) | -0.05 (0.41) | 0.41 |
| Sine Pattern | 0.962 (0.009) | 0.06 (0.46) | 0.47 |
| Patient Pattern 1 | 0.966 (0.007) | 0.08 (0.41) | 0.42 |
| Patient Pattern 2 | 0.963 (0.009) | -0.20 (0.46) | 0.50 |
| Patient Pattern 3 | 0.961 (0.006) | 0.29 (0.46) | 0.55 |
| **0.5 T CNR (non-spherical)** | | | |
| No Motion | 0.960 (0.005) | 0.17 (0.31) | 0.35 |
| Sine Pattern | 0.963 (0.006) | 0.01 (0.35) | 0.35 |
| Patient Pattern 1 | 0.966 (0.005) | 0.19 (0.36) | 0.41 |
| Patient Pattern 2 | 0.966 (0.005) | 0.07 (0.37) | 0.38 |
| Patient Pattern 3 | 0.967 (0.004) | 0.08 (0.37) | 0.38 |
| **0.2 T CNR (spherical)** | | | |
| No Motion | 0.953 (0.010) | 0.26 (0.69) | 0.74 |
| Sine Pattern | 0.950 (0.011) | 0.10 (0.74) | 0.75 |
| Patient Pattern 1 | 0.953 (0.010) | 0.21 (0.70) | 0.73 |
| Patient Pattern 2 | 0.951 (0.011) | -0.11 (0.70) | 0.70 |
| Patient Pattern 3 | 0.948 (0.013) | 0.23 (0.70) | 0.73 |
| **0.2 T CNR (non-spherical)** | | | |
| No Motion | 0.947 (0.015) | -0.06 (0.65) | 0.66 |
| Sine Pattern | 0.940 (0.018) | 0.10 (0.88) | 0.90 |
| Patient Pattern 1 | 0.936 (0.019) | 0.14 (0.88) | 0.90 |
| Patient Pattern 2 | 0.939 (0.019) | 0.22 (0.90) | 0.92 |
| Patient Pattern 3 | 0.935 (0.021) | 0.23 (0.89) | 0.92 |

## 3.3.5. Discussion

Intrafractional tumour tracking, especially for lung tumour cases, is of considerable interest. Inspired by the current success of linac-MR systems, a recent study assessed the possibility of MRI-based tumour tracking.[40] However, to

the best knowledge of the authors, this is the first study exploring the feasibility of intrafractional lung tumour tracking geared towards lower magnetic field strengths. The use of an autocontouring algorithm and an MR compatible lung tumour motion phantom also makes this a unique study.

Our phantom simulates the 0.2/0.5 T relaxation properties of lung tissues and diseased tissues in a 3 T scanner. Using the phantom we approximated the CNR of lung tumour MR images acquired in the 0.2/0.5 T at 4 fps from the well established relationship of $B_0 \propto$ SNR and the addition of Gaussian noise. It should be noted that this experiment is not designed to determine the optimal field strength for the linac-MR, but to determine the feasibility of lung tumour autocontouring with images acquired at field strengths for different linac-MR designs (0.2 T or 0.5 T).

To evaluate the accuracy of our algorithm, we reported Dice's coefficient comparing the autocontoured tumour shapes and the standard ones. Simply reporting the total area of the autocontoured tumour shapes and comparing it to the total area of the standard ones is also a possible method of evaluation. However, this does not indicate whether the contours are actually overlapping, which is the most important criteria evaluating the autocontouring performance of our algorithm. We have found instances where two contours yielding a perfect agreement in terms of area comparisons, while not being near perfect in terms of contour comparisons. This may be the result of an overestimated edge in one region of the contour being compensated by an underestimated edge in a different region of the contour, which will produce misleading conclusions evaluating our

algorithm. As Dice's coefficient is determined primarily by the overlapping area, we have found that it is much more sensitive to these types of errors, and is a better indicator of shape fidelity.

Our algorithm achieved high fidelity of autocontoured tumour shape, Dice's coefficients > 0.96 and > 0.93 in the 0.5 T and 0.2 T equivalent images, respectively. Centroid tracking accuracy using our algorithm was measured in terms of RMSE values, which were < 0.55 mm and < 0.92 mm for the 0.5 T and 0.2 T equivalent images, respectively. As expected, tumour tracking accuracy is improved by the higher CNR provided at 0.5 T. These results show that our autocontouring algorithm is successful in contouring the lung tumour model in both 0.2 T and 0.5 T equivalent images acquired at 3 T with ~ 4 fps imaging rate.

The 0.2/0.5 T equivalent images represent an estimation, based on the best available information, of the achievable tumour CNR at low field scanners acquired at ~ 4 fps. Our results therefore suggest that autocontouring lung tumour will be feasible in both 0.2 T and 0.5 T MR systems. However, there will be inherent variances between individual patients, as well as individual MR scanners and coils. Therefore, patient images that will be acquired at the actual linac-MR may have slightly different CNRs compared to our phantom-based 0.2/0.5 T equivalent images acquired in 3 T. Hence, investigating the autocontouring performance of our algorithm with patient images acquired with the linac-MR will be a subject of future studies.

It is important to note that a very fast autocontouring speed (~ 5 ms for each image) is achieved in this study with a regular 32 bit computer system (Windows7, Intel i7-2600k, 4 GB RAM). This is an important achievement as

minimizing the time delay between tumour detection (i.e. imaging) and actual beam delivery is crucial to the success of a functional intrafractional tumour tracking system.

This study involves the evaluation of our algorithm. A phantom study with exact knowledge of the shape and position of the tumour model is required to validate the algorithm. An advantage of performing this type of phantom study is that it allows for a "gold-standard" measurement for both tumour shape and position, thus permitting the quantification of the autocontouring and tracking capabilities of the algorithm. This is not possible in a patient study mainly due to inter- and intra-observer variability in contouring, and the difficulties associated with the exact independent determination of position of the tumour within a patient. After this study, patient studies can then be done.

The use of a virtual phantom, i.e. creating new images from an original one with the tumour motion and deformation, was considered to evaluate our algorithm. However, it was felt that more conclusive results would be obtained with an actual phantom instead. It would be difficult to properly simulate, in a virtual phantom, the variations in image characteristics, such as signal intensity, noise, contrast, and motion artifacts that would occur in realistic dynamic MR imaging. Furthermore, there would be some level of subjectivity in simulating tumour motion and deformation which would most probably introduce unrealistic characteristics of the tumour (e.g. sharp edges, etc). These would be difficult to adjust appropriately.

Although the real phantom study we have reported demonstrated the possible applicability of low field linac-MR systems for the tracking of lung

tumours, there still remain several issues that would need to be addressed in future studies:

(1) Our phantom is limited to 1D motion in the SI direction, while tumours in patient often have a 3D motion trajectory. In current linac based treatments, as well as in future linac-MR based treatments using our laboratory's designs, radiation beams rotate around the SI axis of the patient. Hence, if intrafractional MR imaging is performed from the beam's eye view, the 2D imaging presented here may be sufficient for tumour tracking in SI and one more direction in that imaging plane. In this scenario, our algorithm can be used to detect in-plane changes in tumour position and adjust collimation accordingly.

However, a potential problem that can arise is through-plane tumour motion (motion orthogonal to the imaging plane). Tumours can potentially move out of the imaging plane. Although numerous studies have demonstrated that the largest lung tumour motions occur in the SI directions, smaller motions in anterior-posterior and left-right directions could contribute to the out of the imaging plane motion.

Potential solutions to this problem include adjusting the slice thickness of the imaging plane to ensure the tumour remains in the imaging plane. Also, our CNR measurements suggest that at 0.5 T, there is potentially enough CNR (10.3 - 12.3) to allow image acceleration via various techniques such as parallel imaging. This opens up the possibility to perform intrafractional multi-slice or 3D imaging, which will be investigated in future studies.

(2) Other factors may arise during clinical situations that are not addressed in this phantom study. Tumours may potentially rotate or change shape during

respiratory motion. Also, during dynamic MR imaging, tumour contrast may fluctuate due to compression and expansion of lung between images. No current state of the art tumour tracking method has the ability to account for these changes.

Nevertheless, our autocontouring algorithm deals with the possible deformations of the tumour shape, as well as inter-image tumour contrast changes. Our algorithm contours each image individually without the need of *a priori* assumptions regarding tumour shape or contrast. The algorithm's performance for autocontouring solid, moving tumours in low field dynamic MR imaging is reasonable with Dice's coefficients > 0.96 and > 0.93 in 0.5 T and 0.2 T equivalent images, respectively. However, the algorithm's performance with shape deformations and contrast fluctuations in real patients' images still requires further investigation.

(3) Our contrast phantoms, imaged in a 3 T MRI, and subsequent noise addition, resulted in an expected CNR of 4.2 - 4.5 and of 10.3 - 12.3 from 0.2 and 0.5 T systems, respectively. However, several factors can actually lead to an improvement in image quality in low field MRI. Firstly, in our experiments, the flip angle is limited by specific absorption rate (SAR) safety limits due to the very short TR required for fast imaging. SAR is proportional to the square of the main magnetic field,[41] so the diminished SAR at low fields will allow greater freedom in choosing flip angles. This may enhance the CNR in bSSFP images.[42] Secondly, banding artifacts, while not affecting the central area of the tumour in our scans, are clearly visible in the periphery of the image in 3 T. These banding artifacts will be considerably less severe in a low field MRI due to the improved local field homogeneity.[43]

Geometric distortion is a potential problem for MRI-based radiation therapy. Our experimental protocol is set-up such that the optical encoder is calibrated to the reference scan. This is acquired prior to the dynamic scan, with the phantom located at the starting position of the dynamic scan. Because geometric distortion is spatially dependent, it is possible that the tumour shown in the MR image is misplaced from its actual position as the phantom moves. Nevertheless, the optical encoder reading is independent and not affected by geometric distortion. Therefore, any tumour positional error due to geometric distortion is encapsulated by our centroid error measurements reported in Sec. 3.3.4, which is < 0.92 mm for all measurements. Geometric distortion in our experiments is relatively minor, mainly because the tumour model trajectory of our phantom is located near the isocenter of the magnet where automatic shimming from the MR system could eliminate most of the magnetic field inhomogeneity. In a patient study where the tumour could be potentially located far from the isocenter of the magnet, i.e. left or right periphery of lung, geometric distortion might be considerably larger. In this case, a more sophisticated geometric distortion correction method will be required.

## *3.4. CONCLUSION*

We have developed a lung tumour autocontouring algorithm and evaluated its performance in low field MR images (0.2 and 0.5 T). In our experiments, the algorithm successfully contoured the shape of a moving tumour from dynamic MR images acquired at 275 ms intervals. Dice's coefficients of > 0.96 and > 0.93 are achieved in 0.5 T and 0.2 T equivalent images respectively, where

autocontouring takes approximately 5 ms for each image. Also, the algorithm was able to track the tumour position during dynamic studies, with RMSE values of < 0.55 mm and < 0.92 mm for 0.5 T and 0.2 T equivalent images respectively. These results demonstrate the feasibility of lung tumour autocontouring in low field MR images, and, by extension, intrafractional lung tumour tracking with our laboratory's linac-MR systems.

## 3.5. REFERENCES


[1] F. Sterzing, R. Engenhart-Cabillic, M. Flentje, and J. Debus, "Image-Guided Radiotherapy A New Dimension in Radiation Oncology," Deutsches Arzteblatt International **108**(16), 274-280 (2011).

[2] C. Plathow, C. Fink, S. Ley, M. Puderbach, M. Eichinger, I. Zuna, A. Schmahl, and H. U. Kauczor, "Measurement of tumor diameter-dependent mobility of lung tumors by dynamic MRI," Radiother. Oncol. **73**(3), 349-354 (2004).

[3] H. Shirato, K. Suzuki, G. C. Sharp, K. Fujita, R. Onimaru, M. Fujino, N. Kato, Y. Osaka, R. Kinoshita, H. Taguchi, S. Onodera, and K. Miyasaka, "Speed and amplitude of lung tumor motion precisely detected in four-dimensional setup and in real-time tumor-tracking radiotherapy," Int. J. Radiat. Oncol. Biol. Phys. **64**(4), 1229-1236 (2006).

[4] H. Shirato, Y. Seppenwoolde, K. Kitamura, R. Onimura, and S. Shimizu, "Intrafractional tumor motion: Lung and liver," Sem. Rad. Onc. **14**(1), 10-18 (2004).

[5] C. Plathow, M. Schoebinger, C. Fink, H. Hof, J. Debus, H. P. Meinzer, and H. U. Kauczor, "Quantification of lung tumor volume and rotation at 3D dynamic parallel MR imaging with view sharing: Preliminary results," Radiology **240**(2), 537-545 (2006).

[6] S. S. Vedam, V. R. Kini, P. J. Keall, V. Ramakrishnan, H. Mostafavi, and R. Mohan, "Quantifying the predictability of diaphragm motion during

respiration with a noninvasive external marker," Med. Phys. **30**(4), 505-513 (2003).

[7] E. Nioutsikou, Y. Seppenwoolde, J. R. N. Symonds-Tayler, B. Heijmen, P. Evans, and S. Webb, "Dosimetric investigation of lung tumor motion compensation with a robotic respiratory tracking system: An experimental study," Med. Phys. **35**(4), 1232-1240 (2008).

[8] R. L. Smith, K. Lechleiter, K. Malinowski, D. M. Shepard, D. J. Housley, M. Afghan, J. Newell, J. Petersen, B. Sargent, and P. Parikh, "Evaluation of Linear Accelerator Gating with Real-Time Electromagnetic Tracking," Int. J. Radiat. Oncol. Biol. Phys. **74**(3), 920-927 (2009).

[9] T. Harada, H. Shirato, S. Ogura, S. Oizumi, K. Yamazaki, S. Shimizu, R. Onimaru, K. Miyasaka, M. Nishimura, and H. Dosaka-Akita, "Real-time tumor-tracking radiation therapy for lung carcinoma by the aid of insertion of a gold marker using bronchofiberscopy," Cancer **95**(8), 1720-1727 (2002).

[10] M. B. Tacke, S. Nill, A. Krauss, and U. Oelfke, "Real-time tumor tracking: automatic compensation of target motion using the Siemens 160 MLC," Med. Phys. **37**(2), 753-761 (2010).

[11] A. Sawant, R. L. Smith, R. B. Venkat, L. Santanam, B. C. Cho, P. Poulsen, H. Cattell, L. J. Newell, P. Parikh, and P. J. Keall, "Toward Submillimeter Accuracy in the Management of Intrafraction Motion: the Integration of Real-Time Internal Position Monitoring and Multileaf Collimator Target Tracking," Int. J. Radiat. Oncol. Biol. Phys. **74**(2), 575-582 (2009).

[12] B. Cho, P. R. Poulsen, A. Sloutsky, A. Sawant, and P. J. Keall, "First Demonstration of Combined Kv/Mv Image-Guided Real-Time Dynamic Multileaf-Collimator Target Tracking," Int. J. Radiat. Oncol. Biol. Phys. **74**(3), 859-867 (2009).

[13] T. Depuydt, D. Verellen, O. Haas, T. Gevaert, N. Linthout, M. Duchateau, K. Tournel, T. Reynders, K. Leysen, M. Hoogeman, G. Storme, and M. D. Ridder, "Geometric accuracy of a novel gimbals based radiation therapy tumor tracking system," Radiother. Oncol. **98**(3), 365-372 (2011).

[14] K. Kitamura, H. Shirato, S. Shimizu, N. Shinohara, T. Harabayashi, T. Shimizu, Y. Kodama, H. Endo, R. Onimaru, S. Nishioka, H. Aoyama, K. Tsuchiya, and K. Miyasaka, "Registration accuracy and possible migration of internal fiducial gold marker implanted in prostate and liver treated with real-time tumor-tracking radiation therapy (RTRT)," Radiother. Oncol. **62**(3), 275-281 (2002).

[15] C. Ozhasoglu and M. J. Murphy, "Issues in respiratory motion compensation during external-beam radiotherapy," Int. J. Radiat. Oncol. Biol. Phys. **52**(5), 1389-1399 (2002).

[16] L. Ekberg, O. Holmberg, L. Wittgren, G. Bjelkengren, and T. Landberg, "What margins should be added to the clinical target volume in radiotherapy treatment planning for lung cancer?," Radiother. Oncol. **48**(1), 71-77 (1998).

[17] J. H. Hendry, B. Jeremic, and E. H. Zubizarreta, "Normal tissue complications after radiation therapy," Rev. Panam. Salud. Publica. **20**(2-3), 151-160 (2006).

[18] B. Fallone, M. Carlone, B. Murray, S. Rathee, T. Stanescu, S. Steciw, K. Wachowicz, and C. Kirkby, "Development of a Linac-MRI System for Real-Time ART," Med. Phys. **34**(6), 2547-2547 (2007).

[19] B. G. Fallone, B. Murray, S. Rathee, T. Stanescu, S. Steciw, S. Vidakovic, E. Blosser, and D. Tymofichuk, "First MR images obtained during megavoltage photon irradiation from a prototype integrated linac-MR system," Med. Phys. **36**(6), 2084-2088 (2009).

[20] J. F. Dempsey, D. Benoit, J. R. Fitzsimmons, A. Haghighat, J. G. Li, D. A. Low, S. Mutic, J. R. Palta, H. E. Romeijn, and G. E. Sjoden, "A device for realtime 3D image-guided IMRT," Int. J. Radiat. Oncol. Biol. Phys. **63**(2), 1095 (2005).

[21] B. W. Raaymakers, J. J. Wlagendijk, J. Overweg, J. G. M. Kok, A. J. E. Raaijmakers, E. M. Kerkhof, R. W. van der Put, I. Meijsing, S. P. M. Crijns, F. Benedosso, M. van Vulpen, C. H. W. de Graaff, J. Allen, and K.

J. Brown, "Integrating a 1.5 T MRI scanner with a 6 MV accelerator: proof of concept," Phys. Med. Biol. **54**(12), N229-N237 (2009).

[22] P. J. Keall, G. S. Mageras, J. M. Balter, R. S. Emery, K. M. Forster, S. B. Jiang, J. M. Kapatoes, D. A. Low, M. J. Murphy, B. R. Murray, C. R. Ramsey, M. B. Van Herk, S. S. Vedam, J. W. Wong, and E. Yorke, "The management of respiratory motion in radiation oncology report of AAPM Task Group 76," Med. Phys. **33**(10), 3874-3900 (2006).

[23] H. Hatabu, J. Gaa, E. Tadamura, K. J. Edinburgh, K. W. Stock, E. Garpestad, and R. R. Edelman, "MR imaging of pulmonary parenchyma with a half-Fourier single-shot turbo spin-echo (HASTE) sequence," Eur J Radiol. **29**(2), 152-159 (1999).

[24] I. Crooks and B. G. Fallone, "A Novel Algorithm for the Edge-Detection and Edge Enhancement of Medical Images," Med. Phys. **20**(4), 993-998 (1993).

[25] J. P. Lewis, "Fast Template Matching," Vision Interface 95, Canadian Image processing and Pattern Recognition Society, 120-123 (1995).

[26] N. Otsu, "A Threshold Selection Method from Gray-Level Histograms," Systems, Man and Cybernetics, IEEE Transactions on **9**(1), 62-66 (1979).

[27] R. C. Gonzalez and R. E. Woods, *Digital Image Processing*, (Prentice Hall, New Jersey, 2002).

[28] H. Hatabu, D. C. Alsop, J. Listerud, M. Bonnet, and W. B. Gefter, "T2*and proton density measurement of normal human lung parenchyma using submillisecond echo time gradient echo magnetic resonance imaging," Eur J Radiol. **29**(3), 245-252 (1999).

[29] H. C. Schmidt, D. Tscholakoff, H. Hricak, and C. B. Higgins, "MR Image-Contrast and Relaxation-Times of Solid Tumors in the Chest, Abdomen, and Pelvis," J Comput Assist Tomogr. **9**(4), 738-748 (1985).

[30] P. A. Bottomley, C. J. Hardy, R. E. Argersinger, and G. Allenmoore, "A Review of H-1 Nuclear-Magnetic-Resonance Relaxation in Pathology - Are T1 and T2 Diagnostic?," Med. Phys. **14**(1), 1-37 (1987).

[31] A. Boss, S. Schaefer, P. Martirosian, C. D. Claussen, F. Schick, and J. F. Schaefer, "Magnetic resonance imaging of lung tissue: Influence of body positioning, breathing and oxygen inhalation on signal decay using multi-echo gradient-echo sequences," Invest Radiol. **43**(6), 433-438 (2008).

[32] C. J. Bergin, G. H. Glover, and J. M. Pauly, "Lung Parenchyma - Magnetic-Susceptibility in MR Imaging," Radiology **180**(3), 845-848 (1991).

[33] K. Scheffler and J. Hennig, "Is TrueFISP a gradient-echo or a spin-echo sequence?," Magn Reson Med. **49**(2), 395-397 (2003).

[34] E. M. Haacke, R. Brown, M. Thompson, and R. Venkatesan, *Magnetic resonance imaging : physical principles and sequence design*, (J. Wiley & Sons, USA, 1999).

[35] T. W. Redpath, "Signal-to-noise ratio in MRI," Br J Radiol. **71**(847), 704-707 (1998).

[36] H. Kato, M. Kuroda, K. Yoshimura, A. Yoshida, K. Hanamoto, S. Kawasaki, K. Shibuya, and S. Kanazawa, "Composition of MRI phantom equivalent to human tissues," Med. Phys. **32**(10), 3199-3208 (2005).

[37] C. T. G. Flear, R. G. Carpenter, and I. Florence, "Variability in the water, sodium, potassium, and chloride content of human skeletal muscle," J Clin Pathol. **18**(1), 74-81 (1965).

[38] J. G. Och, G. D. Clarke, W. T. Sobol, C. W. Rosen, and S. K. Mun, "Acceptance Testing of Magnetic Resonance Imaging Systems - Report of AAPM Nuclear Magnetic Resonance Task Group No. 6.," Med. Phys. **19**(1), 217-229 (1992).

[39] Y. Suh, S. Dieterich, B. Cho, and P. J. Keall, "An analysis of thoracic and abdominal tumour motion for stereotactic body radiotherapy patients," Phys. Med. Biol. **53**(13), 3623-3640 (2008).

[40] L. I. Cervino, J. Du, and S. B. Jiang, "MRI-guided tumor tracking in lung cancer radiotherapy," Phys. Med. Biol. **56**(13), 3773-3785 (2011).

[41] M. A. Bernstein, K. F. King, and X. J. Zhou, *Handbook of MRI pulse sequences*, (Academic Press, Burlington, MA, 2004).

[42] K. Scheffler and S. Lehnhardt, "Principles and applications of balanced SSFP techniques," Eur Radiol. **13**(11), 2409-2418 (2003).

[43] O. Wieben, C. Francois, and S. B. Reeder, "Cardiac MRI of ischemic heart disease at 3 T: Potential and challenges," Eur J Radiol. **65**(1), 15-28 (2008).

# Chapter 4: Evaluation of an autocontouring algorithm using *in-vivo* MR images with various contrast to noise ratios

*A version of this chapter was presented at the 54th annual meeting of the American Association of Physicists in Medicine (AAPM): E. Yip, J. Yun, Z. Gabos, K. Wachowicz, S. Rathee, and B. G. Fallone, "Evaluation of a real time tumour autocontouring algorithm using in-vivo lung MR images with various contrast to noise ratios," presented at the 54th Annual Meeting of the AAPM, Charlotte, NC, July 29 - August 2, 2012.*

## 4.1. INTRODUCTION

In Chapter 3 of this thesis, the feasibility of lung tumour autocontouring in low field MR images (0.2 and 0.5 T) was investigated using a motion phantom scanned with 3 T MRI. Here, 0.2 and 0.5 T were chosen based on our laboratory's linac-MR designs.

This chapter presents our initial works using *in-vivo* data obtained from a single lung cancer patient. The objective of this *in-vivo* study is to verify the feasibility of lung tumour autocontouring in various low field MR images using real patient data.

## *4.2. METHODS*

### 4.2.1. Dynamic *in-vivo* MR imaging

A non-small cell lung cancer (NSCLC) patient with a posterior lung tumour was imaged in a 3 T MRI (Achieva 3 T, Philips Medical Systems, Andover, MA) using a dynamic balanced steady state free precession (bSSFP) sequence (FOV = 40 × 40 $cm^2$, voxel size = 3.1 × 3.1 × 20 $mm^3$, TE = 1.1 ms, TR = 2.2 ms, Dynamic Scan Time = 275 ms) under free breathing for approximately 3 minutes. A sagittal slice was chosen for our study, because it includes anatomical structures near the tumour making the greatest challenge to our autocontouring algorithm. A total of 650 dynamic images were obtained during the 3 minute scan. Among these, a few example images are shown in Fig. 4.1.

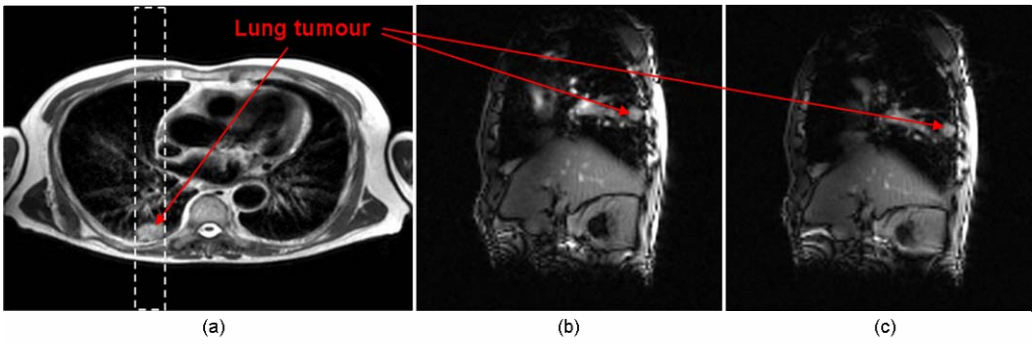


**Figure 4.1 *In-vivo* images of a posterior lung tumour (indicated by red arrows) acquired with 3 T MRI: (a) a transverse view of the patient (a high resolution transverse image is shown here for better visualization of the sagittal imaging plane represented by the white dotted lines), (b) a sagittal dynamic image of the patient at the end of exhale period, (c) a sagittal dynamic image of the patient at the end of inhale period**

### 4.2.2. CNR measurement and modification

Tumour CNR was calculated directly from the 3 T images in the sagittal plane. A region of interest was manually contoured in the lung tumour and

background parenchyma in 15 images (4.1 seconds are required to acquire 15 images, which is approximately 1 breathing cycle). Tumour CNR calculated from each of these 15 images using Eq. 3.3 was averaged and used as the lung tumour CNR at 3 T in this study.

As a first order approximation to simulate low field MR images, we degraded the *in-vivo* images acquired at 3 T to approximate the CNR values at 1.5 – 0.2 T MR images by adding Gaussian noise. Here, linear CNR scaling factors of 2 – 15 were applied respectively, using the approach discussed in Chapter 3 (Sec. 3.2.3.1) of this thesis.

### 4.2.3. Tumour contouring and comparison

Additional to the 3 T images that were actually acquired, several sets of simulated lower field images (1.5 – 0.2 T) were generated using the above process. Tumour contouring was performed with these simulated image data.

#### 4.2.3.1. Manual tumour contouring and intra-observer variability

A radiation oncologist manually outlined tumour contours in all 650 images acquired at 3 T. From the manual contour in each image, a binary mask was generated and considered as a "standard tumour shape" in this study. Also, the first 100 images were re-contoured by the same physician on a different day to test intra-observer variability.

#### 4.2.3.2. Automatic tumour contouring

Our autocontouring algorithm[1] was applied to the 3 T images, as well as other simulated lower field images (1.5 - 0.2 T) to auto-determine the lung tumour

contours. From the automatically determined tumour contour in each image, a binary mask was generated and considered as an "autocontoured tumour shape" in this study. As previously explained in Chapter 3 (Sec. 3.2.2.1.b) of this thesis, the algorithm requires reference contours from the pre-treatment images for optimization of internal parameters. Because the patient was scanned only once in this study, the physician drawn contours from the first 20 images (out of 650 images) were used as reference contours for the parameter optimization.

#### 4.2.3.3. Contour comparison and analysis

We performed a one-to-one comparison of the two masks obtained from the manual and automatic contours. Here, the auto-determined tumour contours from the remaining 630 images (the first 20 images were used for parameter optimization) were compared to the standard contours, and their similarities are evaluated by calculating Dice's coefficient ($D$) as previously described in Chapter 3 (Sec. 3.2.2.1.b, Eq. 3.2).

Additionally, a one-to-one comparison of the centroid position of tumour contour was made between the standard and automatic contours, in order to evaluate the algorithm's ability to track the position of a moving tumour. The distance between the two centroid positions ($\Delta d_{centroid}$) was calculated as

$$\Delta d_{centroid} = \sqrt{\Delta x^2 + \Delta y^2} \qquad \textbf{(Eq. 4.1)}$$

where $\Delta x$ and $\Delta y$ were the displacement between the two centroid positions in $x$ (anterior-posterior) and $y$ (superior-inferior) directions, respectively.

Intra-observer variability was evaluated by calculating $D$ as well as $\Delta d_{centroid}$ between the two sets of manual contours drawn on the first 100 images (drawn by the same physician on different days).

## 4.3. RESULTS

The *in-vivo* images acquired at 3 T were degraded to approximate the CNR values at 0.2, 0.3, 0.5, 1.0, and 1.5 T. The physician's manual tumour contouring was performed only with 3 T images, whereas autocontouring was performed with six different sets of images (0.2 – 3 T).

Figure 4.2 shows a single example image degraded to approximate low fields CNR. In this figure, autocontoured tumour shapes are outlined in green, which were contoured separately in each set of images. Deviation of the autocontour from the standard contour is indicated in red.

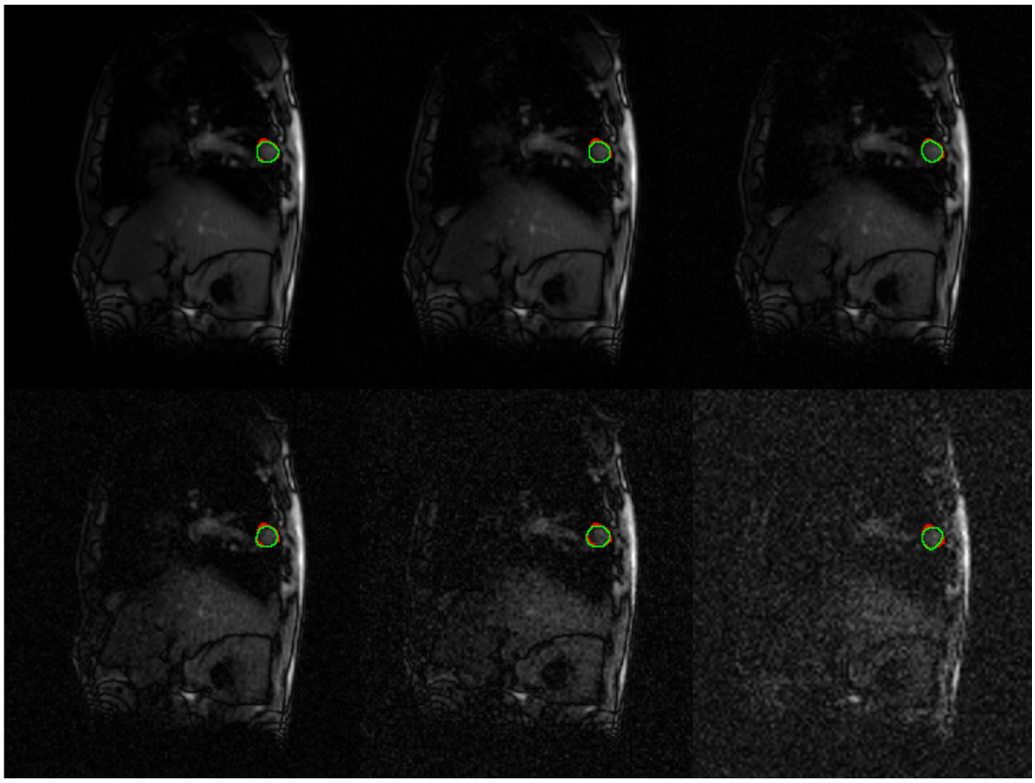

**Figure 4.2 An example lung tumour image degraded to approximate low fields CNR. Top row (from left to right): original 3 T, simulated 1.5 T, and simulated 1 T images. Bottom row (from left to right): simulated 0.5 T, simulated 0.3 T, and simulated 0.2 T images. Autocontoured tumour shapes are shown in green. Deviation of the autocontour (contoured separately in each set of images) from the standard contour is shown in red.**

The result of tumour centroid tracking in superior-inferior (SI) and anterior posterior (AP) directions is shown in Fig. 4.3 and Fig. 4.4 for 3 T image set. Here, the centroid positions of standard (physician drawn) and auto-determined tumour contour in each image are plotted along with the error values. In Fig. 4.3 and Fig. 4.4, the lowest $y$ (SI direction) and $x$ (AP direction) coordinate value of the autocontoured tumour centroid was set as 0 mm, respectively. The maximum extent of tumour motion in SI and AP directions was approximately 26 mm and 6 mm, respectively.

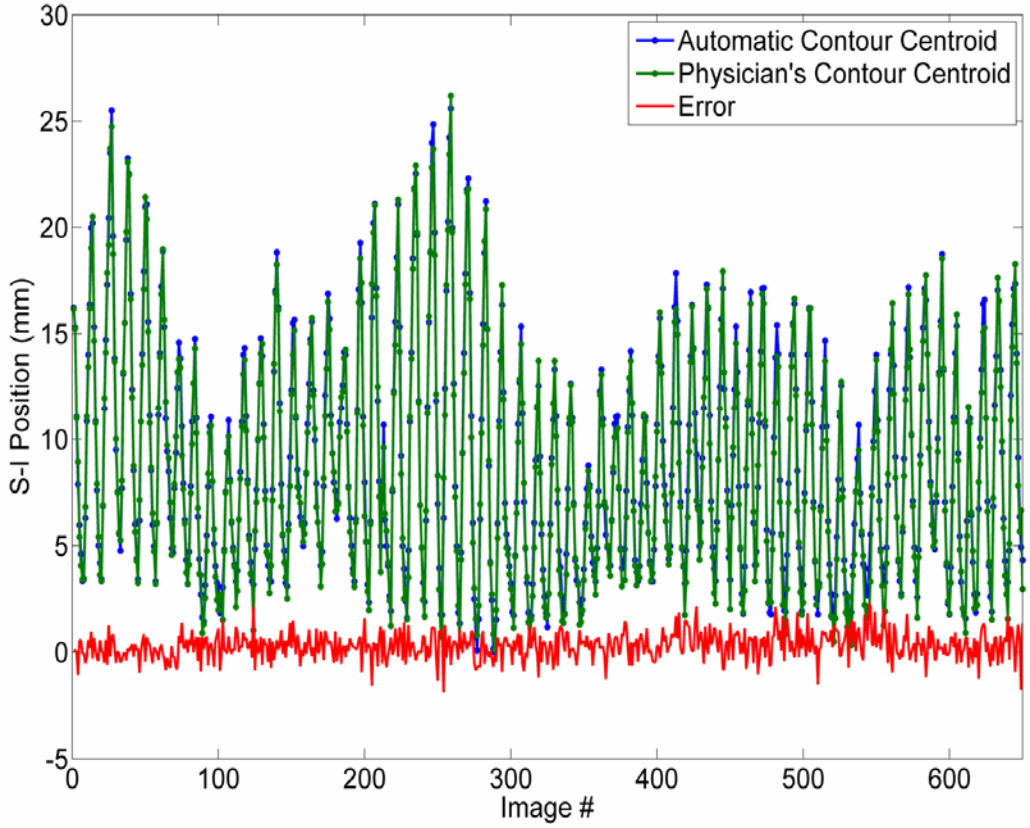


**Figure 4.3 Centroid position comparison between standard (physician drawn) and auto-determined tumour contours in SI direction for 3 T image set (maximum motion range: 26.1 mm).**

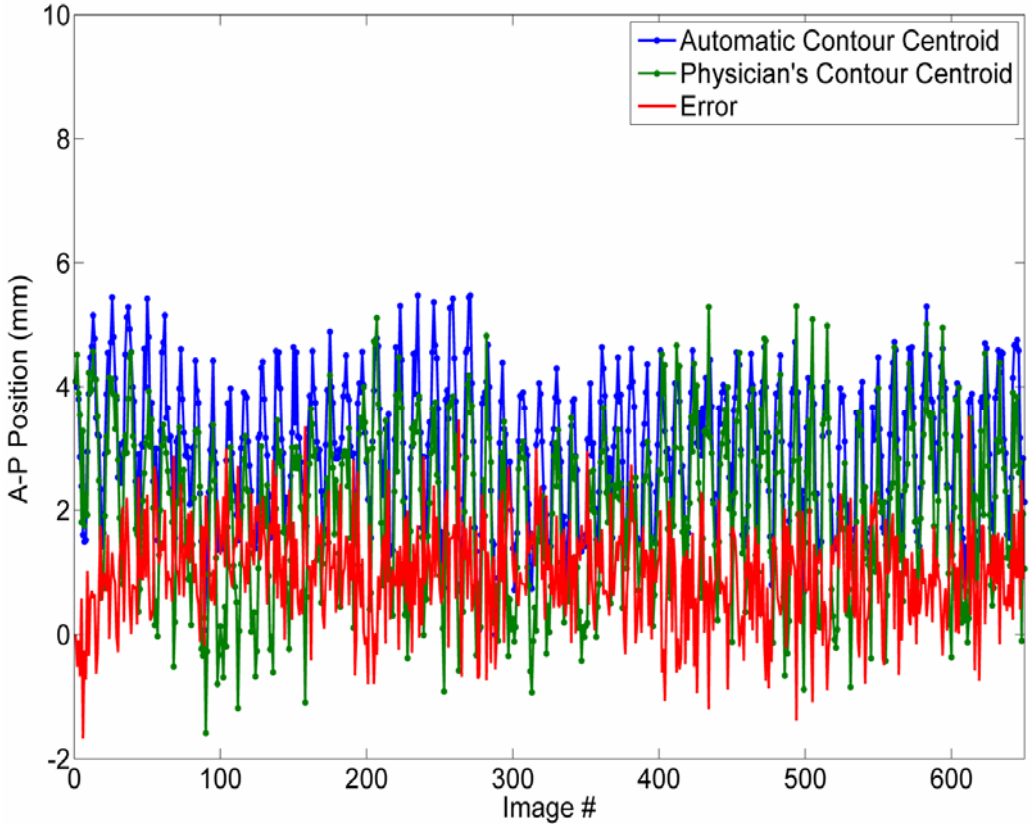


**Figure 4.4 Centroid position comparison between standard (physician drawn) and auto-determined tumour contours in AP direction for 3 T image set (maximum motion range: 5.7 mm).**

Table 4.1 summarizes (1) tumour CNR calculated directly from the 3 T images and from the simulated lower field images, (2) the comparison between standard and auto-determined tumour contours in all field strengths, and (3) the results of the intra-observer variability test.

**Table 4.1 A summary of tumour CNR, comparison between standard and auto-determined tumour contours, and intra-observer variability test.**

| Dataset | $\Delta d_{centroid}$ (mm) Mean (Std) | Dice's coefficient ($D$) Mean (Std) |
|---|---|---|
| 3 T (acquired), CNR = 52 | 1.37 (0.70) | 0.881 (0.033) |
| 1.5 T (simulated), CNR = 26 | 1.38 (0.72) | 0.880 (0.034) |
| 1.0 T (simulated), CNR = 17 | 1.41 (0.72) | 0.878 (0.033) |
| 0.5 T (simulated), CNR = 8.7 | 1.38 (0.69) | 0.875 (0.033) |
| 0.3 T (simulated), CNR = 5.2 | 1.56 (0.83) | 0.870 (0.037) |
| 0.2 T (simulated), CNR = 3.5 | 1.71 (1.15) | 0.836 (0.060) |
| Intra-observer variability test | 0.78 (0.46) | 0.920 (0.026) |

Table 4.2 compares the above result (*in-vivo* study) at 0.2 and 0.5 T to our previous phantom study[1] discussed in Chapter 3 of this thesis. In the phantom study, centroid RMSE (Eq. 3.6) was calculated instead of $\Delta d_{centroid}$ to evaluate 1D target tracking accuracy. Also, the standard target shape was defined more accurately in the phantom study by using a very high resolution (0.4 mm pixel width) MR imaging sequence.

**Table 4.2 Comparison between *in-vivo* and phantom studies at 0.2 and 0.5 T**

| Dataset | *In-vivo* study (2D motion) | | | Phantom study (1D motion)[1] | | |
|---|---|---|---|---|---|---|
| | CNR | Mean $\Delta d_{centroid}$ | Mean $D$ | CNR | Centroid RMSE | $D$ |
| 0.5 T (simulated) | 8.7 | 1.38 mm | 0.88 | 11.5 | < 0.55 mm | > 0.96 |
| 0.2 T (simulated) | 3.5 | 1.71 mm | 0.84 | 4.3 | < 0.92 mm | > 0.93 |

## 4.4. DISCUSSION

As summarized in Table 4.1, mean $\Delta d_{centroid}$ ranged from 1.37 – 1.71 mm at 3 – 0.2 T respectively, showing larger amount of displacement between the centroid positions as the field strength decreased. Mean $D$ ranged from 0.836 – 0.881 at 0.2 – 3 T respectively. Thus, more similarities between standard and auto-determined tumour contours were achieved as the field strength increased. From the intra-observer variability test using 100 images acquired at 3 T, mean $\Delta d_{centroid}$ and mean $D$ of 0.78 mm and 0.920 were achieved, respectively.

Table 4.2 may suggest inferior performance of the autocontouring algorithm in this single patient *in-vivo* study compared to the phantom study. Despite the similar tumour/target CNR in both field strengths, we found ~ 9 % decrease in mean $D$ as well as ~ 0.8 mm increase in mean $\Delta d_{centroid}$ in *in-vivo* study. At current stage, however, it is difficult to make a direct comparison between the phantom and *in-vivo* studies, due to (1) significantly different anatomy of both tumour/target and its surroundings, (2) different amount of uncertainties determining standard tumour/target contours, and (3) different tumour/target motion path (phantom motion was 1D, whereas *in-vivo* tumour motion was 2D). Moreover, contouring uncertainty is inevitable in reality even if a single physician performs all manual contouring as shown in the intra-observer variability test in this study. This might be another reason of the increased autocontouring uncertainty in this *in-vivo* study. Thus, more *in-vivo* studies are required to make a solid conclusion regarding the performance of autocontouring algorithm in *in-vivo* tumour contouring.

For the particular patient scanned in this study, the maximum SI and AP lung tumour motion was approximately 26 mm and 6 mm, respectively. Thus, despite the autocontouring and tracking errors (largest at 0.2 T, where mean $D$ = 0.84 and mean $\Delta d_{centroid}$ = 1.71 mm), intrafractional tumour tracking using our autocontouring algorithm will help to reduce unnecessary radiation dose to its surrounding normal tissues.

## 4.5. CONCLUSION

We performed an initial *in-vivo* study to verify the feasibility of lung tumour autocontouring in low field MR images. From the comparison between standard and auto-determined lung tumour contours, mean $\Delta d_{centroid}$ (measure of tracking accuracy) of 1.37 – 1.71 mm as well as mean $D$ (measure of autocontouring fidelity) of 0.836 – 0.881 were achieved in 3 – 0.2 T equivalent images, respectively. Also, mean $\Delta d_{centroid}$ and mean $D$ of 0.78 mm and 0.920 were achieved from the intra-observer variability test at 3 T, respectively. Compared to our previous phantom study at 0.2 T,[1] ~ 0.8 mm increase in mean $\Delta d_{centroid}$ as well as ~ 9 % decrease in mean $D$ were found in this *in-vivo* study. Although the errors were slightly increased, intrafractional tumour tracking using our autocontouring algorithm will still be helpful to decrease unnecessary normal tissue irradiation, especially for the patient scanned in this study having large range of tumour motion (6 mm and 26 mm in AP and SI directions, respectively).

## 4.6. REFERENCES

[1] J. Yun, E. Yip, K. Wachowicz, S. Rathee, M. Mackenzie, D. Robinson, and B. G. Fallone, "Evaluation of a lung tumor autocontouring algorithm for intrafractional tumor tracking using low-field MRI: A phantom study," Med. Phys. **39**(3), 1481-1494 (2012).

# Chapter 5: An artificial neural network (ANN)-based lung tumour motion predictor for intrafractional MR tumour tracking

*A version of this chapter has been published: J. Yun, M. Mackenzie, S. Rathee, D. Robinson, and B. G. Fallone, "An artificial neural network (ANN)-based lung-tumor motion predictor for intrafractional MR tumor tracking," Med. Phys. 39(7), 4423-4433 (2012).*

## *5.1. INTRODUCTION*

To ensure improved targeting and delivery of highly conformal radiation dose to mobile tumours, several groups are actively researching intrafractional tumour tracking systems.[1-3] Lung tumours are of special interest for tracking, due to their potential for large ranges of motion during treatment delivery. Studies have shown that lung tumours may move up to 50 mm in superior–inferior (SI) direction, 15 mm in anterior–posterior (AP), and 10 mm in left–right (LR) direction during normal breathing.[4, 5]

Krauss *et al*.[6] and Sawant *et al*.[2] performed phantom studies demonstrating the feasibility of 2D intrafractional lung tumour tracking using a Siemens 160 leaf multi-leaf collimator (MLC) and a Varian 120 leaf MLC, respectively. In both studies, a tumour surrogate was driven according to a sinusoidal trajectory and its position was detected via a motion monitoring system developed by Calypso Medical Technologies (Seattle, WA). Cho *et al*. suggested the simultaneous use of kV/MV imaging for 3D intrafractional tracking, where a gold marker was used

as a tumour surrogate.[3] Recently, Cervino *et al*. conducted a feasibility study in regard to MRI-guided lung tumour tracking by following healthy volunteers' lung vascular structures in cine-MR images.[7] Our group at the Cross Cancer Institute has been developing an MRI-based intrafractional lung tumour tracking system by taking advantage of the intrafractional MR imaging feature of the linac-MR that is installed in our laboratory.[8-10]

Although tracking mechanisms may vary, the use of on-line MLC controlling technique (i.e. not pre-programmed leaf motions) for intrafractional beam conformation is common.[2, 3, 6] Ideally, intrafractional tracking would provide target detection and beam delivery simultaneously. However, there exists an inevitable system delay between the two events due to (1) the time requirement to drive each leaf of the MLC to its designated position and (2) computing/processing time. Previously reported system delays range from 160 to 500 ms[2, 3, 6] depending on tracking method. In the case of a lung tumour whose motion-speed is known to be in the range of 4 - 94 mm/s,[11] a system delay of 500 ms could lead to tumour localization errors of up to a maximum of 47 mm. In the presence of this inevitable system delay, a method of predicting tumour motion is highly desirable in order to reduce the localization errors.

Various prediction algorithms have been proposed to compensate for tumour motion during system delay.[12-14] Due to the highly non-linear nature of lung tumour motions which show variable speed and period, several groups have investigated the use of Artificial Neural Networks (ANN) for motion prediction.[15, 16] Although these studies show promising results, the following issues must be

addressed to implement ANN in lung tumour motion prediction for MRI-based tumour tracking.

Firstly, the performance of an ANN is known to be strongly dependent on its structure and initial weights (IW).[17, 18] As Verma *et al*. stated,[14] ANN architecture must be optimized to be used in tumour motion prediction. However, no previous study regarding lung tumour motion prediction has investigated this issue.

Secondly, previous studies assume the tumour position detection at 30 Hz by monitoring the position of external or internal tumour surrogates using optical tracking devices,[15, 16] or a stereoscopic x-ray fluoroscopy system.[12, 13] However, dynamic MR imaging to observe organ motion of lung,[7] intra-thoracic tumour,[19] joint,[20] etc., can typically achieve image-acquisition rates of 3 – 4 frames per second (fps). This rate is recommended for real-time tracking of lung tumour motion[21] and can be achieved using our present linac-MR. Nevertheless, no previous study has been developed and evaluated for predicting lung tumour motion using MRI-based tumour tracking.

To overcome these issues, we propose an ANN-based lung tumour motion predictor for MRI-based intrafractional lung tumour tracking. This chapter describes the ANN design and training methods, implementation of multiple-ANNs, and optimization schemes of ANN structure and IW. The prediction accuracy of our predictor is evaluated using data from 29 lung cancer patients with various possible system delays.

## 5.2. MATERIALS AND METHODS

### 5.2.1. Overview of lung tumour motion prediction

The development of our predictor involves the following points and assumptions: (1) the position of a tumour may be represented by its centroid, (2) the position of tumour centroid in each MR image is automatically detected in real-time (less than 5 ms) using our autocontouring algorithm,[9] (3) signal acquisition time for each MR image is 280 ms, and (4) the amount of system delay, i.e. the time interval between the detection of current tumour position and the beam delivery, of a given tracking system is known.

In our present linac-MR, system delay is approximately 200 ms, which is the sum of : (1) one half of the acquisition time, 140 ms, contributes to system delay assuming the acquired image detects the tumour position at the mid-point of k-space, (2) ~ 35 ms for image reconstruction and processing, and (3) ~ 25 ms for MLC motion.

An overview of the prediction procedure for lung tumour motion is described in Fig. 5.1. In Step 1 of Fig. 5.1, an ANN structure and IW are optimized prior to actual treatment for each patient. A patient typically undergoes treatment over multiple fractions, where, presumably tumour motions in two consecutive fractions are the most similar. During optimization, tumour motion data recorded from a previous fraction is used as a training pattern. We used 8 minutes length of 1D superior-inferior (SI) lung tumour motion pattern. More details regarding training patterns follow in Sec. 5.2.2.

One epoch refers to a single passing of a training pattern (prediction followed by weights corrections) through the ANN during iterative trainings. In Step 2, the optimized ANN structure and IW are further trained for 900 epochs immediately prior to the actual treatment. The training set will be tumour motions recorded from 2 minutes of MR scan immediately prior to the treatment. In our computer platform, approximately 30 seconds are required to run 900 epochs.

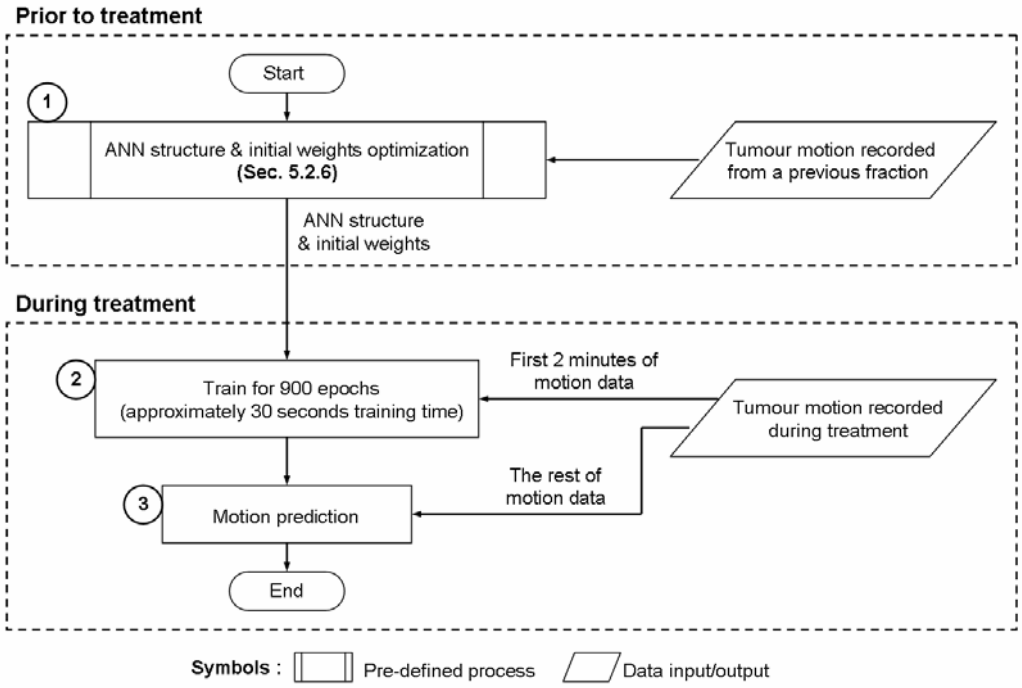


**Figure 5.1 Flowchart for overall lung tumour motion prediction**

All algorithms are coded in LabVIEW 2011 (National Instruments, Austin, TX) and tested on a 32-bit computer system (Windows7, Intel i7-2600k, 4 GB RAM).

### 5.2.2. Patient lung tumour motion data

Our algorithm was verified using data previously reported by Suh *et al*.,[22] who analyzed thoracic and abdominal tumour motions obtained with a Cyberknife Synchrony treatment system (Accuray Incorporated, Sunnyvale, CA). During radiation treatment, 3D tumour positions were estimated and recorded every 40 ms (25 Hz) by both internal and external fiducials for various tumour sites such as lung, liver, pancreas, retroperitoneum, etc. We selected the data from the 29 lung tumour patients. Each patient's data consists of lung tumour motions recorded from 3 consecutive fractions (1 – 5 days apart). From each fraction, we used 8 minutes of the 1D SI lung tumour motion pattern.

### 5.2.3. ANN for lung tumour motion prediction

General explanations regarding ANN are presented in Chapter 2 (Sec. 2.2) of this thesis. The following sections describe a specific type of ANN designed for lung tumour motion prediction in this study.

#### 5.2.3.1. ANN structure

A feed-forward 4 layered ANN structure (1 input layer, 2 hidden layers, and 1 output layer) is developed as shown in Fig. 5.2. Input and hidden layers have an additional bias input of +1, which prevents a zero output when all input values are zero. Detailed explanations can be found in Haykin.[23] Current and previous tumour positions are input to the ANN, which outputs a future tumour position. The number of hidden layers can vary, either 1 or 2, and is determined by ANN structure optimization as explained in Sec. 5.2.6.1.a.

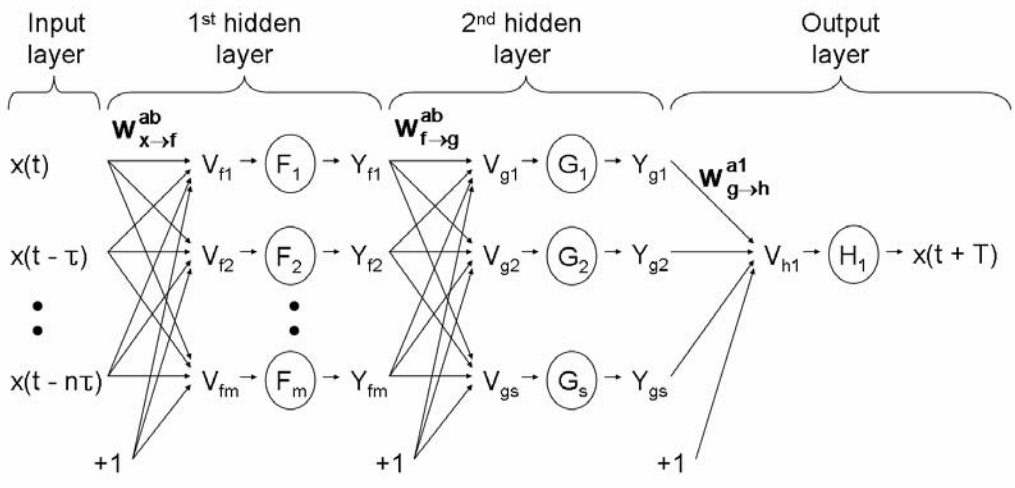


**Figure 5.2 A feed-forward 4 layered ANN structure, where**

$x(t)$ : position of tumour at time $t$,

$\tau$ : time interval between tumour position updates,

$T$ : system delay of a given tracking system,

$V_{cd}$ : input to $d^{th}$ activation function of layer '$c$' (i.e. $V_{gb} = \sum_{a=1}^{m+1} w_{f\to g}^{ab} \cdot Y_{fa}$ ),

$F$, $G$, $H$ : activation function $\Phi(x)=1/(1+\exp(-x))$, $x$ can be $V_{f1,f2,\ldots,fm}$, $V_{g1,g2,\ldots,gs}$, or $V_{h1}$,

$Y_{cd}$ : output from $d^{th}$ activation function of layer '$c$' (e.g. $Y_{f1} = \Phi(V_{f1})$),

$w_{f\to g}^{ab}$ : weight associated with the output of $a^{th}$ neuron in $f$ layer to $b^{th}$ neuron in $g$ layer,

$x(t + T)$ : ANN output (predicted tumour position).

## 5.2.3.2. Back-propagation algorithm and adaptive learning

We used a back-propagation (BP) algorithm[23] for ANN learning, i.e. updating weights. Following the same notations as in Fig. 5.2, we used the following Eqs. 5.1 - 5.3 to update weights during training:

$$w_{new} = w_{previous} + \Delta w \qquad \textbf{(Eq. 5.1)}$$

where, $w_{new}$ : new weight, $w_{previous}$ : previous weight, $\Delta w$ : weight update

For weights associated with output neuron,

$$\Delta w_{g\to h}^{a1} = \eta \cdot \delta_{H1} \cdot Y_{ga} \qquad \textbf{(Eq. 5.2)}$$

where, $\eta$ : learning rate, $\delta_{H1} = e_{H1} \cdot \Phi'(V_{h1})$, $e_{H1}$ = desired output – ANN output, and $\Phi'(V_{h1}) = d\Phi / dV_{h1} = \Phi(V_{h1}) \cdot (1 - \Phi(V_{h1}))$

For weights associated with other neurons,

$$\Delta w_{f \to g}^{ab} = \eta \cdot \delta_{Gb} \cdot Y_{fa} \qquad \textbf{(Eq. 5.3)}$$

where, $\delta_{Gb} = \Phi'(V_{Gb}) \cdot \sum_{a=1}^{s+1} (\delta_{H1} \cdot w_{g \to h}^{a1})$

The BP algorithm requires a proper learning rate ($\eta$) to achieve fast convergence. We implemented an algorithm developed by Behera *et al*.,[24] which can calculate an efficient, self-adaptive learning rate as:

$$\eta = \mu \cdot \frac{\|e_{H1}\|^2}{\left\|\vec{J} \cdot e_{H1}\right\|^2 + \gamma}$$

$$= \mu \cdot \frac{(e_{H1})^2}{\sum_{k=1}^{m}\sum_{c=0}^{n}(\delta_{Fk} \cdot x(t - c \cdot \tau))^2 + \sum_{r=1}^{m}(\delta_{Fr})^2 + \sum_{p=1}^{s}\sum_{q=1}^{m+1}(\delta_{Gp} \cdot Y_{fq})^2 + \sum_{i=1}^{s+1}(\delta_{H1} \cdot Y_{gi})^2 + \gamma} \qquad \textbf{(Eq. 5.4)}$$

where, $\vec{J} = \partial(\text{ANN output}) / \partial \vec{w}$ , $\mu$ : scaling factor, $\gamma$ : small constant to prevent numerical instability of $\eta$ when $e_{H1}$ is near zero. The values of $\mu$ and $\gamma$ are determined to achieve the lowest prediction error using training patterns, and the results are stated in Figs. 5.5 and 5.6.

Adaptive learning is incorporated by continuously updating the weights and $\eta$ of a given ANN during motion prediction. The structure of ANN does not change during prediction. However, the weights and $\eta$ updates occur prior to each prediction immediately following current tumour position detection by the tracking system. This update involves simple matrix calculations that happen

almost instantaneously using our computer system; thus, this is not included in calculating the total system delay.

In this way, the ANN's learning process is not limited to the training sessions alone but continues during the actual tracking session. Using this ANN, our predictor can adapt quickly to tumour motion pattern during the actual tracking session, even when this pattern starts deviating from the one used in training sessions.

### 5.2.4. ANN training for MRI-based tumour tracking

Our tumour motion training data is acquired at 280 ms intervals from MR images obtained from previous treatment fractions. In reality, the system delay will often be different from the time intervals in the training data. To demonstrate that this training scheme can be applied to different system delays, we present ANN training simulations with 280 and 200 ms system delays. Figure 5.3 shows a portion of the training data from one of the 29 patients.

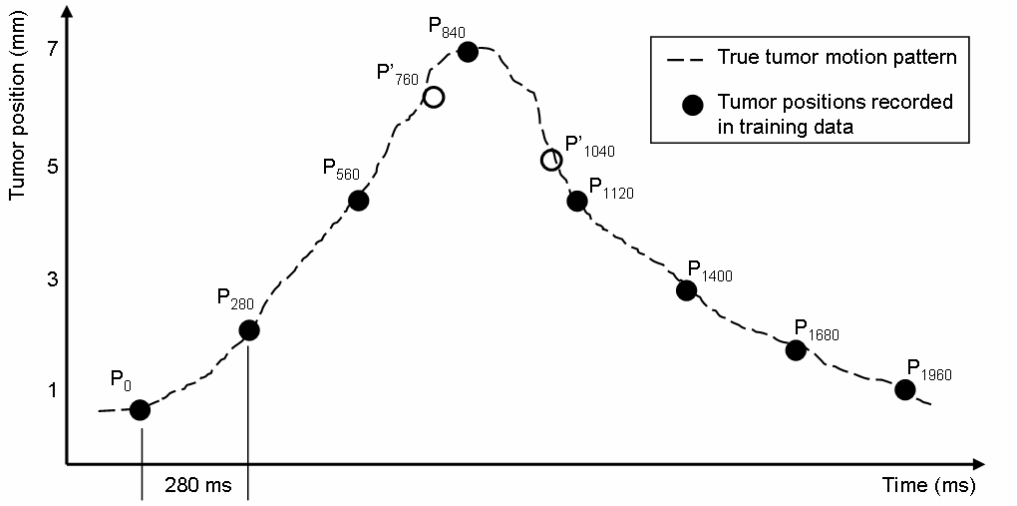


**Figure 5.3 Tumour position in SI direction in training data, $P_t$ : tumour position at time t (ms), $P'_t$ : approximate tumour position at t (ms) – see text for details.**

During ANN training, many numbers of known input/output pairs must be entered to allow the ANN to model the complex relationships between them. These input/output pairs include the previous, as well as future, tumour positions that have been recorded in the training data.

As shown in Fig. 5.2, a single ANN can predict a single output for tumour position. However, the number of inputs to this ANN, i.e. number of previous tumour positions, can vary from patient to patient. Section 5.2.6 explains how our predictor determines the appropriate number of inputs for each patient. Here, our training scheme takes three inputs and is described in the following two examples.

(1) 280 ms system delay: Input/output pairs were generated from the training data described above with a system delay of 280 ms. In Fig. 5.3, $P_0$, $P_{280}$, $P_{560}$ can be used as the ANN inputs of the 1$^{st}$ input/output pair. In this case, the output should be $P_{840}$, because the time interval between $P_{560}$ and $P_{840}$ is the same amount as the system delay. Similarly, if $P_{280}$, $P_{560}$, $P_{840}$ are used as the inputs for the 2$^{nd}$ input/output pair, $P_{1120}$ will be the corresponding output. We can generate many numbers of input/output pairs in this way and train the ANN. The same training method can be used if the system delay is an exact multiple of the time interval between two consecutively known tumour positions in training data.

(2) 200 ms system delay: Because the system delay for our present linac-MR system is 200 ms, a different method is used to generate the input/output pairs. If $P_0$, $P_{280}$, $P_{560}$ are used as the inputs, the output must be $P_{760}$. However, $P_{760}$ is unknown in our training data as shown in Fig. 5.3. Our approach is to approximate $P_{760}$ using linear interpolation between $P_{560}$ and $P_{840}$, which is

referred to as $P'_{760}$. This is a first order approximation which presumes that the lung tumour motion may be reasonably modeled as linear motion between two known tumour positions. Similarly, if $P_{280}$, $P_{560}$, $P_{840}$ are used as the inputs, $P'_{1040}$ will be the corresponding output. Using this method, we are able to train our ANN for any arbitrary system delay.

### 5.2.5. Implementation of multiple ANNs

During tumour tracking, each prediction occurs immediately after a current tumour position is detected. This triggers MLC motion to conform the radiation beam to the tumour at the predicted position.

Frequent tracking failures may occur if a single ANN is used in our predictor. If the time interval between two predictions is greater than the time required to complete the MLC motion, the MLC will stop after reaching set points, i.e. designated leaf positions, and wait for the next prediction to occur. During this time, designated as the "MLC-off time", the tumour will continue to move resulting in tracking failure. On the contrary, if the time interval between two predictions is smaller than the time required for the MLC to reach the predicted position, then the MLC will never reach the set points and miss the tumour.

We propose to employ multiple ANNs in our predictor to reduce tracking failures, which, in itself, is a unique feature developed in this study.

#### 5.2.5.1.Tumour tracking using multiple ANNs

We use seven ANNs, because our imaging rate is 280 ms and we want to predict tumour positions in a 40 ms interval that corresponds to the acquisition

rate of the Suh *et al*.[22] data used to evaluate the performance of the prediction algorithm (the acquisition rate of the Suh *et al*. data is 40 ms, and 280/40 is 7).

The seven ANNs implemented in our predictor have an identical structure. However, we trained them separately so that at each prediction, the predictor can output seven consecutive future tumour positions (40 ms apart, the first one corresponds to the future tumour position after the system delay). In case of 200 ms system delay, the 1st ANN predicts a tumour position at 200 ms in the future, 2nd ANN predicts at 240 ms in the future, 3rd ANN predicts at 280 ms in the future, etc. This is described in Fig. 5.4.

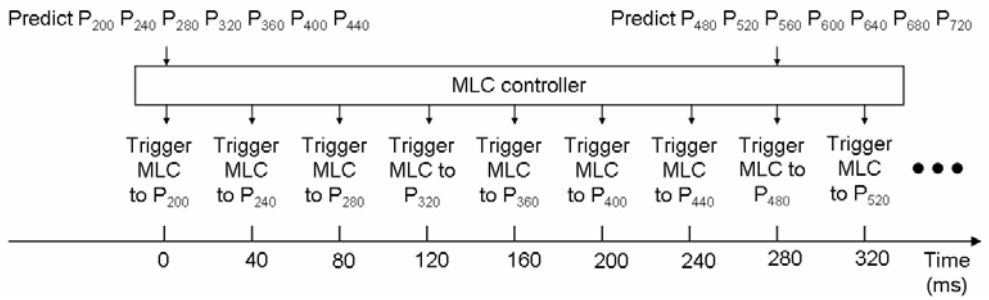


**Figure 5.4 Tumour tracking using seven ANNs, $P_t$ : tumour position at time t (ms).**

At 0 ms, the 1st prediction occurs from seven ANNs predicting $P_{200}$, $P_{240}$, …, $P_{440}$. Using these, the MLC controller triggers MLC motions conforming to the appropriate future tumour positions. For example, at 0 ms, the MLC begins conforming to $P_{200}$; at 40 ms, it starts conforming to $P_{240}$, etc. At 280 ms, the 2nd prediction occurs predicting $P_{480}$, $P_{520}$, …, $P_{720}$, and this triggers new MLC motions.

Using multiple ANNs, we can trigger MLC motions more frequently. We can then verify whether this approach will reduce tracking failures because (1) the MLC-off time between two predictions is decreased, and (2) the MLC can almost

always reach the set points, since the traveling distance at each motion triggering is decreased.

### 5.2.6. Optimizing ANN structure & IW for each patient

ANN structure and IW must be optimized for each patient to ensure the optimal performance of our predictor, because (1) the performance of ANN is known to be strongly dependent on its structure and IW,[17, 18] and (2) there are large patient-to-patient variations in lung tumour motion patterns.

#### 5.2.6.1.Particle Swarm Optimization

Particle Swarm Optimization (PSO) is one type of population based stochastic optimization method, which is inspired by the social behavior of bird flocking or fish schooling.[25] An overview of PSO is presented in Chapter 2 (Sec. 2.3) of this thesis.

We use an improved version of the original PSO algorithm called Modified Particle Swarm Optimization (MPSO)[26] for both ANN structure and IW optimizations. Shi *et al*. demonstrated superior performance of MPSO in finding a global optimum within a reasonable number of iterations.[26] This is particularly advantageous in clinical applications where optimization for each patient must be completed within a reasonable time frame.

In MPSO, each particle's velocity and position are updated in each iteration as:

$$V_{updated} = W \cdot V_{prev} + c_1 \cdot rand_1 \cdot (pbest - P_{prev}) + c_2 \cdot rand_2 \cdot (gbest - P_{prev})$$

**(Eq. 5.5)**

$$P_{updated} = P_{prev} + V_{updated} \quad \textbf{(Eq. 5.6)}$$

where, $V_{updated}$, $P_{updated}$: updated velocity and position of a particle, W: inertia weight, $c_n$: a unitless weight determining the impact of an individual particle's history on the entire swarm's history in $V_{updated}$ calculation, $rand_n$: a random number (0 – 1), *pbest* : personal best solution, *gbest*: global best solution, $V_{prev}$, $P_{prev}$: previous velocity and position of a particle. Detailed calculation methods of *pbest* and *gbest* follow in Sec. 5.2.6.1.a.

We use MPSO to optimize ANN structure and IW for each patient. To achieve this, we must first determine the representation of a particle and a fitness function for each optimization problem. Detailed explanations follow.

#### 5.2.6.1.a. ANN structure optimization

In ANN structure optimization, a specific ANN structure is a solution, i.e. particle. Therefore, each particle's current position and velocity represents a current ANN structure and the degree of its modification, respectively. Our fitness function is an RMSE value between original and predicted tumour positions in the training pattern, where original tumour positions refer to the ones recorded in patient data.

As shown in Fig. 5.2, we can define an ANN structure using an array of three integer variables designating the number of inputs, number of neurons in 1$^{st}$ hidden layer, and number of neurons in 2$^{nd}$ hidden layer. The number of neurons in an output layer is fixed at 1.

For example, [*n*, *m*, *s*] indicates an ANN structure that has *n* number of inputs, *m* number of neurons in the 1$^{st}$ hidden layer, *s* number of neurons in the 2$^{nd}$

hidden layer, and 1 neuron in the output layer. Hence, each particle's position and velocity are both defined by a 1 × 3 integer array. Figure 5.5 shows the ANN structure optimization process.

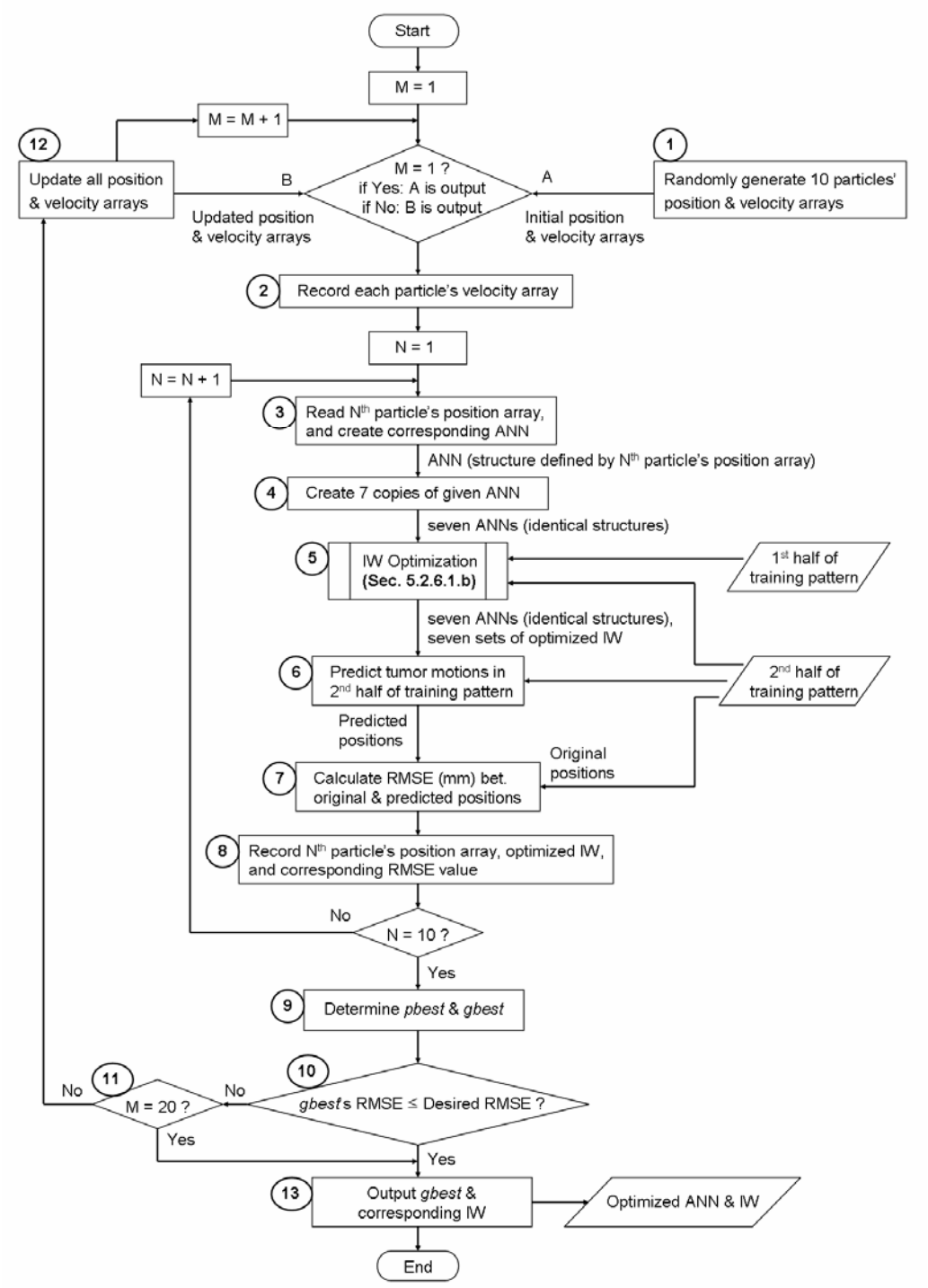


**Figure 5.5 Flow chart for ANN structure optimization. Parameters used: Step 1 (Initial number of inputs: 1 – 10, Initial number of neurons in each layer: 0 - 10, Initial velocity: 0 - 10), Step 6 (μ: 0.6, γ: 0.02, see Eq. 5.4), Step 10 (Desired RMSE = 0.001 mm), Step 12 ($c_n$ = 2, $rand_n$: 0 – 1, Max. velocity: 10, W: 0.4, see Eq. 5.5)**

Step 1 in Fig. 5.5 is performed only in the 1st iteration at M = 1. Here the position and velocity arrays of 10 particles are generated using a random number generator within a user defined range as stated in Fig. 5.5. In Step 2, each particle's velocity array is recorded for later use.

In Step 3, the $N^{th}$ particle's position array is read and its corresponding ANN is created. In Step 4, this ANN is copied 7 times to create seven ANNs that have identical structures. For example, if the 1st particle's position array is [5, 8, 6], the corresponding ANN is created containing 5 inputs, 8 and 6 neurons in the 1st and 2nd hidden layers, and 1 output neuron. This ANN is then copied 7 times.

In Step 5, IW are optimized for each of the seven ANNs using the 1st half of the training pattern. During IW optimization, each ANN is trained for a different amount of system delay. Detailed explanations follow in Sec. 5.2.6.1.b. As a result, seven sets of optimized IW are produced.

In Step 6, the seven ANNs and a corresponding set of optimized IW are used to predict tumour motions in the 2nd half of the training pattern. This generates predicted tumour positions in 40 ms intervals as explained in Sec. 5.2.5.1. Using this result, in Step 7, we can perform one-to-one comparisons between original and predicted tumour positions calculating RMSE values.

Steps 3 – 7 are iterated with all 10 particles' position arrays. After the $N^{th}$ iteration, the $N^{th}$ particle's position array, optimized IW, and corresponding RMSE value are recorded in Step 8. From this record, the algorithm determines *pbest* and *gbest* in Step 9 as described in the following paragraphs.

During optimization, each particle's position array is updated through iterations. Out of the particle's current and previous position arrays, *pbest* is the

one that achieved the lowest RMSE value in Step 7. For example, if the 1st particle's position array has been updated for three iterations (see the outer loop through step 12) as [5, 8, 6] → [10, 18, 7] → [12, 23, 0] with corresponding RMSE values of 2.5 → 1.6 → 1.9, then *pbest* of this particle is [10, 18, 7].

In Step 9, therefore, 10 *pbest* arrays are determined from 10 particles. Out of these, the one with the lowest RMSE value becomes *gbest*. Depending on the results from Steps 10 and 11, the algorithm either updates all particles' position arrays and iteration continues, or the optimization process is terminated.

In Step 12, we first calculate $V_{updated}$ array for each particle using Eq. 5.5 with the parameters stated in Fig. 5.5. Each particle's velocity, position, and *pbest* arrays are obtained from Step 2, Step 8, and Step 9, respectively. *gbest* is obtained from Step 9.

For example, if the 1st particle's position, velocity, *pbest* arrays are [$P_1$, $P_2$, $P_3$], [$V_1$, $V_2$, $V_3$], [$PB_1$, $PB_2$, $PB_3$] respectively, and *gbest* of all particles is [$GB_1$, $GB_2$, $GB_3$], then $V_{updated}$ is calculated as:

$$V_{updated}\ \text{array} = [V_{updated1}, V_{updated2}, V_{updated3}]$$

$$= W\cdot[V_1, V_2, V_3] + c_1\cdot rand_1\cdot([PB_1, PB_2, PB_3] - [P_1, P_2, P_3]) + c_2\cdot rand_2\cdot([GB_1, GB_2, GB_3] - [P_1, P_2, P_3])$$

Hence, $V_{updated1} = W\cdot V_1 + c_1\cdot rand_1\cdot (PB_1 - P_1) + c_2\cdot rand_2\cdot (GB_1 - P_1)$

$$V_{updated2} = W\cdot V_2 + c_1\cdot rand_1\cdot (PB_2 - P_2) + c_2\cdot rand_2\cdot (GB_2 - P_2)$$

$$V_{updated3} = W\cdot V_3 + c_1\cdot rand_1\cdot (PB_3 - P_3) + c_2\cdot rand_2\cdot (GB_3 - P_3)$$

If any component of the $V_{updated}$ array is greater than a user defined maximum velocity stated in Fig. 5.5, that component is replaced with the value of maximum velocity. This is to avoid overly radical changes of the particle's position in each

iteration. After the $V_{updated}$ array is determined, $P_{updated}$ array is calculated using Eq. 5.6 as:

$$P_{updated} \text{ array} = [P_{updated1}, P_{updated2}, P_{updated3}]$$

$$= [P_1, P_2, P_3] + [V_{updated1}, V_{updated2}, V_{updated3}]$$

Hence, $P_{updated1} = P_1 + V_{updated1}$

$P_{updated2} = P_2 + V_{updated2}$

$P_{updated3} = P_3 + V_{updated3}$

Steps 2 – 11 are iterated after all 10 particles' position and velocity arrays are updated. At the end of optimization in Step 13, the algorithm outputs an ANN structure and IW optimized for a given patient.

#### 5.2.6.1.b. IW optimization (Step 5 in Fig. 5.5)

The weights shown in Fig. 5.2 are rational numbers, and one may calculate the number of weights required to link two adjacent layers as: (number of neurons in previous layer + 1) × number of neurons in next layer, where the + 1 term is due to the bias input. For example, if a [*n*, *m*, *s*] structure is given, the total number of IW, referred to as Z, is calculated as: $Z = (n + 1) \times m + (m + 1) \times s + (s + 1) \times 1$. Hence, one set of IW for a [*n*, *m*, *s*] structure is defined by a $1 \times Z$ rational number array.

We have seven ANNs in our predictor, which must be trained for different amounts of system delay. Therefore, a group of IW becomes a solution, i.e. particle, in IW optimization, where this group consists of seven sets of IW. Each particle's current position and velocity represents a current group of IW and the degree of its modification, respectively. Since a group of IW contains seven sets

of IW, each particle's position and velocity are both defined by seven $1 \times Z$ rational number arrays. The same fitness function is used as in ANN structure optimization. Figure 5.6 shows the IW optimization processes.

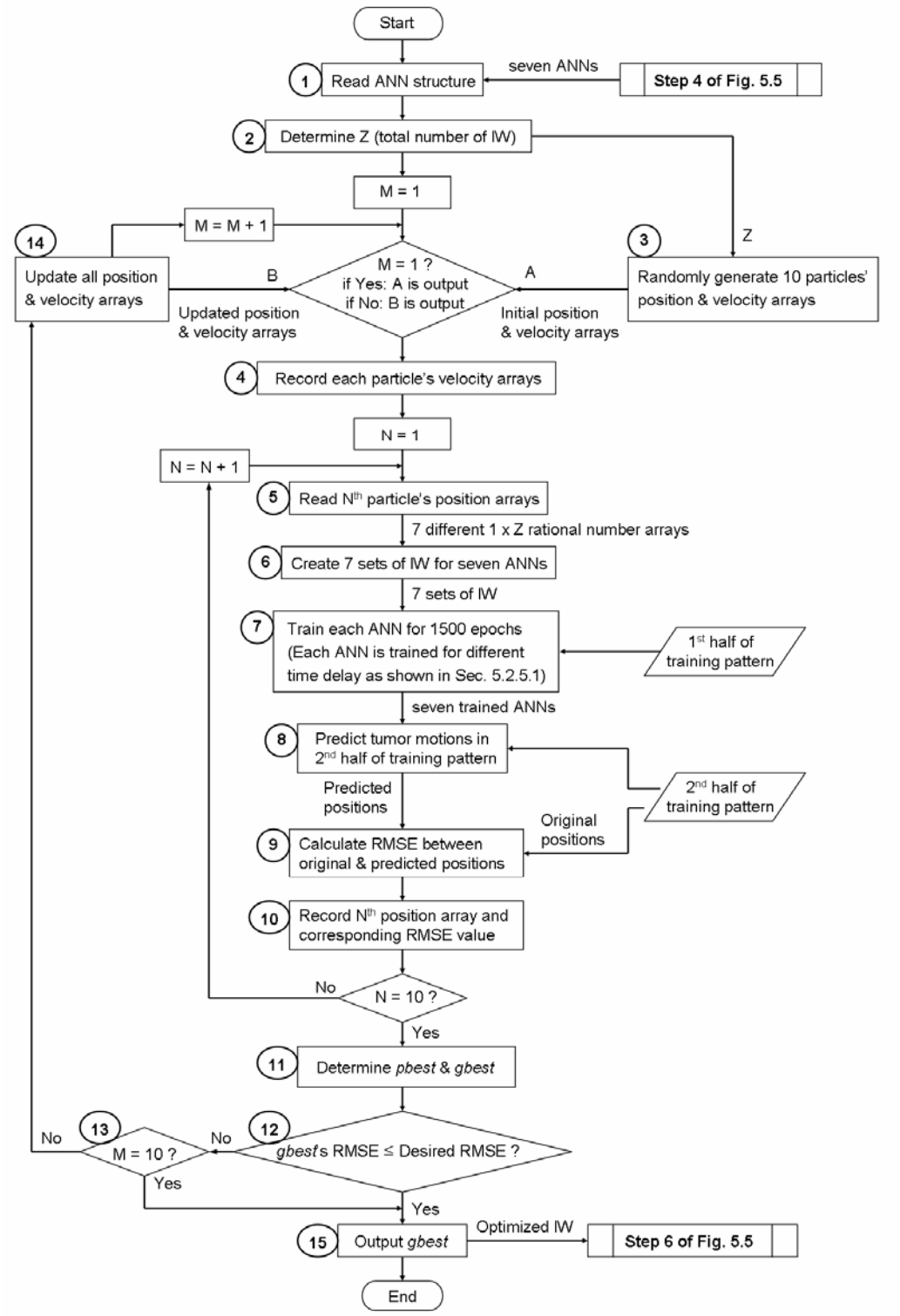


**Figure 5.6 Flow chart for IW optimization. Parameters used: Step 3 (IW and initial velocities: random rational numbers between -1 and 1), Steps 7, 8 (μ: 0.6, γ: 0.02), Step 12 (Desired RMSE = 0.001 mm), Step 14 ($c_n$ = 2, $rand_n$: 0 – 1, Max. velocity/W: 1.5/0.8 and 2/0.6 for one and two hidden layered ANN, respectively)**

In Steps 1 and 2 in Fig. 5.6, we read the ANN structure subject to IW optimization and calculate Z. For example, if the ANN has a [5, 8, 6] structure, Z = $(5 + 1)\times 8 + (8 + 1)\times 6 + (6 + 1)\times 1 = 109$. Because the seven ANNs have identical structures, we only need a single Z value.

Step 3 is performed only in the 1st iteration at M = 1. We generate 10 particles' position and velocity arrays using a random number generator between -1 and 1. In Step 4, each particle's velocity arrays are recorded for later use.

In Steps 5 and 6, the $N^{th}$ particle's position arrays are read and corresponding sets of IW are created. As a result, seven sets of IW are created for the seven ANNs.

In Step 7, the seven ANNs are trained using the 1st half of training pattern. Each ANN is trained for a different amount of system delay for 1500 epochs. The $1^{st}$, $2^{nd}$,…,$7^{th}$ sets of IW are used as a starting point for training the $1^{st}$, $2^{nd}$,…,$7^{th}$ ANNs, respectively.

In Step 8, we use the seven trained ANNs to predict tumour motions in the $2^{nd}$ half of training pattern. This generates predicted tumour positions in 40 ms intervals as explained in Sec. 5.2.5.1. Hence, in Step 9, we can calculate RMSE between the original and predicted tumour positions to evaluate the prediction accuracy.

Steps 5 – 9 are iterated with all 10 particles' position arrays. After the $N^{th}$ iteration, the $N^{th}$ particle's position arrays and corresponding RMSE value are recorded in Step 10. From this record, the algorithm determines *pbest* and *gbest* in Step 11. This process is previously explained in Sec. 5.2.6.1.a in detail.

Depending on the results from Steps 12 and 13, the algorithm either updates all particles' position arrays and iteration continues, or the optimization process is terminated.

In Step 14, $V_{updated}$ and $P_{updated}$ arrays are calculated for each particle using Eqs. 5.5 and 5.6 with the parameters stated in Fig. 5.6. Detailed explanations have been previously given in Sec. 5.2.6.1.a. After all particles' position and velocity arrays are updated, Steps 4 – 13 continue using the updated arrays. At the end of optimization in Step 15, the algorithm outputs the seven sets of IW represented by *gbest* as the optimized IW.

## 5.2.7. Evaluation of the reduction in tracking failures using multiple ANNs

We verified whether using multiple ANNs reduces tracking failures as described in Sec. 5.2.5. Lung tumour tracking was simulated using a Varian 52-leaf MLC, where tumour motion was assumed to be sinusoidal (period: 4 seconds, amplitude: 5 cm) at the imaging plane of our present linac-MR. This tumour motion is sufficient to cover the possible motion range of lung tumours.[4, 5]

The following two cases were tested during one minute of tumour tracking:

(1) MLC motions were triggered every 280 ms, which will occur if a single ANN is used;

(2) MLC motions were triggered every 40 ms, which will occur if seven ANNs are used.

In both cases, mean and standard deviation of the MLC-off time, and the percentage frequency of MLC failure to reach set points were calculated.

## 5.2.8. Evaluation of prediction accuracy using patient data

### 5.2.8.1. Presentation of patient data to ANNs

To evaluate the prediction accuracy of our predictor in a realistic MRI-based tumour tracking scenario, the following processes are performed with the original data from Suh *et al*.[22]

Firstly, to simulate MRI-based tumour tracking that detects tumour positions every 280 ms, every 7$^{th}$ data point is chosen from the original data (40 ms interval between data points $\times 7$ = 280 ms). This generates motion patterns containing lung tumour positions recorded every 280 ms. Secondly, each motion pattern is shifted and normalized, so that the values remain between 0 and 1. This is clinically feasible, and more details follow in Sec. 5.4. It is important to note that only these motion patterns are presented to our predictor, both in ANN training and the motion prediction stages.

### 5.2.8.2. Prediction accuracy comparisons

The prediction accuracy of our predictor is evaluated with 29 patient data sets. Each patient's 1$^{st}$ fraction data is used as a training pattern for the ANN structure and IW optimizations. The result is used to predict tumour motions in the 2$^{nd}$ fraction data. Similarly, 2$^{nd}$ fraction data is used as a training pattern for optimizations, and this result is used to predict tumour motions in the 3$^{rd}$ fraction data.

Evaluation is performed for various amounts of system delay ranging from 120 to 520 ms in 80 ms increments, which encompasses all previously reported system delays in the literature.[2, 3, 6] Prediction accuracy is measured by the RMSE (mm) between original and predicted tumour positions.

To demonstrate the benefit of ANN structure as well as IW optimizations developed in this study, prediction accuracy was compared according to the 4 different cases shown in Table 5.1.

**Table 5.1 Cases tested for prediction accuracy investigation**

| | Case 1 | Case 2 | Case 3 | Case 4 |
|---|---|---|---|---|
| ANN structure optimization | Yes | Yes | No | No |
| IW optimization | Yes | No | Yes | No |

Instead of using an optimized ANN structure for each patient, a single ANN structure (25 inputs, 2 neurons in a hidden layer, 1 output neuron) is employed for all patients in cases 3 and 4. This ANN structure was suggested by Murphy *et al.*[16] for respiratory motion prediction, which is closely correlated to abdominal tumour motions including lung tumour.[27] The IW optimization process is omitted for case 2 and 4. However, an additional 900 epochs training as described in Step 2 of Fig. 5.1 is still performed with randomly generated IW.

One further experiment is performed to assess the necessity of ANN structure optimization not only for each patient, but also for each treatment fraction. In this case, only 1$^{st}$ fraction data is used as a training pattern for ANN structure and IW optimizations, and the result is used to predict tumour motions in both 2$^{nd}$ and 3$^{rd}$ fraction data. Prediction accuracy of 3$^{rd}$ fraction data obtained from this experiment is compared to the result from Case 1, in which the

prediction was performed with an ANN structure specifically optimized to predict tumour motion in 3rd fraction data.

## 5.3. RESULTS

### 5.3.1. Tracking failure comparisons using a single ANN vs. seven ANNs

Table 5.2 compares the MLC-off time between two consecutive predictions and the frequency percentage of MLC failures reaching its set points during one minute of tracking period. Set points are the aimed location of each leaf, and the failures result from MLC speed limitation.

**Table 5.2 Tracking failure comparisons using a single ANN vs. seven ANNs.**

| | Single ANN | Seven ANNs |
|---|---|---|
| MLC motion triggering | every 280 ms | every 40 ms |
| MLC-off time(mean ± std) | 110 ± 87 ms | 15 ± 9 ms |
| Failure to reach set points | 46 % | 0 % |

In the single ANN case, mean MLC-off times show that tumour tracking failed for 110 ms on average between two consecutive MLC triggers. More importantly, the MLC could not reach its set points in 46 % of the overall tracking period. Both of these problems are largely resolved using the seven ANNs approach. In this case the MLC was always able to reach its set points, and the mean MLC-off time was decreased by a factor of more than 7.

### 5.3.2. Prediction performance using optimized ANN and IW

Table 5.3 shows lung tumour motion prediction results simulated from patient data as discussed in Sec. 5.2.8.1. Prediction is performed with optimized ANN structures and optimized IW for each patient and fraction. Optimizations and predictions were repeated 5 times for each patient and fraction. Only mean RMSE values are reported in Table 5.3 as very small variations in RMSE values (less than 0.1 mm) were observed for the 5 trials.

For 120 – 520 ms system delays, 0.5 – 0.9 mm of mean RMSE values (ranges 0.0 - 2.8 mm from 29 patients) are observed, respectively. The entire optimization process (ANN structure and IW optimizations) requires approximately 2.5 hours for each treatment fraction of a given patient, which would need to be performed prior to treatment.

**Table 5.3 Motion prediction results obtained with optimized ANN structure and IW for each patient.**

| Patient | 2nd fraction RMSE (mm) System delay (ms) | | | | | | 3rd fraction RMSE (mm) System delay (ms) | | | | | |
|---|---|---|---|---|---|---|---|---|---|---|---|---|
| | 120 | 200 | 280 | 360 | 440 | 520 | 120 | 200 | 280 | 360 | 440 | 520 |
| 1 | 0.7 | 0.9 | 1.1 | 1.2 | 1.3 | 1.4 | 0.8 | 0.9 | 1.1 | 1.3 | 1.5 | 1.7 |
| 2 | 0.3 | 0.3 | 0.4 | 0.4 | 0.4 | 0.4 | 0.5 | 0.6 | 0.6 | 0.7 | 0.7 | 0.8 |
| 3 | 0.3 | 0.3 | 0.4 | 0.5 | 0.5 | 0.6 | 0.3 | 0.3 | 0.4 | 0.5 | 0.6 | 0.6 |
| 4 | 0.2 | 0.2 | 0.2 | 0.2 | 0.3 | 0.3 | 0.1 | 0.1 | 0.2 | 0.2 | 0.2 | 0.2 |
| 5 | 0.5 | 0.6 | 0.7 | 0.8 | 0.9 | 1.1 | 0.4 | 0.6 | 0.7 | 0.7 | 0.8 | 0.9 |
| 6 | 0.5 | 0.6 | 0.7 | 0.8 | 0.9 | 0.9 | 0.4 | 0.5 | 0.5 | 0.6 | 0.6 | 0.6 |
| 7 | 0.6 | 0.7 | 0.8 | 1.0 | 1.1 | 1.2 | 0.5 | 0.7 | 0.8 | 0.9 | 1.0 | 1.1 |
| 8 | 0.2 | 0.2 | 0.3 | 0.3 | 0.3 | 0.4 | 0.1 | 0.1 | 0.2 | 0.2 | 0.2 | 0.2 |
| 9 | 0.2 | 0.3 | 0.4 | 0.5 | 0.5 | 0.6 | 0.3 | 0.4 | 0.4 | 0.5 | 0.6 | 0.7 |
| 10 | 0.2 | 0.2 | 0.3 | 0.3 | 0.3 | 0.4 | 0.2 | 0.3 | 0.3 | 0.3 | 0.4 | 0.4 |
| 11 | 0.9 | 1.1 | 1.2 | 1.4 | 1.5 | 1.6 | 1.0 | 1.3 | 1.6 | 1.8 | 2.1 | 2.2 |
| 12 | 1.5 | 1.7 | 1.9 | 2.1 | 2.3 | 2.4 | 1.8 | 2.1 | 2.3 | 2.5 | 2.6 | 2.8 |
| 13 | 0.1 | 0.1 | 0.1 | 0.1 | 0.1 | 0.1 | 0.0 | 0.0 | 0.1 | 0.1 | 0.1 | 0.1 |
| 14 | 1.4 | 1.7 | 2.0 | 2.2 | 2.4 | 2.6 | 1.4 | 1.7 | 2.0 | 2.3 | 2.5 | 2.8 |
| 15 | 0.2 | 0.2 | 0.3 | 0.4 | 0.4 | 0.5 | 0.6 | 0.7 | 0.9 | 1.0 | 1.0 | 1.1 |
| 16 | 0.3 | 0.3 | 0.4 | 0.4 | 0.4 | 0.5 | 0.5 | 0.5 | 0.6 | 0.7 | 0.7 | 0.8 |
| 17 | 0.7 | 0.8 | 0.9 | 1.0 | 1.2 | 1.2 | 0.6 | 0.8 | 0.9 | 1.0 | 1.1 | 1.2 |
| 18 | 0.6 | 0.8 | 0.9 | 0.9 | 1.0 | 1.1 | 0.5 | 0.6 | 0.7 | 0.8 | 0.9 | 1.1 |
| 19 | 0.4 | 0.5 | 0.6 | 0.7 | 0.8 | 0.9 | 0.7 | 0.9 | 1.1 | 1.2 | 1.4 | 1.6 |
| 20 | 0.3 | 0.4 | 0.5 | 0.5 | 0.6 | 0.6 | 0.3 | 0.4 | 0.4 | 0.5 | 0.6 | 0.6 |
| 21 | 0.0 | 0.0 | 0.0 | 0.1 | 0.1 | 0.1 | 0.1 | 0.1 | 0.1 | 0.1 | 0.1 | 0.1 |
| 22 | 0.4 | 0.4 | 0.4 | 0.5 | 0.5 | 0.5 | 0.5 | 0.5 | 0.5 | 0.6 | 0.6 | 0.6 |
| 23 | 0.9 | 1.1 | 1.2 | 1.3 | 1.3 | 1.4 | 0.8 | 0.8 | 1.0 | 1.0 | 1.0 | 0.9 |
| 24 | 0.3 | 0.4 | 0.5 | 0.5 | 0.6 | 0.6 | 0.2 | 0.3 | 0.3 | 0.4 | 0.4 | 0.5 |
| 25 | 0.2 | 0.2 | 0.2 | 0.2 | 0.2 | 0.2 | 0.4 | 0.4 | 0.5 | 0.6 | 0.6 | 0.7 |
| 26 | 0.3 | 0.4 | 0.5 | 0.5 | 0.5 | 0.6 | 0.5 | 0.6 | 0.7 | 0.8 | 0.9 | 1.0 |
| 27 | 0.2 | 0.2 | 0.2 | 0.3 | 0.3 | 0.3 | 0.1 | 0.2 | 0.2 | 0.2 | 0.3 | 0.3 |
| 28 | 1.3 | 1.6 | 1.9 | 2.2 | 2.4 | 2.7 | 0.4 | 0.4 | 0.5 | 0.5 | 0.6 | 0.6 |
| 29 | 0.6 | 0.7 | 0.9 | 1.1 | 1.2 | 1.3 | 0.7 | 0.8 | 0.9 | 1.0 | 1.0 | 1.1 |
| Mean | 0.5 | 0.6 | 0.7 | 0.8 | 0.8 | 0.9 | 0.5 | 0.6 | 0.7 | 0.8 | 0.9 | 0.9 |

## 5.3.3. Prediction accuracy comparisons

Table 5.4 compares prediction accuracies of the 4 different cases defined in Table 5.1. Relative mean RMSE values for the 29 patients are calculated with

respect to the largest mean RMSE values for each system delay and fraction. The largest mean RMSE values are obtained from Case 4, where no optimization is performed.

**Table 5.4 Relative mean RMSE values comparison**

| Case | Relative mean RMSE (2nd fraction) System delay (ms) | | | | | | Relative mean RMSE (3rd fraction) System delay (ms) | | | | | |
|---|---|---|---|---|---|---|---|---|---|---|---|---|
| | 120 | 200 | 280 | 360 | 440 | 520 | 120 | 200 | 280 | 360 | 440 | 520 |
| 1 | 0.4 | 0.5 | 0.5 | 0.6 | 0.6 | 0.7 | 0.5 | 0.5 | 0.6 | 0.6 | 0.7 | 0.7 |
| 2 | 0.5 | 0.6 | 0.6 | 0.6 | 0.7 | 0.7 | 0.5 | 0.6 | 0.6 | 0.6 | 0.7 | 0.7 |
| 3 | 0.9 | 0.9 | 0.9 | 0.9 | 0.9 | 0.9 | 0.9 | 0.9 | 0.9 | 0.9 | 0.9 | 0.9 |
| 4 | 1 | 1 | 1 | 1 | 1 | 1 | 1 | 1 | 1 | 1 | 1 | 1 |

By comparing the results between cases 1 and 4, a 30 - 60 % decrease in mean RMSE values is observed over the range of system delays tested. Both ANN structure and IW optimizations decrease prediction errors. Nevertheless, the comparison between cases 2 and 4 (more than 30 % decrease), as well as cases 3 and 4 (10 % decrease) show that ANN structure optimization performs a more important role in error reduction. Detailed results from each patient are plotted in Fig. 5.7.

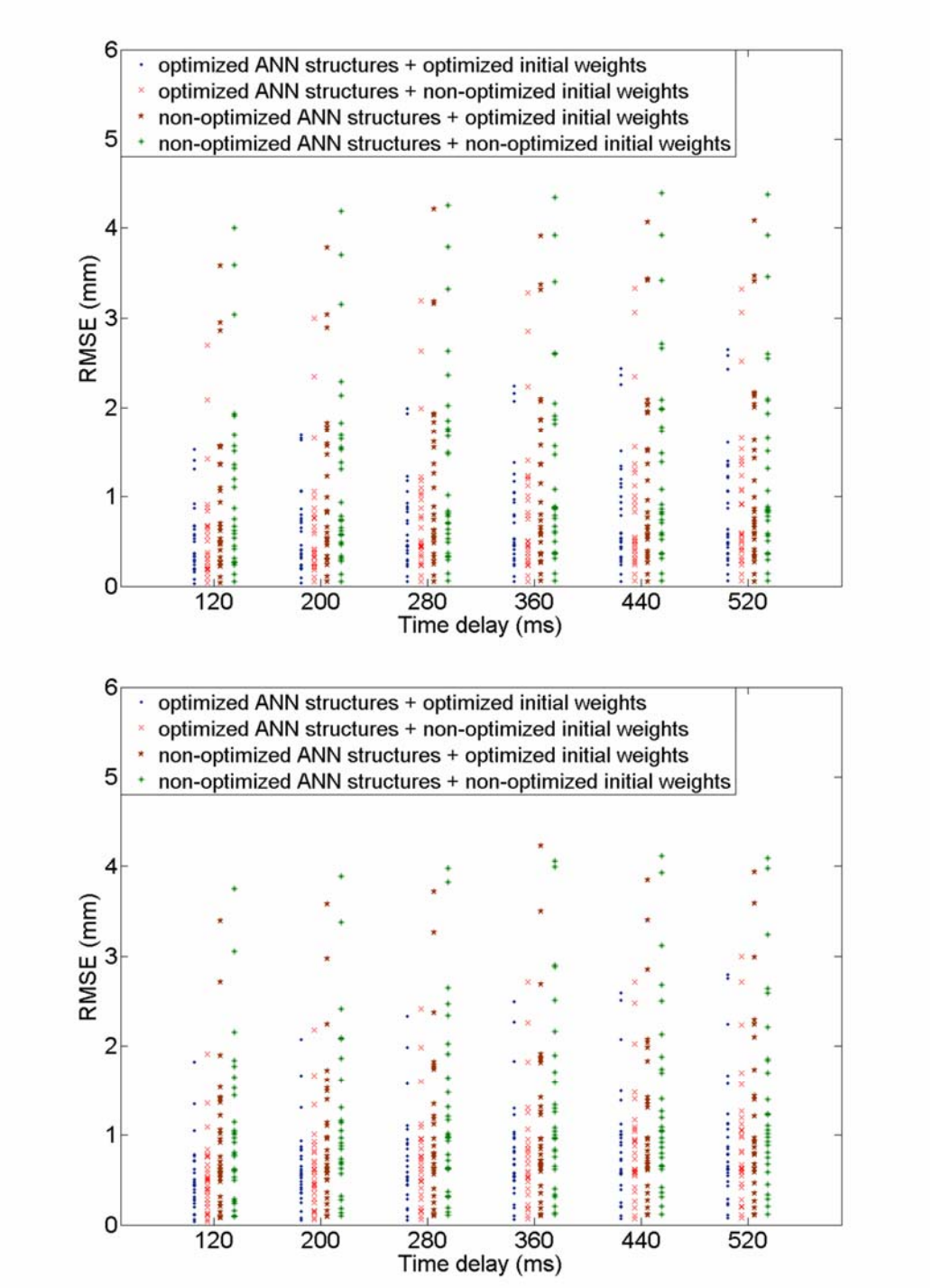


**Figure 5.7 Prediction accuracy comparisons in 4 different cases (top: 2nd fraction prediction, bottom: 3rd fraction prediction)**

Figure 5.8 shows the prediction accuracy of the 3rd fraction data using 2 different sets of ANN structure as: (1) ANN structures optimized to predict 3rd fraction data, and (2) ANN structures optimized to predict 2nd fraction data. Smaller RMSE values are observed in several patients using the ANN structures specifically optimized to predict the 3rd fraction. However, the mean RMSE values from all patients are the same for all system delays in both cases (0.5 - 0.9 mm).

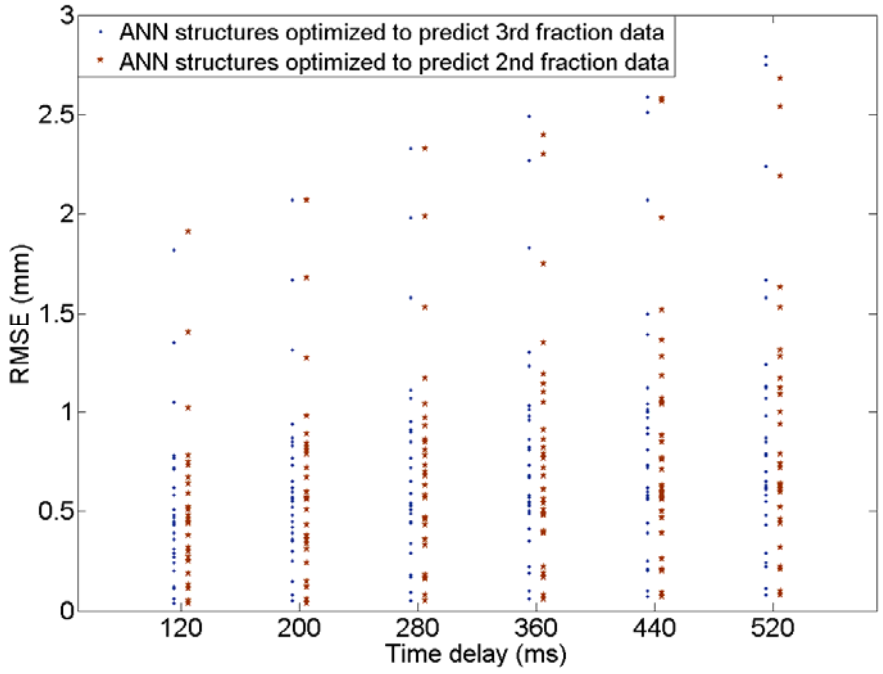


**Figure 5.8 Prediction accuracy of 3rd fraction data using (1) ANN structures optimized to predict 3rd fraction, and (2) ANN structures optimized to predict 2nd fraction**

## *5.4. DISCUSSION*

Superior performance of ANN in respiratory motion prediction over other methods has been reported by comparative studies,[13, 28] and several studies have been conducted in surrogates-based tumour tracking systems.[15, 16] However, we

believe this is the first study utilizing ANN for lung tumour motion prediction in an MRI-based tracking environment.

Real-time lung tumour tracking requires an MR imaging rate of 3 – 4 fps.[21] Currently, this rate cannot be achieved in 3D real-time imaging. However, we proved that 2D real-time MR imaging is feasible at 3.6 fps in our previous study (Dynamic Scan Time = 275 ms, FOV : 40 cm × 40 cm, 3.1 mm × 3.1 mm × 20 mm).[9] Using this, tumour motion data obtained from each MR image would generate good training data.

We have demonstrated the advantage of using multiple ANNs. The MR imaging rate is fixed at every 280 ms. The purpose of implementing multiple ANNs is to reduce the frequency of MLC failures during tumour tracking. The result shown in Table 5.2 clearly demonstrates the advantage of using seven ANNs over a single ANN. Using seven ANNs, MLC was always able to reach its set points, and the mean MLC-off time was decreased by a factor of more than 7.

Seven ANNs are chosen in this study to evaluate the accuracy of our predictor using the Suh *et al*.[22] data. However, in a real case, a larger or smaller number of ANNs can be easily implemented in a given tracking system depending on the expected MR imaging rate and the frequency of MLC motion triggering.

The advantage of optimizing ANN structures and IW for each patient has been investigated. There is a 30 – 60 % decrease of mean RMSE values if ANN structure and IW are optimized, in comparison to motion prediction using a single ANN structure and randomly chosen IW. This was obtained using seven ANNs of an identical structure. Because each of these ANNs corresponds to a different amount of system delay, it may be possible to further improve the prediction

accuracy if we optimize each ANN structure for its specific system delay. This will allow ANN structure changes among the seven ANNs, which will be a subject of future studies.

The entire optimization process for each treatment fraction of a given patient takes approximately 2.5 hours on the computer platform used, which would mandate calculations to be performed prior to treatment. Faster computers can, of course, be introduced for faster calculations.

The results shown in Fig. 5.8 suggest no significant advantage in prediction performance using fraction specific ANN structure optimization. This is based on the 3 consecutive fractions of motion data available in this study. However, further investigations are required with patient data obtained from a larger number of consecutive fractions.

As explained in Sec. 5.2.8.1, after every $7^{th}$ data point is chosen from the original tumour motion pattern, each motion pattern is shifted and normalized before it is presented to the ANN. This is clinically feasible as the characteristics of a given patient's lung tumour motion, such as the maximum amplitude and mean position, can be observed just before the beam delivery through the 2.5 minute training session as shown in Step 2 of Fig. 5.1. Thus, an appropriate amount of shifting and a proper normalization factor can be determined for each treatment fraction.

Moreover, this should be implemented as a safety feature for motion prediction using ANN, because the normalization factor can be used as an upper limit for future tumour positions. In our ANN design shown in Fig. 5.2, the output value must stay between 0 and 1. Therefore, the maximum future tumour position

that can be predicted by our ANN is restricted by the normalization factor, even if the ANN starts to diverge during treatment.

This study is focused on predicting 1D lung tumour motion in the SI direction. Lung tumours may, however, move up to 15 mm in anterior-posterior, and 10 mm in left-right directions during normal breathing.[4, 5] Therefore, predicting future tumour positions in a realistic 3D space is an important issue in intrafractional MR tumour tracking. Extension of our predictor to this matter will be very straightforward, and will be investigated in future studies.

## 5.5. CONCLUSION

A new ANN-based lung tumour motion predictor is developed for MRI-based intrafractional tumour tracking. The MR imaging rate was fixed at 280 ms. The predictive performance of the predictor was evaluated in its ability to predict tumour positions in 40 ms intervals that corresponded to the acquisition rate of independent test patient data (acquired every 40 ms) obtained elsewhere.[22]

Three practical issues regarding ANN implementation in MRI-based lung tumour tracking, namely (1) selecting proper ANN structures and IW, (2) reducing tracking failures, and (3) developing ANN training methods, are addressed in this study. The performance-accuracy of our predictor is evaluated with data from 29 lung cancer patients simulating clinically realistic situations.

Mean RMSE values of 0.5 – 0.9 mm (ranges 0.0 - 2.8 mm from 29 patients) are achieved by our predictor for system delays ranging from 120 – 520 ms. The advantage of using a patient specific ANN structure and IW optimizations is shown by the 30 - 60 % decrease in mean RMSE values in

motion prediction as compared to results achieved with a single ANN structure and randomly chosen IW. Also, the results suggest no significant advantage in prediction performance from a fraction specific ANN structure optimization.

## 5.6. REFERENCES


[1] M. B. Tacke, S. Nill, A. Krauss, and U. Oelfke, "Real-time tumor tracking: automatic compensation of target motion using the Siemens 160 MLC," Med. Phys. **37**(2), 753-761 (2010).

[2] A. Sawant, R. L. Smith, R. B. Venkat, L. Santanam, B. C. Cho, P. Poulsen, H. Cattell, L. J. Newell, P. Parikh, and P. J. Keall, "Toward Submillimeter Accuracy in the Management of Intrafraction Motion: the Integration of Real-Time Internal Position Monitoring and Multileaf Collimator Target Tracking," Int. J. Radiat. Oncol. Biol. Phys. **74**(2), 575-582 (2009).

[3] B. Cho, P. R. Poulsen, A. Sloutsky, A. Sawant, and P. J. Keall, "First Demonstration of Combined Kv/Mv Image-Guided Real-Time Dynamic Multileaf-Collimator Target Tracking," Int. J. Radiat. Oncol. Biol. Phys. **74**(3), 859-867 (2009).

[4] H. Shirato, Y. Seppenwoolde, K. Kitamura, R. Onimura, and S. Shimizu, "Intrafractional tumor motion: Lung and liver," Sem. Rad. Onc. **14**(1), 10-18 (2004).

[5] C. Plathow, C. Fink, S. Ley, M. Puderbach, M. Eichinger, I. Zuna, A. Schmahl, and H. U. Kauczor, "Measurement of tumor diameter-dependent mobility of lung tumors by dynamic MRI," Radiother. Oncol. **73**(3), 349-354 (2004).

[6] A. Krauss, S. Nill, M. Tacke, and U. Oelfke, "Electromagnetic Real-Time Tumor Position Monitoring and Dynamic Multileaf Collimator Tracking Using a Siemens 160 MLC: Geometric and Dosimetric Accuracy of an Integrated System," Int. J. Radiat. Oncol. Biol. Phys. **79**(2), 579-587 (2010).

[7] L. I. Cervino, J. Du, and S. B. Jiang, "MRI-guided tumor tracking in lung cancer radiotherapy," Phys. Med. Biol. **56**(13), 3773-3785 (2011).

[8] B. G. Fallone, B. Murray, S. Rathee, T. Stanescu, S. Steciw, S. Vidakovic, E. Blosser, and D. Tymofichuk, "First MR images obtained during megavoltage photon irradiation from a prototype integrated linac-MR system," Med. Phys. **36**(6), 2084-2088 (2009).

[9] J. Yun, E. Yip, K. Wachowicz, S. Rathee, M. Mackenzie, D. Robinson, and B. G. Fallone, "Evaluation of a lung tumor autocontouring algorithm for intrafractional tumor tracking using low-field MRI: A phantom study," Med. Phys. **39**(3), 1481-1494 (2012).

[10] J. Yun, M. MacKenzie, D. Robinson, S. Rathee, B. Murray, and B. G. Fallone, "Real-Time MR Tumour Tracking Using a Linac-MR System," presented at the 56th Annual Meeting of the COMP, Ottawa, ON, June 16-19, 2010.

[11] H. Shirato, K. Suzuki, G. C. Sharp, K. Fujita, R. Onimaru, M. Fujino, N. Kato, Y. Osaka, R. Kinoshita, H. Taguchi, S. Onodera, and K. Miyasaka, "Speed and amplitude of lung tumor motion precisely detected in four-dimensional setup and in real-time tumor-tracking radiotherapy," Int. J. Radiat. Oncol. Biol. Phys. **64**(4), 1229-1236 (2006).

[12] G. C. Sharp, S. B. Jiang, S. Shimizu, and H. Shirato, "Prediction of respiratory tumour motion for real-time image-guided radiotherapy," Phys. Med. Biol. **49**(3), 425-440 (2004).

[13] A. Krauss, S. Nill, and U. Oelfke, "The comparative performance of four respiratory motion predictors for real-time tumour tracking," Phys. Med. Biol. **56**(16), 5303-5317 (2011).

[14] P. S. Verma, H. M. Wu, M. P. Langer, I. J. Das, and G. Sandison, "Survey: Real-Time Tumor Motion Prediction for Image-Guided Radiation Treatment," Computing in Science & Engineering **13**(5), 24-35 (2011).

[15] J. H. Goodband, O. C. L. Haas, and J. A. Mills, "A comparison of neural network approaches for on-line prediction in IGRT," Med. Phys. **35**(3), 1113-1122 (2008).

[16] M. J. Murphy and D. Pokhrel, "Optimization of an adaptive neural network to predict breathing," Med. Phys. **36**(1), 40-47 (2009).

[17] H. R. Maier and G. C. Dandy, "The effect of internal parameters and geometry on the performance of back-propagation neural networks: an empirical study," Environmental Modelling & Software **13**(2), 193-209 (1998).

[18] L. F. A. Wessels and E. Barnard, "Avoiding false local minima by proper initialization of connections," IEEE Transactions on Neural Networks **3**(6), 899-905 (1992).

[19] C. Plathow, S. Ley, C. Fink, M. Puderbach, W. Hosch, A. Schmahl, J. Debus, and H. U. Kauczor, "Analysis of intrathoracic tumor mobility during whole breathing cycle by dynamic MRI," Int. J. Radiat. Oncol. Biol. Phys. **59**(4), 952-959 (2004).

[20] P. Yen, R. W. Katzberg, M. H. Buonocore, and J. Sonico, "Dynamic MR Imaging of the Temporomandibular Joint Using a Balanced Steady-State Free Precession Sequence at 3T," AJNR Am J Neuroradiol. **34**(3), E24-26 (2013).

[21] P. J. Keall, G. S. Mageras, J. M. Balter, R. S. Emery, K. M. Forster, S. B. Jiang, J. M. Kapatoes, D. A. Low, M. J. Murphy, B. R. Murray, C. R. Ramsey, M. B. Van Herk, S. S. Vedam, J. W. Wong, and E. Yorke, "The management of respiratory motion in radiation oncology report of AAPM Task Group 76," Med. Phys. **33**(10), 3874-3900 (2006).

[22] Y. Suh, S. Dieterich, B. Cho, and P. J. Keall, "An analysis of thoracic and abdominal tumour motion for stereotactic body radiotherapy patients," Phys. Med. Biol. **53**(13), 3623-3640 (2008).

[23] S. S. Haykin, *Neural networks : a comprehensive foundation*, 2nd ed. (Prentice Hall, Upper Saddle River, NJ, 1999).

[24] L. Behera, S. Kumar, and A. Patnaik, "A novel learning algorithm for feedforward networks using Lyapunov function approach," in Proceedings of International Conference on Intelligent Sensing and Information Processing, Chennai, India, Jan 4-7, 2004.

[25] J. Kennedy and R. Eberhart, "Particle swarm optimization," in Proceedings of the 1995 IEEE International Conference on Neural Networks, Perth, Australia, Nov. 27-Dec. 1, 1995.

[26] Y. H. Shi and R. Eberhart, "A modified particle swarm optimizer," in Proceedings of the 1998 IEEE International Conference on Evolutionary Computation, Anchorage, Alaska, May 4-9, 1998.

[27] Y. Tsunashima, T. Sakae, Y. Shioyama, K. Kagei, T. Terunuma, A. Nohtomi, and Y. Akine, "Correlation between the respiratory waveform measured using a respiratory sensor and 3D tumor motion in gated radiotherapy," Int. J. Radiat. Oncol. Biol. Phys. **60**(3), 951-958 (2004).

[28] M. J. Murphy and S. Dieterich, "Comparative performance of linear and nonlinear neural networks to predict irregular breathing," Phys. Med. Biol. **51**(22), 5903-5914 (2006).

# Chapter 6: Brushed permanent magnet DC MLC motor operation in an external magnetic field

*A version of this chapter has been published: J. Yun, J. St. Aubin, S. Rathee, and B. G. Fallone, "Brushed permanent magnet DC MLC motor operation in an external magnetic field," Med. Phys. **37**(5), 2131-2134 (2010).*

## *6.1. INTRODUCTION*

Linac-MR hybrid systems have been proposed[1, 2] as well as a cobalt-MR system[3] in order to achieve real-time image guided radiotherapy. Using the magnetic resonance (MR) imager to visualize the tumour and critical structure locations in real-time during treatment, a more conformal treatment can be delivered providing dose escalation at the tumour and greater normal tissue sparing. Delivery of the radiotherapy treatment will be performed with the use of multileaf collimators (MLCs), not only allowing the execution of intensity modulated radiotherapy (IMRT), but also enabling intrafractional tumour tracking.[4] Various motors have been created for use in strong magnetic fields such as MR environments,[5] but current Varian MLC technology uses brushed permanent magnet DC (BPMDC) motors. The close proximity of the MLCs to the MR imager can create artifacts in the MR imaging volume caused by RF noise from the BPMDC motors, as well as motor malfunction due to the large MR fringe fields. Our laboratory has shown that the negative effects of RF motor noise in MR images are mitigated through the use of appropriate RF shielding around

the motors as shown in Chapter 7 of this thesis.[6] Magnetic interference would be entirely eliminated with use of MR compatible motors.[5] In this chapter, however, we investigate the effect of external magnetic field on the functionality of BPMDC motors such as those used in Varian MLC systems. The fringe magnetic fields from a linac-MR hybrid system will intersect the motors at various angles depending on the installation geometry as well as on collimator rotation. This chapter presents a characterization of Varian MLC BPMDC motor operation at various orientations in external magnetic fields.

## 6.2. MATERIALS AND METHODS

The motors were placed in the magnetic field of an EEV M4261 electromagnet (Chelmsford, England) capable of generating magnetic fields up to 2000 G and the field strengths were measured using a SENIS GmbH (Zurich, Switzerland) three-axis magnetic field transducer. The BPMDC motors investigated were a MicroMo Electronics (Clearwater, FL) 20 V carriage motor, a MicroMo Electronics 24 V leaf motor used with Varian (Palo Alto, CA) 52 leaf MKII MLC systems, as well as Maxon Motor (Sachseln, Switzerland) 12 V half leaf and 12 V full leaf motors used with Varian 120 leaf Millennium MLC systems. The motors were assemblies consisting of a magnetic encoder for positional and speed information, the permanent magnet motor itself, and a gearbox. All the motors were tested in three orientations with the permanent magnet poles of the motors aligned 1) parallel to the electromagnet poles, 2) antiparallel to the electromagnet poles, and 3) perpendicular to the electromagnet poles. The one exception is for the carriage motor, which was too large to place its

permanent magnet poles perpendicular to the poles of the electromagnet, so no experiment was possible in this configuration. The three orientations mentioned above were investigated due to the MLC motor orientations with respect to the fringe magnetic fields of our biplanar MR magnet (Fig. 6.1). At a 0° collimator rotation, the magnetic fringe field will be aligned either parallel or antiparallel to the poles of the motors, while at a 90° collimator rotation, the magnetic fringe field will be perpendicular to the poles of the motors. Since our MR imager and linac rotate in unison,[1] the change in motor orientation with respect to the fringe field is solely caused by collimator rotation. It is expected that even the alternate linac-MR or cobalt-MR designs proposed,[2, 3] which incorporate a collimator rotation, will have their MLC motors exposed to magnetic fringe fields in the directions being investigated. Due to axisymmetry of the magnets used in the other proposed designs, the fringe fields at the MLC are not expected to change upon azimuthal rotation of the treatment gantry with respect to the magnet.

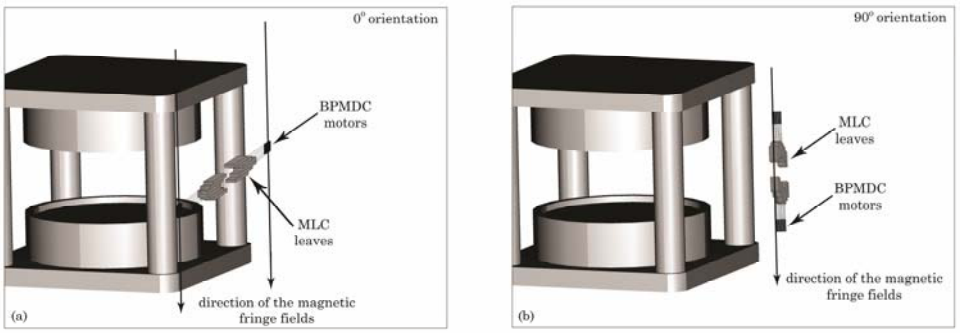


**Figure 6.1 (a) MLC and magnetic fringe field orientation for a 0° collimator rotation. The poles of the permanent magnet are aligned either parallel or antiparallel to the bi-planar magnet poles in this orientation. (b) MLC and magnetic fringe field orientation for a 90° collimator rotation. The poles of the permanent magnet are aligned perpendicular to the bi-planar magnet poles in this orientation.**

The motors were operated continuously for a minute both in the forward and reverse directions for each external magnetic field strength. The motors were driven in magnetic fields of increasing strength until any one component of the motor (encoder, permanent magnet motor, or gearbox) failed, at which point the entire motor was considered to have failed. An encoder failure was established when its output motor speed differed from an independent optical tachometer. Permanent motor failure would indicate that more than the maximum manufacturer specified current was drawn. Excessive mechanical noise and wear was considered as gearbox failure. The motor characterization consisted of measuring motor speed in revolutions per minute (RPM) and current (mA) as the magnetic field strength increased. The changes in motor speed and current from those with no applied external field were measured as a function of external magnetic field strength. Two fixed loading scenarios were used when testing the motors: Motors' self-load due to friction and gear box (i.e., no external load) and an equivalent external load to what the motors would experience in clinical use (i.e., clinical load). The clinical load was measured to cause an increase of 5 – 10 mA in current drawn by the motors when driving a MLC leaf. All motors were driven using a variable voltage DC power supply. The motor speed was read from the motor's encoder using National Instruments (Austin, TX) MID-7654 4 axis servo motor driver integrated with their LABVIEW 8.5 software, and verified with a model 1726 Ametek digital optical tachometer (Largo, FL). Lastly, the current was read from a Uni-Trend Group Ltd. (Kwun Tong, Hong Kong) UT55 digital multimeter.

## 6.3. RESULTS AND DISCUSSION

In all orientations, with one exception, the magnetic encoder failed before the motor or gearbox when exposed to an external magnetic field. The field at which the encoder failed for each motor depended on the components, sensitivity, and orientation of the encoder in the external magnetic field. In every case, failure of the encoder arose when the external field strength was large enough to saturate the Hall sensor of the encoder used for measuring the change in magnetic field as the armature rotated. The motor and gearbox assembly showed no increase in temperature above the manufacturer's set limits (< 85 °C) as they were cool to the touch, nor did the current exceed the manufacturer's set limits in fields of up to 2000 G. The one exception where the permanent magnet motor itself failed before the encoder was the Maxon Motor 12 V full leaf MLC motor, which was unable to maintain a consistent speed at 1500 ± 10 G with its poles perpendicular to the electromagnet poles.

Considering that in normal operation the collimator can rotate the MLCs ± 90°, the minimum field strength at which the encoder fails between the parallel/antiparallel orientations and the perpendicular orientation sets the limit before motor failure. For example, in the case of the 24 V MicroMo Electronics leaf motor, the encoder worked at a field of no greater than 450 G when its poles were perpendicular to the electromagnet poles. A ± 90° rotation would place its poles in either a parallel or antiparallel orientation where the motor could sustain up to 800 G without encoder failure. However, the limit on this motor is 450 G set by the perpendicular pole orientation since the motor must operate clinically in

either orientation. Table 6.1 illustrates the changes in current and motor speed for the maximum field strength after which the encoder failed.

**Table 6.1 The maximum magnetic field strength the motors could sustain before failure is given together with the change in current and motor speed (in RPM) for each orientation tested.**

| | 0 G | | Field strength (±10 G) | Parallel pole alignment | | Antiparallel pole alignment | | Perpendicular pole alignment | |
|---|---|---|---|---|---|---|---|---|---|
| | RPM | Current (mA) | | ΔRPM | ΔCurrent (mA) | ΔRPM | ΔCurrent (mA) | ΔRPM | ΔCurrent (mA) |
| 24 V leaf motor | 982 | 4.7 | 450 | 29±2 | 1.4±0.4 | -14±2 | 0.7±0.4 | 32±2 | 1.6±0.4 |
| 20 V carriage motor | 148 | 0.8 $x10^2$ | 2000 | 79±2 | 1.0±0.1 $x10^2$ | 4±2 | 0.3±0.1 $x10^2$ | N/A | N/A |
| 12 V half leaf motor | 672 | 4.8 | 700 | 56±2 | 0.6±0.4 | -15±2 | 0±1 | 63±2 | 11.2±0.4 |
| 12 V full leaf motor | 614 | 18.0 | 600 | 45±2 | 4±1 | -2±2 | 0±2 | 39±2 | 35±1 |

The results of the motor characterization in terms of changes in current and motor speed are presented in Figs. 6.2 and 6.3 for the 24 V leaf motor and MicroMo Electronics 20 V carriage motor, respectively, while the results for the Maxon Motor 12 V half leaf and full leaf motors are given in Figs. 6.4 and 6.5, respectively. The results were identical within measurement error when the motors were run in forward or reverse directions, and the motors showed no sign of difficulty reversing direction in any magnetic field strength or orientation studied. The changes in motor speed and current were found to be identical in the clinical load or no-load experiments due to the relatively small loading of the MLC leaves. The trends seen in Figs. 6.2 – 6.5 are the result of a complicated interaction between the changes in backward electromotive force generated by the

armature rotation and increases in mechanical and magnetic losses with increases in motor speed.

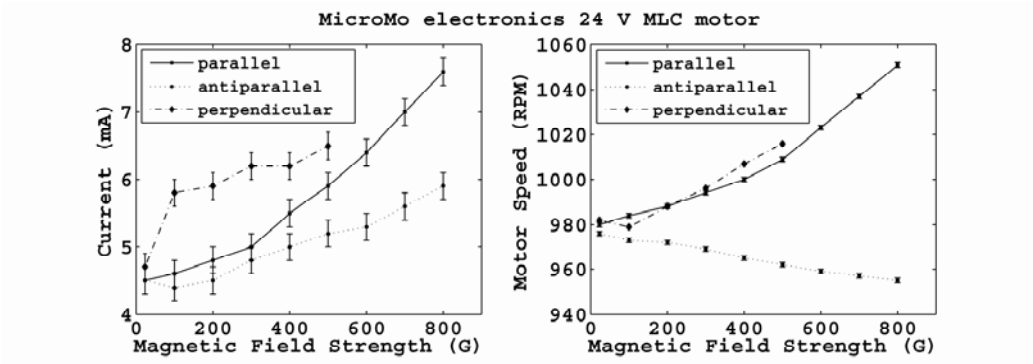


**Figure 6.2 The changes in current and motor speed are given for the MicroMo electronics 24 V MLC leaf motor.**

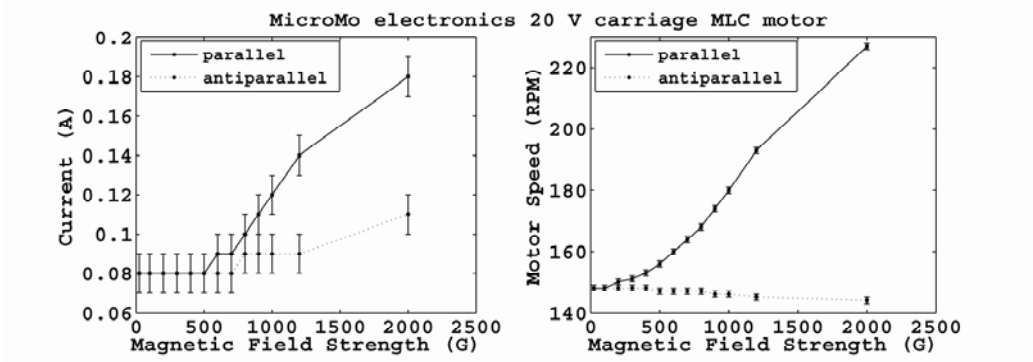


**Figure 6.3 The changes in current and motor speed are given for the MicroMo Electronics 20 V MLC carriage motor. The motor was larger than the bore of the electromagnet in the perpendicular orientation, so no data were obtained.**

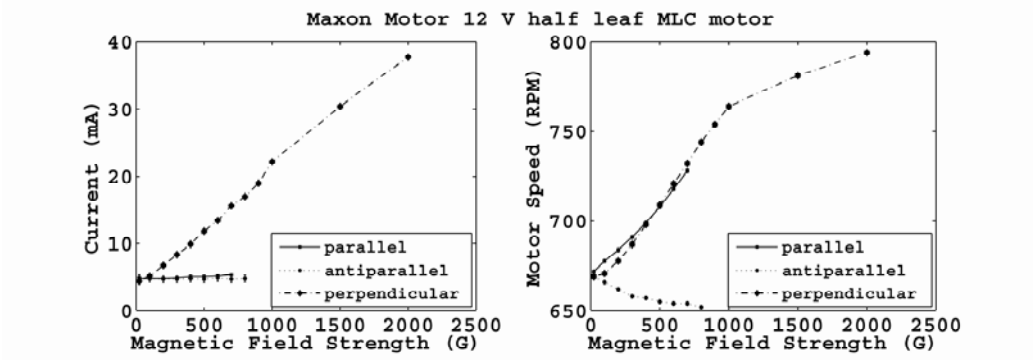


**Figure 6.4 The changes in current and motor speed are given for the Maxon Motor 12 V half leaf MLC motor.**

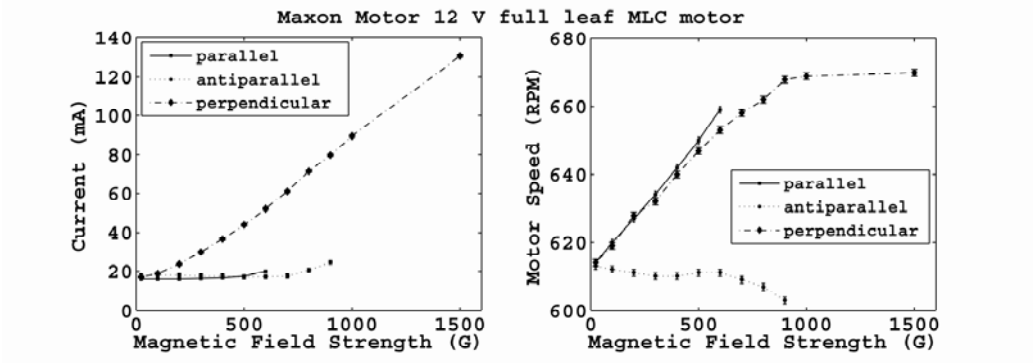


**Figure 6.5 The changes in current and motor speed are given for the Maxon Motor 12 V full leaf MLC motor.**

Any changes in motor speed would translate into an increasing or decreasing leaf speed. For example, from Table 6.1, the maximum increase of 63 ± 2 RPM was observed for the 12 V half leaf motor which would translate into a 0.121 ± 0.004 cm/s increase in leaf speed. In the antiparallel direction, a reduction of 15 ± 2 RPM was observed translating into a 0.029 ± 0.004 cm/ s reduction in leaf speed. The Millennium MLC system, together with Varian ECLIPSE treatment planning software, typically uses a maximum projected leaf speed of 2.5 cm/s at isocenter, which translates into speed of around 1.3 cm/s at the carriage. It has also been shown that the motors are in fact able to drive the leaves with a projected speed of around 3.5 cm/s at isocenter,[7] which translates into a leaf speed of around 1.8 cm/s at the carriage. Current MLC motor driver boards monitor each motor position individually through the encoder, and modify each leaf position individually over time, maintaining a 1.3 cm/s motor speed as well as accounting for motor to motor variability due to manufacturing differences and wear. Thus, changes in leaf speed quoted above caused by an external magnetic field would likely still be compensated by the MLC motor driver board.

As the carriage motors and MLC leaf motors work together, the allowable magnetic field in which the MLC system as a whole can operate is limited by the motor with the lowest tolerance. This means that for the Millennium MLC system, the full leaf motor's field strength limit of 600 G restricts the entire system's operating limit. Therefore, when a linac-MR system is designed, if the fringe magnetic fields at the location of the Millennium MLC system is greater than 600 G, appropriate magnetic shielding would be required. The largest expected fringe field strength at the MLC motors due to a large scale 0.2 T biplanar magnet is 1300 G. Preliminary investigations have shown that simple passive shielding can be designed to reduce the fringe fields from 1300 to below 600 G without altering the magnetic field homogeneity in the imaging volume beyond shimmable limits. However, detailed magnetic shielding design is beyond the scope of this work. The strength of the magnetic fringe field at the location of the MLCs for other magnets depends on the strength of magnetic field generated, their geometry, as well as their active shielding, but it is expected that the MLC BPMDC motors can still be shielded to less than 600 G. By incorporating the previously determined requirement for RF shielding,[6] and using appropriately designed magnetic shielding to ensure the BPMDC motors are not subjected to a magnetic field larger than the determined tolerances, current off-the-shelf Varian MLC systems can be used in a linac-MR system.

## 6.4. CONCLUSIONS

Four different BPMDC motors used in Varian MLC systems were tested in magnetic fields of increasing strength at various orientations to determine an operational limit for each motor. No increase in temperature or current over the manufacturer's tolerances was observed for field strengths up to 2000 G. The magnetic encoder was observed to fail before the permanent magnet motor or gearbox which set the magnetic field tolerance of the whole motor assembly. Thus, currently manufactured Varian MLC systems using the BPMDC motors tested could be used with linac-MR systems to provide intrafractional tumour tracking, provided the necessary steps are taken to ensure the motor RF noise is shielded and the motors operate in a magnetic environment whose intensity is below their field strength tolerances.

## 6.5. REFERENCES


[1] B. G. Fallone, B. Murray, S. Rathee, T. Stanescu, S. Steciw, S. Vidakovic, E. Blosser, and D. Tymofichuk, "First MR images obtained during megavoltage photon irradiation from a prototype integrated linac-MR system," Med. Phys. **36**(6), 2084-2088 (2009).

[2] B. W. Raaymakers, J. J. Wlagendijk, J. Overweg, J. G. M. Kok, A. J. E. Raaijmakers, E. M. Kerkhof, R. W. van der Put, I. Meijsing, S. P. M. Crijns, F. Benedosso, M. van Vulpen, C. H. W. de Graaff, J. Allen, and K. J. Brown, "Integrating a 1.5 T MRI scanner with a 6 MV accelerator: proof of concept," Phys. Med. Biol. **54**(12), N229-N237 (2009).

[3] J. F. Dempsey, D. Benoit, J. R. Fitzsimmons, A. Haghighat, J. G. Li, D. A. Low, S. Mutic, J. R. Palta, H. E. Romeijn, and G. E. Sjoden, "A device for realtime 3D image-guided IMRT," Int. J. Radiat. Oncol. Biol. Phys. **63**(2), 1095 (2005).

[4] B. Cho, P. R. Poulsen, A. Sloutsky, A. Sawant, and P. J. Keall, "First Demonstration of Combined Kv/Mv Image-Guided Real-Time Dynamic Multileaf-Collimator Target Tracking," Int. J. Radiat. Oncol. Biol. Phys. **74**(3), 859-867 (2009).

[5] R. Gassert, A. Yamamoto, D. Chapuis, L. Dovat, H. Bleuler, and E. Burdet, "Actuation Methods for Applications in MR Environments," Concepts in Magnetic Resonance Part B: Magnetic Resonance Engineering **29B**(4), 191-209 (2006).

[6] M. Lamey, J. Yun, S. Rathee, and B. G. Fallone, "Radio frequency noise from an MLC: a feasibility study of the use of an MLC for linac-MR systems," Phys. Med. Biol. **55**(4), 981-994 (2010).

[7] K. Wijesooriya, C. Bartee, J. V. Siebers, S. S. Vedam, and P. J. Keall, "Determination of maximum leaf velocity and acceleration of a dynamic multileaf collimator: Implications for 4D radiotherapy," Med. Phys. **32**(4), 932-941 (2005).

# Chapter 7: Radio frequency noise from an MLC: a feasibility study of the use of an MLC for linac-MR systems

*A version of this chapter has been published: M. Lamey, J. Yun, S. Rathee, and B. G. Fallone, "Radio frequency noise from an MLC: a feasibility study of the use of an MLC for linac-MR systems," Phys. Med. Biol.* ***55****(4), 981-994 (2010).*

## *7.1. INTRODUCTION*

A problem encountered in fractionated radiotherapy is the day-to-day patient set-up error and internal organ movement during treatment.[1-4] Image-guided radiotherapy (IGRT) aims to reduce dose to normal tissue surrounding tumours by reducing the margins needed to account for organ motion, thereby minimizing potential side effects of radiotherapy. IGRT is not a new concept; considerable work has been and is currently being pursued to develop imaging systems to guide radiotherapy.[5, 6] The next significant step toward improving tumour-normal tissue delineation involves the use of real-time imaging during radiotherapy treatment. The use of magnetic resonance (MR) images with exquisite soft tissue contrast will enable reductions in the irradiated normal tissue volume around the cancerous tissue. Several groups are currently working on integrating MR imaging with a megavoltage teletherapy unit.[7-10] Our group at the Cross Cancer Institute in Edmonton, Alberta, Canada, has successfully integrated a 0.22 T MR with a linear accelerator (linac-MR). The linac produces a 6 MV

photon beam irradiating objects located inside the 0.22 T bi-planar MR magnet through one of its openings. The goal of our linac-MR project is to enable acquisition of MR images of the patient prior to and during irradiation.

Recently, we have reported on the radio frequency (RF) emissions from medical linear accelerators.[11] Due to the deleterious effects of the extraneous RF noise on MR imaging systems, all possible RF sources in a linac-MR system must be investigated. It is common practice to use multi-leaf collimators (MLC) for conformal or intensity-modulated radiotherapy (IMRT) to shape dose distribution around the target volume. Several groups are actively studying the use of an MLC for real-time tumour tracking and the effects of MLC movement during radiotherapy.[12-17] It is well known that the DC motors which drive the MLC leaves can produce RF noise.[18, 19] Incorporation of an MLC into a linac-MR system could create magnetic and RF interferences; these possible interferences must be studied.

This investigation reports on the results of the study on the RF interference mentioned above. Using commercially available electric (*E*) and magnetic (*H*) field probes, the frequency spectrum of the RF noise from functioning MLC motors was measured as a function of the magnetic field applied to the motors (this chapter uses the convention of *H* when referring to magnetic field strength and *B* when referring to the magnetic field). In addition, MR images of a phantom were acquired with our linac-MR system in order to study the effect of RF noise produced by the motors driving MLC leaves on the signal-to-noise ratio (SNR) and difference maps of the MR images.

## 7.2. THEORY

The measured RF noise from moving MLC leaves is presented as an RF power spectral density after subtracting background levels. Time domain signals from the *E* and *H* field probes were used to obtain measured spectral density, *M(f),* in each case as follows.

$$M(f) = \sqrt{\frac{\sum_{i=1}^{N} |DFT(f)_i|^2}{N}} \qquad \textbf{(Eq. 7.1)}$$

where $DFT_i(f)$ is the discrete Fourier transform of one time domain acquisition, and N is the number of averages used in the estimation of *M(f)*.

The measured values, *M(f)*, from the *E* and *H* probes are related to the corresponding field strengths by applying a performance factor *PF(f)*. For example, the *E* field is related to the measurement as follows.

$$E = M(f) \cdot PF(f) \qquad \textbf{(Eq. 7.2)}$$

Substitute *H* for *E* in Eq. 7.2 for the *H* field. A thorough analysis of the performance factors for the near field probes can be found in Burke *et al*.[11] The approximate power spectral density (*P*) of the RF noise was then calculated using the following formula:

$$P_{upper} = \frac{E \cdot H}{2} \qquad \textbf{(Eq. 7.3)}$$

The use of this equation provides an upper limit to the measured power. The background levels were subtracted from the measured power with the MLC moving:

$$P = PF_E(f) \cdot PF_H(f)[M_E(f) \cdot M_H(f) - M_{Eb}(f) \cdot M_{Hb}(f)]/2 \quad \textbf{(Eq. 7.4)}$$

where the individual subscripts refer to the *E* or *H* fields, and the subscripts *Eb* and *Hb* refer to the measured background fields. The variance of the *E* or *H* field is related to the variances in *M(f)* and *PF*(*f*). The variance on the background subtracted power density, *P(f)*, increases with decreasing frequency as shown below. Due to the uncertainty of the performance factors we assign an error of 10% to them. Since 1000 averages were taken in estimating *M(f)*, the error in *M(f)* was determined to be negligible compared to the error in the performance factors. With the estimation of a 10% error in the performance factors and neglecting errors in *M(f)*, and using error propagation rules, it can be shown that the error in the power above background as a function of frequency is given by

$$\delta P(f) = 0.07 PF_E(f) PF_H(f)[M_E(f) M_H(f) - M_{Eb}(f) M_{Hb}(f)] \quad \textbf{(Eq. 7.5)}$$

Both *E* and *H* field performance factors increase as frequency decreases. Therefore, the variance on the power increases at lower frequencies.

We have investigated the emissions of RF noise from DC motors. Models of the emissions of RF noise from DC motors have been suggested. Suriano *et al.*[18] suggest a model which consists of a monopole antenna above a ground plane. When interpreting our data this model was adopted.

## 7.3. MATERIALS

An EEV M4261 electromagnet (now e2v, Chelmsford, England) with a DCS 33-33 (Sorensen, Azusa, CA, USA) power supply was used to produce a *B* field. The MLC motors were placed in the electromagnet poles thus subjecting the

MLC motors to the *B* field. The size of the electromagnet was such that approximately half of the motors of one side of the Varian 52-leaf MLC were in the field. With one motor driving one MLC leaf the *E* and *H* fields were measured using a near field HZ-11 probe set (Rohde and Schwarz, Munich, Germany). The *E* probe measures the total *E* field strength while the *H* probe was used to measure the three individual orthogonal components of the *H* field strength; these three components were added in quadrature to obtain the total *H* field strength. A 3M12-2-2-0.2T (Senis Gmbh, Zurich, Switzerland) Hall probe with a three-axis type C-H3A-E3D-1%-0.2T magnetic field transducer was used to measure the applied *B* field on the MLC motors under test. The RF noise from three motors was investigated: (1) a 24 V DC brushed motor used in a Varian 52-leaf MLC (Part: 886603-03, Micro MO Electronics, Clearwater, FL, USA), (2) a 24 V DC brushed motor used in a Varian 120 Millennium MLC (Part: 344516, Maxon Motor, Sachseln, Switzerland) and (3) a 48 V brushless DC fan motor (Part: 4712KL-07W-B30, NMB Technologies Corporation, Chatsworth, CA, USA). One thousand DFT averages were taken for each of the Varian 52-leaf, Varian Millennium and brushless fan motors. The field probes were used to measure the power spectral densities in the following cases: (1) the background RF without motor movement, (2) the RF noise due to functioning motors without an applied *B* field, (3) the RF noise produced by functioning motors subjected to 50, 100 or 500 Gauss *B* field and (4) the RF noise produced from 13 functioning Varian 52-leaf motors driving 13 MLC leaves as a function of distance from the MLC with no applied *B* field.

The motor drive board contains 26 H-Bridge chips, which were used to control all motors with a 400 W power supply (SMQ400PS24-C, XP Power, Haw Par Technocentre, Singapore). For real-time control of many motors (on/off, direction), a PCI-bus control module based on field programmable gate arrays was used (National Instruments, Austin, TX). To program and implement motion patterns of the MLC, LabVIEW v.8.5 (National Instruments, Austin, TX) was used.

In a separate investigation, MR images of a phantom were acquired with our 0.22 T linac-MR system.[7] One half of a Varian 52-leaf MLC was placed near the MR magnet and phantom images were acquired while 13 MLC leaves were moved. In one case, the MLC and the associated cables were non-shielded while in the other case the MLC and cables were shielded. The phantom was an acrylic rectangular cuboid (15.95 × 15.95 × 25.4 $mm^3$) with three holes of diameters 2.52, 3.45 and 4.78 mm drilled into it, inserted into a 22.5 mm diameter tube and filled with a 10 mM solution of CuSO4. The MR console is as described by Fallone *et al.*,[7] a TMX NRC (National Research Council of Canada, Institute of Biodiagnostics, Winnipeg, MB, Canada). The console software is based on Python programming language (Python Software Foundation, www.python.org), version 2.3.4, to allow the user full control of development and modification of pulse sequences. Analogic (Analogic Corporation, Peabody, MA) AN8295 gradient coil amplifiers and AN8110 3 kW RF power amplifiers are used in the TMX NRC system.

## 7.4. METHODS

The *E* and *H* field strengths were measured at distances perpendicular to the movement of the MLC leaves. The set-up used to measure the RF noise is shown in Fig. 7.1. This was done since the RF noise at the position of an MR coil is the quantity of interest. The time domain signal from the field probes was first amplified using a Rohde and Schwarz broadband preamplifier (model 7405-907BNL), and then transferred from the oscilloscope to a PC using a Keithley KUSB 488 GPIB interface (Keithley Instruments Inc., Cleveland, OH). The software program DADiSP (DSP Development Corporation, Newton, MA) was then used for calculating the *E* and *H* field spectral density, as per Eq. 7.1.

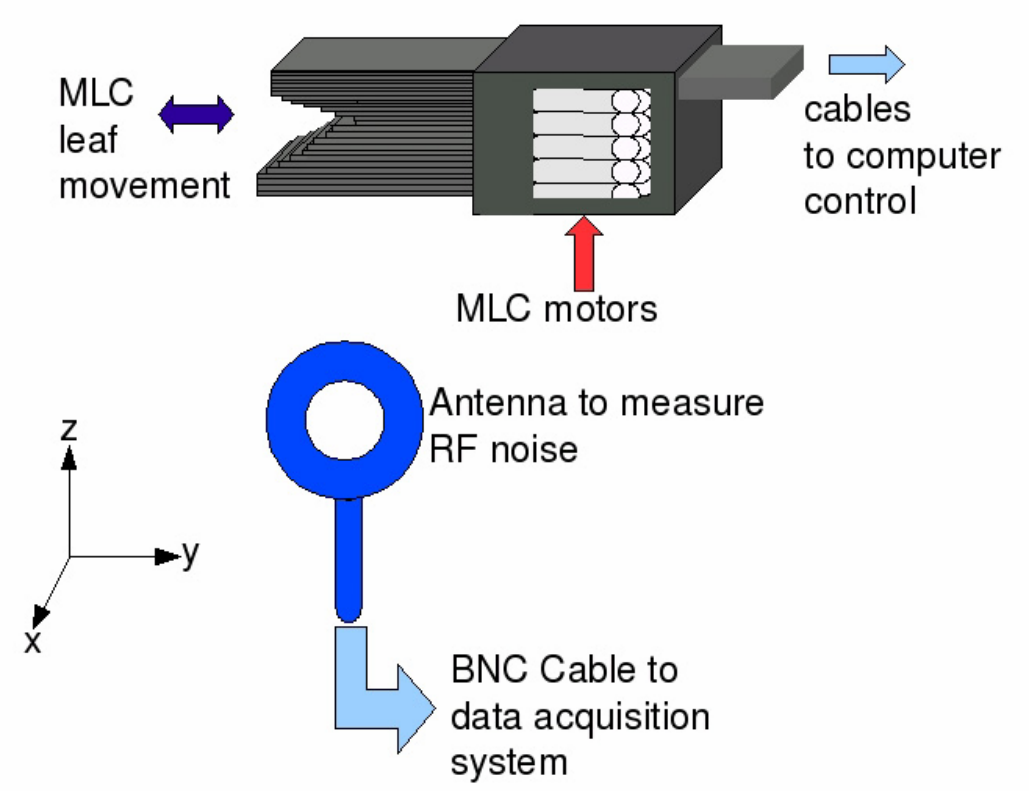


**Figure 7.1 Set-up used to measure the RF noise from a functioning MLC. A loop antenna was used to measure the individual magnetic field strength components while a 'ball' probe was used to measure the total electric field strength. Not shown is the electromagnet used when a *B* field was applied to the MLC motors.**

The resulting DFTs had bin widths of 50 kHz in the frequency domain. As mentioned previously, the number of signal averages in Eq. 7.1 was 1000 for each of the three motors investigated. The approximate power spectral density of the RF noise was then calculated using Eq. 7.3, which provides an upper limit to the measured power. The measured background power spectral density was subtracted from the RF power spectral density produced by functioning motors in each case. Two distinct power spectral density measurements were taken: (1) the RF noise from a single continuously functioning motor as a function of the applied *B* field at a distance of 50 cm and (2) the RF noise as a function of

distance from one half of a Varian 52-leaf system with 13 motors continuously moving at the distances of 50, 70 and 100 cm. For measurements near background, the standard deviation was estimated by measuring 20 background power spectrums, each of which was done with 1000 averages. The standard deviation of these background power spectrums at each frequency was then used as our estimate of the error.

The set-up used for the imaging study is shown in Fig. 7.2. Firstly, an MR image was acquired with the MLC not present. Secondly, MR images were taken with the MLC at a specific distance from the center of the magnet, first with the MLC static and then with 13 leaves moving. Images were acquired with the MLC plus cables unshielded and shielded.

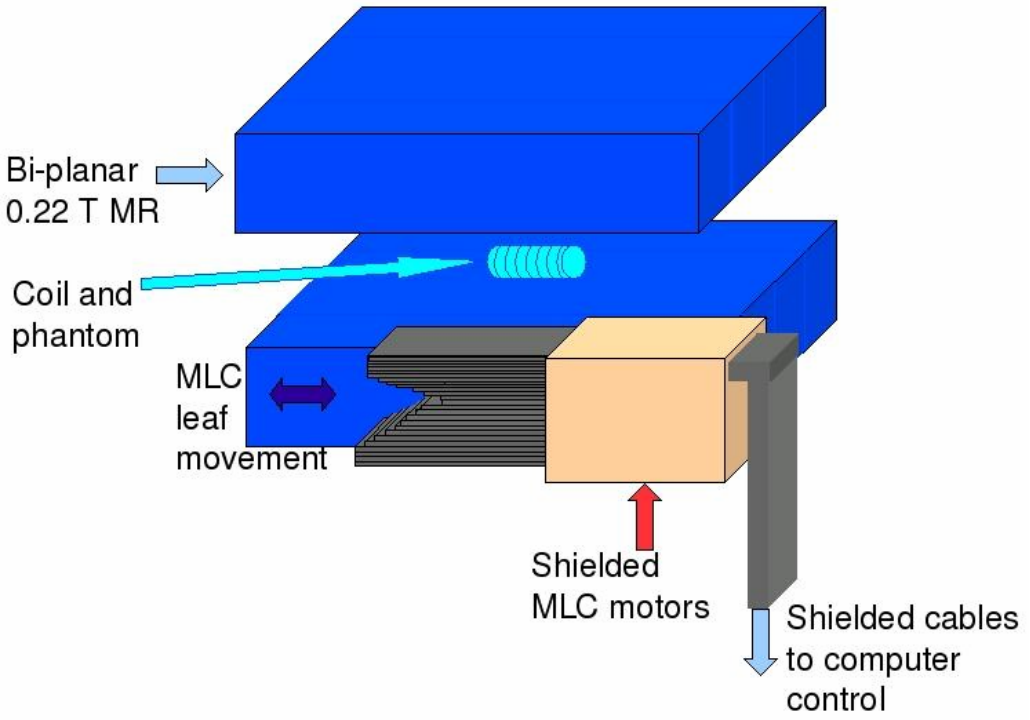


**Figure 7.2 Set-up used to acquire images of a phantom while 13 leaves of an MLC were moved continuously. Images were taken with the MLC leaves static and then moving as well as with the MLC motors and cables non-shielded and shielded.**

The shielding consisted of a copper box enclosing the motors used to drive the MLC leaves. A prototype rectangular MLC shielding box (8.75″ × 9.25″ × 4″) was fabricated which has five closed faces. Each face was manufactured using 0.02″ thick copper sheets. A small slit was cut out from one of the faces to allow the MLC control cables to pass into the copper box. The MLC was inserted into the copper box via the open face. After insertion, the open seams between the MLC and RF shielding box were sealed with conductive copper tape. The ribbon cables used to control movement of the motors were wrapped in aluminum foil. Any small holes or seams were covered over with conductive copper tape or filled with copper wool. In this experiment 13 MLC leaves were moved at a time from a Varian 52-leaf system. The MLC was placed on a stand such that the approximate height of the leaves and motors was the same as that of the coil used to image in the 0.22 T MR. Images with stationary MLC leaves investigated a possible magnetic effect from the presence of the MLC. The distances presented herein are those from the face of the MLC to the center of the MR coil, which was located approximately at the center of the MR magnet. Images were taken in four different orientations of MLC and imaging coil: (1) the MLC and coil oriented as shown in Fig. 7.2, (2) the coil as shown in Fig. 7.2 and the MLC leaves oriented vertically, (3) the MLC leaves oriented vertically, and the coil and phantom rotated 90° toward the MLC and (4) the MLC as shown in Fig. 7.2 and the coil and phantom rotated 90° toward the MLC. The following settings were used in a gradient echo MR imaging sequence; flip angle: 60°, slice width: 5 mm, acquisition size: 128 (read), 128 (phase encode), FOV: 50 × 50 $mm^2$, TR: 300 ms,

TE: 35 ms, 1 signal average. The resulting image quality or change in image quality was evaluated using the SNR and image subtraction (MLC leaves stationary to MLC leaves moving for the same orientation and distance). The SNR for each resulting image was calculated by taking the mean pixel intensity in a solution containing region inside the largest of the three holes in the phantom, divided by the standard deviation in a similar sized region of the noise near one of the corners of the image, thereby avoiding any possible artifact effects in the phase or read encode directions.

## 7.5. RESULTS

Figure 7.3 shows the measured RF noise by the *E* field probe in the time domain from a Millennium motor. The 'spike' shown is one of the larger spikes in both amplitude and duration.

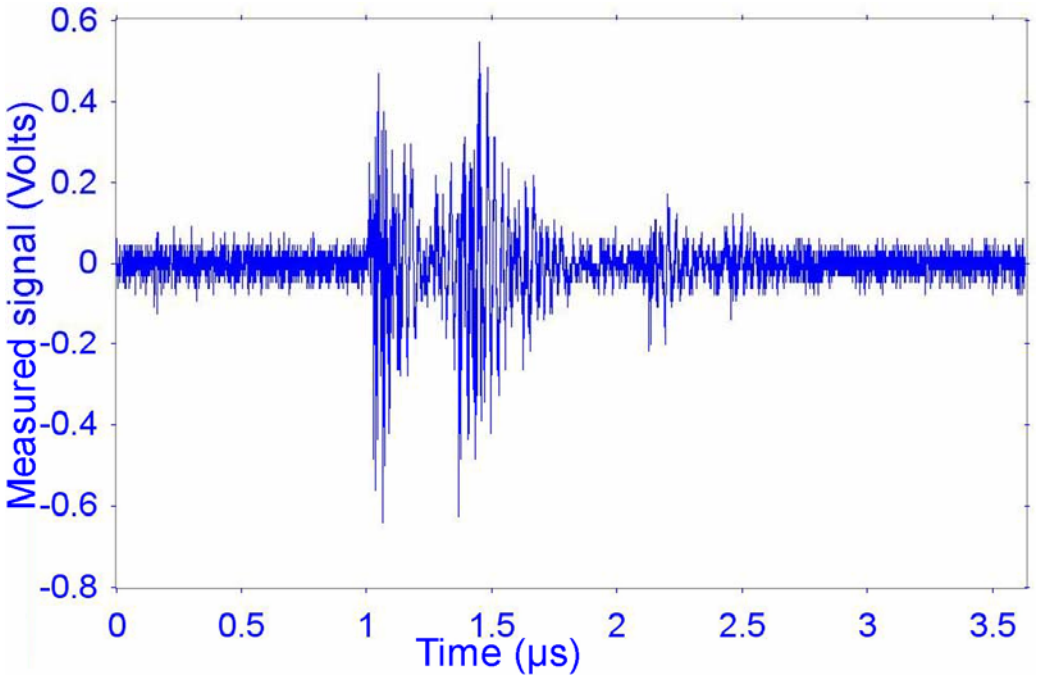


**Figure 7.3 One of the larger RF 'spikes' as measured by the *E* probe and broadband preamplifier from the Millennium MLC motor. These spikes were resolved by a time domain resolution of 0.5 ns. The measurement is taken in a clinical vault with the experimental set-up shown in Fig. 7.1.**

Figures 7.4 - 7.6 show the results of the RF power spectral density above background as a function of the applied *B* field for each of the three motors investigated at a measurement distance of 50 cm. Data have been shown in the frequency range 8 – 70 MHz, and these data are then useful for all linac-MR systems operating with an MR between 0.2 and 1.5 T.

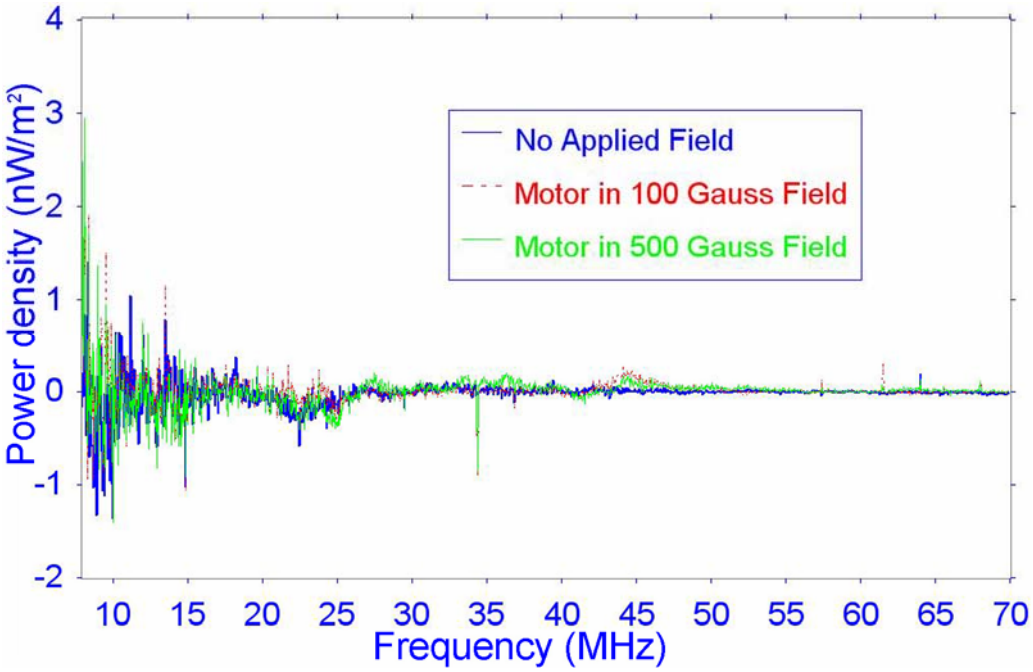


**Figure 7.4 Background subtracted RF noise power spectral density measured from a Varian 52-leaf MLC motor as a function of the applied magnetic field at 50 cm.**

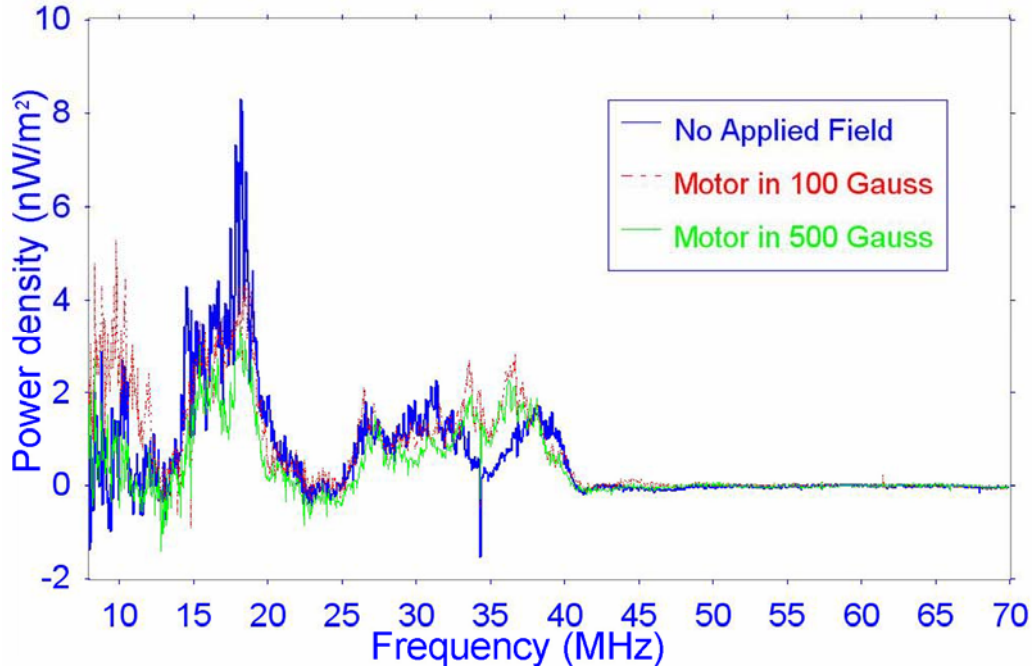


**Figure 7.5 Background subtracted RF power spectral density measured from a Millennium MLC motor as a function of the applied magnetic field at 50 cm.**

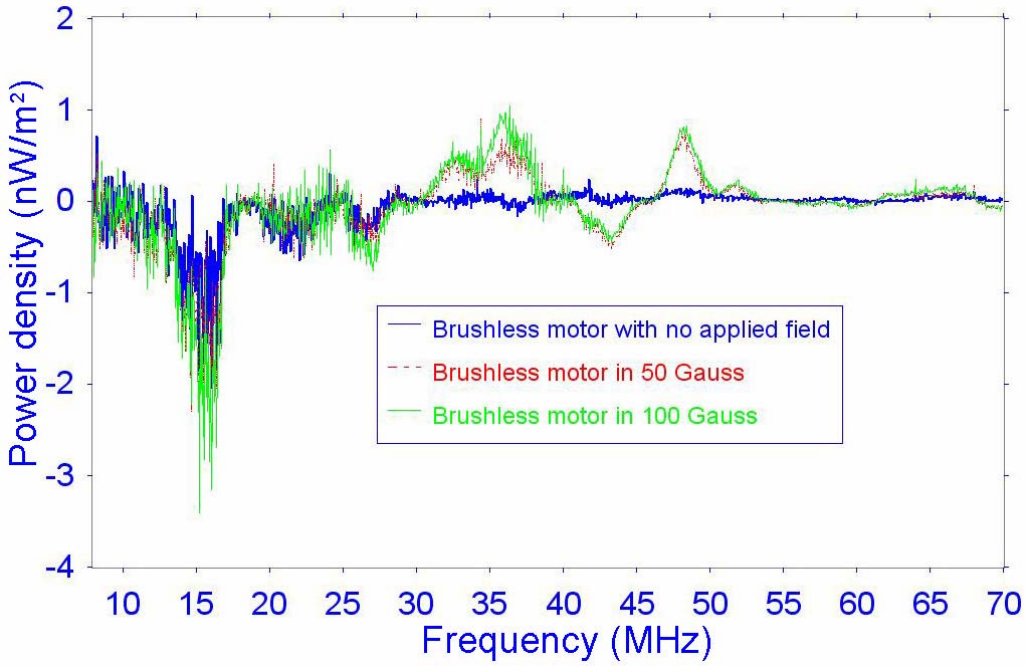


**Figure 7.6 Background subtracted RF power spectral density as measured from a brushless fan motor as a function of the applied magnetic field, 50 cm from the motor.**

Figure 7.7 shows the measured power spectral density from 13 motors driving 13 leaves from a Varian 52-leaf MLC at the distances of 50, 70 and 100 cm.

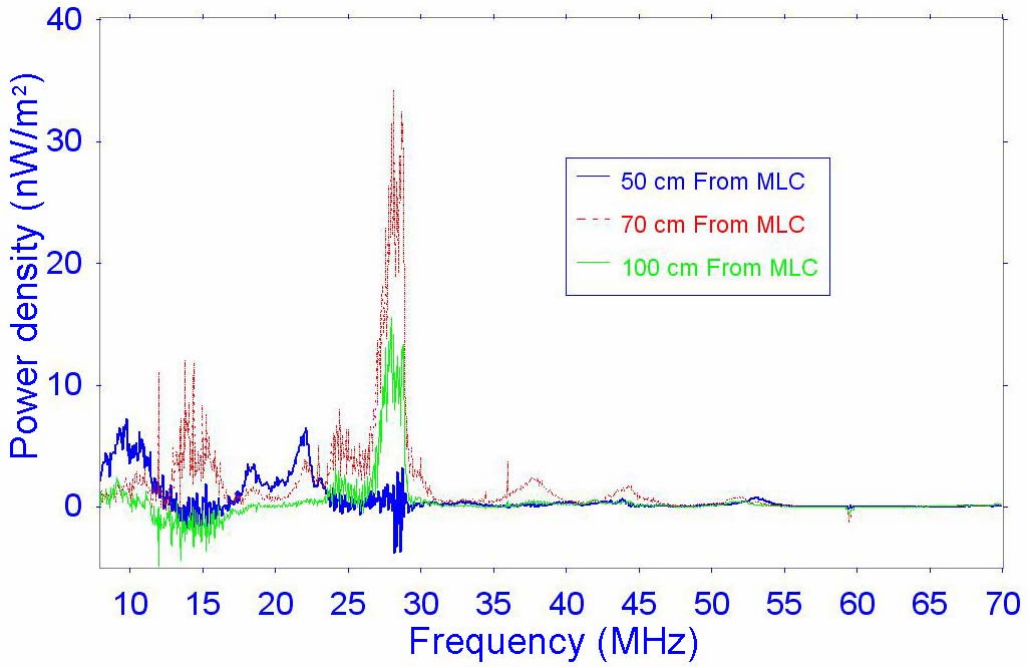


**Figure 7.7 Background subtracted RF power spectral density as a function of distance from a Varian 52-leaf MLC with 13 leaves moving. No magnetic field was applied to the motors in this case.**

Figure 7.8 shows the three individually measured Cartesian magnetic field strength components in the range 8 – 70 MHz, clearly showing that one component, *Hy*, of the measured field dominates. In this case 13 motors from one bank of the Varian 52-Leaf MLC were continuously moved. The Cartesian orientations with respect to the MLC are shown in Fig. 7.1; specifically *Hy* is along the same direction as the MLC leaf movement or the motor axis.

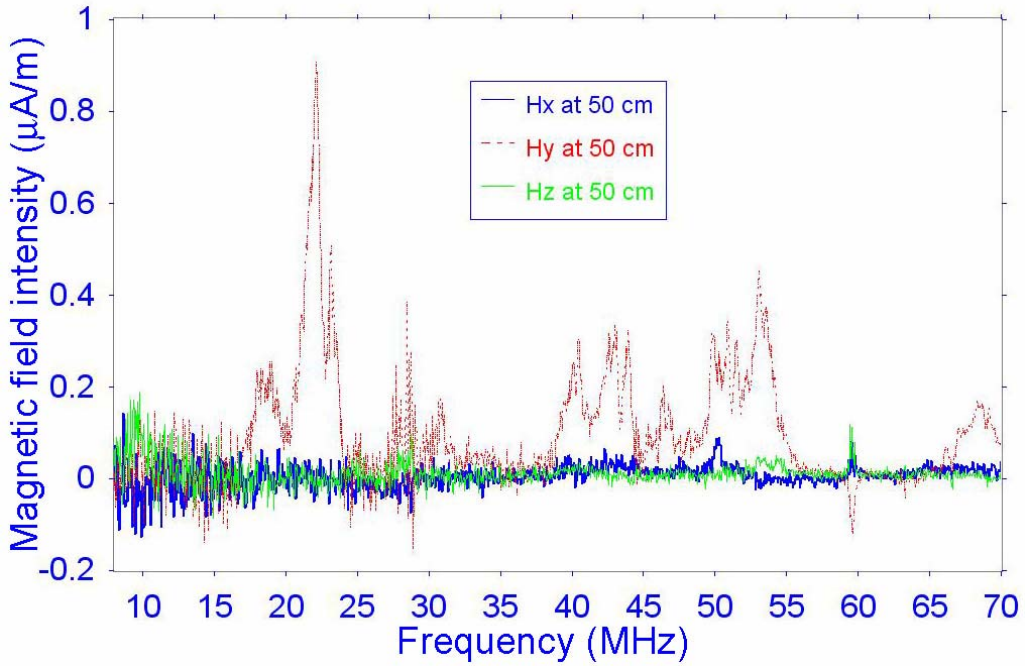


**Figure 7.8 Background subtracted individual Cartesian components of the magnetic field strength from the MLC, with 13 leaves moving. The Cartesian orientations with respect to the MLC orientation are shown in Fig. 7.1.**

The second part of the study involved imaging a phantom while 13 leaves of a Varian MLC system were moved (Fig. 7.2). Table 7.1 shows the results of the measured SNR for each of the previously described orientations used. For each orientation the SNR is shown with the MLC unshielded, leaves stationary and moving (columns 2 and 3), and then with the MLC shielded, leaves stationary and moving (columns 4 and 5).

**Table 7.1 SNRs of the image of a phantom with half of a Varian 52-leaf MLC brought near the MR. SNRs shown are for the MLC stationary and 13 MLC leaves moving both in the non-shielded and shielded cases.**

| Distance (cm) | No shielding | | With shielding | |
|---|---|---|---|---|
| | SNR MLC stationary | SNR MLC moving | SNR MLC stationary | SNR MLC moving |
| | | First orientation | | |
| 70 | 48 | 29 | 49 | 51 |
| 100 | 46 | 46 | 52 | 49 |
| | | Second orientation | | |
| 70 | 46 | 35 | 52 | 53 |
| 100 | 45 | 44 | 51 | 52 |
| | | Third orientation | | |
| 70 | 57 | 48 | 57 | 58 |
| 100 | 58 | 56 | 58 | 58 |
| | | Fourth orientation | | |
| 70 | 56 | 51 | 58 | 56 |
| 100 | 59 | 57 | 56 | 55 |

An acquired image in the second orientation (i.e. coil as in Fig. 7.2) with no MLC present is shown in Fig. 7.9.

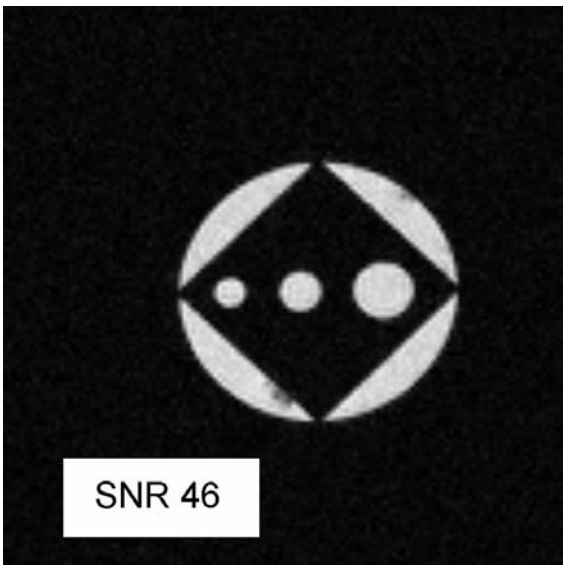


**Figure 7.9 MR image of a phantom acquired in the second orientation with the MLC away from the MRI.**

The acquired images with the MLC at 70 cm from the MR coil for each unshielded and shielded case in the second orientation are shown in Fig. 7.10.

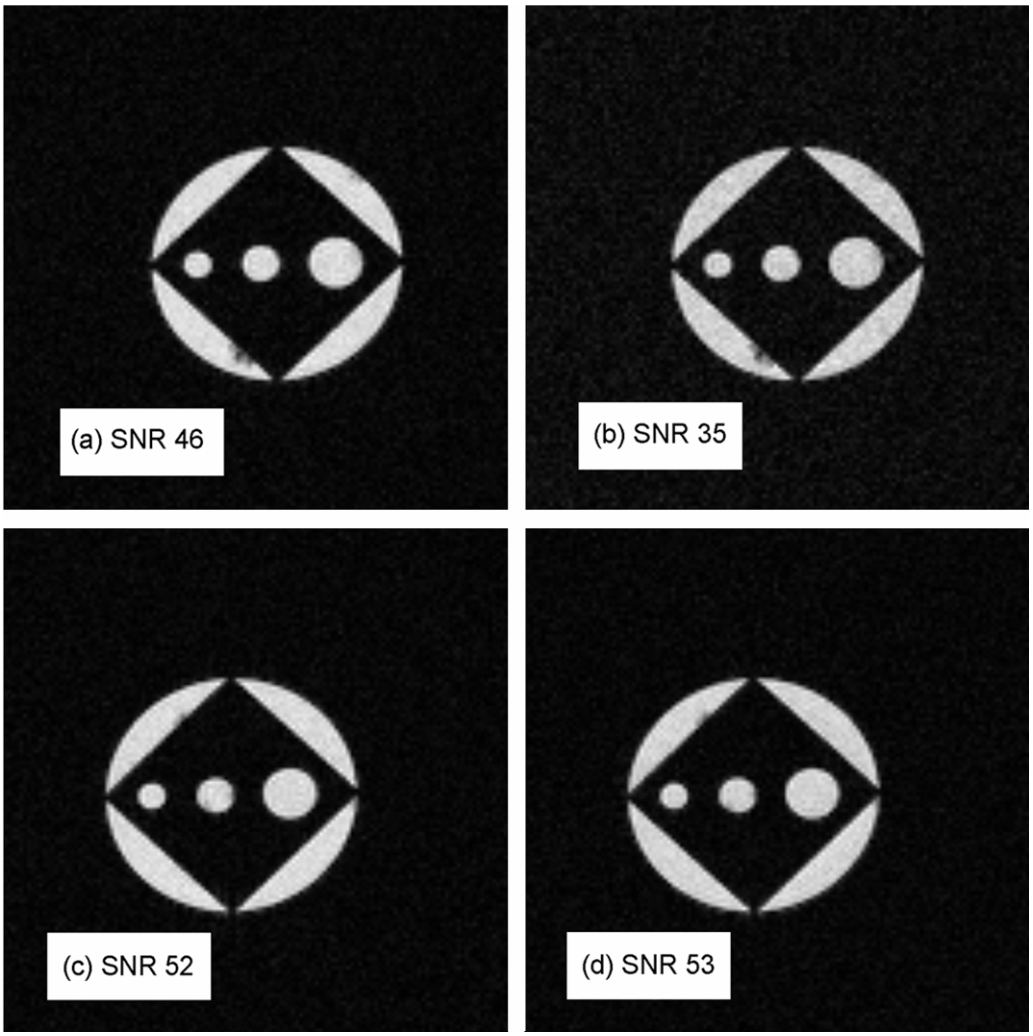


**Figure 7.10 Images at 70 cm obtained with the second orientation: (a) MLC unshielded and stationary, (b) MLC unshielded and 13 leaves moving, (c) MLC shielded and stationary and (d) MLC shielded and 13 leaves moving.**

Figure 7.11 shows the subtraction of Fig. 7.10.c and Fig. 7.10.d; this is the case where the MLC is shielded.

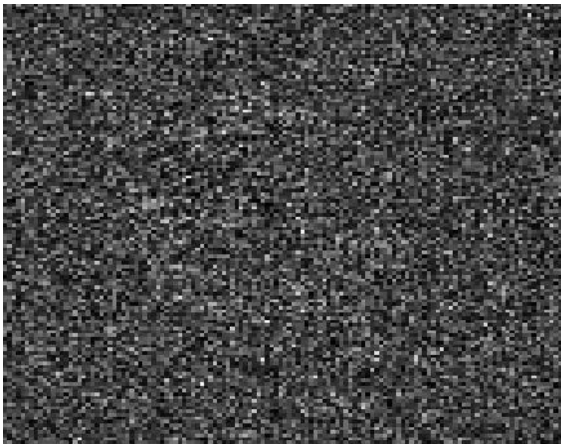

**Figure 7.11 Subtracted image with the MLC and phantom in the second orientation. The MLC and cables were shielded; Fig. 7.10.c and Fig. 7.10.d were used for the subtraction.**

Figures 7.9 and 7.10.a illustrate that no difference in the SNR was measurable when the MLC is located 70 cm from the MRI coil compared to when the MLC is not present or near the MRI.

In a separate investigation the SNR degradation of the MR image was determined by moving a different number of MLC leaves. With the MLC stationary and located at 70 cm from the MRI coil, we measured an SNR of 72 in the MR image. When 6, 12, 18 and 24 motors were moved at a time, the SNR in an acquired image dropped to 54, 42, 44 and 39 respectively. Several images were acquired for each scenario to determine the reproducibility of the measured SNR. Five images acquired with 12 motors operating produced SNRs within 42 ± 5. The SNR did not always decrease with increasing number of motors since some motors produced more noise than others. However, when 24 motors were shielded using the prototype box, no degradation in SNR compared to the stationary MLC was observed.

## 7.6. DISCUSSION

The use of an MLC during the radiotherapy process will be important for linac-MR systems, which can take advantage of real-time tumour imaging and tracking with dynamic MLC delivery. With the close proximity to an MR unit, the MLC leaves and the motors used to drive them will be placed in a magnetic field. The motors will also produce RF noise which can degrade image quality. The RF power spectral density was measured from three motors as a function of the applied magnetic field to the motors. In the time domain, we could see small spikes of measured noise when the MLC motors were running. These spikes were more prevalent for the Millennium MLC motors. The Millennium MLC motor also ran faster thus contributing to the increase in visible RF noise. The difference in motor speed was observed while the motors from millennium MLC and 52-leaf MLC drove the MLC leaves simultaneously. These small spikes seen in the time domain are a result of arcing between the brushes and commutator bars in the motors resulting in the production of broadband noise.[18] The spike shown in Fig. 7.3 lasts on the order of a few microseconds. However, generally these spikes were on the order of a hundredth to a few tenths of microseconds. No visible RF noise above background was seen in the time domain when the brushless fan motor was operating, although in the frequency domain a small amount is visible (Fig. 7.6).

Although small infrequent spikes were seen in the time domain for the Varian 52-leaf motor, no significant RF noise above background was seen in Fig. 7.4. For the Millennium MLC motor (Fig. 7.5), there is a small dependence on the

applied *B* field. In the frequency range 15 – 20 MHz, the RF power reduces for higher applied *B* field. No other systematic dependence can be seen. Above 40 MHz there seems to be no measured RF noise, and therefore our measurements indicate that little or no RF noise exists at the Larmor frequency for MR systems around or above 1 T. The function and RF noise production by a brushless fan was investigated since brushless motors produce less RF noise.[20] Above an applied field of 100 G the brushless fan motor showed both audible and visible (slower revolutions per minute) strain; therefore, no results above 100 G are shown for this motor. This noticeable strain was likely due to the reduced magnetic shielding around the fan motor as compared to that of the MLC motors used. Near 15 MHz and between 30 and 55 MHz there seemed to be a dependence on the applied *B* field. The authors are uncertain as to why the measured power density seems to dip below that of background around 15 MHz; this effect requires further investigation. When the RF noise from 13 motors from a Varian 52-leaf MLC was studied as a function of distance (Fig. 7.7), no clear dependence could be seen.

The increased noise in the measured RF noise power spectral density at lower frequencies in Figs. 7.4, 7.6, and 7.8 is a result of the increasing performance factor of both the *E* and *H* probes. The variance on the measured power spectral density is proportional to the product of the *E* and *H* antenna factors (as shown above); these factors increase as frequency decreases, therefore leading to larger variance at lower frequencies. Near the lower frequencies shown in Figs. 7.4 - 7.8, the background subtracted power spectral density dips below zero. This does not mean that the actual power is negative, which would be

unphysical; this occurred since we were trying to measure powers similar to that of the background power. Besides the small area near 15 MHz in Fig. 7.6, the data illustrate that on average we could not differentiate between the measured background power and that of the power emitted by the motors. The background was subtracted in the frequency domain since, if subtracted in the time domain, it would lead to misleading results near lower frequencies with all the data shown being positive. In such a case one would then presume an average power above zero existed, which is not the case.

As previously stated, to estimate the error in our background subtracted power spectral densities, the standard deviation at a particular frequency was determined from 20 background measurements. The errors at 8, 10, 15, 20 30 and 50 MHz are estimated as 0.8, 0.7, 0.3, 0.1, 0.07 and 0.07 nW/m$^2$. The data shown in Figs. 7.4 - 7.8 become 'noisy' near 10 MHz and below, because the estimation of the error is similar to the variance in the data shown in these plots. The standard deviations at 1 and 2 MHz were 10 and 4 nW/m$^2$.

Suriano *et al*.[18] propose a model for the emission of RF noise from a DC motor. The model consists of a monopole above a grounding plane with arcing from the brushes to commutator acting as the input source. A monopole above a ground plane acts as a dipole antenna; the *E* and *H* near fields are given in Balanis *et al*.[21] A dipole antenna preferentially emits power perpendicular to the axis of the dipole, while no power is emitted by the dipole along its axis. When measuring the RF noise perpendicular to the direction of MLC motion (as shown in Fig. 7.1), the model predicts a single *H* field component. The data presented in Fig. 7.8 agree with this model and with the specific component expected to be

present. When data are measured along the direction of motion of the MLC leaves, the model predicts zero measured power. We measured the power along the MLC leaf movement axis and found that in the same frequency range shown (8 – 70 MHz), the power spectral density is below 1 $nW/m^2$. We might expect a small amount due to the fact that our cable system did not present a perfectly straight and rigid monopole. Thus, these measurements qualitatively support this prediction. We do not purport to say that the model by Suriano *et al*.[18] has been rigorously validated, but only that our measurements of the three Cartesian components of the *H* field both perpendicular and parallel to the movement of the MLC leaves support the model.

Images of the phantom were taken by placing the MLC at the distances of 70 and 100 cm (Fig. 7.10) from the MR coil. From the SNR data presented in Table 7.1, we can see that when the MLC was unshielded the measured SNR was reduced in each of the MLC-coil orientations when the MLC was functioning. However, also shown in Table 7.1 is the measured SNR when the MLC motors and cabling were shielded. In each of the shielded orientations there was neither visible difference between the images nor any experimentally significant difference in the measured SNR obtained with and without continuous MLC motion. These results illustrate that we can effectively shield the RF noise produced by an MLC to the extent that no degradation in image quality and SNR occurs. In each case several images were taken and no effects of the RF noise produced by the shielded MLC plus cables were noticeable. Below 70 cm magnetic effects from the MLC casing to the MR started to become noticeable; therefore, the RF noise could not be studied independently of these magnetic

effects. When the MLC was placed at 60 cm from the center of the MR, image artifacts were seen even when the MLC was stationary. For our linac-MR system we are fabricating an MLC casing which will be constructed of non-magnetic materials to reduce magnetic effects. We note that an MLC positioned at 70 cm is further away from isocenter than current clinical systems; however, for a linac-MR system the MLC may be placed around 70 cm from isocenter. In Table 7.1 there is also a slight difference between the measured SNR when the MLC was shielded as compared to that when the MLC was not shielded (for instance even when the MLC was held static). This difference was due to having to re-orient the phantom or reposition the MLC; thus, the same image slice may not have been imaged. However from one static MLC image to the associated image with the MLC moving nothing was changed in the set-up. The parameter of interest was the change in SNR (or image quality) from the static MLC case to the associated SNR for a functioning MLC.

Images of the phantom were subtracted from one MLC stationary case to the associated MLC leaves moving case. The results for the second orientation (Fig. 7.11) showed that when the MLC motors and cables were shielded the images were nearly identical. When the MLC was shielded, no visible differences between the MLC leaves stationary and MLC leaves moving images could be seen.

When the MR image data were viewed in *k*-space, random noise was seen when the MLC was functioning and unshielded. This random noise in *k*-space leads to an overall increase in the noise of the image. After the MLC was shielded however, this random noise was not seen in *k*-space.

The final position of the MLC with respect to the MRI center has not been determined. Fallone *et al.*[7] reported on the fringe field of our prototype system. In the range 50 – 70 cm from the MRI center the measured fringe fields were in the range of 20 – 250 Gauss. If no magnetic shield is constructed for the MLC the motors themselves will be subjected to these fringe fields. The operation of the MLCs in a magnetic field is an important consideration for linac-MR systems. Qualitatively during the acquisition of our measurements, the brushed MLC motors used in this work showed no strain or change in operation, such as motor speed, when subjected to a 500 Gauss field.

## 7.7. CONCLUSIONS

We have shown that the RF noise produced by a continuously functioning MLC can be effectively shielded. No difference can be seen in image quality when the shielded MLC was stationary and when the motors were used to drive the leaves. The currently used Varian 52-leaf MLC motors and Varian Millennium 120-leaf MLC motor did not show any trouble operating in up to a 500 Gauss applied field, nor did they produce a significant change in radiated RF noise. If brushless motors are to be used in place of brushed motors for reduced RF noise production, magnetic shielding may be required. This study has shown that an MLC can be incorporated into a linac-MR system.

## 7.8. REFERENCES

[1] K. M. Langen and D. T. L. Jones, "Organ motion and its management," Int. J. Radiat. Oncol. Biol. Phys. **50**(1), 265-278 (2001).

[2] S. Webb, "Motion effects in (intensity modulated) radiation therapy: a review," Phys. Med. Biol. **51**(13), R403-R425 (2006).

[3] E. Rietzel, S. J. Rosenthal, D. P. Gierga, C. G. Willett, and G. T. Y. Chen, "Moving targets: detection and tracking of internal organ motion for treatment planning and patient set-up," Radiother. Oncol. **73**(2), S68-S72 (2004).

[4] M. van Herk, "Errors and margins in radiotherapy," Sem. Rad. Onc. **14**(1), 52-64 (2004).

[5] D. Verellen, M. D. Ridder, and G. Storme, "A (short) history of image-guided radiotherapy," Radiother. Oncol. **86**(1), 4-13 (2008).

[6] T. Bortfeld, "IMRT: a review and preview," Phys. Med. Biol. **51**(13), R363-R379 (2006).

[7] B. G. Fallone, B. Murray, S. Rathee, T. Stanescu, S. Steciw, S. Vidakovic, E. Blosser, and D. Tymofichuk, "First MR images obtained during megavoltage photon irradiation from a prototype integrated linac-MR system," Med. Phys. **36**(6), 2084-2088 (2009).

[8] C. Kirkby, T. Stanescu, S. Rathee, M. Carlone, B. Murray, and B. G. Fallone, "Patient dosimetry for hybrid MRI-radiotherapy systems," Med. Phys. **35**(3), 1019-1027 (2008).

[9] J. J. W. Lagendijk, B. W. Raaymakers, A. J. E. Raaijmakers, J. Overweg, K. J. Brown, E. M. Kerkhof, R. W. van der Put, B. Hardemark, M. van Vutpen, and U. A. van der Heide, "MRI/linac integration," Radiother. Oncol. **86**(1), 25-29 (2008).

[10] J. Dempsey, B. Dionne, J. Fitzsimmons, A. Haghigat, J. Li, D. Low, S. Mutic, J. Palta, H. Romeijn, and G. Sjoden, "A real-time MRI guided external beam radiotherapy delivery system," Med. Phys. **33**(6), 2254 (2006).

[11] B. Burke, M. Lamey, S. Rathee, B. Murray, and B. G. Fallone, "Radio frequency noise from clinical linear accelerators," Phys. Med. Biol. **54**(8), 2483-2492 (2009).

[12] A. Sawant, R. Venkat, V. Srivastava, D. Carlson, S. Povzner, H. Cattell, and P. Keall, "Management of three-dimensional intrafraction motion through real-time DMLC tracking," Med. Phys. **35**(5), 2050-2061 (2008).

[13] S. Nill, J. Unkelbach, L. Dietrich, and U. Oelfke, "Online correction for respiratory motion: evaluation of two different imaging geometries," Phys. Med. Biol. **50**(17), 4087-4096 (2005).

[14] H. C. Chen, A. Wu, E. D. Brandner, D. E. Heron, M. S. Huq, N. J. Yue, and W. C. Chen, "Dosimetric evaluations of the interplay effect in respiratory-gated intensity-modulated radiation therapy," Med. Phys. **36**(3), 893-903 (2009).

[15] S. Webb and T. Bortfeld, "A new way of adapting IMRT delivery fraction-by-fraction to cater for variable intrafraction motion," Phys. Med. Biol. **53**(18), 5177-5191 (2008).

[16] S. Webb, "The effect on IMRT conformality of elastic tissue movement and a practical suggestion for movement compensation via the modified dynamic multileaf collimator (dMLC) technique," Phys. Med. Biol. **50**(6), 1163-1190 (2005).

[17] S. Webb, "Quantification of the fluence error in the motion-compensated dynamic MLC (DMLC) technique for delivering intensity-modulated radiotherapy (IMRT)," Phys. Med. Biol. **51**(7), L17-L21 (2006).

[18] C. R. Suriano, J. R. Suriano, G. Thiele, and T. W. Holmes, "Prediction of radiated emissions from DC motors," 1998 International Symposium on Electromagnetic Compatibility, Denver, CO, Aug 24-28, 1998.

[19] M. A. Jabbar and M. A. Rahman, "Radio frequency interference of electric motors and associated controls," IEEE Industry Applications **27**(1), 27-31 (1991).

[20] R. Valentine, *Motor Control Electronics Handbook*, (McGraw-Hill, New York, 1998).

[21] C. A. Balanis, *Antenna theory: analysis and design*, (John Wiley and Sons, New York, 2005).

# Chapter 8: First demonstration of intrafractional tumour-tracked irradiation using 2D phantom MR images on a prototype linac-MR

*A version of this chapter has been published: J. Yun, K. Wachowicz, M. Mackenzie, S. Rathee, D. Robinson, and B. G. Fallone, "First Demonstration of Intrafractional Tumor-Tracked Irradiation using 2D Phantom MR Images on a Prototype linac-MR," Med. Phys. 40(5), 051718 (12pp.) (2013).*

## *8.1. INTRODUCTION*

Intrafractional tracking of mobile tumours is of considerable interest. Several groups are actively researching intrafractional tumour tracking systems[1-3] to deliver highly conformal radiation dose to mobile tumours. Krauss *et al.*[4] and Sawant *et al.*[2] have performed phantom studies demonstrating the feasibility of 2D intrafractional lung tumour tracking. In these studies, a tumour surrogate was driven according to a sinusoidal trajectory and its position was detected using a monitoring system developed by Calypso Medical Technologies (Seattle, WA). Cho *et al.*[3] suggested the simultaneous use of kV/MV imaging for 3D intrafractional tracking, where a gold marker was used as a tumour surrogate. Also, commercial systems are available to perform intrafractional tumour tracking.[5-7]

Despite the wide variety of tracking techniques, all current tracking methods utilize indirect tracking through the use of internal and/or external

tumour surrogates. Reliance on surrogates, however, has been shown to be problematic for accurate tumour tracking because (1) implanted seeds, for liver and prostate tumours,[8] have been shown to migrate by 5.1 mm and 4.5 mm from their initial positions, respectively. In some cases, the seeds might be completely dislodged during the course of the radiation treatment. Imura *et al*., in a study of 57 patients, reported that 25 % of total surrogates was lost during the course of lung tumour treatments;[9] (2) tracking using external surrogates assumes good correlations between internal tumour motion and external surrogate displacement, whereas mismatches between tumour and surrogates up to 9 mm have been shown;[10, 11] and (3) any deformation of tumour shape is completely unknown during tracking. Moreover, since the implanted seeds are usually placed only within the tumour, the motion of the nearby soft tissue and healthy organs, and their relationship to the tumour, are not known during tracking. Therefore, to account for the uncertainty in correlation between tumour position and surrogates, extended regions surrounding the lesion must be irradiated in order to ensure sufficient target coverage.[12]

Although modern imaging systems can provide 3D or 4D anatomical information, all imaging systems are still surrogates to the actual tumour shape, size and location. In 2008, it was claimed that the imaging modalities used in cancer treatment must be improved by three to four orders of magnitude in terms of their tumour-to-background ratio, in order to make meaningful impact on cancer treatment.[13] While the improvements of imaging systems are in progress, the limitations of relying on imaging in radiation treatment need to be acknowledged.

In contemporary radiation treatment process, computed tomography (CT) based target definition is the standard of care. However, large efforts have been made to incorporate magnetic resonance imaging (MRI) in target definition due to its superior soft tissue contrast that enables to visualize tumour extent in more detail.[14, 15] A recent study investigated the dose calculation accuracy for different tumour sites (lung, prostate, brain, head and neck) from 40 patients using MRI data, and compared it to CT based treatment plans. Here, the target volume was defined on MR images and registered to the CT images. Whether the treatment plan was based on CT or MRI, this study showed that nearly the same number of monitor units (< 1.6 % difference) were required to deliver the prescribed dose.[16]

Our group at the Cross Cancer Institute reported the first integrated radiotherapy-MR system known as a linac-MR.[17] With this system we have investigated the requirements for MRI-based intrafractional tumour tracking. These requirements include (1) characterization of multi-leaf collimator (MLC) motor operation in an external magnetic field,[18] (2) measurement of radio frequency (RF) noise from MLC and shielding technique,[19] (3) development of lung tumour autocontouring software[20] compatible with MR images, and (4) development of lung tumour motion prediction software for MRI-based tracking.[21]

We have focused on lung tumour tracking due to the potential for a large range of motion during treatment delivery. Various studies have shown that lung tumour may move up to 40 mm in superior–inferior (SI), 15 mm in anterior–posterior (AP), and 10 mm in left–right (LR) directions during normal breathing.[22-24] Volume changes up to 20 % and rotations up to 50 degrees with

respect to each axis have also been reported.[25] Several methods have been used to reduce the range of respiratory motion in radiotherapy, including active-breathing control (ABC) or forced shallow breathing with abdominal compression (FSB).[26] In ABC, the patient must follow the breathing instructions, thus many infirm patients may have difficulties to comply. FSB may cause problems for the patients with particularly poor pulmonary function, and those with percutaneous gastrostomy tube. Similarly, the patients with large abdominal aortic aneurysms may not be suitable for FSB.[27] Because it is not always possible to apply the methods of respiratory motion reduction, we focused on tracking lung tumour motions during normal breathing.

In this chapter, we present the first physical demonstration of intrafractional tumour tracking using 2D MR images that is built upon our previous investigations.[18-21] An MR compatible motion phantom was used to simulate tumour motion during beam delivery. We present our experimental set-up, different tracking scenarios that we tested, and their results.

## *8.2. MATERIALS AND METHODS*

### 8.2.1. Experimental set-up

#### 8.2.1.1. Linac-MR and MLC

Figure 8.1 shows our set-up for tracking experiments. We used a prototype linac-MR for intrafractional MR imaging and simultaneous beam delivery. A Varian 52-leaf MK-II MLC was used for beam collimation during tracking, which

was controlled by in-house built software and electronics. In this study, 10 MLC leaves (5 in each carriage, MLC-L and MLC-R in Fig. 8.1) were used for tracking.

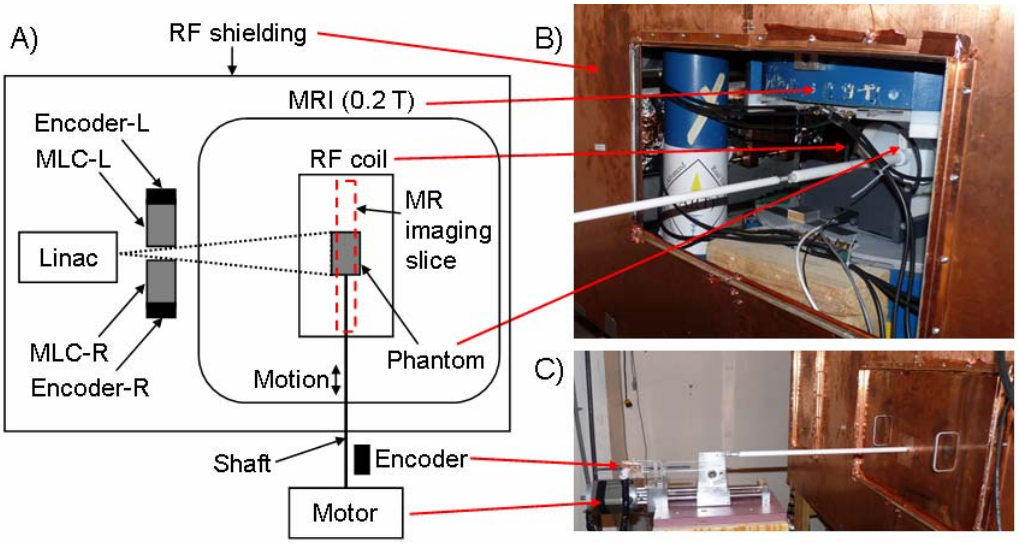


**Figure 8.1 Experimental set-up: A) brief diagram of entire set-up (top down view), B) prototype linac-MR and phantom setting with RF cage open, C) side view with RF cage closed**

All MR images were acquired using a balanced steady state free precession (bSSFP) technique in the beam's eye view (BEV) plane (FOV = 256 mm × 192 mm, 2 mm × 2 mm × 30 mm, TE = 1.3 ms, TR = 2.6 ms, Dynamic Scan Time = 250 ms, i.e. 4 fps). A top down view of MR imaging slice is indicated in Fig. 8.1.A, which is at the center of the magnet and perpendicular to the beam. A sample sequence used to perform tracking in this study is shown in Fig. 8.2. More details regarding bSSFP sequence can be found in Bernstein.[28]

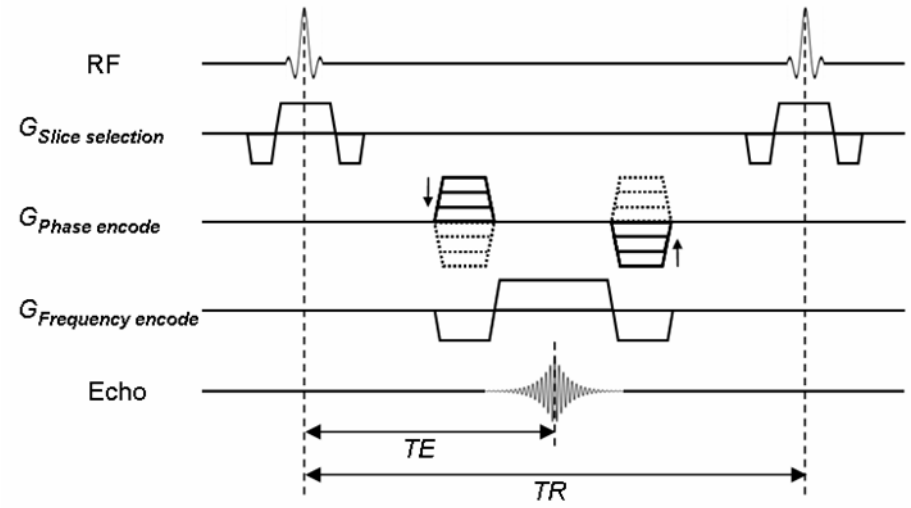


**Figure 8.2 Sample bSSFP sequence used to perform tracking in this study**

### 8.2.1.2. MR compatible motion phantom

Figure 8.1 illustrates the phantom set-up during tracking experiments. A more detailed phantom design is shown in Fig. 8.3. Our phantom was driven by a programmable motor using a shaft that is both non-magnetic and non-conductive to create 1D motion along the axis of the RF coil as indicated in Fig. 8.3.D. This creates phantom motion in the direction perpendicular to the x-ray beam along the leaf motion direction of the MLC.

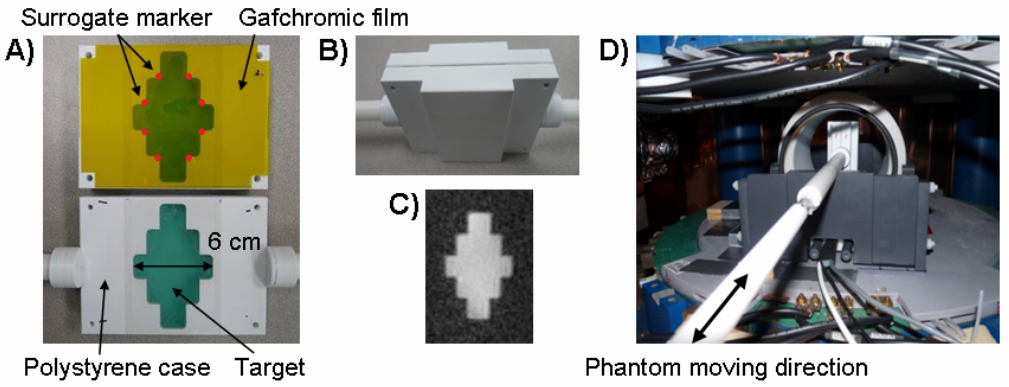


**Figure 8.3 Motion phantom: A) phantom parts, B) assembled phantom, C) MR image during tracking and beam delivery, D) phantom and RF coil placed in the linac-MR**

This phantom is made of two symmetrical parts as shown in Fig. 8.3.A. Here, the central custom-shaped target represents a tumour volume, which is composed of 70 g/l of porcine skin gelatin containing approximately 10 mM of aqueous copper sulfate ($CuSO_4$:$5H_2O$) and 0.1 % sodium benzoate ($NaC_6H_5CO_2$). $T_1$ and $T_2$ values of the target material were measured to be approximately 22 and 16 ms, respectively. Copper sulfate was added to reduce the relaxation times of the gel, which allowed for better-quality $T_1$-weighted imaging used extensively for scouting. Sodium benzoate was added as a preservative. Density of the target material was measured to be 0.99 g/ml, which is very similar to water. Because the target material is mostly composed of water with a small amount of skin gelatin, the effective atomic number of the target material should be equal to that of water, which is known to be 3.4.[29] A small impact of this material on the dose delivered to the film does not influence the result of this study, because film comparisons are all relative. In *in-vivo* MR images using the bSSFP sequence, the lung background is darker than the tumour.[30] For our phantom, the target is embedded in a polystyrene case that contributes no MR signal in the bSSFP imaging sequence generating darker background to the target, and provides a rigid casing to contain the target material.

We inserted Gafchromic EBT2 film (International Specialty Products, Wayne, NJ) between the two cases to measure radiation exposure during tracking. To compare radiation exposures in different films, the following registration technique was used. Prior to irradiation, each film was placed and fixed on the case as shown in Fig. 8.3.A. Then, we visually inspected the 8 inner corners of the

phantom shape and manually marked them on the film using permanent ink. These are referred to as surrogate markers as indicated by red dots in Fig. 8.3.A.

Figure 8.3.B shows the phantom in its assembled state. An MR image of this phantom acquired during the tracking experiment is shown in Fig. 8.3.C illustrating the MR signal from the gelatin "tumour" surrounded by background signal. This image was taken while the phantom and MLC were in motion during beam delivery. RF noise from the MLC is shielded using the method developed in a previous study.[19] Figure 8.3.D shows the phantom and RF coil placed in the linac-MR.

#### 8.2.1.3. MLC and phantom position monitoring during tracking

Each MLC leaf is driven by a DC servo motor located in the back of the carriage. Each motor has a magnetic encoder that detects rotor position, which in turn, provides leaf position. Hence, 10 encoders (5 in each carriage, Encoder-L and Encoder-R in Fig. 8.1) were used to sense and monitor leaf motions in this study. The DC servo motors were controlled by motor drivers programmed through LabVIEW scripts (LabVIEW 2011, National Instruments, Austin, TX) implemented on a field programmable gate arrays (FPGA) chip.

Our motion phantom has an optical encoder (Fig. 8.1) placed on the shaft that measures phantom position. The optical encoder reading was primary feedback to a separate motor driver that was programmed to control phantom motions.

During the tracking experiments, we recorded all encoder readings from each MLC leaf and the phantom. All encoder readings were taken at the same

instance every 50 ms and time-stamped using an internal clock (millisecond resolution) in the LabVIEW software.

### 8.2.1.4. Tumour motion simulation

We drove our phantom following a pre-programmed motion pattern during the tracking experiments. The phantom was moving in the read encoding direction. The speed of phantom when the image was taken depends on the asynchronous phase of motion pattern, ranges from 0 to 3.1 cm/s. Two different motion patterns were used in this study to simulate tumour motions: (1) a sine pattern (period: 6.7 s, motion range: 4 cm, max. speed: 1.8 cm/s) representing ideal, periodic tumour motions, and (2) a modified cosine pattern (period: 5.1 s, motion range: 4 cm, max. speed: 3.1 cm/s), following the form $y(t) = a \cdot \cos^4(t) + b$, which represents more realistic lung tumour motions with time $t$ and constants $a$ and $b$. Lujan *et al.*[31] suggested the modified cosine pattern to model breathing motions, which is shown to be related to abdominal tumour motions including lung tumours.[32] These two patterns have been used in previous studies to validate surrogate based tracking systems.[1-4] The motion range and period of these motion patterns were determined in reference to the previously reported lung tumour motions in the SI directions.[22, 23] Specifically, the motion range was selected from the extreme end of the spectrum to challenge the tracking system.

### 8.2.1.5. Beam calibration to MR images

As shown in Fig. 8.1.A, MLC is the only beam compensator/collimator used in the linac-MR. The relationship between MLC leaf positions and

corresponding beam shape and position at the imaging slice indicated in Fig. 8.1.A was established through film measurements. Based on this, we performed the following steps to calibrate the radiation beam to MR images.

Firstly, MR images were acquired when the phantom was placed at 3 known locations within the imaging plane: (1) at the center of the magnet (i.e. equilibrium position), (2) 2 cm inward from the equilibrium position along the motion direction in Fig. 8.1.A, and (3) 2 cm outward from the equilibrium position. The 2 cm displacement was chosen to encompass the potential motion range of the phantom used in this study.

Secondly, we controlled the MLC to conform the radiation beam to the target shown in the MR images at the above 3 locations. The accurate beam shape concordance with MR image was confirmed with film measurements. From this, we established the relationship between the imaging coordinates of the MRI and MLC leaf positions for 3 different locations in the imaging plane.

The MLC leaf positions for any other possible locations tracked using the intrafractional MR images were calculated by linear interpolation between the 3 calibration points.

## 8.2.2. Software development for intrafractional tumour tracking

### 8.2.2.1. Autocontouring software

An autocontouring software used in this study is based on our previously developed autocontouring algorithm,[20] which determines both the shape and position (i.e. centroid) of a tumour from each intrafractional MR image in less

than 5 ms. The software was developed to perform with 2D MR images. There exist five parameters that may impact the accuracy of autocontouring within this software, thus the values of these parameters must be determined prior to autocontouring. Parameter optimization uses images that are acquired prior to tracking and contain the outlined target. The autocontouring software is fully automatic in its determination of the parameters as indicated in Sec. 3.2.2.1.b of this thesis (also published in Yun *et al*.,[20] Sec. II.A.1.b) More discussions regarding the parameter optimization process in this study follow in Sec. 8.2.3.1 of this thesis.

#### 8.2.2.2. System delay and motion prediction software

System delay is the time interval between the detection of current tumour position data (i.e. image acquisition) and the beam delivery upon the MLC reaching the target position. In our tracking method using the linac-MR, system delay is comprised of image acquisition, image processing, and MLC motion times.

To determine the amount of system delay, we performed tumour tracking without a motion prediction capability using both motion patterns. During this test, the positional changes of the phantom and MLC were monitored via the optical and magnetic encoder readings respectively, as explained in Sec. 8.2.1.3. These motion data were plotted as a function of time, and we calculated system delay from the time difference between the two curves. The result was used as input to our motion prediction software as shown in Step 6 in Fig. 8.4.

We developed motion prediction software to compensate for the tumour motion during system delay. Artificial neural networks (ANN) were used in this software to predict future tumour positions based on the previous ones. The performance of ANN is known to be strongly dependent on its structure and initial weights (IW).[33, 34] That is, prediction accuracy of our software for a given patient's motion pattern might be very sensitive to the ANN. In our previous study using the recorded data of 29 lung cancer patients, the root mean squared error (RMSE) in motion prediction was reduced by 30 - 60 % when using patient specific ANN and IW compared to a single ANN and IW.[21] For this reason, ANN and IW are optimized and trained prior to motion prediction. More explanations on these processes follow in Sec. 8.2.3.1 – Sec. 8.2.3.2. As a result, we were able to use ANN for motion prediction, which was specifically optimized for a given motion pattern. Detailed software design and optimization process are presented in Yun *et al*.[21] Also, it is important to clarify that the prediction performance of our software does not depend on any relationship between the phase of motion and the timing of imaging event. There was no synchronization of the imaging clock and motion control in our experiments.

## 8.2.3. Methodology for intrafractional tracking

Figure 8.4 describes our tracking process, which was developed in accordance with the following scenario:

(1) Two sessions of pre-tracking MR scans are performed using the linac-MR as indicated in Steps 1 and 9 in Fig. 8.4. Both of these sessions proceed with the same MR sequence, phantom set-up and the motion pattern that would be used

in the actual intrafractional tracking experiments.

(2) During tracking, the linac-MR provides 2D intrafractional, dynamic MR imaging of a target (Step 14). An MR imaging slice, perpendicular to the beam direction, with 30 mm thickness is selected to visualize the target as shown in Fig. 8.3.C. No synchronization is necessary between the phase of phantom motion and imaging sequences (i.e. intrafractional MR imaging may begin at a randomly chosen time point).

All of our software was coded in LabVIEW 2011 and executed on 32 bit computer system (Windows7, Intel i7-2600k, 4 GB RAM).

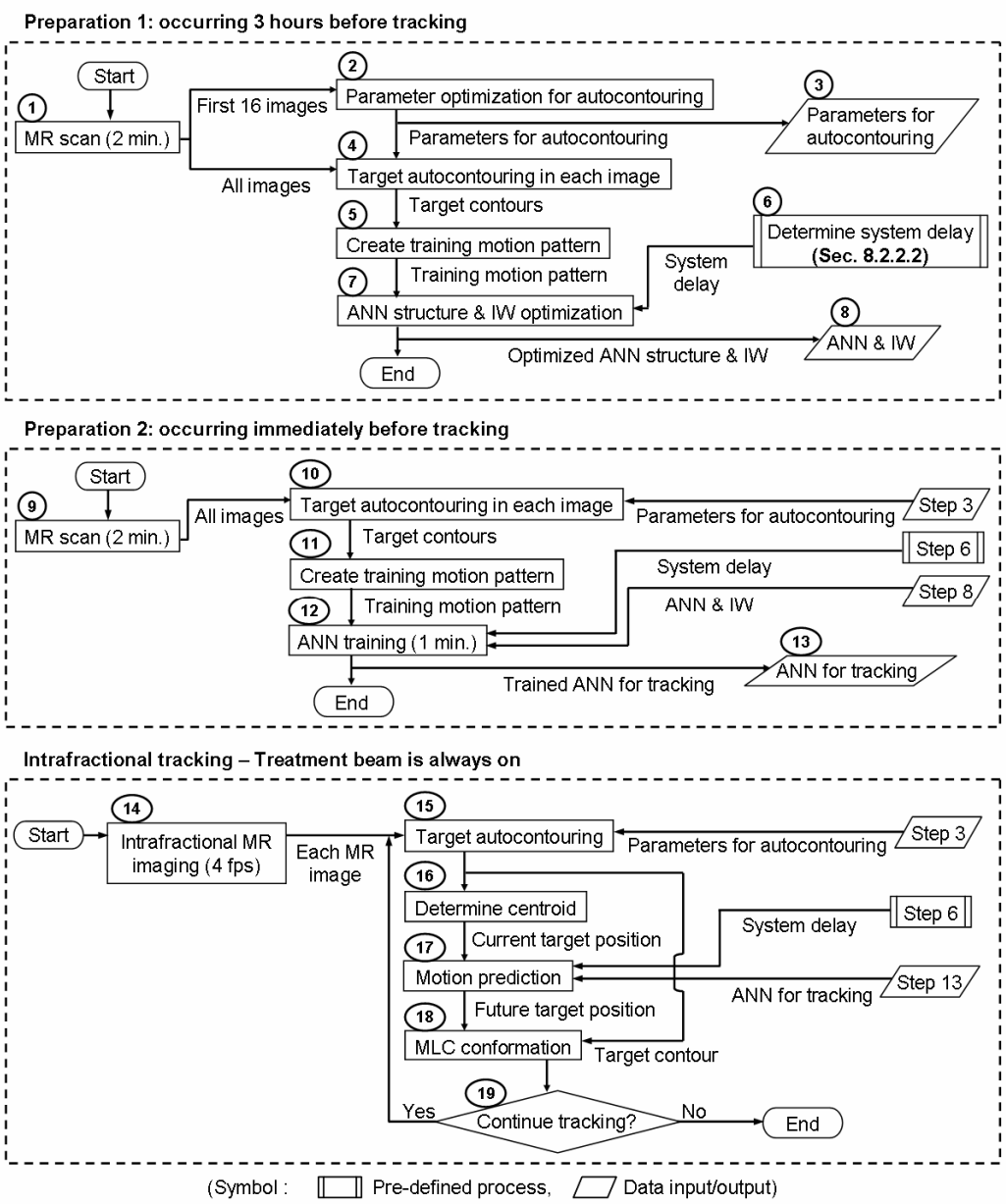


**Figure 8.4 Overview of intrafractional tumour tracking**

## 8.2.3.1. Preparation 1

In Preparation 1 (Steps 1 – 8 in Fig. 8.4), we optimize (1) parameters for the autocontouring software, and (2) the ANN structure and IW for motion

prediction software. This occurs 3 hours before tracking, which is the time requirement to execute Steps 1 – 8 in our computer system.

In Step 1, a pre-tracking MR scan is performed for 2 minutes at a 4 fps imaging rate, acquiring 480 images. In Step 2, the parameters required for the autocontouring software are optimized using the images from Step 1. We chose to use the first 16 images (4 seconds length) in Step 2, because 4 seconds is sufficient to cover the peak-to-peak movement of the phantom following the motion patterns used in this study. The target shown in each of these 16 images is manually contoured, and our software searches for the parameters that can produce an autocontoured target shape that is the most similar to the manual one in each image. Due to this algorithm, the accuracy of manual contouring is an important factor determining autocontouring performance. The manual contouring should be done by an expert user (e.g. radiation oncologist) if autocontouring were to be applied to *in-vivo* images. In this study, however, accurate manual contouring was relatively easy due to the high contrast between the target and the background region. It is important to clarify that tumour contouring during the actual tracking session is fully automatic. Our software only uses the manual contours to arrive at the best parameters that will be used for autocontouring. The optimized parameters are stored in Step 3.

In Step 4, all images from Step 1 are autocontoured using the parameters from Step 2 in conjuction with the autocontouring software. In Step 5, our software (1) calculates the centroid position of the target from the autocontoured target shape in each image, and (2) records the centroid position in each image as a function of time. This record is referred to as a training motion pattern as used in

the motion prediction software. The training pattern, and the amount of system delay determined in Step 6 serve as input to Step 7 for the ANN structure and IW optimizations. Step 6 is explained earlier in Sec. 8.2.2.2. In Step 8, an optimized ANN structure and IW are stored.

### 8.2.3.2. Preparation 2

In Preparation 2 (Steps 9 – 13 in Fig. 8.4), we further train the optimized ANN using the most recent tumour motion data. Preparation 2 occurs immediately prior to actual tumour tracking and takes approximately 3 minutes to complete.

In Step 9, a pre-tracking MR scan is performed for 2 minutes. In Steps 10 and 11, all images from Step 9 are autocontoured, and a training pattern is created. In Step 12, we train the ANN obtained from Step 8 for 1 minute using the training pattern and system delay from Steps 11 and 6, respectively. The ANN is trained for approximately 10000 epochs during 1 minute, where one epoch refers to a single passing of a training pattern (prediction followed by weight corrections) through the ANN during iterative trainings. ANN training uses the training pattern solely derived from the image data and does not use the phantom motion encoder values. A detailed training process is presented in our previous publication.[21] The trained ANN is stored in Step 13. Table 8.1 provides the summary of time requirements to perform Steps 1 – 13.

**Table 8.1 Summary of time requirements to perform Steps 1 - 13**

| Process | | Time |
|---|---|---|
| Preparation 1 | 1st MR scan (Step 1) | 2 min. |
| | ANN optimization (Step 7) | ~ 3 hrs |
| Preparation 2 | 2nd MR scan (Step 9) | 2 min. |
| | ANN training (Step 12) | 1 min. |
| Total time requirement | | ~ 3 hrs |

### 8.2.3.3. Intrafractional tracking

The treatment beam is continuously on while Steps 14 – 19 are executed during intrafractional tracking. In Step 14, tracking begins with intrafractional MR imaging at 4 fps while the phantom is undergoing one of the two motion patterns simulating the tumour motion. Each MR image is autocontoured immediately after the acquisition in Step 15, using the parameters from Step 3.

In Step 16, our software determines the centroid position of the target contour, i.e. a current target position. This is input to Step 17 in order to predict a future target position. The prediction occurs using the ANN and system delay from Steps 13 and 6, respectively. For example, if the system delay is 500 ms, Step 17 will output a target position at 500 ms in the future.

In Step 18, the MLC conforms to the target contour at its predicted future position using the results from Steps 15 and 17. Here, the MLC leaf positions are determined as the following: (1) the leaf positions are calculated to conform the MLC beam shape to the autocontoured target shape from Step 15, and (2) these leaf positions are shifted to translate the MLC shape to a future target position (i.e. centroid) obtained from Step 17. Depending on the result from Step 19, Steps 15 - 18 are iterated on each intrafractional MR image, or tracking is terminated.

It is important to note that Step 17, predicting the future tumour position, occurs at the same rate as the imaging frequency during tracking. This is because approximately the same amount of time (a few ms difference) is required to execute Steps 14 – 16 for each image. This result can be generalized to other imaging frequencies. Since each image was acquired at 4 fps (i.e. every 250 ms) in this study, the prediction occurred at the same rate, every 250 ms. If we use a different MR imaging rate for tracking; for example, 5 fps (i.e. every 200 ms), then the prediction will occur every 200 ms.

### 8.2.4. Demonstration of intrafractional tracking

We demonstrated intrafractional MR tumour tracking according to the 4 different scenarios shown in Table 8.2. Each scenario was tested using two motion patterns as mentioned in Sec. 8.2.1.4 with 2 minutes beam on time (100 MU/min).

**Table 8.2 Tracking scenarios**

| | Scenario 0 (S0) | S1 | S2 | S3 | S4 |
|---|---|---|---|---|---|
| Phantom motion | No | No | Yes | Yes | Yes |
| Beam margin | None | Maximum | None | None | None |
| MLC tracking | No | No | No | Yes | Yes |
| Motion prediction | No | No | No | No | Yes |

Scenario 0 (S0) generates a "gold-standard" result, because radiation delivery to a static or moving target will be identical if we track the target perfectly. S0 was performed prior to each scenario, and the film exposed in other scenarios was registered and compared to the film from S0.

S1 simulates the situation of applying the maximum margin around the target covering the full extent of target motion. Thus the wider, fixed beam will

irradiate the moving target and the target is expected to remain inside the beam portal at all times. To demonstrate S1, we would ideally fix the Gafchromic film to measure the beam port with maximum margin and image the moving target in real-time using MRI. This requires physical separation of the film from the moving phantom, and the registration of film image with MR images to show that the target is always inside the beam. However, due to our phantom design where the film must travel with the phantom, we fixed the phantom at its equilibrium position and delivered radiation with the maximum beam margin to determine the beam width required to cover the moving target without tracking.

Scenarios S2 – S4 are performed with the moving phantom. In S2, the MLC is conformed to the equilibrium target contour and location with no beam margin during beam delivery, representing radiation delivery without accounting for tumour motion. In S3, MLC tracking is enabled without motion prediction, i.e. beam follows the phantom motion without motion prediction capability. In S4, the motion prediction feature is enabled in addition to MLC tracking. The last scenario represents the mode of operation envisaged for future clinical systems.

### 8.2.5. Tracking accuracy evaluation

We evaluated the tracking accuracy of each scenario using the following methods:

(1) Observing encoder readings of phantom and MLC

During tracking experiments, we recorded encoder readings from phantom and MLC every 50 ms. As explained earlier, there was no synchronization of the imaging clock and the phase of phantom motion in our experiments. Using the

encoder readings, we plotted the position changes of the phantom and MLC during tracking as a function of time, and observed the time difference between the two curves in each scenario. The time difference here should ideally be zero if the tracking is perfect.

(2) Film measurements

There was no difference in total time spent in generating the films for each of the scenarios. All films were digitized approximately 12 hrs after exposure, using a VIDAR VXR film digitizer (VIDAR Systems Corporation, Herndon, VA) at $0.36 \times 0.36$ mm$^2$ resolution. The digitized optical density was converted to dose (cGy) using our in-house developed software.[35] We then compared (1) 80 % - 20 % penumbra width (i.e. the distance between two points receiving 80 % and 20 % of the maximum dose), and (2) beam width at 50 % of the maximum dose in each scenario. These were calculated from the profiles as indicated in Fig. 8.6.

## *8.3. RESULTS*

### 8.3.1. Encoder readings of phantom and MLC

We monitored and recorded the positional changes of the phantom and each MLC leaf during tracking through encoder readings. This yielded 11 sets of motion data (1 from the phantom encoder, 10 from the MLC encoder). As explained earlier, all encoder readings were taken at the same instance every 50 ms and time-stamped. These motion data were normalized and plotted as a function of time. From these, we calculated the MLC encoder reading shown in Fig. 8.5, which is an average of 5 encoder readings from Encoder-R in Fig. 8.1.A.

The averaging was performed due to the following reason. Although we tracked the rigid target undergoing translational motion, there exist slight motor-to-motor variations in encoder readings, because (1) each motor drives each MLC leaf conforming to the autocontoured target shape, and (2) the autocontoured target shape can slightly change, within 1 pixel on the edges, as the quality of intrafractional MR images are not identical during tracking experiments. This caused approximately 2 % variation in target size among the images. Nevertheless, because the variability of the 5 encoder readings was small (~ 3 %), we reported the average of 5 encoder readings to provide better representation of MLC motions as a whole in Fig. 8.5.

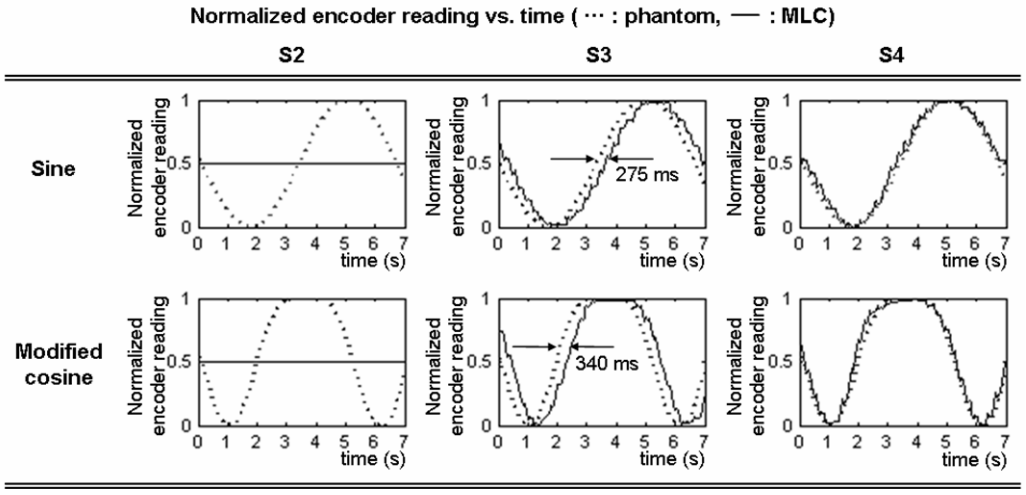


**Figure 8.5 Encoder reading comparisons from phantom and MLC (recorded every 50 ms during tracking). The readings correspond to scenarios S2 - S4 and the two motion patterns are shown.**

In S2 plots (sine and modified cosine) shown in Fig. 8.5, dotted lines indicate phantom motions following both motion patterns. There is no MLC motion in S2, therefore the encoder reading is represented as a straight line.

To find the amount of system delay, we performed tumour tracking without a motion prediction capability. S3 plots in Fig. 8.5 show the position changes of the phantom and MLC during this test in both motion patterns, and we calculated system delay from the time difference between the two curves. For example, in case of the sine pattern, the S3 plot shows constant lagging of MLC motion curve behind the phantom motion curve. The two motion curves were best matched when shifted by 275 ms, which is the amount of system delay. The same method was used to calculate 340 ms system delay in the modified cosine pattern. The difference in the amount of system delays is due to different target speeds (maximum speed of 1.8 and 3.1 cm/s in sine and modified cosine patterns respectively); hence, there are different time requirements for MLC tracking in two motion patterns. Using these system delay values, our motion prediction software was optimized and trained for each motion pattern prior to tracking as explained in Sec. 8.2.3.1.

S4 plots show no observable time difference between the two curves, indicating the phantom motion during system delay is more accurately tracked by the MLC due to the enabling of the motion prediction feature.

### 8.3.2. Film measurement

Figure 8.6 shows the films exposed in different tracking scenarios (S0 – S4). S0 was performed prior to each scenario, and each film exposed in S1 – S4 was registered to the film from S0 using surrogate markers as explained in Sec. 8.2.1.2. All films were digitized, and their optical density values were converted to dose (cGy). Dose profiles were calculated along the white dashed line indicated

in Fig. 8.6. The open beam dose profiles are not flat due to a slight misalignment of the beam and the flattening filter in the linac-MR. The dose rates are similar to those of clinical 600 C units (50, 100, 150, 200, 250 cGy/min at isocenter)

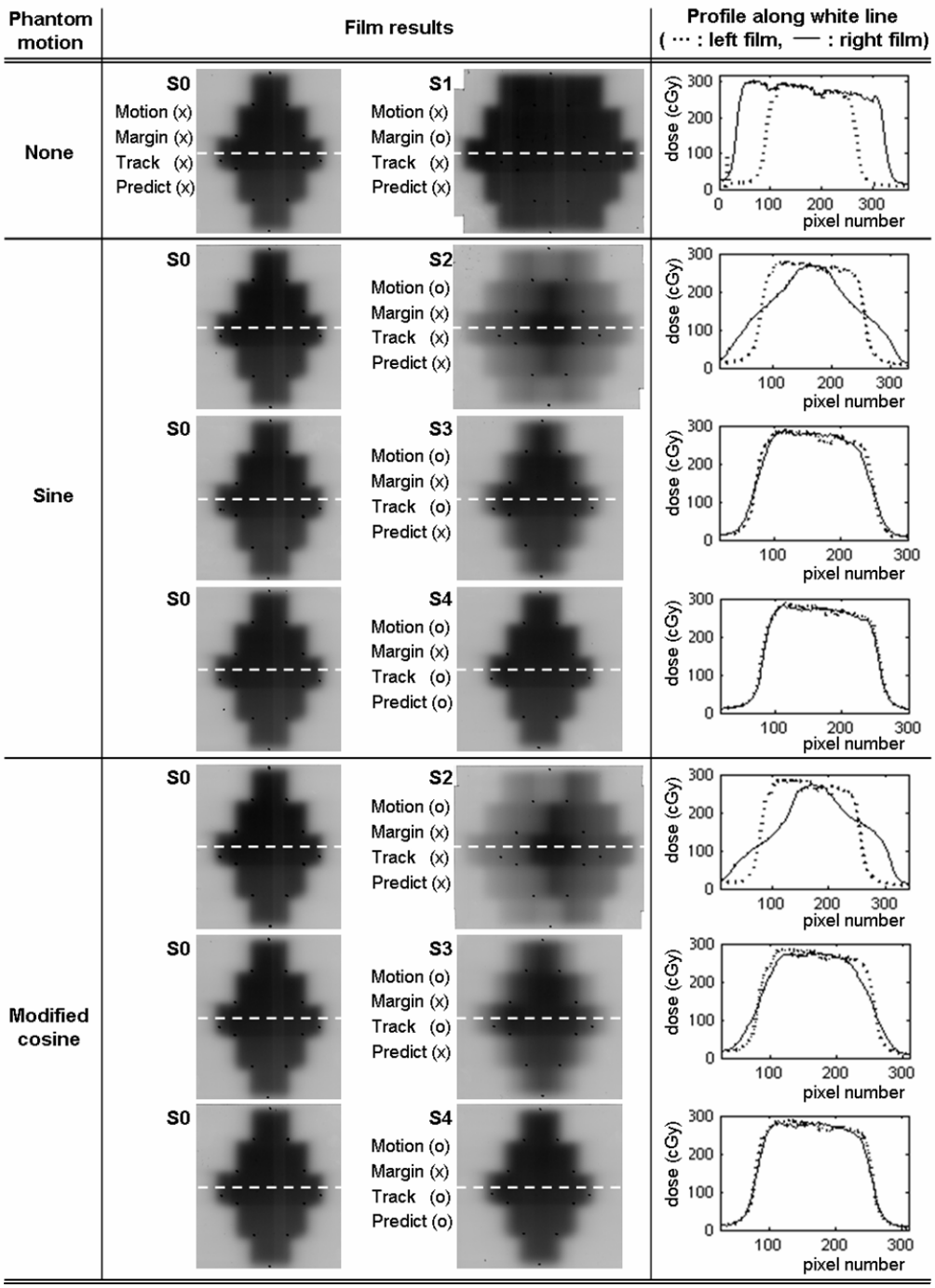


**Figure 8.6 Film measurement in different scenarios using the sine and modified cosine motion patterns.**

In S1, the target is fully irradiated, but much larger volume than the designed target in this experiment is irradiated. In S2, the amount of unnecessary dose is decreased. However, we cannot deliver sufficient dose to the target.

In S3, unnecessary dose to surrounding region is substantially decreased by enabling tracking feature. However, there still exist hot and cold spots, and general mismatch of penumbra, when comparing S0 and S3 dose profiles. This is due to target motions during system delay, which will be increased as the speed of target motion increases. Comparing S3 dose profiles from both motion patterns, the area of hot and cold spots and penumbra mismatch are larger when we use the modified cosine pattern which has a faster target speed.

In S4, we delivered highly conformal dose to the moving target by adding a motion prediction feature. Dose profiles between static and moving target cases show good agreement in both motion patterns. It should be noted that no margin for target motion is included in scenarios S2 - S4.

From visual inspection, the shape of the high dose region covering the target in S4 films shows the sharpest edges compared to the blurred ones shown in S2 and S3 films. In Table 8.3, we compared (1) beam width at 50 %, and (2) 80 % - 20 % penumbra width from the dose profile in each tracking scenario. Here, S0 values are averaged from all S0 dose profiles shown in Fig. 8.6.

**Table 8.3 Beam and penumbra width in different scenarios**

| Phantom motion | None | | Sine | | | Modified cosine | | |
|---|---|---|---|---|---|---|---|---|
| Tracking scenario | S0 | S1 | S2 | S3 | S4 | S2 | S3 | S4 |
| 50 % beam width (mm) | 62.5 | 103.4 | 63.5 | 62.4 | 62.0 | 63.6 | 61.9 | 62.2 |
| 80 % - 20 % penumbra width (mm) | 6.9 | 7.0 | 33.0 | 11.5 | 7.3 | 34.1 | 15.8 | 8.6 |

The measured value of 50 % beam width stays within ± 1 mm in all scenarios except S1 that represents the deliberately introduced geometric margin

to account for the target motion. The measured value of 80 % - 20 % penumbra width is increased up to 27 mm in S2 and 9 mm in S3 compared to S0. In S4, however, the increase in penumbra width is limited to 0.4 mm and 1.7 mm in the sine and modified cosine patterns, respectively.

## 8.4. DISCUSSION

This study presents the first demonstration of intrafractional tumour tracking using 2D MR images. Using a prototype linac-MR, our tracking system automatically tracks the motion and delivers radiation onto the moving target. The MRI-guided tumour tracking study by Crijns *et al.*[36] does not perform intrafractional 2D imaging of the tumour and does not address the system delay, discussed in Sec 8.2.2.2, introduced mainly by the MLC motion.

The dosimetric advantage of intrafractional tracking in treating mobile tumours is clearly shown in Fig. 8.6. Using our tracking method, we delivered highly conformal dose to a moving target simulating 1D lung tumour motions in SI direction. Compared to static target irradiation, 50 % beam width remained within 0.5 mm, and the 80 % - 20 % penumbra width increased by 0.4 and 1.7 mm in moving target irradiations using the sine and modified cosine motion patterns respectively. The difference in penumbra width in these two motion patterns arises due to the maximum target speed, 1.8 and 3.1 cm/s at maximum, respectively. These results are applicable to the current phantom and experimental situation. Further investigations are required to demonstrate the proper operation of our tracking system with the patient or patient-like situations. Also, for the same reason, it is difficult to discuss the impact of our results on an intensity-

modulated radiation therapy (IMRT) delivery at current stage, even though several studies have discussed applying IMRT combined with real-time tracking capability.[37-40]

Various prediction algorithms including using ANN have been proposed to compensate for tumour motion during system delay.[41-44] Although it would be interesting to incorporate these previously developed algorithms in our tracking system and compare the results, the following main problem exists in reality: all previously developed algorithms assumed the tumour position detection at 30 Hz by monitoring the position of tumour surrogates using optical tracking devices, or a stereoscopic x-ray fluoroscopy system. However, current MR imaging can typically achieve image acquisition rates of 3 – 4 fps. Due to this significant difference in detection rates, we had to develop a new algorithm designed specifically for MRI-based tumour tracking. This report presents the tumour tracking performance achieved by using our prediction algorithm. If a new algorithm for MRI-based tracking is developed in future, then a comparison study can be performed.

Our motion prediction algorithm functioned well in our tracking system, where a large amount of system delay is inevitable due to MR image acquisition and image processing time. We expect that our algorithm will also function for other non MRI-based modern tracking systems, which should have much shorter system delay time without having to perform MR imaging. The system delay in a real clinical system can be determined by either of the following two methods: (1) a pre-treatment MR scan will provide tumour motions in several breathing cycles. The phantom can then be programmed to undergo this motion pattern and the

system delay can be determined using the same method as described in Sec. 8.2.2.2; (2) the system delay mainly depends on tumour speed. Thus, a lookup table of system delay can be created as a function of tumour speed. The patient specific system delay can then be looked up from this table based on the patient's tumour speed obtained from the pre-treatment MR scan.

We used the motion patterns that are stable and perfectly periodic in this study. However, it is unreasonable to expect such high reproducibility in patient breathing motions. This inevitable challenge will mainly affect the motion prediction performance of the tracking system. To minimize the errors in motion prediction due to inter- or intrafractional instability of motion patterns, the following two features are implemented in our motion prediction software: (1) to deal with interfractional motion changes, the software was designed to re-optimize its ANN for each fraction of the treatment. In this process, the tumour motion data recorded from a previous fraction is used as a training motion pattern, presuming that tumour motions in two consecutive fractions are the most similar; (2) to deal with intrafractional motion changes, adaptive learning is incorporated in the software by continuously updating the weights and learning rate ($\eta$) of a given ANN during motion prediction in real-time. The weights and $\eta$ represent the knowledge and convergence rate of ANN, respectively. More explanations can be found in Haykin.[45] In this way, the ANN's learning process is not limited to the training session alone but continues during the actual tracking session, and our predictor can adapt to the intrafractional changes in motion pattern to a certain degree.

Because accurate motion prediction is essential for successful intrafractional tracking, we evaluated the prediction performance of our software using realistic lung tumour motions in our previous study.[21] Here, the 1D superior–inferior lung tumour motions of 29 lung cancer patients were used to test our software for various system delays of 120 – 520 ms, in increments of 80 ms. For 280 ms and 360 ms system delays that are more relevant to this study, mean RMSE values of 0.7 mm and 0.8 mm (ranges 0.1 – 2.5 mm) were observed, respectively. Proving these results through actual tracking experiments using realistic lung tumour motions will be a subject of future study.

We focused on tracking 1D translational motions of a rigid target in this study. Real tumour motion, however, includes translation, rotation, as well as volume changes. For example, lung tumour shows 3D displacement with volume changes and rotational motions during normal breathing. Hence, the next step will be demonstrating more realistic tumour tracking in 3D space. Currently, we can accomplish 2D MR imaging with 4 fps imaging rate to track lung tumour motions. However, a potential problem that can arise is through plane tumour motion (motion orthogonal to the imaging plane), even though numerous studies have demonstrated that the largest lung tumour motions occur in SI directions. Potential solutions to this problem could be adjusting the orientation and slice thickness of the imaging plane to capture the SI directional tumour motion and ensure the tumour remains in the imaging plane.

Tumour shape deformation during beam delivery due to rotation, volume changes, and other reasons is another challenge. To evaluate tracking performance in these situations, we must develop an MRI compatible, deformable motion

phantom that has accurate deformation reproducibility. This requires simultaneous implementation of known patterns of motion and deformation. The phantom used in this study contains a simulated target of rigid shape in order to show practicality of tracking. Nevertheless, our tracking system is not limited to rigid body tracking. Our tracking method is based on (1) determining both the shape and location of the target from each MR image, and (2) reshaping and moving the MLC accordingly in real-time. To achieve this, our autocontouring software was designed to deal with possible deformations of the tumour shape, and it contours each image individually without the need of *a priori* assumptions regarding tumour shape or contrast. The autocontouring performance of the software used in this study was previously evaluated through a phantom study (circular and non-circular tumour shapes),[20] as well as an *in-vivo* study.[46] In both studies, autocontoured targets/tumours were compared to standard, manual contours. Here, it was shown that the autocontouring accuracy decreases with lower contrast-to-noise ratio (CNR) of the target/tumour in MR images. Nevertheless, if CNR > 5, autocontours have an average centroid displacement < 1 mm and < 2 mm, as well as Dice's coefficient > 93 % and > 83 % compared to the standard contours in the phantom and *in-vivo* study, respectively. This might be an indication of the CNR level required for successful autocontouring; however, more investigation is needed to evaluate the software performance with deformable target shapes. This future study will include developing a deformable phantom.

This study was carried out to demonstrate the technical aspect of MRI-based tracking using a phantom. Current phantom design and target shape were decided considering several factors including MLC leaf width, prototype linac-

MR geometry, and RF coil size. The phantom may represent a more suitable condition for contrast in the images as it does not include the susceptibility issues occurring at the air-tissue interface of human lung. Further studies using realistic phantoms, human volunteers and/or patients are required.

## 8.5. CONCLUSION

We have demonstrated intrafractional MR tumour tracking using a prototype linac-MR. An MR compatible motion phantom was used to simulate tumour motions during 2 minutes of irradiation. Different tumour tracking scenarios were tested with two different phantom motion patterns.

We delivered highly conformal dose to a moving target using predictive tumour tracking. Compared to static target irradiation, 50 % beam width remains virtually unchanged, < 0.5 mm, and the increase in 80 % - 20 % penumbra width is less than 1.7 mm in moving target irradiation. These results illustrate potential dosimetric advantages of intrafractional MR tumour tracking in treating mobile tumours as shown for the phantom case.

## 8.6. REFERENCES


1 M. B. Tacke, S. Nill, A. Krauss, and U. Oelfke, "Real-time tumor tracking: automatic compensation of target motion using the Siemens 160 MLC," Med. Phys. **37**(2), 753-761 (2010).

2 A. Sawant, R. L. Smith, R. B. Venkat, L. Santanam, B. C. Cho, P. Poulsen, H. Cattell, L. J. Newell, P. Parikh, and P. J. Keall, "Toward Submillimeter Accuracy in the Management of Intrafraction Motion: the Integration of Real-Time Internal Position Monitoring and Multileaf Collimator Target Tracking," Int. J. Radiat. Oncol. Biol. Phys. **74**(2), 575-582 (2009).

[3] B. Cho, P. R. Poulsen, A. Sloutsky, A. Sawant, and P. J. Keall, "First Demonstration of Combined Kv/Mv Image-Guided Real-Time Dynamic Multileaf-Collimator Target Tracking," Int. J. Radiat. Oncol. Biol. Phys. **74**(3), 859-867 (2009).

[4] A. Krauss, S. Nill, M. Tacke, and U. Oelfke, "Electromagnetic Real-Time Tumor Position Monitoring and Dynamic Multileaf Collimator Tracking Using a Siemens 160 MLC: Geometric and Dosimetric Accuracy of an Integrated System," Int. J. Radiat. Oncol. Biol. Phys. **79**(2), 579-587 (2010).

[5] S. S. Vedam, V. R. Kini, P. J. Keall, V. Ramakrishnan, H. Mostafavi, and R. Mohan, "Quantifying the predictability of diaphragm motion during respiration with a noninvasive external marker," Med. Phys. **30**(4), 505-513 (2003).

[6] E. Nioutsikou, Y. Seppenwoolde, J. R. N. Symonds-Tayler, B. Heijmen, P. Evans, and S. Webb, "Dosimetric investigation of lung tumor motion compensation with a robotic respiratory tracking system: An experimental study," Med. Phys. **35**(4), 1232-1240 (2008).

[7] T. Harada, H. Shirato, S. Ogura, S. Oizumi, K. Yamazaki, S. Shimizu, R. Onimaru, K. Miyasaka, M. Nishimura, and H. Dosaka-Akita, "Real-time tumor-tracking radiation therapy for lung carcinoma by the aid of insertion of a gold marker using bronchofiberscopy," Cancer **95**(8), 1720-1727 (2002).

[8] K. Kitamura, H. Shirato, S. Shimizu, N. Shinohara, T. Harabayashi, T. Shimizu, Y. Kodama, H. Endo, R. Onimaru, S. Nishioka, H. Aoyama, K. Tsuchiya, and K. Miyasaka, "Registration accuracy and possible migration of internal fiducial gold marker implanted in prostate and liver treated with real-time tumor-tracking radiation therapy (RTRT)," Radiother. Oncol. **62**(3), 275-281 (2002).

[9] M. Imura, K. Yamazaki, H. Shirato, R. Onimaru, M. Fujino, S. Shimizu, T. Harada, S. Ogura, H. Dosaka-Akita, K. Miyasaka, and M. Nishimura, "Insertion and fixation of fiducial markers for setup and tracking of lung

tumors in radiotherapy," Int. J. Radiat. Oncol. Biol. Phys. **63**(5), 1442-1447 (2005).

[10] D. Ionascu, S. B. Jiang, S. Nishioka, H. Shirato, and R. I. Berbeco, "Internal-external correlation investigations of respiratory induced motion of lung tumors," Med. Phys. **34**(10), 3893-3903 (2007).

[11] D. P. Gierga, J. Brewer, G. C. Sharp, M. Betke, C. G. Willett, and G. T. Y. Chen, "The correlation between internal and external markers for abdominal tumors: Implications for respiratory gating," Int. J. Radiat. Oncol. Biol. Phys. **61**(5), 1551-1558 (2005).

[12] L. Ekberg, O. Holmberg, L. Wittgren, G. Bjelkengren, and T. Landberg, "What margins should be added to the clinical target volume in radiotherapy treatment planning for lung cancer?," Radiother. Oncol. **48**(1), 71-77 (1998).

[13] J. V. Frangioni, "New technologies for human cancer imaging," J Clin Oncol. **26**(24), 4012-4021 (2008).

[14] V. S. Khoo and D. L. Joon, "New developments in MRI for target volume delineation in radiotherapy," Br J Radiol. **79**(Special Issue 1), S2-S15 (2006).

[15] L. A. Dawson and C. Menard, "Imaging in Radiation Oncology: A Perspective," Oncologist **15**(4), 338-349 (2010).

[16] J. H. Jonsson, M. G. Karlsson, M. Karlsson, and T. Nyholm, "Treatment planning using MRI data: an analysis of the dose calculation accuracy for different treatment regions," Radiat Oncol. **5**(62), 1-8 (2010).

[17] B. G. Fallone, B. Murray, S. Rathee, T. Stanescu, S. Steciw, S. Vidakovic, E. Blosser, and D. Tymofichuk, "First MR images obtained during megavoltage photon irradiation from a prototype integrated linac-MR system," Med. Phys. **36**(6), 2084-2088 (2009).

[18] J. Yun, J. St. Aubin, S. Rathee, and B. G. Fallone, "Brushed permanent magnet DC MLC motor operation in an external magnetic field," Med. Phys. **37**(5), 2131-2134 (2010).

[19] M. Lamey, J. Yun, S. Rathee, and B. G. Fallone, "Radio frequency noise from an MLC: a feasibility study of the use of an MLC for linac-MR systems," Phys. Med. Biol. **55**(4), 981-994 (2010).

[20] J. Yun, E. Yip, K. Wachowicz, S. Rathee, M. Mackenzie, D. Robinson, and B. G. Fallone, "Evaluation of a lung tumor autocontouring algorithm for intrafractional tumor tracking using low-field MRI: A phantom study," Med. Phys. **39**(3), 1481-1494 (2012).

[21] J. Yun, M. Mackenzie, S. Rathee, D. Robinson, and B. G. Fallone, "An artificial neural network (ANN)-based lung-tumor motion predictor for intrafractional MR tumor tracking," Med. Phys. **39**(7), 4423-4433 (2012).

[22] C. Plathow, C. Fink, S. Ley, M. Puderbach, M. Eichinger, I. Zuna, A. Schmahl, and H. U. Kauczor, "Measurement of tumor diameter-dependent mobility of lung tumors by dynamic MRI," Radiother. Oncol. **73**(3), 349-354 (2004).

[23] H. Shirato, K. Suzuki, G. C. Sharp, K. Fujita, R. Onimaru, M. Fujino, N. Kato, Y. Osaka, R. Kinoshita, H. Taguchi, S. Onodera, and K. Miyasaka, "Speed and amplitude of lung tumor motion precisely detected in four-dimensional setup and in real-time tumor-tracking radiotherapy," Int. J. Radiat. Oncol. Biol. Phys. **64**(4), 1229-1236 (2006).

[24] H. Shirato, Y. Seppenwoolde, K. Kitamura, R. Onimura, and S. Shimizu, "Intrafractional tumor motion: Lung and liver," Sem. Rad. Onc. **14**(1), 10-18 (2004).

[25] C. Plathow, M. Klopp, C. Fink, A. Sandner, H. Hof, M. Puderbach, F. Herth, A. Schmahl, and H. U. Kauczor, "Quantitative analysis of lung and tumour mobility: comparison of two time-resolved MRI sequences," Br J Radiol. **78**(933), 836-840 (2005).

[26] P. J. Keall, G. S. Mageras, J. M. Balter, R. S. Emery, K. M. Forster, S. B. Jiang, J. M. Kapatoes, D. A. Low, M. J. Murphy, B. R. Murray, C. R. Ramsey, M. B. Van Herk, S. S. Vedam, J. W. Wong, and E. Yorke, "The management of respiratory motion in radiation oncology report of AAPM Task Group 76," Med. Phys. **33**(10), 3874-3900 (2006).

[27] S. S. Lo, B. S. Teh, J. J. Lu, and T. E. Schefter, *Stereotactic Body Radiation Therapy*, (Springer-Verlag Berlin and Heidelberg GmbH & Co. K, Berlin, 2012).

[28] M. A. Bernstein, K. F. King, and X. J. Zhou, *Handbook of MRI pulse sequences*, (Academic Press, Burlington, MA, 2004).

[29] M. L. Taylor, R. L. Smith, F. Dossing, and R. D. Franich, "Robust calculation of effective atomic numbers: The Auto-Zeff software," Med. Phys. **39**(4), 1769-1778 (2012).

[30] S. Rajaram, A. J. Swift, D. Capener, A. Telfer, C. Davies, C. Hill, R. Condliffe, C. Elliot, J. Hurdman, D. G. Kiely, and J. M. Wild, "Lung Morphology Assessment with Balanced Steady-State Free Precession MR Imaging Compared with CT," Radiology **263**(2), 569-577 (2012).

[31] A. E. Lujan, E. W. Larsen, J. M. Balter, and R. K. Ten Haken, "A method for incorporating organ motion due to breathing into 3D dose calculations," Med. Phys. **26**(5), 715-720 (1999).

[32] Y. Tsunashima, T. Sakae, Y. Shioyama, K. Kagei, T. Terunuma, A. Nohtomi, and Y. Akine, "Correlation between the respiratory waveform measured using a respiratory sensor and 3D tumor motion in gated radiotherapy," Int. J. Radiat. Oncol. Biol. Phys. **60**(3), 951-958 (2004).

[33] H. R. Maier and G. C. Dandy, "The effect of internal parameters and geometry on the performance of back-propagation neural networks: an empirical study," Environmental Modelling & Software **13**(2), 193-209 (1998).

[34] L. F. A. Wessels and E. Barnard, "Avoiding false local minima by proper initialization of connections," IEEE Transactions on Neural Networks **3**(6), 899-905 (1992).

[35] S. D. Thomas, M. Mackenzie, G. C. Field, A. M. Syme, and B. G. Fallone, "Patient specific treatment verifications for helical tomotherapy treatment plans," Med. Phys. **32**(12), 3793-3800 (2005).

[36] S. P. M. Crijns, B. W. Raaymakers, and J. J. W. Lagendijk, "Proof of concept of MRI-guided tracked radiation delivery: tracking one-dimensional motion," Phys. Med. Biol. **57**(23), 7863-7872 (2012).

[37] L. Papiez, D. Rangaraj, and P. Keall, "Real-time DMLC IMRT delivery for mobile and deforming targets," Med. Phys. **32**(9), 3037-3048 (2005).

[38] Y. L. Suh, A. Sawant, R. Venkat, and P. J. Keall, "Four-dimensional IMRT treatment planning using a DMLC motion-tracking algorithm," Phys. Med. Biol. **54**(12), 3821-3835 (2009).

[39] R. L. Smith, A. Sawant, L. Santanam, R. B. Venkat, L. J. Newell, B. C. Cho, P. Poulsen, H. Catell, P. J. Keall, and P. J. Parikh, "Integration of Real-Time Internal Electromagnetic Position Monitoring Coupled with Dynamic Multileaf Collimator Tracking: an Intensity-Modulated Radiation Therapy Feasibility Study," Int. J. Radiat. Oncol. Biol. Phys. **74**(3), 868-875 (2009).

[40] D. McQuaid, M. Partridge, J. R. N. Symonds-Tayler, P. M. Evans, and S. Webb, "Experimental Validation of a Target Tracking IMRT Delivery with Conventional MLCs," Clinical Oncology **21**(3), 243-244 (2009).

[41] G. C. Sharp, S. B. Jiang, S. Shimizu, and H. Shirato, "Prediction of respiratory tumour motion for real-time image-guided radiotherapy," Phys. Med. Biol. **49**(3), 425-440 (2004).

[42] A. Krauss, S. Nill, and U. Oelfke, "The comparative performance of four respiratory motion predictors for real-time tumour tracking," Phys. Med. Biol. **56**(16), 5303-5317 (2011).

[43] J. H. Goodband, O. C. L. Haas, and J. A. Mills, "A comparison of neural network approaches for on-line prediction in IGRT," Med. Phys. **35**(3), 1113-1122 (2008).

[44] M. J. Murphy and D. Pokhrel, "Optimization of an adaptive neural network to predict breathing," Med. Phys. **36**(1), 40-47 (2009).

[45] S. S. Haykin, *Neural networks : a comprehensive foundation*, 2nd ed. (Prentice Hall, Upper Saddle River, NJ, 1999).

[46] E. Yip, J. Yun, Z. Gabos, K. Wachowicz, S. Rathee, and B. G. Fallone, "Evaluation of a Real Time Tumour Autocontouring Algorithm Using In-Vivo Lung MR Images with Various Contrast to Noise Ratios," presented at the 54th Annual Meeting of the AAPM, Charlotte, NC, July 29 - August 2, 2012.

# Chapter 9: Summary and conclusions

Intrafractional tumour tracking is of considerable interest as a means to minimize the PTV in treating mobile tumours. Despite the large research efforts, all currently available tracking systems share the same fundamental limitation, namely, the lack of intrafractional tumour imaging. Because the target/tumour cannot be seen during treatment beam delivery, these systems must rely on indirect tracking mechanisms using internal and/or external tumour surrogates. This approach has been shown to be problematic for accurate tumour tracking.

The linac-MR system at the CCI enables intrafractional MR imaging of a tumour. Utilizing this novel feature, this thesis sought to develop a direct, non-surrogate based intrafractional tumour tracking system and physically demonstrate its feasibility by delivering highly conformal dose to a moving target undergoing simulated lung tumour motions. Using linac-MR, our tracking system no longer suffers from the lack of tumour imaging during beam delivery. Moreover, our system is free of ionizing radiation and invasive implantation of surrogates.

This thesis addressed the requirements for MRI-based intrafractional tumour tracking. Emphasis was given to lung tumours due to their potential for complicated, large ranges of intrafractional motions.

To provide research background and motivation, Chapter 1 reviewed modern external beam radiation therapy techniques and discussed their shortcomings in treating mobile tumours. Then, justification for this research was stated. Chapter 2 presented theories that are relevant to this research including

magnetic resonance imaging (MRI), artificial neural networks (ANN), and particle swarm optimization (PSO).

Chapter 3 introduced our approach to automatic lung tumour contouring, which is the first step of intrafractional tumour tracking process. We developed an autocontouring algorithm to determine both the shape and position of a lung tumour from each intrafractional MR image. Our prototype linac-MR is equipped with 0.2 T MRI, whereas the next system will have 0.5 T MRI. Due to this, the autocontouring algorithm was evaluated using an in-house built lung motion phantom that allows simulation of MR images with the expected lung tumour contrast-to-noise ratio (CNR) at 0.5 and 0.2 T by using a single 3 T scanner. Autocontoured tumour shapes were compared to real tumour shapes, and Dice's coefficients of $> 0.96$ and $> 0.93$ were achieved in 0.5 and 0.2 T equivalent images, respectively. Also, the position of a tumour (centroid) calculated from the autocontoured tumour shape was tracked and compared to the position from the real one, and root mean squared error (RMSE) values of $< 0.55$ and $< 0.92$ mm were achieved in 0.5 and 0.2 T equivalent images, respectively. A very fast autocontouring speed, $< 5$ ms per image, was also achieved, which is an essential feature for a functional intrafractional tumour tracking system.

Chapter 4 presented our initial work using *in-vivo* data obtained from a single non-small cell lung cancer (NSCLC) patient. The patient was imaged in a 3 T MRI for 3 minutes at approximately 4 fps imaging speed. These 3 T images were degraded to simulate lower fields MR images at 0.2 – 1.5 T by adding Gaussian noise, assuming linear CNR scaling with respect to the field strength. Using these image sets, the feasibility of lung tumour autocontouring in various

low field MR images was verified as the following: (1) a radiation oncologist manually drew tumour contours in all 3 T images, which were considered as the standard contours. (2) Our software auto-determined tumour contours in the 3 T images, as well as all other simulated lower field MR images. (3) The two contours (standard and auto-determined) were compared by calculating Dice's coefficients ($D$) as well as $\Delta d_{centroid}$ (displacement between the centroid positions of the two contours). From the comparison, mean $D$ (measure of autocontouring fidelity) of 0.836 – 0.881 as well as mean $\Delta d_{centroid}$ (measure of tracking accuracy) of 1.37 – 1.71 mm were achieved in 3 – 0.2 T equivalent images, respectively. In addition, we tested intra-observer variability by calculating $D$ and $\Delta d_{centroid}$ between the same physician's contours drawn on two different days (100 images acquired at 3 T were used). From this, mean $D$ and mean $\Delta d_{centroid}$ of 0.920 and 0.78 mm were achieved.

Chapter 5 presented our tumour motion prediction software designed specifically for MRI-based tracking environment. We developed the software to compensate for the tumour motions during system delay (the time interval between the detection of current tumour position and the beam delivery upon the MLC reaching the target position) in MRI-based intrafractional lung tumour tracking. An artificial neural network (ANN) was used in our software, which was trained to output a future tumour position based on current and previous tumour positions. A method of optimizing a patient specific ANN structure and its initial weights (IW) was also developed. Prediction accuracy of the software was evaluated using the 1D superior–inferior lung tumour motions of 29 lung cancer patients for system delays of 120 – 520 ms, in increments of 80 ms. For these

system delays, mean RMSE values of 0.5 – 0.9 mm (ranges 0.0 – 2.8 mm from 29 patients) were achieved between original and predicted tumour positions. The advantage of using a patient specific ANN structure and IW optimizations was shown by the 30 – 60 % decrease in mean RMSE values in motion prediction as compared to the results obtained with a single ANN structure and randomly chosen IW.

Chapter 6 discussed the effect of strong external magnetic field on the functionality of MLC motors. This needs to be investigated, because the MLC would be exposed to the external fringe magnetic fields of the linac-MR systems. The changes in motor speed and current were measured for varying external magnetic field strengths up to 2000 G. These changes in motor characteristics were measured for three orientations of the motor in the external magnetic field, simulating changes in motor orientations due to installation and/or collimator rotations. In addition, the functionality of the associated magnetic motor encoder was tested. The tested motors are: (1) both half and full leaf motors used with Varian 120 leaf Millennium MLC, (2) a leaf motor used with Varian 52 leaf MKII MLC, and (3) a carriage motor. In most cases, the magnetic encoder of the motors failed prior to any damage to the gearbox or the permanent magnet motor itself. The measured limits of the external magnetic fields were found to vary by the motor type. The leaf motor used with a Varian 52 leaf MKII MLC system tolerated up to 450 ± 10 G. The carriage motor tolerated up to 2000 ± 10 G. The motors used with the Varian 120 leaf Millennium MLC system were found to tolerate a maximum of 600 ± 10 G.

Chapter 7 presented appropriate RF shielding around the MLC motors to mitigate the negative effects of RF motor noise in MR images. This must be studied, because MLC motors would be located in the fringe field of the linac-MR and create RF noise. The RF noise power spectral density from a Varian 52-leaf MLC motor, a Varian Millennium MLC motor and a brushless fan motor was measured as a function of the applied magnetic field using a near field probe set. Above 40 MHz there seemed to be no measured RF noise. Below 40 MHz, the Millennium MLC motor showed more noise than the Varian 52-leaf motor or the brushless fan motor. In both MLC motors, no significant change in radiated RF noise was found as the magnetic field increased up to 500 G. Images of a phantom were taken by the prototype linac-MR system with the MLC placed in close proximity to the magnet. Several orientations of the MLC in both shielded and non-shielded configurations were studied. For the case of a non-shielded MLC and associated cables, the signal-to-noise ratio (SNR) was reduced when 13 MLC leaves were in motion during imaging. When the MLC and associated cables were shielded, however, the measured SNR of the images with and without MLC motion was experimentally the same.

Chapter 8 described the first physical demonstration of intrafractional tumour-tracked irradiation using a linac-MR. Our tracking system includes the two software components presented in Chapters 3 and 5, as well as hardware components (linac-MR, MLC, and a motion phantom). During tracking, treatment beam was delivered for 2 minutes to a moving target that was undergoing simulated lung tumour motions. Two different motion patterns were used in this study to simulate tumour motions: (1) a sine pattern (period: 6.7 s, amplitude: 4

cm, max. speed: 1.8 cm/s) representing ideal, periodic tumour motions, and (2) a modified cosine pattern (period: 5.1 s, amplitude: 4 cm, max. speed: 3.1 cm/s) representing more realistic lung tumour motions. The accuracy of tumour tracking was evaluated by (1) observing phantom and MLC motions, and (2) comparing radiation exposure of the target by film measurements from series of tracking experiments. Comparing the results from moving target irradiation with our tracking system to static target irradiation, 50 % beam width revealed minimal differences of < 0.5 mm, while the increase in 80 % - 20 % penumbra width was limited to 0.4 and 1.7 mm in the sine and modified cosine patterns, respectively.

In this research, we developed software & hardware components of a direct, non-surrogate based tumour tracking system. We reported the first physical demonstration of intrafractional tumour-tracked irradiation using a prototype linac-MR, by delivering highly conformal treatment beam to a moving target undergoing lung tumour motions. The performance of our tracking system shown in this research illustrates potential dosimetric advantages of intrafractional MR tumour tracking in treating mobile tumours as shown for the phantom study.

Several future projects can be initiated from the work presented in this thesis.

(1) A human-sized 2$^{nd}$ linac-MR system is being installed at the CCI. Using this system, further investigations are required to demonstrate the proper operation of our tracking system with the patient or patient-like situations.

(2) The performance of autocontouring algorithm was evaluated with lung phantom images, as well as the *in-vivo* images from a single patient. In order

to ensure the autocontouring capability in realistic situations, more studies using multiple sets of *in-vivo* data are required.

(3) The accuracy of motion prediction was evaluated with 1D tumour motion scenario. Since lung tumour motions occur in 3D in reality, the motion prediction software requires further development to accommodate 3D tumour motion predictions.

In an ideal radiotherapy scenario, the treatment beam would be tightly conformed to the tumour and continuously adapted to the tumour motion. In this thesis, we have demonstrated the feasibility of this scenario through a 1D motion phantom study using the prototype linac-MR. As the linac-MR system at the CCI continues to evolve, more realistic, patient-like tumour tracking experiments will be possible. This will lead to further improvement of our tracking system presented in this thesis, one more step towards its eventual clinical implementation.

# Bibliography


[1] L. E. Antonuk, "Electronic portal imaging devices: a review and historical perspective of contemporary technologies and research," Phys. Med. Biol. **47**(6), R31-R65 (2002)……...10

[2] C. A. Balanis, *Antenna theory: analysis and design*, (John Wiley and Sons, New York, 2005)……..186

[3] L. Behera, S. Kumar, and A. Patnaik, "A novel learning algorithm for feedforward networks using Lyapunov function approach," in Proceedings of International Conference on Intelligent Sensing and Information Processing, Chennai, India, Jan 4-7, 2004……...123

[4] C. Beltran, M. G. Herman, and B. J. Davis, "Planning target margin calculations for prostate radiotherapy based on intrafraction and interfraction motion using four localization methods," Int. J. Radiat. Oncol. Biol. Phys. **70**(1), 289-295 (2008)…….13

[5] C. J. Bergin, G. H. Glover, and J. M. Pauly, "Lung Parenchyma - Magnetic-Susceptibility in MR Imaging," Radiology **180**(3), 845-848 (1991)……77

[6] M. A. Bernstein, K. F. King, and X. J. Zhou, *Handbook of MRI pulse sequences*, (Academic Press, Burlington, MA, 2004)……49-50, 96, 196

[7] T. S. Berrang, P. T. Truong, C. Popescu, L. Drever, H. A. Kader, M. L. Hilts, T. Mitchell, S. Y. Soh, L. Sands, S. Silver, and I. A. Olivotto, "3D ultrasound can contribute to planning CT to define the target for partial breast radiotherapy," Int. J. Radiat. Oncol. Biol. Phys. **73**(2), 375-383 (2009)……12

[8] J. Beutel, H. L. Kundel, and R. L. Van Metter, *Handbook of Medical Imaging, Volume 1. Physics and Psychophysics*, (SPIE, Bellingham, WA, 2000)……..34

[9] P. J. Biggs, M. Goitein, and M. D. Russell, "A diagnostic x-ray field verification device for a 10 MV linear-accelerator," Int. J. Radiat. Oncol. Biol. Phys. **11**(3), 635-643 (1985)……...9

[10] F. Bloch, "Nuclear Induction," Physical Review **70**(7-8), 460-474 (1946)……...……...34, 36-37

[11] T. Bortfeld, "IMRT: a review and preview," Phys. Med. Biol. **51**(13), R363-R379 (2006)……...165

[12] A. Boss, S. Schaefer, P. Martirosian, C. D. Claussen, F. Schick, and J. F. Schaefer, "Magnetic resonance imaging of lung tissue: Influence of body positioning, breathing and oxygen inhalation on signal decay using multi-echo gradient-echo sequences," Invest Radiol. **43**(6), 433-438 (2008)….77

[13] P. A. Bottomley, C. J. Hardy, R. E. Argersinger, and G. Allenmoore, "A Review of H-1 Nuclear-Magnetic-Resonance Relaxation in Pathology - Are T1 and T2 Diagnostic?," Med. Phys. **14**(1), 1-37 (1987)...76-77, 80-81

[14] T. R. Brown, B. M. Kincaid, and K. Ugurbil, "NMR Chemical Shift Imaging in Three Dimensions," Proceedings of the National Academy of Sciences of the United States of America **79**(11), 3523-3526 (1982)..44-45

[15] B. Burke, M. Lamey, S. Rathee, B. Murray, and B. G. Fallone, "Radio frequency noise from clinical linear accelerators," Phys. Med. Biol. **54**(8), 2483-2492 (2009)…….....166-167

[16] R. W. Byhardt, J. D. Cox, A. Hornburg, and G. Liermann, "Weekly localization films and detection of field placement errors," Int. J. Radiat. Oncol. Biol. Phys. **4**(9-10), 881-887 (1978)……9

[17] L. I. Cervino, J. Du, and S. B. Jiang, "MRI-guided tumor tracking in lung cancer radiotherapy," Phys. Med. Biol. **56**(13), 3773-3785 (2011)…….. …….……...91, 117-118

[18] A. Chandra, L. Dong, E. Huang, D. A. Kuban, L. O'Neill, I. Rosen, and A. Pollack, "Experience of ultrasound-based daily prostate localization," Int. J. Radiat. Oncol. Biol. Phys. **56**(2), 436-447 (2003)……..12

[19] G. B. Chavhan, P. S. Babyn, B. G. Jankharia, H.-L. M. Cheng, and M. M. Shroff, "Steady-State MR Imaging Sequences: Physics, Classification, and Clinical Applications," Radiographics **28**(4), 1147-1160 (2008)……..49

[20] H. C. Chen, A. Wu, E. D. Brandner, D. E. Heron, M. S. Huq, N. J. Yue, and W. C. Chen, "Dosimetric evaluations of the interplay effect in respiratory-gated intensity-modulated radiation therapy," Med. Phys. **36**(3), 893-903 (2009)…….166

[21] B. Cho, P. R. Poulsen, A. Sloutsky, A. Sawant, and P. J. Keall, "First Demonstration of Combined Kv/Mv Image-Guided Real-Time Dynamic Multileaf-Collimator Target Tracking," Int. J. Radiat. Oncol. Biol. Phys. **74**(3), 859-867 (2009)……...…16, 63, 116-117, 140, 154, 192, 200

[22] S. P. M. Crijns, B. W. Raaymakers, and J. J. W. Lagendijk, "Proof of concept of MRI-guided tracked radiation delivery: tracking one-dimensional motion," Phys. Med. Biol. **57**(23), 7863-7872 (2012)…….217

[23] I. Crooks and B. G. Fallone, "A Novel Algorithm for the Edge-Detection and Edge Enhancement of Medical Images," Med. Phys. **20**(4), 993-998 (1993)……...70, 73

[24] L. A. Dawson and C. Menard, "Imaging in Radiation Oncology: A Perspective," Oncologist **15**(4), 338-349 (2010)…….194

[25] L. A. Dawson and M. B. Sharpe, "Image-guided radiotherapy: rationale, benefits, and limitations," Lancet Oncology **7**(10), 848-858 (2006)…11-12

[26] J. Dempsey, B. Dionne, J. Fitzsimmons, A. Haghigat, J. Li, D. Low, S. Mutic, J. Palta, H. Romeijn, and G. Sjoden, "A real-time MRI guided external beam radiotherapy delivery system," Med. Phys. **33**(6), 2254 (2006)……...165

[27] J. F. Dempsey, D. Benoit, J. R. Fitzsimmons, A. Haghighat, J. G. Li, D. A. Low, S. Mutic, J. R. Palta, H. E. Romeijn, and G. E. Sjoden, "A device for realtime 3D image-guided IMRT," Int. J. Radiat. Oncol. Biol. Phys. **63**(2), 1095 (2005)…….18-19, 64, 154, 156

[28] T. Depuydt, D. Verellen, O. Haas, T. Gevaert, N. Linthout, M. Duchateau, K. Tournel, T. Reynders, K. Leysen, M. Hoogeman, G. Storme, and M. D. Ridder, "Geometric accuracy of a novel gimbals based radiation therapy tumor tracking system," Radiother. Oncol. **98**(3), 365-372 (2011)….15, 63

[29] J. Dinkel, C. Hintze, R. Tetzlaff, P. E. Huber, K. Herfarth, J. Debus, H. U. Kauczor, and C. Thieke, "4D-MRI analysis of lung tumor motion in patients with hemidiaphragmatic paralysis," Radiother. Oncol. **91**(3), 449-454 (2009)……..18

[30] G. G. Echner, W. Kilby, M. Lee, E. Earnst, S. Sayeh, A. Schlaefer, B. Rhein, J. R. Dooley, C. Lang, O. Blanck, E. Lessard, C. R. Maurer Jr, and W. Schlegel, "The design, physical properties and clinical utility of an iris collimator for robotic radiosurgery," Phys. Med. Biol. **54**(18), 5359-5380 (2009)…….16

[31] R. Eisberg and R. Resnick, *Quantum Physics of Atoms, Molecules, Solids, Nuclei, and Particles*, 2nd edition. (John Wiley & Sons, Inc., USA, 1985).. ……..31-32

[32] L. Ekberg, O. Holmberg, L. Wittgren, G. Bjelkengren, and T. Landberg, "What margins should be added to the clinical target volume in radiotherapy treatment planning for lung cancer?," Radiother. Oncol. **48**(1), 71-77 (1998)……...13, 17, 64, 193

[33] B. Fallone, M. Carlone, B. Murray, S. Rathee, T. Stanescu, S. Steciw, K. Wachowicz, and C. Kirkby, "Development of a Linac-MRI System for

Real-Time ART," Med. Phys. **34**(6), 2547-2547 (2007)……...64

[34] B. G. Fallone, B. Murray, S. Rathee, T. Stanescu, S. Steciw, S. Vidakovic, E. Blosser, and D. Tymofichuk, "First MR images obtained during megavoltage photon irradiation from a prototype integrated linac-MR system," Med. Phys. **36**(6), 2084-2088 (2009)…….. ……18, 20, 64, 117, 154, 156, 165, 170, 189, 194

[35] C. T. G. Flear, R. G. Carpenter, and I. Florence, "Variability in the water, sodium, potassium, and chloride content of human skeletal muscle," J Clin Pathol. **18**(1), 74-81 (1965)……80

[36] J. V. Frangioni, "New technologies for human cancer imaging," J Clin Oncol. **26**(24), 4012-4021 (2008)……193

[37] M. Fuss, B. J. Salter, S. X. Cavanaugh, C. Fuss, A. Sadeghi, C. D. Fuller, A. Ameduri, J. M. Hevezi, T. S. Herman, and C. R. Thomas, "Daily ultrasound-based image-guided targeting for radiotherapy of upper abdominal malignancies," Int. J. Radiat. Oncol. Biol. Phys. **59**(4), 1245-1256 (2004)……12

[38] R. Gassert, A. Yamamoto, D. Chapuis, L. Dovat, H. Bleuler, and E. Burdet, "Actuation Methods for Applications in MR Environments," Concepts in Magnetic Resonance Part B: Magnetic Resonance Engineering **29B**(4), 191-209 (2006)……...154-155

[39] M. J. Ghilezan, D. A. Jaffray, J. H. Siewerdsen, M. van Herk, A. Shetty, M. B. Sharpe, S. Z. Jafri, F. A. Vicini, R. C. Matter, D. S. Brabbins, and A. A. Martinez, "Prostate gland motion assessed with cine-magnetic resonance imaging (cine-MRI)," Int. J. Radiat. Oncol. Biol. Phys. **62**(2), 406-417 (2005)……...18

[40] D. P. Gierga, J. Brewer, G. C. Sharp, M. Betke, C. G. Willett, and G. T. Y. Chen, "The correlation between internal and external markers for abdominal tumors: Implications for respiratory gating," Int. J. Radiat. Oncol. Biol. Phys. **61**(5), 1551-1558 (2005)……17, 193

[41] P. Giraud, E. Morvan, L. Claude, F. Mornex, C. Le Pechoux, J. M. Bachaud, P. Boisselier, V. Beckendorf, M. Morelle, and M. O. Carrere, "Respiratory Gating Techniques for Optimization of Lung Cancer Radiotherapy," J Thorac Oncol. **6**(12), 2058-2068 (2011)……14

[42] R. C. Gonzalez and R. E. Woods, *Digital Image Processing*, (Prentice Hall, New Jersey, 2002)……..74

[43] J. H. Goodband, O. C. L. Haas, and J. A. Mills, "A comparison of neural network approaches for on-line prediction in IGRT," Med. Phys. **35**(3),

1113-1122 (2008)……...…..117-118, 146, 218

[44] B. A. Groh, J. H. Siewerdsen, D. G. Drake, J. W. Wong, and D. A. Jaffray, "A performance comparison of flat-panel imager-based MV and kV cone-beam CT," Med. Phys. **29**(6), 967-975 (2002)…….10-11

[45] E. M. Haacke, R. Brown, M. Thompson, and R. Venkatesan, *Magnetic resonance imaging : physical principles and sequence design*, (J. Wiley & Sons, USA, 1999)…….77-78

[46] S. Han-Oh, B. Y. Yi, F. Lerma, B. L. Berman, M. Gui, and C. Yu, "Verification of MLC based real-time tumor tracking using an electronic portal imaging device," Med. Phys. **37**(6), 2435-2440 (2010)……..16

[47] T. Harada, H. Shirato, S. Ogura, S. Oizumi, K. Yamazaki, S. Shimizu, R. Onimaru, K. Miyasaka, M. Nishimura, and H. Dosaka-Akita, "Real-time tumor-tracking radiation therapy for lung carcinoma by the aid of insertion of a gold marker using bronchofiberscopy," Cancer **95**(8), 1720-1727 (2002)……...15, 63, 192

[48] H. Hatabu, D. C. Alsop, J. Listerud, M. Bonnet, and W. B. Gefter, "T2*and proton density measurement of normal human lung parenchyma using submillisecond echo time gradient echo magnetic resonance imaging," Eur J Radiol. **29**(3), 245-252 (1999)……...76, 81

[49] H. Hatabu, J. Gaa, E. Tadamura, K. J. Edinburgh, K. W. Stock, E. Garpestad, and R. R. Edelman, "MR imaging of pulmonary parenchyma with a half-Fourier single-shot turbo spin-echo (HASTE) sequence," Eur J Radiol. **29**(2), 152-159 (1999)……...…67

[50] S. S. Haykin, *Neural networks : a comprehensive foundation*, 2nd ed. (Prentice Hall, Upper Saddle River, NJ, 1999)…...54-55, 57, 121-122, 219

[51] N. He, C. M. Xie, W. D. Wei, C. C. Pan, W. Y. Wang, N. Lv, and P. H. Wu, "A new, preoperative, MRI-based scoring system for diagnosing malignant axillary lymph nodes in women evaluated for breast cancer," Eur J Radiol. **81**(10), 2602-2612 (2012)……18

[52] J. H. Hendry, B. Jeremic, and E. H. Zubizarreta, "Normal tissue complications after radiation therapy," Rev. Panam. Salud. Publica. **20**(2-3), 151-160 (2006)……...13, 64

[53] C. W. Hurkmans, P. Remeijer, J. V. Lebesque, and B. J. Mijnheer, "Set-up verification using portal imaging; review of current clinical practice," Radiother. Oncol. **58**(2), 105-120 (2001)……7, 8

[54] ICRU, *Prescribing, Recording and Reporting Photon Beam Therapy,*

*Report 50*, (ICRU, Bethesda, 1993)…….4

[55] ICRU, *Prescribing, Recording and Reporting Photon Beam Therapy, Report 62*, (ICRU, Bethesda, 1999)…….4

[56] M. Imura, K. Yamazaki, H. Shirato, R. Onimaru, M. Fujino, S. Shimizu, T. Harada, S. Ogura, H. Dosaka-Akita, K. Miyasaka, and M. Nishimura, "Insertion and fixation of fiducial markers for setup and tracking of lung tumors in radiotherapy," Int. J. Radiat. Oncol. Biol. Phys. **63**(5), 1442-1447 (2005)……....17, 193

[57] National Cancer Institute fact sheet 7.1: radiation therapy for cancer. http://www.cancer.gov/cancertopics/factsheet/Therapy/radiation (2010)...2

[58] D. Ionascu, S. B. Jiang, S. Nishioka, H. Shirato, and R. I. Berbeco, "Internal-external correlation investigations of respiratory induced motion of lung tumors," Med. Phys. **34**(10), 3893-3903 (2007)……17, 193

[59] M. K. Islam, T. G. Purdie, B. D. Norrlinger, H. Alasti, D. J. Moseley, M. B. Sharpe, J. H. Siewerdsen, and D. A. Jaffray, "Patient dose from kilovoltage cone beam computed tomography imaging in radiation therapy," Med. Phys. **33**(6), 1573-1582 (2006)…….11

[60] M. A. Jabbar and M. A. Rahman, "Radio frequency interference of electric motors and associated controls," IEEE Industry Applications **27**(1), 27-31 (1991)……...166

[61] D. A. Jaffray and J. H. Siewerdsen, "Cone-beam computed tomography with a flat-panel imager: Initial performance characterization," Med. Phys. **27**(6), 1311-1323 (2000)……11

[62] D. A. Jaffray, J. H. Siewerdsen, J. W. Wong, and A. A. Martinez, "Flat-panel cone-beam computed tomography for image-guided radiation therapy," Int. J. Radiat. Oncol. Biol. Phys. **53**(5), 1337-1349 (2002)……11

[63] S. B. Jiang, "Technical aspects of image-guided respiration-gated radiation therapy," Medical Dosimetry **31**(2), 141-151 (2006)……...…13-14

[64] J. H. Jonsson, M. G. Karlsson, M. Karlsson, and T. Nyholm, "Treatment planning using MRI data: an analysis of the dose calculation accuracy for different treatment regions," Radiat Oncol. **5**(62), 1-8 (2010)…….194

[65] Y. Kamino, K. Takayama, M. Kokubo, Y. Narita, E. Hirai, N. Kawawda, T. Mizowaki, Y. Nagata, T. Nishidai, and M. Hiraoka, "Development of a four-dimensional image-guided radiotherapy system with a gimbaled X-ray head," Int. J. Radiat. Oncol. Biol. Phys. **66**(1), 271-278 (2006)….15-16

[66] H. Kato, M. Kuroda, K. Yoshimura, A. Yoshida, K. Hanamoto, S. Kawasaki, K. Shibuya, and S. Kanazawa, "Composition of MRI phantom equivalent to human tissues," Med. Phys. **32**(10), 3199-3208 (2005)…...79

[67] P. J. Keall, G. S. Mageras, J. M. Balter, R. S. Emery, K. M. Forster, S. B. Jiang, J. M. Kapatoes, D. A. Low, M. J. Murphy, B. R. Murray, C. R. Ramsey, M. B. Van Herk, S. S. Vedam, J. W. Wong, and E. Yorke, "The management of respiratory motion in radiation oncology report of AAPM Task Group 76," Med. Phys. **33**(10), 3874-3900 (2006)……..…….
……..13, 67, 118, 147, 195

[68] J. Kennedy and R. Eberhart, "Particle swarm optimization," in Proceedings of the 1995 IEEE International Conference on Neural Networks, Perth, Australia, Nov. 27-Dec. 1, 1995……58, 128

[69] F. M. Khan, *The physics of radiation therapy*, 3rd ed. (Lippincott Williams & Wilkins, Philadelphia, 2010)…… 5-6

[70] V. S. Khoo and D. L. Joon, "New developments in MRI for target volume delineation in radiotherapy," Br J Radiol. **79**(Special Issue 1), S2-S15 (2006)……...194

[71] S. Kim and T.-S. Suh, "Imaging in radiation therapy," Nuclear engineering and technology **38**(4), 327-342 (2006)……..12

[72] C. Kirkby, B. Murray, S. Rathee, and B. G. Fallone, "Lung dosimetry in a linac-MRI radiotherapy unit with a longitudinal magnetic field," Med. Phys. **37**(9), 4722-4732 (2010)……..21

[73] C. Kirkby, T. Stanescu, S. Rathee, M. Carlone, B. Murray, and B. G. Fallone, "Patient dosimetry for hybrid MRI-radiotherapy systems," Med. Phys. **35**(3), 1019-1027 (2008)……165

[74] K. Kitamura, H. Shirato, S. Shimizu, N. Shinohara, T. Harabayashi, T. Shimizu, Y. Kodama, H. Endo, R. Onimaru, S. Nishioka, H. Aoyama, K. Tsuchiya, and K. Miyasaka, "Registration accuracy and possible migration of internal fiducial gold marker implanted in prostate and liver treated with real-time tumor-tracking radiation therapy (RTRT)," Radiother. Oncol. **62**(3), 275-281 (2002)……..17, 63, 193

[75] S. S. Korreman, A. N. Pedersen, T. J. Nottrup, L. Specht, and H. Nystrom, "Breathing adapted radiotherapy for breast cancer: Comparison of free breathing gating with the breath-hold technique," Radiother. Oncol. **76**(3), 311-318 (2005)……...14

[76] A. Krauss, S. Nill, and U. Oelfke, "The comparative performance of four respiratory motion predictors for real-time tumour tracking," Phys. Med.

Biol. **56**(16), 5303-5317 (2011)……117-118, 146, 218

[77] A. Krauss, S. Nill, M. Tacke, and U. Oelfke, "Electromagnetic Real-Time Tumor Position Monitoring and Dynamic Multileaf Collimator Tracking Using a Siemens 160 MLC: Geometric and Dosimetric Accuracy of an Integrated System," Int. J. Radiat. Oncol. Biol. Phys. **79**(2), 579-587 (2010)……..…..116-117, 140, 192, 200

[78] D. A. Kuban, L. Dong, R. Cheung, E. Strom, and R. De Crevoisier, "Ultrasound-based localization," Sem. Rad. Onc. **15**(3), 180-191 (2005)…. ……12

[79] J. J. W. Lagendijk, B. W. Raaymakers, A. J. E. Raaijmakers, J. Overweg, K. J. Brown, E. M. Kerkhof, R. W. van der Put, B. Hardemark, M. van Vutpen, and U. A. van der Heide, "MRI/linac integration," Radiother. Oncol. **86**(1), 25-29 (2008)……..165

[80] M. Lamey, J. Yun, S. Rathee, and B. G. Fallone, "Radio frequency noise from an MLC: a feasibility study of the use of an MLC for linac-MR systems," Phys. Med. Biol. **55**(4), 981-994 (2010)..... ……..2, 155, 162, 194-195, 199

[81] K. M. Langen and D. T. L. Jones, "Organ motion and its management," Int. J. Radiat. Oncol. Biol. Phys. **50**(1), 265-278 (2001)……7, 165

[82] J. Lattanzi, S. McNeeley, W. Pinover, E. Horwitz, I. Das, T. E. Schultheiss, and G. E. Hanks, "A comparison of daily CT localization to a daily ultrasound-based system in prostate cancer," Int. J. Radiat. Oncol. Biol. Phys. **43**(4), 719-725 (1999)……..12

[83] J. P. Lewis, "Fast Template Matching," Vision Interface 95, Canadian Image processing and Pattern Recognition Society, 120-123 (1995)……72

[84] S. S. Lo, B. S. Teh, J. J. Lu, and T. E. Schefter, *Stereotactic Body Radiation Therapy*, (Springer-Verlag Berlin and Heidelberg GmbH & Co. K, Berlin, 2012)…….……13, 195

[85] A. E. Lujan, E. W. Larsen, J. M. Balter, and R. K. Ten Haken, "A method for incorporating organ motion due to breathing into 3D dose calculations," Med. Phys. **26**(5), 715-720 (1999)……200

[86] H. R. Maier and G. C. Dandy, "The effect of internal parameters and geometry on the performance of back-propagation neural networks: an empirical study," Environmental Modelling & Software **13**(2), 193-209 (1998)…….58, 118, 128, 203

[87] C. A. McBain, A. M. Henry, J. Sykes, A. Amer, T. Marchant, C. M.

Moore, J. Davies, J. Stratford, C. McCarthy, B. Porritt, P. Williams, V. S. Khoo, and P. Price, "X-ray volumetric imaging in image-guided radiotherapy: The new standard in on-treatment imaging," Int. J. Radiat. Oncol. Biol. Phys. **64**(2), 625-634 (2006)……..11

[88] D. McQuaid, M. Partridge, J. R. N. Symonds-Tayler, P. M. Evans, and S. Webb, "Experimental Validation of a Target Tracking IMRT Delivery with Conventional MLCs," Clinical Oncology **21**(3), 243-244 (2009)...218

[89] S. Midgley, R. M. Millar, and J. Dudson, "A feasibility study for megavoltage cone beam CT using a commercial EPID," Phys. Med. Biol. **43**(1), 155-169 (1998)……11

[90] M. J. Murphy and S. Dieterich, "Comparative performance of linear and nonlinear neural networks to predict irregular breathing," Phys. Med. Biol. **51**(22), 5903-5914 (2006)……146

[91] M. J. Murphy and D. Pokhrel, "Optimization of an adaptive neural network to predict breathing," Med. Phys. **36**(1), 40-47 (2009)…… ……..117-118, 140, 146, 218

[92] S. Mutic, "First Commercial Hybrid MRI-IMRT System," presented at the 54th Annual Meeting of the AAPM, Charlotte, NC, July 29 - August 2, 2012……..18-19

[93] S. Nill, J. Unkelbach, L. Dietrich, and U. Oelfke, "Online correction for respiratory motion: evaluation of two different imaging geometries," Phys. Med. Biol. **50**(17), 4087-4096 (2005)……..166

[94] E. Nioutsikou, Y. Seppenwoolde, J. R. N. Symonds-Tayler, B. Heijmen, P. Evans, and S. Webb, "Dosimetric investigation of lung tumor motion compensation with a robotic respiratory tracking system: An experimental study," Med. Phys. **35**(4), 1232-1240 (2008)…….63, 192

[95] J. G. Och, G. D. Clarke, W. T. Sobol, C. W. Rosen, and S. K. Mun, "Acceptance Testing of Magnetic Resonance Imaging Systems - Report of AAPM Nuclear Magnetic Resonance Task Group No. 6.," Med. Phys. **19**(1), 217-229 (1992)……...80-81

[96] N. Otsu, "A Threshold Selection Method from Gray-Level Histograms," Systems, Man and Cybernetics, IEEE Transactions on **9**(1), 62-66 (1979).. ……....74

[97] C. Ozhasoglu and M. J. Murphy, "Issues in respiratory motion compensation during external-beam radiotherapy," Int. J. Radiat. Oncol. Biol. Phys. **52**(5), 1389-1399 (2002)……...14, 63

[98] L. Papiez, D. Rangaraj, and P. Keall, "Real-time DMLC IMRT delivery for mobile and deforming targets," Med. Phys. **32**(9), 3037-3048 (2005).... ……..218

[99] C. Plathow, C. Fink, S. Ley, M. Puderbach, M. Eichinger, I. Zuna, A. Schmahl, and H. U. Kauczor, "Measurement of tumor diameter-dependent mobility of lung tumors by dynamic MRI," Radiother. Oncol. **73**(3), 349-354 (2004)……..……62, 116, 138, 149, 194, 200

[100] C. Plathow, M. Klopp, C. Fink, A. Sandner, H. Hof, M. Puderbach, F. Herth, A. Schmahl, and H. U. Kauczor, "Quantitative analysis of lung and tumour mobility: comparison of two time-resolved MRI sequences," Br J Radiol. **78**(933), 836-840 (2005)…….195

[101] C. Plathow, S. Ley, C. Fink, M. Puderbach, W. Hosch, A. Schmahl, J. Debus, and H. U. Kauczor, "Analysis of intrathoracic tumor mobility during whole breathing cycle by dynamic MRI," Int. J. Radiat. Oncol. Biol. Phys. **59**(4), 952-959 (2004)……..18, 118

[102] C. Plathow, M. Schoebinger, C. Fink, H. Hof, J. Debus, H. P. Meinzer, and H. U. Kauczor, "Quantification of lung tumor volume and rotation at 3D dynamic parallel MR imaging with view sharing: Preliminary results," Radiology **240**(2), 537-545 (2006)…….….62, 72

[103] B. W. Raaymakers, J. J. Wlagendijk, J. Overweg, J. G. M. Kok, A. J. E. Raaijmakers, E. M. Kerkhof, R. W. van der Put, I. Meijsing, S. P. M. Crijns, F. Benedosso, M. van Vulpen, C. H. W. de Graaff, J. Allen, and K. J. Brown, "Integrating a 1.5 T MRI scanner with a 6 MV accelerator: proof of concept," Phys. Med. Biol. **54**(12), N229-N237 (2009)…….. ……..…….18, 64, 154, 156

[104] I. Rabinowitz, J. Broomberg, M. Goitein, K. McCarthy, and J. Leong, "Accuracy of radiation-field alignment in clinical-practice," Int. J. Radiat. Oncol. Biol. Phys. **11**(10), 1857-1867 (1985)……..……9

[105] S. Rajaram, A. J. Swift, D. Capener, A. Telfer, C. Davies, C. Hill, R. Condliffe, C. Elliot, J. Hurdman, D. G. Kiely, and J. M. Wild, "Lung Morphology Assessment with Balanced Steady-State Free Precession MR Imaging Compared with CT," Radiology **263**(2), 569-577 (2012)……..198

[106] T. W. Redpath, "Signal-to-noise ratio in MRI," Br J Radiol. **71**(847), 704-707 (1998)……..78

[107] E. Rietzel, S. J. Rosenthal, D. P. Gierga, C. G. Willett, and G. T. Y. Chen, "Moving targets: detection and tracking of internal organ motion for treatment planning and patient set-up," Radiother. Oncol. **73**(2), S68-S72 (2004)……...165

[108] C. Saw, E. Brandner, R. Selvaraj, H. Chen, M. Saiful Huq, and D. Heron, "A review on the clinical implementation of respiratory-gated radiation therapy," Biomed Imaging Interv J **3**(1), e40 (2007)……13-14

[109] A. Sawant, R. L. Smith, R. B. Venkat, L. Santanam, B. C. Cho, P. Poulsen, H. Cattell, L. J. Newell, P. Parikh, and P. J. Keall, "Toward Submillimeter Accuracy in the Management of Intrafraction Motion: the Integration of Real-Time Internal Position Monitoring and Multileaf Collimator Target Tracking," Int. J. Radiat. Oncol. Biol. Phys. **74**(2), 575-582 (2009)…….……...…….63, 116-117, 140, 192, 200

[110] A. Sawant, R. Venkat, V. Srivastava, D. Carlson, S. Povzner, H. Cattell, and P. Keall, "Management of three-dimensional intrafraction motion through real-time DMLC tracking," Med. Phys. **35**(5), 2050-2061 (2008)... ……15, 166

[111] K. Scheffler and J. Hennig, "Is TrueFISP a gradient-echo or a spin-echo sequence?," Magn Reson Med. **49**(2), 395-397 (2003)……..…77

[112] K. Scheffler and S. Lehnhardt, "Principles and applications of balanced SSFP techniques," Eur Radiol. **13**(11), 2409-2418 (2003)……96

[113] H. C. Schmidt, D. Tscholakoff, H. Hricak, and C. B. Higgins, "MR Image-Contrast and Relaxation-Times of Solid Tumors in the Chest, Abdomen, and Pelvis," J Comput Assist Tomogr. **9**(4), 738-748 (1985)……76, 80-81

[114] G. C. Sharp, S. B. Jiang, S. Shimizu, and H. Shirato, "Prediction of respiratory tumour motion for real-time image-guided radiotherapy," Phys. Med. Biol. **49**(3), 425-440 (2004)……117-118, 218

[115] Y. H. Shi and R. Eberhart, "A modified particle swarm optimizer," in Proceedings of the 1998 IEEE International Conference on Evolutionary Computation, Anchorage, Alaska, May 4-9, 1998……...59-60, 128

[116] H. Shirato, Y. Seppenwoolde, K. Kitamura, R. Onimura, and S. Shimizu, "Intrafractional tumor motion: Lung and liver," Sem. Rad. Onc. **14**(1), 10-18 (2004)……...…….62, 116, 138, 149, 194

[117] H. Shirato, S. Shimizu, K. Kitamura, T. Nishioka, K. Kagei, S. Hashimoto, H. Aoyama, T. Kunieda, N. Shinohara, H. Dosaka-Akita, and K. Miyasaka, "Four-dimensional treatment planning and fluoroscopic real-time tumor tracking radiotherapy for moving tumor," Int. J. Radiat. Oncol. Biol. Phys. **48**(2), 435-442 (2000)……16

[118] H. Shirato, S. Shimizu, T. Kunieda, K. Kitamura, M. van Herk, K. Kagei, T. Nishioka, S. Hashimoto, K. Fujita, H. Aoyama, K. Tsuchiya, K. Kudo,

and K. Miyasaka, "Physical aspects of a real-time tumor-tracking system for gated radiotherapy," Int. J. Radiat. Oncol. Biol. Phys. **48**(4), 1187-1195 (2000)……14

[119] H. Shirato, K. Suzuki, G. C. Sharp, K. Fujita, R. Onimaru, M. Fujino, N. Kato, Y. Osaka, R. Kinoshita, H. Taguchi, S. Onodera, and K. Miyasaka, "Speed and amplitude of lung tumor motion precisely detected in four-dimensional setup and in real-time tumor-tracking radiotherapy," Int. J. Radiat. Oncol. Biol. Phys. **64**(4), 1229-1236 (2006)…….62, 117, 194, 200

[120] R. L. Smith, K. Lechleiter, K. Malinowski, D. M. Shepard, D. J. Housley, M. Afghan, J. Newell, J. Petersen, B. Sargent, and P. Parikh, "Evaluation of Linear Accelerator Gating with Real-Time Electromagnetic Tracking," Int. J. Radiat. Oncol. Biol. Phys. **74**(3), 920-927 (2009)…….16, 63

[121] R. L. Smith, A. Sawant, L. Santanam, R. B. Venkat, L. J. Newell, B. C. Cho, P. Poulsen, H. Catell, P. J. Keall, and P. J. Parikh, "Integration of Real-Time Internal Electromagnetic Position Monitoring Coupled with Dynamic Multileaf Collimator Tracking: an Intensity-Modulated Radiation Therapy Feasibility Study," Int. J. Radiat. Oncol. Biol. Phys. **74**(3), 868-875 (2009)……..218

[122] P. Y. Song, M. Washington, F. Vaida, R. Hamilton, D. Spelbring, B. Wyman, J. Harrison, G. T. Y. Chen, and S. Vijayakumar, "A comparison of four patient immobilization devices in the treatment of prostate cancer patients with three dimensional conformal radiotherapy," Int. J. Radiat. Oncol. Biol. Phys. **34**(1), 213-219 (1996)……8

[123] F. Sterzing, R. Engenhart-Cabillic, M. Flentje, and J. Debus, "Image-Guided Radiotherapy A New Dimension in Radiation Oncology," Deutsches Arzteblatt International **108**(16), 274-280 (2011).…….9, 12, 62

[124] Y. Suh, S. Dieterich, B. Cho, and P. J. Keall, "An analysis of thoracic and abdominal tumour motion for stereotactic body radiotherapy patients," Phys. Med. Biol. **53**(13), 3623-3640 (2008)…….. ……..15, 82, 121, 127, 139, 147, 149

[125] Y. L. Suh, A. Sawant, R. Venkat, and P. J. Keall, "Four-dimensional IMRT treatment planning using a DMLC motion-tracking algorithm," Phys. Med. Biol. **54**(12), 3821-3835 (2009)……218

[126] C. R. Suriano, J. R. Suriano, G. Thiele, and T. W. Holmes, "Prediction of radiated emissions from DC motors," 1998 International Symposium on Electromagnetic Compatibility, Denver, CO, Aug 24-28, 1998…… ……..166, 168, 184, 186-187

[127] M. Suzuki, Y. Nishimura, K. Nakamatsu, M. Okumura, H. Hashiba, R.

Koike, S. Kanamori, and T. Shibata, "Analysis of interfractional set-up errors and intrafractional organ motions during IMRT for head and neck tumors to define an appropriate planning target volume (PTV)- and planning organs at risk volume (PRV)-margins," Radiother. Oncol. **78**(3), 283-290 (2006)……...13

[128] W. Swindell, R. G. Simpson, J. R. Oleson, C.-T. Chen, and E. A. Grubbs, "Computed tomography with a linear accelerator with radiotherapy applications," Med. Phys. **10**(4), 416-420 (1983)……..11

[129] M. B. Tacke, S. Nill, A. Krauss, and U. Oelfke, "Real-time tumor tracking: automatic compensation of target motion using the Siemens 160 MLC," Med. Phys. **37**(2), 753-761 (2010)…….63, 116, 192, 200

[130] M. L. Taylor, R. L. Smith, F. Dossing, and R. D. Franich, "Robust calculation of effective atomic numbers: The Auto-Zeff software," Med. Phys. **39**(4), 1769-1778 (2012)……198

[131] S. D. Thomas, M. Mackenzie, G. C. Field, A. M. Syme, and B. G. Fallone, "Patient specific treatment verifications for helical tomotherapy treatment plans," Med. Phys. **32**(12), 3793-3800 (2005)…….211

[132] Y. Tsunashima, T. Sakae, Y. Shioyama, K. Kagei, T. Terunuma, A. Nohtomi, and Y. Akine, "Correlation between the respiratory waveform measured using a respiratory sensor and 3D tumor motion in gated radiotherapy," Int. J. Radiat. Oncol. Biol. Phys. **60**(3), 951-958 (2004)…... ……..……140, 200

[133] R. Valentine, *Motor Control Electronics Handbook*, (McGraw-Hill, New York, 1998)……..185

[134] M. van Herk, "Errors and margins in radiotherapy," Sem. Rad. Onc. **14**(1), 52-64 (2004)…….165

[135] S. S. Vedam, V. R. Kini, P. J. Keall, V. Ramakrishnan, H. Mostafavi, and R. Mohan, "Quantifying the predictability of diaphragm motion during respiration with a noninvasive external marker," Med. Phys. **30**(4), 505-513 (2003)……..63, 192

[136] D. Verellen, M. D. Ridder, and G. Storme, "A (short) history of image-guided radiotherapy," Radiother. Oncol. **86**(1), 4-13 (2008)...8, 10-11, 165

[137] P. S. Verma, H. M. Wu, M. P. Langer, I. J. Das, and G. Sandison, "Survey: Real-Time Tumor Motion Prediction for Image-Guided Radiation Treatment," Computing in Science & Engineering **13**(5), 24-35 (2011)….. ……..….117-118

[138] R. Wagman, E. Yorke, E. Ford, P. Giraud, G. Mageras, B. Minsky, and K. Rosenzweig, "Respiratory gating for liver tumors: Use in dose escalation," Int. J. Radiat. Oncol. Biol. Phys. **55**(3), 659-668 (2003)……...14

[139] C. Walter, J. Boda-Heggemann, H. Wertz, I. Loeb, A. Rahn, F. Lohr, and F. Wenz, "Phantom and in-vivo measurements of dose exposure by image-guided radiotherapy (IGRT): MV portal images vs. kV portal images vs. cone-beam CT," Radiother. Oncol. **85**(3), 418-423 (2007)……...10

[140] S. Webb, "The effect on IMRT conformality of elastic tissue movement and a practical suggestion for movement compensation via the modified dynamic multileaf collimator (dMLC) technique," Phys. Med. Biol. **50**(6), 1163-1190 (2005)…….166

[141] S. Webb, "Motion effects in (intensity modulated) radiation therapy: a review," Phys. Med. Biol. **51**(13), R403-R425 (2006)……165

[142] S. Webb, "Quantification of the fluence error in the motion-compensated dynamic MLC (DMLC) technique for delivering intensity-modulated radiotherapy (IMRT)," Phys. Med. Biol. **51**(7), L17-L21 (2006)……166

[143] S. Webb and T. Bortfeld, "A new way of adapting IMRT delivery fraction-by-fraction to cater for variable intrafraction motion," Phys. Med. Biol. **53**(18), 5177-5191 (2008)……166

[144] M. Weissbluth, C. J. Karzmark, R. E. Steele, and A. H. Selby, "The stanford medical linear accelerator. 2. installation and physical measurements," Radiology **72**(2), 242-253 (1959)……..9

[145] L. F. A. Wessels and E. Barnard, "Avoiding false local minima by proper initialization of connections," IEEE Transactions on Neural Networks **3**(6), 899-905 (1992)……...58, 118, 128, 203

[146] O. Wieben, C. Francois, and S. B. Reeder, "Cardiac MRI of ischemic heart disease at 3 T: Potential and challenges," Eur J Radiol. **65**(1), 15-28 (2008). ……96

[147] K. Wijesooriya, C. Bartee, J. V. Siebers, S. S. Vedam, and P. J. Keall, "Determination of maximum leaf velocity and acceleration of a dynamic multileaf collimator: Implications for 4D radiotherapy," Med. Phys. **32**(4), 932-941 (2005)…….161

[148] T. R. Willoughby, P. A. Kupelian, J. Pouliot, K. Shinohara, M. Aubin, M. Roach, L. L. Skrumeda, J. M. Balter, D. W. Litzenberg, S. W. Hadley, J. T. Wei, and H. M. Sandler, "Target localization and real-time tracking using the calypso 4D localization system in patients with localized prostate cancer," Int. J. Radiat. Oncol. Biol. Phys. **65**(2), 528-534 (2006)…….16

[149] J. Q. Wu, D. Ruan, B. Cho, A. Sawant, J. Petersen, L. J. Newell, H. Cattell, and P. J. Keall, "Electromagnetic Detection and Real-Time DMLC Adaptation to Target Rotation During Radiotherapy," Int. J. Radiat. Oncol. Biol. Phys. **82**(3), E545-E553 (2012)……16

[150] P. Yen, R. W. Katzberg, M. H. Buonocore, and J. Sonico, "Dynamic MR Imaging of the Temporomandibular Joint Using a Balanced Steady-State Free Precession Sequence at 3T," AJNR Am J Neuroradiol. **34**(3), E24-26 (2013)……...118

[151] E. Yip, J. Yun, Z. Gabos, K. Wachowicz, S. Rathee, and B. G. Fallone, "Evaluation of a Real Time Tumour Autocontouring Algorithm Using In-Vivo Lung MR Images with Various Contrast to Noise Ratios," presented at the 54th Annual Meeting of the AAPM, Charlotte, NC, July 29 - August 2, 2012……..2, 221

[152] J. Yun, M. Mackenzie, S. Rathee, D. Robinson, and B. G. Fallone, "An artificial neural network (ANN)-based lung-tumor motion predictor for intrafractional MR tumor tracking," Med. Phys. **39**(7), 4423-4433 (2012)... ……..…2, 194-195, 203, 207, 220

[153] J. Yun, M. MacKenzie, D. Robinson, S. Rathee, B. Murray, and B. G. Fallone, "Real-Time MR Tumour Tracking Using a Linac-MR System," presented at the 56th Annual Meeting of the COMP, Ottawa, ON, June 16-19, 2010……...……117

[154] J. Yun, J. St. Aubin, S. Rathee, and B. G. Fallone, "Brushed permanent magnet DC MLC motor operation in an external magnetic field," Med. Phys. **37**(5), 2131-2134 (2010)…….2, 194-195

[155] J. Yun, K. Wachowicz, M. Mackenzie, S. Rathee, D. Robinson, and B. G. Fallone, "First demonstration of intrafractional tumor-tracked irradiation using 2D phantom MR images on a prototype linac-MR," Med. Phys. **40**(5), 051718 (12pp.) (2013)……...2

[156] J. Yun, E. Yip, K. Wachowicz, S. Rathee, M. Mackenzie, D. Robinson, and B. G. Fallone, "Evaluation of a lung tumor autocontouring algorithm for intrafractional tumor tracking using low-field MRI: A phantom study," Med. Phys. **39**(3), 1481-1494 (2012)……. ……...2, 106, 112, 114, 117, 119, 147, 194-195, 201-202, 221